Gasification and Combustion Modeling for Porous Char Particles

by

Simcha Lev Singer

B.S., Mechanical Engineering
Northwestern University, 2004

S.M., Mechanical Engineering
Massachusetts Institute of Technology, 2006

ARCHIVES
MASSACHUSETTS INSTITUTE
OF TECHNOLOGY
JUN 28 2012
LIBRARIES

Submitted to the Department of Mechanical Engineering in Partial Fulfillment of the Requirements for the Degree of

Doctor of Philosophy in Mechanical Engineering

at the

MASSACHUSETTS INSTITUTE OF TECHNOLOGY

JUNE 2012

© 2012 Massachusetts Institute of Technology. All rights reserved.

Signature of Author . . . .
Department of Mechanical Engineering
May 18, 2012

Certified by. . . . .
Ahmed F. Ghoniem
Ronald C. Crane (1972) Professor of Mechanical Engineering
Thesis Supervisor

Accepted by. . . . .
David E. Hardt
Chairman, Department Committee on Graduate Students

Gasification and Combustion Modeling for Porous Char Particles

by

Simcha Lev Singer

Submitted to the Department of Mechanical Engineering on 18 May 2012, in Partial Fulfillment
of the Requirements for the Degree of Doctor of Philosophy in
Mechanical Engineering

Abstract

Gasification and combustion of porous char particles occurs in many industrial applications. Reactor-scale outputs of importance depend critically on processes that occur at the particle-scale. Because char particles often possess a wide range of pore sizes and react under varying operating conditions, predictive models which can account for the numerous physical and chemical processes and time-dependent boundary conditions to which a particle is subjected are necessary. A comprehensive, transient, spherically symmetric model of a reacting, porous char particle and its surrounding boundary layer has been developed and validated. The model accounts for heterogeneous and homogeneous reactions, pore structure evolution, gas transport in and around the porous particle, thermal annealing, fragmentation and ash behavior.

To model the pore structure evolution, an extension of the random pore model has been developed which allows different pore sizes to grow at different rates, depending on the instantaneous pore-scale reactant penetration at a given location within the particle. This is accomplished by incorporating pore-scale effectiveness factors, consistent with the random pore geometry, into equations for the growth of individual pore sizes. This framework allows the evolution of the char with local conversion to adapt to changes in boundary conditions (reactants, temperature) and the development of intra-particle gradients, rather than being pre-determined by the initial pore structure.

The effects of char gasification reactions during oxy-combustion of pulverized coal are not fully understood. The single particle char consumption model is used with output from CFD simulations of high-volatile oxy-coal combustion to analyze representative regions and trajectories along which char particle burning occurs. These realistic, time-dependent boundary conditions are used to assess the importance of the gasification reactions to the overall rate of char consumption. As conversion proceeds, gasification reactions, when significant, can alter the location within the particle where char consumption occurs, further affecting the rate of conversion by inducing structural changes that can accelerate peripheral fragmentation.

Thesis Supervisor: Ahmed F. Ghoniem
Title: Ronald C. Crane (1972) Professor of Mechanical Engineering

Acknowledgements

I would like to sincerely thank my advisor, Prof. Ghoniem, for giving me the opportunity to participate in this research project. Working on, and thinking about, my research has become something that I truly enjoy. I also would like to thank Prof. Ghoniem for his guidance over the past five years. He has given clear direction to my work, allowed me the right amount of independence and kept me focused on the big picture whenever I had the tendency to get bogged down. I would also like to thank my thesis committee members: Prof. Beer, Prof. Brisson and Prof. Green, whose advice and suggestions have helped to guide my research.

I gratefully acknowledge BP for their financial support during my PhD studies and for the many teleconferences in which their team has participated. These have not only provided beneficial feedback, but have spurred me to make steady progress along the way.

Throughout the past five years I have had the honor of working with many, many talented colleagues in the Reacting Gas Dynamics Lab, both graduate students and post-docs. Most of the lab-members with whom I have overlapped have helped me in some way and without their assistance and friendship my time in the RGD lab would have been less productive and less enjoyable. In particular, I would like to acknowledge Mayank Kumar, Rory Monaghan, Cheng Zhang and Cristina Botero, my colleagues on the BP-sponsored coal gasification project, as well as Lei Chen, with whom I have worked on oxy-combustion and with whom I have had many productive discussions over the past four years.

I would like to thank my parents, brothers, sister and grandmother for their support throughout my time in graduate school. My parents have always given me encouragement and excellent advice, about school and about life. It was really great having my brother, Elisha, live in Cambridge for a couple of years during my time in graduate school. Finally, I would like to thank my amazing wife, Ariel, for her love, support and her understanding of the schedule (both on the scale of days and years) associated with graduate-student life.

Table of Contents

Abstract..3
Acknowledgments..5
Table of Contents..6
List of Figures..9
List of Tables..15
Chapter 1. Introduction..17
    1.1 Solid Fuel Gasification and Combustion..17
    1.2 Motivation..17
    1.3 Stages of Solid Fuel Gasification..19
    1.4 Classification of Char Consumption Models..21
        1.4.1 Global Models..24
        1.4.2 Modeling Zone II Behavior..26
            1.4.2.1 Effectiveness Factor Models..27
            1.4.2.2 Conservation Equation-based Models..30
            1.4.2.3 Discrete Models..31
    1.5 Approach of this Thesis..32
    1.6 Thesis Outline..33
    Nomenclature and References (Ch. 1)..34

Chapter 2. Modeling the Physics and Chemistry of Char Consumption..39
    2.1 Conservation Equation-based Single Particle Models..39
        2.1.1 Literature Review..39
        2.1.2 Developments in the Current Approach..42
        2.1.3 Basic Model Equations..43
    2.2 Pore Structure Evolution..46
    2.3 Transport in the Porous Medium..48
    2.4 Transport in the Gas Phase..55
    2.5 Thermal Annealing..56
    2.6 Kinetics..60
    2.7 Fragmentation..65

2.8 Ash Behavior..68
2.9 Conclusions..75
Nomenclature and References (Ch. 2) 76

Chapter 3. An Adaptive Random Pore Model for Multimodal Pore Structure Evolution...........85
3.1 Introduction..85
3.2 The Random Pore Model...89
3.3 Adaptive Random Pore Model...95
3.4 Pore-Scale Effectiveness Factors...99
3.5 Method for Determination of Intrinsic Kinetic Rates...........................112
3.6 Results and Discussion..113
3.7 Conclusions...133
Nomenclature and References (Ch. 3) 135

Chapter 4. Numerical Approach...141
4.1 Numerical Implementation..141
4.2 Calculation of properties...149
Nomenclature and References (Ch. 4)...150

Chapter 5. Model Validation and Demonstration.......................................155
5.1 Introduction...155
5.2 Inputs and Experiments for Model Validation......................................155
5.3 Model Validation and Discussion..166
5.4 Effect of Flux Model..187
5.5 Demonstration of Ash Adherence Sub-model......................................192
5.6 Conclusions...195
References (Ch. 5) 196

Chapter 6. Applications of the Single Particle Char Consumption Model..........................199
6.1. The Influence of Gasification Reactions during Oxy-Combustion....................199
6.1.1. Introduction...199
6.1.2 CFD Modeling of a Pilot-Scale Oxyfuel Coal Combustion Test Facility..201
6.1.3 Application of Single Particle Char Consumption Model...................202

6.1.4. Results and Discussion..205
6.1.4.1. CFD Simulation and Particle Trajectories........................205
6.1.4.2. Single Particle Model at Constant Particle Size..................209
6.1.4.3. Single Particle Model with Fragmentation........................219
6.1.4.4. Sensitivity to Kinetic Parameters..................................223
6.1.4.5. Sensitivity to Pore Structure.......................................224
6.1.5 Conclusions...228
6.2. Entrained Flow Gasification..229
6.2.1. Introduction...229
6.2.2. Langmuir-Hinshelwood Kinetic Expressions & Char Characterization...230
6.2.3. Particle Trajectories and Thermal Annealing................................232
6.2.4. Conclusions...238
References (Ch.6) 239

Chapter 7. Conclusions and Future Work...241
7.1. Conclusions...241
7.2. Potential Applications of the Single Particle Model.........................243
References (Ch. 7) 244

Appendix..245
A.1. Flux Sub-model...245
A.2. Relation between the RPM Structural Parameter ψ_{RPM} and the ARPM.............247
References (Appendix) 251

List of Figures

Figure 1.1: Schematic of reactant concentration in and around a reacting porous particle, for the kinetically limited regime (red), the pore diffusion limited regime (green) and the boundary layer diffusion limited regime (blue)..21

Figure 1.2: Arrhenius plot illustrating regimes of char gasification. Measured activation energy corresponds to slope of line..22

Figure 1.3: Schematic illustration of species concentration and gas temperature in the particle boundary layer for (a) the single film model and (b) the double film model. Vertical line represents the char particle surface...25

Figure 3.1: Schematic illustration of the need to consider all *j-i* intersections but only a fraction, η_k, of *j-k* intersections when calculating $L_j^{'}$ 105

Figure 3.2: Schematic of the redistribution of the actual uneven conversion (gray pore) to a conversion which is uniform along the pore axis (white pore)...110

Figure 3.3: Rate versus conversion using the ARPM with five pore size bins, the RPM based on the entire pore size distribution, the RPM using the pore size distribution excluding micropores and experimental values, for (a) char sample B in air at 728 K and (b) char sample E in air at 703 K.........119

Figure 3.4: Rate versus conversion using the ARPM with different numbers of pore size bins compared to the experimentally measured values for char sample B in air at 728 K..................................122

Figure 3.5: Normalized, local surface area evolution with local conversion for different radial locations in a 128 μm diameter spherical particle with the properties of char sample B, in an environment of 10% H_2O, 40% CO_2 and 50% N_2 at 2000 K and 1 atm...123

Figure 3.6: Final true conversion profiles for char B [9] in 10% H_2O, 40% CO_2 and 50% N_2 at 2000 K and 1 atm..125

Figure 3.7: Evolution of micropore effectiveness factors with local conversion for both reactions, for char sample B in an environment of 10% H_2O, 40% CO_2 and 50% N_2 at 2000 K and 1 atm......................127

Figure 3.8: Evolution of normalized surface area with conversion for char sample B reacting in kinetic control, when exposed first to a gasifying atmosphere followed by an oxidizing one and vice versa, according to the RPM (for which there is no difference) and the ARPM.....................................128

Figure 3.9: Evolution of normalized total and individual surface areas, S_i, with conversion for char sample B reacting under kinetic control, predicted by the ARPM, (a) when exposed first to the oxidizing atmosphere and (b) when exposed first to the gasifying atmosphere..130

Figure 3.10: Evolution of X and $X_{True,i}$ on each pore size (a) when exposed first to an oxidizing atmosphere and (b) when exposed first to an atmosphere of CO_2 and H_2O..................................132

Figure 4.1: Schematic of discretization of the spatial coordinate..142

Figure 5.1: Procedure of Su and Perlmutter to extrapolate the reaction rate to the conversion at which the pore size distribution has also been measured, using the assumption that the pore structure evolution parameter of the ARPM is constant...157

Figure 5.2: Normalized rate versus conversion for the low temperature oxidation data summarized in D'amore et al. and comparison with the random pore model, with full participation of all pores and with the assumption that micropores do not participate whatsoever...159

Figure 5.3: Distribution of remaining active sites for annealing after heat treatment to different temperatures for 1800 s, using the results shown in Table 5.4 to calculate the "post-production" distribution of Spherocarb...165

Figure 5.4: Bulk gas (and calculated particle) temperatures along the reactor for cases 2, 4 and 5........167

Figure 5.5: Experimental and simulation results for conversion versus time for cases 2, 4 and 5.........168

Figure 5.6: Experimental and simulation results for particle temperature versus time for cases 2, 4 and 5, for (a) the entire reactor and (b) a magnification of the region of high particle temperatures...............169

Figure 5.7: Final conversion profiles for (a) conversion on all pores and (b) conversion attributable to reaction on micro- and meso-pores...171

Figure 5.8: Species mole fraction profiles in and around burning Spherocarb particles, at two different times for (a)-(b): Case 2, (c)-(d): Case 4 and (e)-(f): Case 5..173

Figure 5.9: Effect of variation of σ_{H_2O} on conversion (top) and particle temperature (bottom) for cases 2 and 5..176

Figure 5.10: Effect of variation of σ_{H_2O} micropore conversion profiles for cases 2 and 5................177

Figure 5.11: Effect of variation of σ_{H_2O} on surface area evolution for cases 2 and 5...............178

Figure 5.12: Conversion versus time for case 2, using the RPM and the ARPM, both of which with and without gasification reactions turned on...179

Figure 5.13: Particle temperature versus time, for case 2, using the RPM and the ARPM, both of which with and without gasification reactions turned on...179

Figure 5.14: Normalized total surface area versus total conversion, for case 2, using the RPM and the ARPM, both of which with and without gasification reactions turned on..................................180

Figure 5.15: Conversion versus time for case 5, using the RPM and the ARPM, both of which with and without gasification reactions turned on...181

Figure 5.16: Particle temperature versus time, for case 5, using the RPM and the ARPM, both of which with and without gasification reactions turned on...181

Figure 5.17: Normalized total surface area versus total conversion, for case 2, using the RPM and the ARPM, both of which with and without gasification reactions turned on..................................183

Figure 5.18: Conversion profiles, on micro-, meso- and macro- pores, with gasification reactions on and off, for (a) Case 2, using the ARPM, (b) Case 2, using the RPM, (c) Case 5, using the ARPM and (d) Case 5, using the RPM....184

Figure 5.19: Calculated particle temperature for cases 2, 4 and 5, each with the concurrent annealing sub-model turned on and off....185

Figure 5.20: Distribution of fraction of active sites remaining after Spherocarb production and after the simulated particle temperature time history, for (a) Case 2, (b) Case 4 and (c) Case 5....187

Figure 5.21: Comparison of total conversion versus time for the FSM and the DGM using several calculations of the average pore size, for combustion conditions....188

Figure 5.22: Comparison of total conversion versus time for the FSM and the DGM using several calculations of the average pore size, for gasification conditions....190

Figure 5.23: Diffusive and convective fluxes of CO_2 and H_2O in and around a char particle in a gasifying environment....191

Figure 5.24: Evolution of normalized ash (open symbols) and char (closed symbols) radii with time for three combinations of ash "melting temperature" and ash volume fraction....193

Figure 5.25: Particle temperature versus time for the same three combinations of ash "melting temperature" and ash volume fraction....194

Figure 5.26: Total Porosity profiles throughout conversion for (a) 20% ash, T_m=1450 K particle, and (b) 10% ash, T_m=1400 K particle....195

Figure 6.1: CFD simulation results for (a) temperature, (b) oxygen, (c) carbon dioxide and (d) steam distributions in the 100 kW_{th} pilot scale test facility under oxyfuel combustion with 29% oxygen....206

Figure 6.2: Histories of gas temperature and oxygen mole fraction along several coal particle trajectories in the CFD simulation. Trajectories with solid lines (PM1 and PM2) were chosen to be investigated using the comprehensive char combustion model....208

Figure 6.3: O_2 and CO_2 mole fractions, temperature and char conversion profiles in and around char particles at overall conversions of 25% and 75%, with gasification reactions turned off and on. (a) Pre-Flame region, (b) Flame region, and (c) Post-Flame region..210

Figure 6.4: (a) Char consumption rates vs. conversion for the three regions, without gasification reactions, and (b) the ratio of the rates calculated with and without gasification..211

Figure 6.5: Contribution to total char consumption rate for reaction on different pore sizes, with gasification reactions turned both on and off, for (a) the flame region and (b) the post-flame region.....213

Figure 6.6: Evolution of the normalized total and mesoporous surface areas with gasification reactions on and off, for the post-flame region..214

Figure 6.7: Variation of the normalized, local surface area with local conversion for the particle interior (r = 4 μm) and exterior (r = 48 μm), with gasification reactions both on and off, for (a) the flame region and (b) the post-flame region..215

Figure 6.8: Char consumption rates versus time along the two typical trajectories (PM1 and PM2), each with gasification reactions turned off (open symbols) and on (closed symbols), as indicated in the legend..216

Figure 6.9: Final conversion profiles for each pore size throughout the PM2 trajectory particle, for (a) gasification reactions neglected and (b) gasification reactions turned on..218

Figure 6.10: Evolution of total conversion with time, for fragmenting and constant radius particles, for gasification reactions both on and off, for the post-flame region..220

Figure 6.11: Evolution of total conversion with time, for fragmenting and constant radius particles, for gasification reactions both on and off, for (a) the PM1 trajectory particle and (b) the PM2 trajectory particle..220

Figure 6.12: Difference in total and apparent conversion vs. time between cases with gasification reactions turned on and off, for PM2......222

Figure 6.13: Char consumption rates for with and without considering gasification reactions, for high and low ΔE_a kinetics, for (a) the base case, highly microporous particle and (b) a non-microporous particle with a lower surface area......225

Figure 6.14: Ratio of char consumption rates with and without consideration of gasification reactions, for the four rows of Table 6.3, for PM2 trajectory particles......227

Figure 6.15: Ratio of surface area participating in the C+CO_2 reaction to the total, initial surface area, as a function of position and time, for the high ΔE_a kinetics and the PM2 trajectory, for (a) the highly microporous (high SA) particle and (b) the non-microporous (low SA) particle......227

Figure 6.16: Mole fraction profiles in and around a 70 μm radius particle, at t = 0.1 s, in the low temperature region......234

Figure 6.17: Conversion profiles throughout a 70 μm radius particle in the low temperature region at several times......235

Figure 6.18: Total conversion versus time for the base case and cases where the particle is exposed to the high temperature boundary conditions......236

Figure 6.19: Calculated effectiveness factors versus time for the base case, the temperature spike at 0.1 s and the temperature spike at 0.6 s......237

Figure A.1: Mole fraction profiles in and around a 57 μm radius particle, under gasification conditions, using (a) N2 as the n^{th} species and (b) CO as the n^{th} species in the calculation......247

List of Tables

Table 1.1: Advantages and disadvantages of the four approaches to char consumption modeling.........32

Table 3.1: Marginal probabilities for each *j-k* intersection (column entries) and its nearest neighbor (row entries), and the combinations which satisfy the thinning criteria..107

Table 3.2: Parameters employed in testing the ARPM with chars B and E from the experiments of Su and Perlmutter...117

Table 3.3: Kinetic parameters used for gasification reactions..124

Table 5.1: Parameters employed in pore size distribution of Spherocarb char...............................156

Table 5.2: Kinetic parameters (pre-annealing) for Spherocarb combustion and gasification..............162

Table 5.3: Annealing measurements and calculations for Spherocarb subject to different heat treatment temperatures at a constant time of 1800 s...164

Table 5.4: Parameters determined for heat treatment of Spherocarb...165

Table 5.5: Boundary conditions for Cases 2, 4 and 5..167

Table 5.6: Discretized pore size distribution for "char B"..189

Table 6.1: Kinetic parameters used for combustion and gasification reactions..............................204

Table 6.2: Bulk gas conditions in the three regions identified for char consumption.......................207

Table 6.3: Kinetic and pore structure parameters for sensitivity study. Top row corresponds to the base case..225

Table 6.4: Apparent kinetic parameters used in entrained flow gasification simulations..................231

Table 6.5: Discrete pore size distribution used in entrained flow gasification simulations.................232

Table 6.6: Boundary conditions used in simulating the gasification of char particles subject to recirculation to the post-flame zone..233

1. Introduction

1.1. Solid Fuel Gasification and Combustion

Gasification and combustion of solid fuels is widely used for power generation and chemicals production. Coal combustion accounted for almost 45% of total electricity generation in the United States in 2010 and the share was even higher in countries like China, India and Australia. In total, 42% of world electricity generation came from coal in 2010 [1]. Utilization of coal comprised 21% of primary energy consumption in the U.S. in 2010 [2] and 29.6% of worldwide energy consumption [3]. These fractions are projected to stay relatively constant over the next two decades, even as total world energy consumption continues to grow [2]. Coal and coke combustion is also important in the steel and metallurgical industries.

Gasification of coal is well-established as a means to produce chemical precursors used in a variety of industries. Integrated-gasification-combined-cycle plants offer a possible path toward coal utilization for electricity generation with limited CO_2 emissions. There is also interest in using biomass in gasification applications and there are many similarities between biomass and coal gasification.

1.2. Motivation

Modeling furnaces, boilers and gasifiers is critical to optimizing their design and operation, because full-scale experimentation and measurement can be difficult in such harsh environments. Entrained flow gasifiers are beset with reliability and cost issues. Failure of the injectors and refractory lining resulting from the high operating temperatures and harsh conditions (the presence of corrosive ash and solid particles) are common challenges. Inefficient space utilization is another concern, as it is unclear whether entrained flow gasifiers fully utilize their large volumes. In gasification and combustion systems, the presence of unconverted char is obviously problematic. While some unconverted char can be re-circulated, char trapped in slag could prevent the slag from being used for other purposes and, of course, contributes to a reduction in the cold gas efficiency of the gasifier. Similar considerations apply to unconverted char exiting with the fly ash from a furnace. Fouling deposits on downstream heat transfer surfaces are also a concern. Finally, sub-optimal operating conditions, such as using too much oxygen in entrained flow gasification, can lead to efficiency and economic penalties.

All of the problems described above are reactor-scale issues. However, processes that occur at the scale of individual fuel particles have the potential to influence reactor-scale outputs. This isn't surprising, considering that the vast majority of the energy input to the reactor is in the form of solid fuel particles. Therefore, the rate and manner of particle conversion ultimately affects all reactor-scale variables. From a modeling perspective, this implies that models at the particle-scale can influence the results of reactor-scale models.

This has been demonstrated by recent work in this laboratory using reduced order models and computational fluid dynamics simulations of entrained flow gasifiers. For instance, it was shown by CFD simulation that the morphological model employed to described char particle evolution could have a significant effect on the carbon conversion at the gasifier exit [4]. Elsewhere, the species, temperature and conversion profiles along a gasifier have been shown to be sensitive to the diameter of the char particles [5]. Similar conclusions regarding the importance of the char structure evolution model have been drawn based on a simplified gasifier model [6]. Simulations based on a reduced order model [7] have demonstrated that the relative level of reactor-scale char conversion when using CO_2 vs. H_2O coal slurry, can depend on the intra-particle diffusion resistance; a parameter that is highly dependent on the model employed for individual char particles [8].

Beyond their importance in contributing to the fidelity of reactor-scale models, single particle models can be used in their own right for fundamental studies. These could potentially lead to the development of improved analytical or simplified single particle models to be used in conjunction with reactor-scale models, to inform decisions about what phenomena should be included in simplified models, to gain insight into particle-scale processes to help determine the operating conditions or design of reactors, or to design particle-scale experiments.

1.3. Stages of Solid Fuel Gasification

When a coal particle reaches ~400 °C, the macromolecular network of which it is comprised begins to decompose in a highly complex manner, releasing light gases and tars [9]. This process is called devolatilization, or pyrolysis when it occurs in a non-reactive environment. For entrained flow gasifiers this process is typically completed after several milliseconds [10] and pulverized coal furnaces also subject particles to very high heating rates and short devolatilization times. The volatiles undergo homogeneous reactions and are converted into ultimate products much faster than the solid char. Much experimental and modeling effort has gone into the study of devolatilization, which has given rise to three comprehensive devolatilization models for coal particles that predict volatile yields, rates and to various extents, composition, based on a characterization of the parent coal: FLASHCHAIN [11], Chemical Percolation Devolatilization (CPD) [12], and the Functional Group Depolymerization, Vaporization, and Cross-linking (FG-DVC) model [13]. These models have many commonalities: they use analytical methods to characterize the coal, they model the breakdown of the macromolecular network structure, they use first order rate laws with distributed activation energies for light gas release, depolymerization and metaplast cross-linking, and they all use a network model for tar release [14]. They differ in the assumptions about the network geometries of the structure, the chemistry of the bridge breaking and cross-linking, the definition of "tar" and in the statistical methods employed [15]. Modeling devolatilization is primarily an organic chemistry problem and it is thought that any of the three models above can yield satisfactory results [14].

As the volatiles escape, the structure and constituents of the solid fuel particles can change drastically as the char (which consists of mostly solid carbon and ash inclusions) is formed and this affects most subsequent physical and chemical processes [16]. For this reason, when modeling *char* combustion or gasification, it is necessary to have experimental characterization of the char formed under relevant devolatilization conditions, rather than just characterization of the parent coal particle. It is hypothesized that for softening coals, volatile transport occurs through bubble migration during the plastic stage of devolatilization [17,18], and this process, as well as the swelling of the coal, is key to determining the resultant char structure [9]. Chars from such coals often possess a large central void and are called cenospheres. They are known to form in higher quantities at high pressures and heating rates [9]. For non-softening coals, like typical lignites and anthracites, the char structure formed is similar to an enlargement of the original pore structure of the coal. Chars from these coals typically form more dense char particles with a more uniform pore structure, but are typically less spherical.

This thesis is limited to the modeling of char consumption. In entrained flow gasification and pulverized coal combustion environments, char consumption, whether by oxidation (reaction with O_2) or gasification (reaction with CO_2, H_2O and in some cases, H_2) is significantly slower than devolatilization and the homogeneous reaction of the volatiles. From a practical and modeling perspective, the reaction of the char can be thought of as a rate-limiting-step for the entire solid fuel combustion or gasification process.

1.4. Classification of Char Consumption Models

There are many physical and chemical processes that occur during char consumption and these will be discussed in detail in Ch. 2. However, at the most basic level, char consumption can be visualized as a competition between transport and chemistry that, for most parent fuels and conditions, occurs *within* the porous char particles. This is shown schematically in Fig. 1.1, which illustrates the concentration of reactant outside and within a porous particle, for different relative rates of reaction and transport.

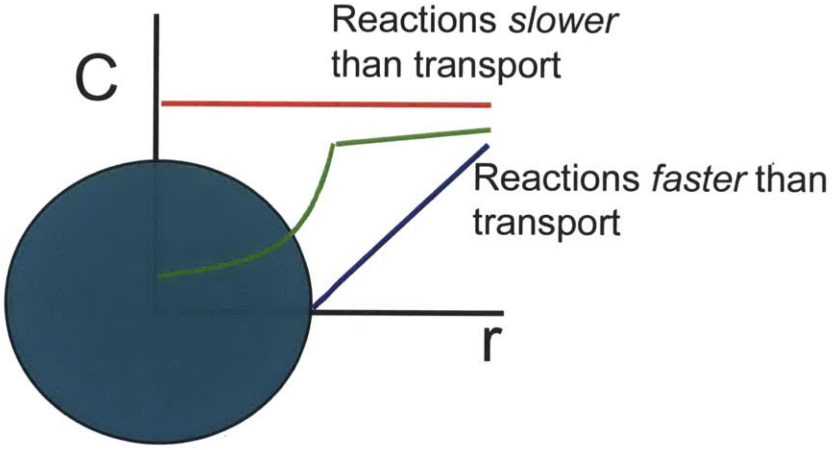

Figure 1.1. Schematic of reactant concentration in and around a reacting porous particle, for the kinetically limited regime (red), the pore diffusion limited regime (green) and the boundary layer diffusion limited regime (blue).

The phenomenon of porous char consumption is often classified into one of three idealized regimes, depending on the location within the particle where the reaction occurs [19]. For a given particle size, the regime of reaction depends most strongly on the temperature to which the particle is exposed. This is shown schematically in Fig. 1.2, with colors that correspond to the concentration profiles shown in Fig. 1.1.

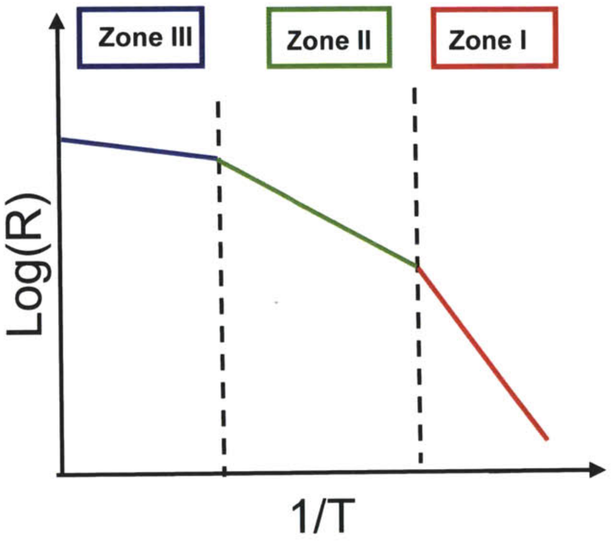

Fig. 1.2. Arrhenius plot illustrating regimes of char gasification. Measured activation energy corresponds to slope of line.

In regime I, known as the kinetically controlled regime, the reaction rate is slow enough relative to diffusion such that the reaction occurs uniformly throughout the particle, with full penetration of reactants. In this limit the particle size is constant and the measured kinetic parameters (activation energy and reaction order) are free from distortions. At the opposite limit, regime III, when reaction occurs much faster than the transport of reactants to/within the particle, reaction is confined to the external surface of the particle and the particle density remains constant throughout conversion. This is known as external diffusion control. For this regime, the measured activation energy approaches zero. Between these two extremes lie cases in which reactant concentration gradients exist within the particle, known as regime II, for which kinetics and transport through the pore structure both influence the char consumption process. In this regime, the measured activation energy is roughly half its true value.

In reality, in regime II, external concentration gradients also may play a role, while in regime III, reaction isn't purely confined to the external surface, since partial penetration into pores intersecting the outer surface must occur to some extent [20]. Nonetheless, this "three zone theory" is useful for the interpretation and planning of experiments as well as for the determination of the modeling strategy to be employed.

When one is certain that char consumption is always controlled by kinetics, the effects of transport are unimportant and may be neglected, leaving much-simplified reaction rate expression to be solved for the particle. Similarly, when boundary layer diffusion is the rate controlling step, char consumption may be modeled without accounting for intra-particle transport, although the modeling is slightly more involved than in the case of kinetic control (depending on how much detail is incorporated into modeling zone I). In the intermediate situation (zone II), some method of accounting for the interaction between intra-particle transport and heterogeneous kinetics is necessary.

Broadly speaking, four approaches to char consumption modeling are taken in the literature and these will be described in turn.

1.4.1. Global Models

The simplest types of models are "global models", which vary in complexity, but always treat the particle as impervious to reactant transport. Any effects of intra-particle diffusion, if present, are lumped into one of the parameters of the model, typically a kinetic rate constant. Similarly, any effects due to the char particle's internal surface area are also lumped into the model parameters, since global models are based on the particle's external surface area. This implies that such models are generally not transferable to other fuels or reactor conditions other than those for which the model parameters have been determined.

A common approach of global models is to assume that the reaction occurs in steady-state and thus, to equate the rates of boundary layer diffusion and chemical reaction [21]:

$$\Re = k_D \left(C_{bulk} - C_S \right) = k C_s^n \tag{1.1}$$

The mass-transfer coefficient, k_D, can be evaluated from correlations or using simple diffusion expressions and the kinetic constants typically take Arrhenius form and ideally, are evaluated experimentally for the particular char of interest. Within the context of global models, it is also possible to account for effects such as gas-phase reactions or particle size reduction.

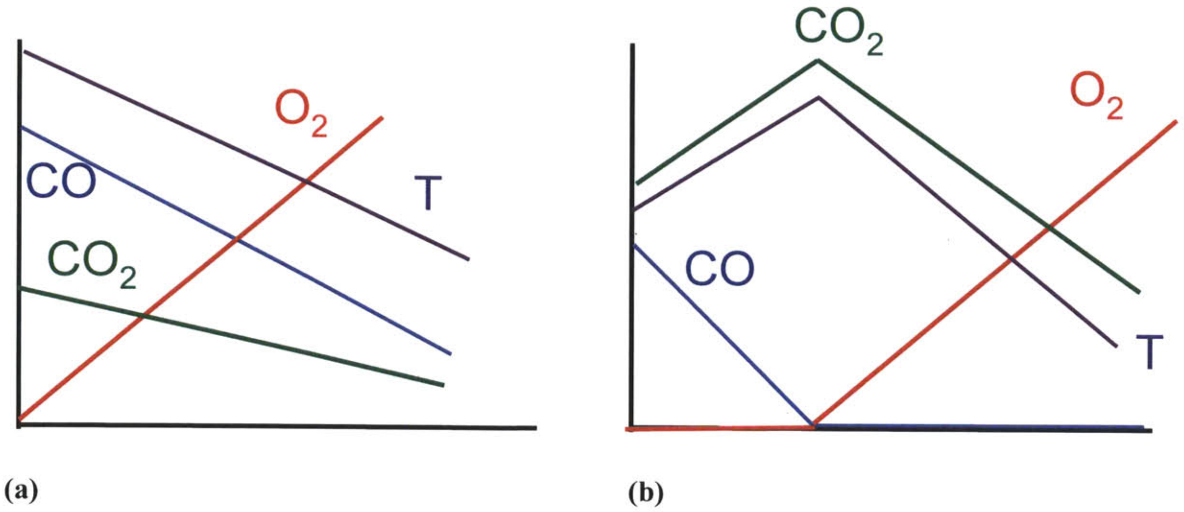

Fig. 1.3. Schematic illustration of species concentration and gas temperature in the particle boundary layer for (a) the single film model and (b) the double film model. Vertical line represents the char particle surface.

For example, for the case of char oxidation, the single film models assume a zero rate of reaction of carbon monoxide with oxygen in the particle's boundary layer, while the double film model assumes the homogeneous reaction is instantaneous and the char consumption occurs via the reaction of carbon and carbon dioxide at the particle surface [22]. The trends of species concentration and temperature in the boundary layer surrounding the burning particle are shown in Fig. 1.3 for these two limiting models. The recently developed moving flame front model assumes an intermediate, although somewhat inconsistent situation: an infinitesimal CO flame exists in the boundary layer, but between the flame and the particle surface, CO and O_2 coexist but do not react whatsoever [23]. The location of the flame adjusts itself to produce the maximum rate of char oxidation. All of these models ignore the effects of gas transport within the particle.

Assuming that the reaction occurs on the external particle surface, it is not difficult to calculate the rate of reduction in char particle size when using a global model. This can be considered a type of "shrinking core model," although that term can also be applied within the context of other modeling strategies. It is also possible to approach the reduction in particle size empirically, by using correlations for the variation of diameter (and density) with overall conversion [24]. Such an approach has the advantage of being applicable to any mechanism of size reduction, but of course, requires experimental knowledge of the behavior of the particular char and reaction conditions of interest.

Global models have the advantage of simplicity; typically only explicit algebraic expressions need to be solved. Thus, within CFD simulations, in which hundreds or thousands of particles are tracked and repeated calculations are required, global models are often employed. In cases where char particles are of low porosity or the reaction occurs near the limit of external diffusion control, such models can produce results of sufficient accuracy since the lumped internal behavior is of little consequence. Nonetheless, such models must be applied with care, since even in high temperature situations, kinetics or internal diffusion may begin to play a role later in the combustion or gasification process, when particle sizes have been sufficiently reduced, or as temperatures decrease far away from the burners.

1.4.2. Modeling Zone II Behavior

Most char combustion [25] and entrained flow gasification systems [26] operate in a regime such that kinetics, internal diffusion and boundary layer diffusion are all of importance, at least in some regions of the reactors . This necessitates models that can account for the intra-particle diffusion and reaction in some way. Unlike global models, the heterogeneous reaction is assumed to occur mostly on the internal pore surface area, which is orders of magnitude larger than the external area, in these more detailed models. Broadly speaking, three general approaches to such models exist: the effectiveness factor approach, models based on conservation equations and discrete methods. These will be discussed next.

1.4.2.1. Effectiveness Factor Models

The phenomenon of char consumption, whether via gasification or combustion, shares many mathematical similarities with problems of heterogeneous catalysis. The effectiveness factor approach was first derived for catalytic applications [27]. The goal of this approach is to obtain a reasonably accurate solution for the overall reaction rate without resolving the particle spatially, in order to minimize the computational effort. The effectiveness factor is defined as the ratio of the actual reaction rate for the entire porous particle to the ideal rate if there were no intra-particle diffusion limitations whatsoever, i.e. if the surface reactant concentrations prevailed throughout the entire particle. The effectiveness factor is calculated based on integration of a quasi-steady, reaction-diffusion equation for a single reactant through the porous medium (shown below in spherical coordinates, although it is equally applicable to other simple geometries),

$$\frac{d^2C_i}{dr^2}+\frac{2}{r}\frac{dC_i}{dr}=\frac{SkC_i^n}{D_{eff}}. \tag{1.2}$$

By using the non-dimensional Thiele modulus, Φ_i, one can predict an overall reaction rate for the particle, $\Re_{i,actual}$, using only information about species concentrations at the *surface*, $C_{i,s}$, without having to determine the species profiles throughout the entire particle,

$$\Re_{i,actual} = \eta_i \Re_{i,S} = \eta_i \left(\nu_{C,i} S_{app} k(T_p) C_{i,s}{}^{n} \right) \tag{1.3}$$

$$\eta_i = \frac{3}{\Phi_i} \left(\frac{1}{\tanh \Phi_i} - \frac{1}{\Phi_i} \right) \tag{1.4}$$

$$\Phi_i = R \sqrt{\frac{SkC_{i,s}^{n-1}}{D_{eff}}} \, . \tag{1.5}$$

The reaction rate(s) can be related to the change in particle mass, *m*, or conversion, *X*, through a single ordinary differential equation

$$\frac{dX}{dt} \equiv -\frac{1}{m_0} \frac{dm}{dt} = \frac{-M_C}{\rho_T (1-\phi_0)} \sum_i \eta_i \nu_{C,i} S_{app} k(T_p) C_{i,s}{}^{n} \, . \tag{1.6}$$

Since the calculation of the effectiveness factors requires information about the values of reactant concentrations at the particle surface, algebraic equations for the transport of each species *i*, from the bulk, through a boundary layer and to the particle surface can also be incorporated into the formulation. For example, for quasi steady-state conditions and accounting for Stefan flow, this requires an algebraic equation for each species *i* [20,26],

$$k_D P(x_{i,bulk} - x_{i,s}) + x_{i,s} \sum_i q_{rxn,i} = q_{rxn,i} \tag{1.7}$$

where $q_{rxn,i}$, the reaction rate of species i per unit geometrical particle area in [mol /m^2 s], is related to the effectiveness factor and is given by

$$q_{rxn,i} = \eta_i \nu_i S k_i (C_i)^{n_i} \frac{R}{3}. \tag{1.8}$$

In a CFD simulation, for each particle that is tracked, an ODE is also solved for the particle's momentum. Furthermore, another ODE is often required to determine the particle's temperature, especially for combustion conditions, in which the char particle temperature can often surpass that of the surrounding gas by several hundred degrees. For an isothermal particle, we have

$$mc_p \frac{dT_p}{dt} = 4\pi R^2 \left(-\sum_i q_{rxn,i} h_i + q_{convection} + q_{radiation} \right). \tag{1.9}$$

Thus, in typical CFD simulations, there are three ordinary differential equations associated with each solid particle [28]. However, for other applications, if the only desired quantity is the reaction rate, it is possible to apply the effectiveness factor approach without incorporating any ODEs, using only Eqs. (1.2)-(1.4).

The effectiveness factor approach is computationally manageable and provides a means of accounting for zone II behavior. For certain situations it can be adapted to account for some complicating effects, such as a change in the number of moles of gas upon reaction (which occurs during char consumption) and various reaction rate forms. Since it relies upon intrinsic kinetics, it can be applied to varying boundary conditions. However, there is still a significant amount of simplification involved in this approach and in particular, when it is applied to non-catalytic heterogeneous reactions, modeling the evolution of the internal pore structure presents challenges. In the presence of intra-particle diffusion limitations, the conversion, and therefore the surface area and effective diffusivity, vary spatially within the particle, and this is not accounted for by the effectiveness factor approach. Furthermore, phenomena such as peripheral fragmentation are not incorporated in the effectiveness factor approach. To address these and other issues, a higher fidelity approach is necessary.

1.4.2.2. Conservation Equation-based Models

The conservation equation-based approach is free from the limitations described above, but it comes at the price of greater computational cost. Equations of balance for gas species, energy, mass, and solid material are written for the particle and possibly for some region outside of the char particle. Since it would be impossible to solve partial differential equations describing the transport within the actual pore-space due to its utter complexity, local volume averaging must be performed, in order to treat the composite structure of solid and pores as a single entity [29]. This averaging must be performed over a volume that is larger than the pore dimensions but small enough to capture gradients through the particle. Using this description, temperature, mole fractions, char conversion, etc. become smooth functions of position within the particle and transport, thermodynamic and reactivity coefficients depend on the locally averaged pore structure.

Since the set of partial/ordinary differential equations will be solved numerically, rather than analytically, there is great freedom to implement complex sub-models that might be necessary to describe the behavior of the gas-porous solid system. Further advantages of the conservation equation approach are the spatial resolution it provides and the ability to apply the model to conditions other than those in which experiments were performed. However, this approach is typically too computationally expensive to implement directly in CFD simulations. Also, to use this type of model as a predictive tool, it is necessary to have a physical and kinetic characterization of the char, or reasonable assumptions for the required inputs. Finally, near the percolation threshold, the porosity at which the char's pore space undergoes drastic changes in its connectivity, the continuum approach may not be valid because the length-scale over which volume averaging must be performed becomes too large to resolve particle-scale gradients [29].

1.4.2.3. Discrete Models

The discrete approach to char consumption modeling is able to capture phenomena that are not well-modeled using the continuum approach described above [29]. These may include percolation events and the evolution of a disordered structure that is not amenable to a continuum description. No assumptions about the connectivity of the pore-space or solid are required. Ash coalescence and fragmentation are types of events that are better studied using a discrete approach [30,31].

In this approach, the porous medium is represented by a network, with each node being assigned an identity: pore, volatile, char, ash, etc. Due to computational limitations, the size of the entire network typically cannot be as large as an actual particle if the sizes of the pores are as small as those of the actual pore system. Statistical techniques such as Monte Carlo and random walks are employed to determine the evolution of the network, together with rules invoked to determine when a node-changing event has occurred. The discrete approach is very computationally expensive. Assumptions about the network (e.g. coordination number) are required and the complexity of the reaction and transport is sometimes limited due to computational expense.

Table 1.1. Advantages and disadvantages of the four approaches to char consumption modeling.

	Implementable in CFD	Applies in all conditions	Spatial Resolution	Comprehensive and Flexible	Applies to all Structures
Global Models	Yes	No	No	No	No
Effectiveness Factor	Yes	Yes	No	No	No
Conservation Equations	No	Yes	Yes	Yes	No
Discrete Models	No	Yes	Yes	No	Yes

1.5. Approach of this Thesis

Table 1.1 summarizes the advantages and disadvantages to the four approaches to char consumption modeling outlined above. It should be emphasized that the choice of a modeling strategy depends on the particular goals and applications of the single particle modeling. In this thesis, the conservation equation approach has been selected and will be discussed in the next chapters. The reason for selecting this approach is due to its ability to account for structural gradients that are present in zone II for non-catalytic gas-solid reactions, the comprehensive nature of this type of model and its applicability to varying boundary conditions. These three advantages are important for entrained flow gasification, oxy-combustion and air combustion systems, in which reaction often occurs in the regime governed by intra-particle diffusion, multiple reactants may be present simultaneously, structural evolution can have a major impact and in which the boundary conditions to which char particles are exposed may vary depending on operating conditions or even for a given particle as it moves through the reactor. However, the effectiveness factor approach will also be utilized in Ch. 3, as a sub-model within the conservation equation based model.

1.6. Thesis Outline

In Ch. 2, the relevant chemical, transport and morphological processes occurring during char consumption will be discussed. The literature will reviewed and sub-models accounting for these processes will be presented. For some phenomena, new modeling strategies will be developed. The modeling framework and the sub-models incorporated therein will be described. In Ch. 3, a more detailed development will be presented for a particular sub-model: that of pore structure evolution. The pore structure evolution model that is developed enables greater flexibility and adaptability to varying conditions than existing pore structure evolution models. Chapter 4 will present the numerical approach used in solving the equations of the char consumption model. Chapter 5 consists of a validation study and demonstration of the model's capabilities. Sensitivity to certain parameters and the effects of particular sub-models will be discussed. Finally, Ch. 6 applies the single particle model to two cases of interest: oxy-fuel combustion and entrained flow gasification.

Nomenclature

C	concentration (mol/m$^3_{gas}$)
c_p	specific heat for char particle (J/kg K)
D	diameter of char particle (m)
D_{eff}	effective diffusion coefficient (m^2/s)
h	heat of reaction (J/mol)
k	intrinsic reaction rate constant (mol$_C$ /m^2_C s (mol$_{gas}$/m^3)^n)
k_D	diffusive mass transfer coefficient (mol/m^2 s atm) or (mol/m^2 s mol$_{gas}$/m^3))
m	mass of char particle (kg)
M_C	molecular weight of char (g/mol)
n	reaction order (-)
P	ambient pressure (atm)
q_{rxn}	reaction rate based on geometric surface area (mol i/m$^2_{ext}$ s)
$q_{convection}$	convective heat flux (W/m^2)
$q_{radiation}$	radiative heat flux (W/m^2)
r	radial position within particle (m)
R	radius of char particle (m)
$\Re$	heterogeneous reaction rate (mol$_C$/m^3 s)
S	internal surface area (m^2_C/m^3)
t	time (s)
T_p	particle temperature (K)
V	particle volume (m^3)
X	total char conversion (-)

x_i	mole fraction (mol *i*/mol total)

Greek Symbols

ϕ	porosity (m^3_{pore}/m^3_{Total})
η	effectiveness factor (-)
ν	stoichiometric coefficient (mol/mol)
ρ	density (kg/m^3)
Φ	Thiele modulus (-)

Subscripts

0	at initial time $t=0$
app	apparent (density or conversion)
bulk	bulk property
C	char
D	diffusion
i	species *i*
p	particle
s	surface property
T	true (density)

References

[1] World Coal Association: Coal Statistics (www.worldcoal.org/resources/coal-statistics/), 2010.

[2] EIA Annual Energy Outlook, Early Release Overview (www.eia.gov/forecasts/aeo/er/early_fuel.cfm), 2012.

[3] BP Statistical Review of World Energy (www.bp.com/statisticalreview), 2011.

[4] M. Kumar, C. Zhang, R.F. Monaghan, S.L. Singer, A.F. Ghoniem, Proceedings of the Asme International Mechanical Engineering Congress and Exposition (2010) 383-395.

[5] C. Chen, M. Horio, T. Kojima, Chemical Engineering Science 55 (2000) 3875-3883.

[6] G. Liu, H.R. Rezaei, J.A. Lucas, D.J. Harris, T.F. Wall, Fuel 79 (2000) 1767-1779.

[7] R.F.D. Monaghan, A.F. Ghoniem, Fuel 91 (2012) 61-80.

[8] C. Botero, R.P. Field, H.J. Herzog, A.F. Ghoniem, Submitted to the Clearwater Coal Conference (2012) 1-13.

[9] J. Yu, J.A. Lucas, T.F. Wall, Progress in Energy and Combustion Science 33 (2007) 135-170.

[10] S. Niksa, G.-su Liu, R.H. Hurt, Progress in Energy and Combustion Science 29 (2003) 425-477.

[11] S. Niksa, Molecular Physics 394 (1995) 384-394.

[12] T.H. Fletcher, A.R. Kerstein, A Chemical Percolation Model for Devolatilization: Summary, 2000.

[13] S.P. Zhao Y, Serio MA, Bassilakis R, Proceedings of the Combustion Institute 25 (1994) 553-560.

[14] A. Williams, R. Backreedy, R. Habib, J.M. Jones, M. Pourkashanian, Fuel 81 (2002) 605-618.

[15] K.L. Smith, L.D. Smoot, T.H. Fletcher, in:, L.D. Smoot (Ed.), Fundamentals of Coal Combustion, Amsterdam, 1993, pp. 131-298.

[16] K. Matsuoka, H. Akiho, W.-chun Xu, R. Gupta, Science And Technology 84 (2005) 63-69.

[17] M. Oh, W.A. Peters, J.B. Howard, AIChE Journal 35 (1989) 775-792.

[18] J. Yu, J. Lucas, T. Wall, G. Liu, C. Sheng, Combustion and Flame 136 (2004) 519-532.

[19] P.L. Walker, F. Rusinko Jr., L.G. Austin, in:, D.. Elwey, P.W. Selwood, P.B. Weisz (Eds.), Advances in Catalysis, Vol XI, 1959, pp. 133-221.

[20] J. Hong, Modeling Char Oxidation as A Function of Pressure Using an Intrinsic Langmuir Rate Equation, Brigham Young University, 2000.

[21] I. Smith, Symposium (International) on Combustion 19 (1982) 1045-1065.

[22] H.S. Caram, N.R. Amundson, 16 (1977) 171-181.

[23] M. Zhang, J. Yu, X. Xu, Combustion and Flame 143 (2005) 150-158.

[24] R.E. Mitchell, R.H. Hurt, L.L. Baxter, D.R. Hardesty, Sandia Report 92-8208: Compilation of Sandia Coal Char Combustion Data and Kinetic Analysis, 1992.

[25] I.W. Smith, Combustion and Flame 17 (1971) 303-314.

[26] G.-su Liu, S. Niksa, Progress in Energy and Combustion Science 30 (2004) 679-717.

[27] E.W. Thiele, Industrial and Engineering Chemistry 31 (1939) 916-920.

[28] M. Kumar, A.F. Ghoniem, Energy & Fuels 26 (2012) 464-479.

[29] M. Sahimi, G.R. Gavalas, T.T. Tsotsis, Chemical Engineering Science 45 (1990) 1443-1502.

[30] M. Sahimi, T.T. Tsotsis, Physical Review Letters 59 (1987) 888-891.

[31] F. Miccio, P. Salatino, W. Tina, Proceedings of the Combustion Institute 28 (2000) 2163-2170.

Chapter 2. Modeling the Physics and Chemistry of Char Consumption

This chapter surveys the physical processes and accompanying models and sub-models necessary to implement a comprehensive, spatially-resolved model for char gasification or combustion. The first section, 2.1, discusses the general modeling framework and the subsequent sections describe important sub-models for transport, reaction and morphological processes. In each section, relevant literature is discussed and the approach incorporated in the present modeling framework is described.

2.1. Conservation Equation-based Single Particle Models

2.1.1. Literature Review

Spatially-resolved models of reacting single char particles in the literature are numerous, but typically fall into one of two broad categories: models which focus on the intra-particle transport-reaction-structural coupling and models that focus on processes in the particle boundary layer, be it complex chemistry [1–5], flow patterns [6–8], or both [9]. The model described in this thesis falls into the former category, so contributions to that class of model that employ the conservation equation-based approach will be discussed briefly, with their salient features, as they pertain to the model which will be described here, emphasized.

Gavalas employed the random capillary model [10] to predict the porosity and surface area evolution using the pore growth variable, q, as the equation for local solid conversion in a one-dimensional, pseudo-steady state simulation of a multi-modal porous char particle reacting isothermally with oxygen [11]. A simplified version of the Feng and Stewart model (FSM) [12] was incorporated into the species equation to model the oxygen flux and an equation for the position of the particle surface as the char particle experienced peripheral fragmentation was derived [11]. Bhatia and Perlmutter incorporated the random pore model (RPM) [13], which, it can be shown (see Appendix A.2), is equivalent to Gavalas' random capillary model, into a one-dimensional, pseudo-steady state simulation of a reacting porous particle [14].

Sotirchos and Amundson [15,16] formulated a general model for transient, one-dimensional combustion and gasification of porous char, allowing for heterogeneous and homogeneous reactions and pore-structure-dependent transport and thermodynamic parameters. The isobaric Dusty Gas Model (DGM [17]) was employed for calculating the fluxes through the porous particle. An average pore radius for macropores was assumed to be constant throughout conversion and was used in calculating Knudsen diffusion coefficients. For both constant radius [15] and shrinking [16] particles, conservation equations for species, mass and energy were solved within the particle and for a quiescent boundary layer of thickness equal to the particle's radius. Ballal et al. incorporated seven species into a similar framework and studied the effects of reactant concentration on ignition, quenching and burnout behavior [18]. A later paper by Morell et al. [19] allowed for pressure buildup within the porous particle, which is a requirement for consistency between the porous medium fluxes and the stoichiometry in a reacting system [20]. While the Dusty Gas expressions for the individual fluxes reduce to the Stefan-Maxwell equations when the porosity is set to unity (for representation of a gas phase boundary layer), the Dusty Gas model expression for the total flux (convective velocity) does not reduce to the correct gas phase expression.

Reyes and Jensen [21], and Srinivasachar et al. [22], employed a Bethe lattice to model the pore structure and used percolation concepts to determine the effective transport coefficients for an evolving, porous char structure, within a continuum description of char gasification and combustion. Shrinking from fragmentation was incorporated, and Srinivasachar et al. employed the Dusty Gas Model to determine the porous medium fluxes. A mass-transfer coefficient together with an expression for the non-equimolar fluxes was used as the boundary condition for the species equation at the char particle surface.

Biggs and Agarwal also employed percolation concepts in a continuum model of the oxidization of a porous char particle [23]. The Dusty Gas Model was to calculate the fluxes, and in the boundary layer within the emulsion phase of a fluidized bed, the large pore limit of the DGM was employed. The energy equation was also solved in the particle and the boundary layer.

Wang and Bhatia modeled slow char particle gasification with peripheral fragmentation, heterogeneous and homogeneous reaction and a bi-disperse Dusty Gas Model for the porous medium fluxes [24]. The total pressure was allowed to vary within the particle and the Maxwell-Stefan relations were used to calculate the diffusion fluxes in the boundary layer. Uniform particle temperature and negligible Stefan flow in the particle boundary layer were assumed.

Zolin and Jensen [25] modified and implemented the annealing model of Suuberg et al. [26] and Hurt et al. [27] *concurrently* with a quasi-steady single particle char oxidation model. Peripheral fragmentation was also incorporated in the model.

Cai and Zygourakis formulated a model for highly porous char consisting of spherical cavities (macropores) surrounding microporous, spherical grains [28]. The species and energy balances for a pseudo-binary mixture were applied to the macropores and the reaction source terms, representing consumption of the spherical grains at each radial location in the char, contained a grain effectiveness factor representing the Knudsen-diffusion-limited rate of reaction in the microporous grains. The particles were assumed not to shrink because the high ash content resulted in an ash shell of constant radius.

Mitchell et al. modeled the oxidation of an isothermal particle using a six step heterogeneous reaction mechanism [29]. Although not explicitly stated, it appears that particle shrinkage was accomplished in a piece-wise manner by removing the outermost grid-point once its local conversion was complete.

2.1.2. Developments in the Current Approach

Many coal and biomass char particles are known to possess multi-modal pore structures which evolve substantially over the course of conversion in kinetically-limited or mixed kinetic/intra-particle diffusion-limited conditions. The evolution of the pore structure has a major effect on the particle's surface area and on the ability of gaseous reactants to diffuse through the char structure. It has been shown experimentally that different reactants have varying degrees of success at penetrating and reacting on micropores and small mesopores [30–36]. Furthermore, during entrained flow gasification or oxy-combustion, char particles are subjected to different reactions concurrently or sequentially, implying that different pore sizes may grow at different rates, affecting the evolution of the surface area and intra-particle transport processes. In Ch. 3 an adaptive random pore model (ARPM) is developed which extends the original random pore model to allow different pore sizes to grow at different rates, depending on the instantaneous interplay of kinetics and transport, at the pore scale, at different locations within a char particle.

This thesis incorporates the ARPM into a comprehensive, predictive, single particle gasification model which is consistent with the evolving, multi-modal pore structure. Gas transport within the porous structure is modeled using the flux relations of Feng and Stewart, which together with the ARPM, provide a consistent and predictive method for handling the interplay of transport and pore structure evolution, as both are based on a geometry consisting of straight cylindrical capillaries with various radii. The model presented is also comprehensive in nature, somewhat like a spatially-resolved analogue of the CBK model [27], in that it can account for concurrent annealing, particle shrinkage (either due to fragmentation or simply from reaction) and the possibility of ash adherence on the particle surface. Incorporation of the fragmentation and ash sub-models, however, requires some assumptions and fitting parameters not required by the basic version of the model, making those sub-models less predictive and more useful as qualitative tools.

2.1.3. Basic Model Equations

To apply a continuum-based approach to the modeling of a porous medium, it is necessary to employ the concept of volume averaging, in which properties are defined as averages over a representative volume that is larger than the length-scale of the pores, yet smaller than the characteristic scale of gradients of species, temperature, etc. Therefore, large voids that appear in cenospheric or sponge-like char particle should not be treated as pores and included in the averaging [37], but must be handled explicitly in the particle-scale geometry if a continuum approach is to be employed in a situation with significant species gradients through the particle. In the context of a one-dimensional model, a cenospheric particle with a single spherical void at its center can be treated with the boundary conditions described by Loewenberg [38], however more complex, asymmetric, sponge-like void morphologies would need to be treated with a full three-dimensional simulation if the continuum approach were to be applied with fidelity to the actual pore structure.

Aside from the validity of volume averaging, which was discussed in Ch. 1, another consideration in applying a continuum approach is whether the structure has sufficient connectivity for the smooth-field hypothesis to hold [20]. If the initial porosity or connectivity of the char particle is too low, writing partial differential equations for the porous-medium species and mass conservation is problematic, as discussed by Sahimi et al. [39]. These two limitations must be kept in mind: the connectivity of the pore structure must be sufficient, yet the pores must be small enough to allow for meaningful averaging of properties.

Our approach consists of solving the differential equations of balance inside a spherically symmetric porous particle with an arbitrary initial porosity profile and in the surrounding boundary layer, for gas species mole fractions, thermal energy, overall mass and solid consumption on various pore sizes,

$$\phi_{Tot} C \frac{\partial x_j}{\partial t} = -\nabla \circ J_j - N_{Tot} \circ \nabla x_j + \sum_k \nu_{j,k} \Re_k \left(\sum_{pore\ i} \eta_{i,k} S_i \right) - x_j \sum_j \sum_k \nu_{j,k} \Re_k \left(\sum_{pore\ i} \eta_{i,k} S_i \right) \tag{2.1}$$

$$(\rho c_p)_{eff} \frac{\partial T}{\partial t} = \nabla \circ (k_{eff} \nabla T) - \sum_j (N_j c_{p,j}) \circ \nabla T + \sum_k -\Delta h_r \Re_k \left(\sum_{pore\ i} \eta_{i,k} S_i \right) \tag{2.2}$$

$$\frac{\partial (\phi_{Tot} C)}{\partial t} + \nabla \circ N_{Tot} = \sum_j \sum_k \nu_{j,r} \Re_k \left(\sum_{pore\ i} \eta_{i,k} S_i \right) \tag{2.3}$$

$$\frac{dq_i}{dt} = \frac{-MW_C}{\rho_{True}} \sum_k \eta_{i,k} \nu_{C,k} \Re_k \tag{2.4}$$

These equations and the sub-models they require will be discussed in this and the next chapter. The overall material balance, Eq. (2.3), can be re-written in terms of the pressure, p. Differential equations for the recession of the particle's radius, ds/dt and ash layer radius, dr_{ash}/dt, can also be included and will be discussed later. Note that only n-1 species equations (Eq. (2.1)) are solved since the mole fractions, x_j, sum to unity.

The reaction terms in Eqs. (2.1)-(2.3) contain the factor $\left(\sum_{pore\ i} \eta_{i,k} S_i\right)$, which represents the pore surface area ($m^2{}_C/m^3{}_{Tot}$) participating in a given heterogeneous reaction. For homogeneous reactions, k, this term should be replaced with ϕ_{Tot} ($m^3{}_{gas}/m^3{}_{Tot}$), the total porosity, since homogeneous reaction rates, $\Re_k$, have units of ($mol/m^3{}_{gas}$ s), whereas intrinsic heterogeneous reaction rates have units of ($mol/m^2{}_C$ s) in the conservation-equation approach.

The boundary conditions at the center of the particle, $r=0$, are dictated by spherical symmetry,

$$\frac{\partial x_j}{\partial r} = 0,\ \frac{\partial T}{\partial r} = 0,\ \frac{\partial p}{\partial r} = 0. \tag{2.5a}$$

The diffusive fluxes, J_j, and total flux, N_{Tot}, are also zero at the particle center. Far from the particle, at $r = r_{bulk}$, Direchlet boundary conditions are assigned to the species, temperature and pressure,

$$x_j = x_{j,bulk}(t),\ T = T_{bulk}(t),\ p = p_{bulk}. \tag{2.5b}$$

At the interface between the porous solid and gas phase, $r = s(t)$, all variables are continuous, as are all fluxes, with the exception of the heat flux, which is discontinuous due to radiative exchange between the surface of the particle and the walls, surrounding gas (outside the domain, however, since the gas-phase is modeled as radiatively non-participating) or other particles:

$$(-k_{eff}\nabla T)_{s-} = (-k_{eff}\nabla T)_{s+} + q_{rad}\,. \tag{2.5c}$$

The bulk boundary conditions may be functions of time to allow for a realistic representation of the conditions to which a char particle is exposed as it moves through a reactor. Boundary conditions are not required for the pore growth variables, q_i, the interface positions at the edge of the char, s, and ash layer, r_{ash} (if it exists), since these variables are governed by ordinary differential equations. Initial conditions (t=0) for pressure, temperature and species mole fractions are typically prescribed as uniform profiles, set to known values if available or simply equal to the initial boundary conditions. The influence of the species mole fraction initial conditions on the solution fades away very quickly. Initial values of the pore growth variables are zero and the interface position is set equal to the initial particle radius, r_0.

2.2 Pore Structure Evolution

Since non-catalytic gas-solid reactions occur on solid surfaces, the amount of surface area available for reaction will directly affect the rate of solid conversion. For most chars, the internal surface area is orders of magnitude larger than the external surface area of the same particles, so the relevant area is the internal area on the pore walls. Furthermore, it has long been observed that the rate of reaction of many chars varies throughout conversion in the kinetic regime (e.g.

[40–42]), which is partly attributable to the fact that the consumption of the solid changes the amount of surface area available for reaction. Despite the fact that the total surface area may not be fundamentally related to the reaction rate [33] since heterogeneous reactions may only occur on reactive sites, it has nonetheless been established that the total surface area is, in general, proportional to the reactive surface area, so that models for evolution of the pore surface area (the total surface area) are useful in capturing the change in reaction rate with conversion [43]. The constant of proportionality between total pore area, S, and reactive area is simply absorbed into the kinetic pre-exponential factor.

The development of a pore structure evolution model for the oxidation and gasification of char particles with a range of pore sizes will be discussed in more detail in Ch. 3. This model estimates the surface area *participating* in a given reaction, a term which appears in Eqs. (2.1)-(2.3). Here, a very brief overview of pore structure evolution models in the literature will be provided. Isolated pore models assume pores pass through the entire sample without consideration of overlap with other pores [44]. It is also possible to simply fit experimental data for the variation of reaction rate with conversion to empirical equations or, alternatively, to assume that the surface area decreases linearly with conversion, although both of these approaches lack a fundamental basis. Simons developed a class of pore structure evolution models based on the concept of a pore-tree, which assumes straight cylindrical pores that branch from larger to smaller [45] and which overlap as reaction proceeds. The random pore models, upon which the model presented in Ch. 3 is based, assume the pore space consists of randomly located and oriented cylindrical pores that overlap [10,13]. Any distribution of pore radii is acceptable, so the random pore models have great flexibility in matching experimental data. Ballal and Zygourakis developed structural evolution models based upon a similar idea as the random pore models, although the mathematics is more involved [46]. Due to their simplicity, flexibility and success at reproducing experimental data, the random pore models have become the most widely used models for pore structure evolution in non-catalytic gas-solid reactions. As will be discussed in the following section, the assumption of randomly located and oriented pores also facilitates simplification of porous medium flux models.

2.3. Transport in the Porous Medium

In addition to determining the surface area available for heterogeneous reactions, the evolving porous structure also plays a role in the intra-particle species transport. While the DGM doesn't explicitly account for multi-modal pore structures, the FSM can be used with any pore size distribution and has the advantage that the adjustable parameters of the DGM are determined solely by the pore size distribution, given certain assumptions [12,20]. The drawback of the FSM is its assumption of a thoroughly connected pore structure, which may overestimate the fluxes at low porosities. Essentially, the FSM applies the flux relations of the DGM to a single pore, and then integrates the given fluxes over all pore sizes and orientations to calculate the flux of each species through the porous medium. This is tractable when the pore space is assumed to be composed of randomly located and oriented cylindrical capillaries. Unless otherwise noted, the results presented in later chapters employ the FSM as the porous medium flux sub-model, although the DGM has also been incorporated as an option in the modeling framework.

The DGM can be expressed in many different forms [20], one of which separates the $n-1$ independent diffusion fluxes, J_j (the sum of the diffusive fluxes is zero), from the total flux, N_{Tot},

$$\sum_{s\neq j}\frac{x_s J_j - x_j J_s}{\Delta_{j,s}} = -\frac{p}{RT}\nabla x_j - \frac{x_j}{RT}\left(1 - \frac{1}{D_{Kn,j,eff}\sum_s \frac{x_s}{D_{Kn,s,eff}}}\right)\nabla p\,, \tag{2.6a}$$

where,

$$\frac{1}{\Delta_{j,s}} = \frac{1}{D_{j,s,eff}} + \frac{1}{D_{Kn,s,eff}D_{Kn,j,eff}\sum_t \frac{x_t}{D_{Kn,t,eff}}}\,, \tag{2.6b}$$

and

$$N_{Tot} = -\frac{\sum_s \frac{J_s}{D_{Kn,s,eff}}}{\sum_s \frac{x_s}{D_{Kn,s,eff}}} - \frac{1}{RT}\left(\frac{B_0 p}{\mu} + \frac{1}{\sum_s \frac{x_s}{D_{Kn,s,eff}}}\right)\nabla p\,. \tag{2.7}$$

The *effective* diffusion coefficients (Knudsen, $D_{Kn,s,eff}$ and continuum, $D_{j,s,eff}$) include a factor which accounts for the *total* porosity (as well as the tortuosity). This form is convenient for pairing with the gas boundary layer, in which only *n-1* Maxwell-Stefan equations are independent. The diffusive fluxes can be re-written in (*n*-1) x (*n*-1) matrix form as [20]:

$$\underline{J} = [\overline{\overline{B_f}}]^{-1} \times \underline{RHS}\,, \tag{2.8}$$

where,

$$B_f(j,j)=\frac{x_j}{\Delta_{j,n}}+\sum_{\substack{s=1\\ s\neq j}}^{n}\frac{x_s}{\Delta_{j,s}}, \tag{2.9a}$$

$$B_f(j,s)=-x_j\left(\frac{1}{\Delta_{j,s}}-\frac{1}{\Delta_{j,n}}\right), \tag{2.9b}$$

and

$$RHS_j=-\frac{p}{RT}\nabla x_j-\frac{x_j}{RT}\left(1-\frac{1}{D_{Kn,j,eff}\sum_s\frac{x_s}{D_{Kn,s,eff}}}\right)\nabla p. \tag{2.10}$$

Following the derivation of Feng and Stewart [12] and the summary by Jackson [20], the *n* molar fluxes in the Feng and Stewart model can also be formulated in terms of the *n-1* diffusive fluxes, J_j, and the total flux, N_{Tot}. This begins by writing the equations for diffusive and total flux in a single pore and using the combination of diffusive and pressure-driven fluxes employed by the Dusty Gas Model to represent J_j and N_{Tot}, with the effective coefficients replaced by those appropriate for cylinders of radius R:

$$\underline{J}=\int_{\Omega}\int_{R}\overrightarrow{l_{\Omega}}\underline{J}(R,\Omega)f(R,\Omega)dRd\Omega \tag{2.11}$$

$$N_{Tot}=\int_{\Omega}\int_{R}\overrightarrow{l_{\Omega}}N_{Tot}(R,\Omega)f(R,\Omega)dRd\Omega \tag{2.12}$$

where $f(R,\Omega)dRd\Omega$ is defined as the fraction of porosity associated with pores of radius R and orientation Ω and $\overrightarrow{l_\Omega}$ is a unit vector along the axis of a pore with orientation Ω. In Eq. (2.7) one recognizes that $B_0 = R^2/8$, as appropriate for Poisuille flow and *effective* Knudsen and molecular diffusion coefficients are no longer necessary, since in a single capillary, they are given by $D_{Knudsen,\,j} = \frac{2R}{3}\sqrt{\frac{8\overline{R}T}{\pi MW_j}}$ and the unmodified binary diffusion coefficients, $D_{j,k}$. The fluxes J_j can be written in explicit form using matrix inversion to solve for $\underline{J}$, just as was done for the Dusty Gas model, but with $\left[B_f\right]^{-1}$ employing the coefficients above and the vector $\underline{RHS}$ also written for a single pore, which requires the gradients of pressure and mole fractions along the pores to be expressed as:

$$\frac{dp}{dl} = \overrightarrow{l_\Omega} \circ \nabla p \tag{2.13a}$$

$$\frac{dx_j}{dl} = \overrightarrow{l_\Omega} \circ \nabla x_j \tag{2.13b}$$

where, as mentioned above [20], p and x_j are smooth field values. Making these substitutions in (2.11), one obtains,

$$\underline{J} = \int_\Omega \int_R \left[B_f\right]^{-1} \overrightarrow{l_\Omega}\overrightarrow{l_\Omega} \circ \underline{RHS}\, f(R,\Omega)\, dRd\Omega. \tag{2.14}$$

Since $\left[B_f\right]^{-1}$ and $\underline{RHS}$ do not depend on the orientation, they can be factored out of that integral, following Feng and Stewart and Jackson [12,20], yielding

$$\underline{J}=\int_R [B_f]^{-1}\underline{RHS}\left[\int_\Omega \overrightarrow{l_\Omega}\overrightarrow{l_\Omega}\, f(R,\Omega)\,d\Omega\right]dR\,. \tag{2.15}$$

Defining the tortuosity tensor, $\overline{\overline{\kappa(R)}}$, by [12,20]:

$$dR\int_\Omega \overrightarrow{\delta_\Omega}\overrightarrow{\delta_\Omega}\, f(R,\Omega)d\Omega=\overline{\overline{\kappa(R)}}d\phi(R)\,, \tag{2.16}$$

one obtains an equation for the *n-1* smooth field diffusion fluxes

$$\underline{J}=\int_R [B_f]^{-1}\underline{RHS}\,\overline{\overline{\kappa(R)}}\,d\phi(R)\,. \tag{2.17}$$

To make Eq. (2.17) tractable, certain assumptions must be invoked. Fortunately, the discrete random pore geometry employed by the ARPM enables such a simplification. The discrete pore size distribution allows the replacement of the integral with a summation and it can be shown that the second order tortuosity tensor is isotropic when the pore orientations are isotropically distributed, as they are with the RPM. This implies that, for our one-dimensional spherically symmetric geometry, $\overline{\overline{\kappa(R)}}$ can be replaced with a scalar, which is equal to 1/3 (Appendix A.1). The final equation for the smooth-field diffusion fluxes is given by

$$\underline{J} = \frac{1}{3}\left\{ \sum_{pore\ i} \phi_i \underline{J}_i \right\}, \tag{2.18}$$

where the vector of fluxes in each pore size, *i*, is

$$\underline{J}_i = [B_f]_i^{-1} \times \underline{RHS}_i . \tag{2.19}$$

Substitution of the pore-scale total fluxes into (2.12) proceeds along similar lines, using the expression of the Dusty Gas model with permeability and diffusion coefficients appropriate for a single capillary. Substituting into Eq. (2.12), one obtains

$$N_{Tot} = \int_R \int_\Omega \vec{l_\Omega} \left(\frac{-\sum_s \frac{J_s}{D_{Kn,s}}}{\sum_s \frac{x_s}{D_{Kn,s}}} \right) f(R,\Omega)\, d\Omega\, dR + \int_R \int_\Omega \vec{l_\Omega} \frac{-1}{\bar{R}T} \left(\frac{R^2 p}{8\mu} + \frac{1}{\sum_s \frac{x_s}{D_{Kn,s}}} \right) \nabla p \circ \vec{l_\Omega} f(R,\Omega)\, d\Omega\, dR . \tag{2.20}$$

Factoring out terms independent of pore orientation and proceeding in the same manner as above, the smooth field total flux is given by

$$N_{Tot} = -\sum_{pore\ i} \phi_i \left(\frac{\sum_s \frac{J_{s,i}}{D_{Kn,s,i}}}{\sum_s \frac{x_s}{D_{Kn,s,i}}} \right) - \frac{\nabla p}{3\bar{R}T} \sum_{pore\ i} \phi_i \left(\frac{R_i^2 p}{8\mu} + \frac{1}{\sum_s \frac{x_s}{D_{Kn,s,i}}} \right), \tag{2.21}$$

in which $J_{s,i}$ are the components of the diffusion fluxes in pore *i,* for each species, *s*.

As discussed by Jackson [20] and others [47,48] the development of the FSM assumes that the smooth field approximation is valid in all pore sizes. This means that the pore space is thoroughly cross-linked, such that the scalar projection of the smooth field, particle-scale species gradients in the direction of a pore axis yields the species gradient in that pore. If the pore-space is cross-linked sufficiently, this assumption is typically satisfied for larger pores, but in the presence of fast reactions, smooth field concentration gradients may be incorrect for micropores, since the high surface area to volume ratio implies significant reaction and species gradients along the micropores, irrespective of their orientation within the particle. The ARPM is useful in approximating when the smooth field assumption breaks down, since pore-scale effectiveness factors (discussed in Ch. 3) less than unity imply significant gradients along a pore. For gasification conditions, simulations generally indicate that the fluxes in micropores may not satisfy the smooth field assumption, while fluxes in larger pores do so. For oxidation reactions, small mesopores may also fail to satisfy the smooth field assumption, while it is generally satisfied in larger mesopores and macropores.

For a first order reaction, Jackson derives a correction factor to apply to pores in which large pore-scale gradients exist, to be used in conjunction with a smooth-field flux model [20]. The method solves the same pore scale reaction-diffusion equation used in deriving the effectiveness factor, but with boundary conditions that account for particle scale smooth field gradients, and calculates the fluxes through the pore. This method is not applicable to non-linear reactions. As Jackson has noted, the contribution of the micropores to the overall flux is, in most cases, small compared with the total flux. This has been confirmed in our simulations. For this reason, it was deemed safe to neglect the micropore contribution to the gas transport.

Finally, as discussed by Gavalas [10] regarding the FSM, it is known that the assumption of straight, infinite, cylindrical capillaries is not strictly accurate, given the modest aspect ratio of pores encountered in practice and the fact that much of the pore volume is overlapped by more than one pore, especially later in conversion. While this is not a problem in terms of assigning the porosities in the context of the (adaptive) random pore model, it does alter the idealized geometry on which the FSM is based. For this reason, following the idea of the bi-disperse DGM developed in [24], in place of the pore radius, R_i, in the FSM we have employed a hydraulic radius for each pore size: $r_{h,i} = 2\phi_i / S_i$. This is used in Eq. (2.21) and in calculating the Knudsen diffusion coefficients used in the FSM.

2.4. Transport in the Gas Phase

In the surrounding gas film in which the char particle is entrained, mass transfer occurs via continuum diffusion and radial convection due mainly to Stefan flow (the net creation of gas phase molecules from heterogeneous reactions). The Maxwell-Stefan equations can be solved for the diffusive fluxes of *n-1* species, where it has been assumed that pressure gradients in the boundary layer are negligible, giving [49]:

$$\sum_s \frac{x_s J_j - x_j J_s}{D_{j,s}} = -\frac{p}{RT} \nabla x_j . \tag{2.22}$$

The n^{th} diffusive flux can be obtained from the constraint that the fluxes sum to zero. Equation (2.22) can also be arranged in matrix form,

$$\underline{J} = [\overline{\overline{B_f}}]^{-1} \times \underline{RHS} \tag{2.23a}$$

$$B_f(j,j) = \frac{x_j}{D_{j,n}} + \sum_{\substack{s=1 \\ s \neq j}}^{n} \frac{x_s}{D_{j,s}} \tag{2.23b}$$

$$B_f(j,s) = -x_j \left(\frac{1}{D_{j,s}} - \frac{1}{D_{j,n}} \right) \tag{2.23c}$$

$$RHS_j = -\frac{p}{RT} \nabla x_j \tag{2.23d}$$

The radial velocity in the boundary layer is calculated from Eq. (2.3), since total pressure is almost constant outside the particle and a separate equation for the gas phase momentum is not necessary. Within the particle, Eq. (2.3) is used to calculate the pressure since pressure may build up within the porous structure.

It was verified that the choice of the n^{th} species did not affect the numerical results. Appendix A.1 shows plots of species mole fractions using the model described here and in later chapters, using both CO and N_2 as the n^{th} species, with indistinguishable results. However, it is computationally faster to use, as the n^{th} species, a species that is present in larger mole fractions.

2.5. Thermal Annealing

Annealing is a high temperature process that reduces the reactivity of solid fuel particles. It is often cited as one of the main causes of unconverted carbon in combustion and entrained flow gasification systems [27,50]. Carbon present in fly ash often is observed to be highly ordered at the atomic level [51]. Despite the relatively high carbon conversions achieved in such systems, a typical coal with 10% (by weight) ash inclusions that is reacted to 99% carbon conversion will result in ash that contains ~8% carbon, rendering it unusable in concrete applications [52].

Based largely on analysis using X-ray diffraction (XRD), annealing is thought to be caused by an increase in atomic ordering of the carbon matrix, similar to the process of graphitization [26,50]. Annealing has been shown to reduce the reactivity, compared to an un-annealed char, by up to two orders of magnitude [53], with potentially even greater reductions [27]. Jenkins et al. found that when subject to identical heat treatments between 873 and 1273 K, the loss of oxidation reactivity was highest for lignite char, followed by bituminous and anthracite char, respectively [40]. Senecca et al. found that deactivation of coal chars was more severe than deactivation of petcoke [54] and Zolin et al. found that char from leached wheat straw deactivated to a greater degree than coal char and petcoke [53]. In general, it is thought that the more disordered a carbon's structure, the greater the propensity for annealing.

In addition to increasing the ordering of the char structure, annealing is also thought to affect the char's reactivity via transformations of the dispersed catalytic inorganic inclusions in the char, if present in significant quantities [50,55,56]. This is believed to occur via a sintering – induced loss of catalytic activity for the heterogeneous char oxidation and gasification reactions. It has also been suggested, based on XRD analysis, that the two phases interact to reduce the char's reactivity: inorganic inclusions act as catalytic sites to increase the ordering of nearby carbon crystallites, the latter being directly correlated with the char's reactivity [56]. Loss of char surface area during heat treatment may play a role as well, although this is thought to be less of a factor than atomic carbon and mineral rearrangements [54]. The presence of oxygen during annealing has been shown to mitigate annealing, to some degree, when the temperature is below 1200 °C, possibly due to the fact that oxygen chemisorbs in this temperature range and inhibits the rearrangement of graphene layers [57].

The annealing model originally developed by Suuberg et al. [26] and its subsequent modifications [27,53] has been applied in this study. This model is able to describe the experimentally observed rapid reduction and subsequent plateau in reactivity when char is subjected to an isothermal heat treatment, as well as the observation that the activation energy for annealing increases for higher temperature heat treatments [27]. The interpretation of these observations is that fresh char contains active sites with a distribution of activation energies for annealing, E_d. Initially, the char undergoes rapid atomic rearrangements upon heating, but as the lower activation energy rearrangements approach completion, further solid-phase transformations require ever higher temperatures. Hurt et al. employed a log-normal distribution for the initial annealing activation energies [27], while Zolin et al. used a shifted gamma distribution based on experiments performed with a variety of chars [53].

In this study, the initial normalized distribution of active sites, F, as a function of annealing activation energies, E_d, is a shifted gamma function,

$$F(E_d, t=0) = \frac{(E_d-\delta)^{\alpha-1}}{\Gamma(\alpha)\beta^{\alpha}} \exp\left(-\frac{(E_d-\delta)}{\beta}\right) . \qquad (2.24)$$

Annealing destroys active sites as a first order process in the remaining active sites, for *each* annealing activation energy,

$$\left(\frac{\partial F}{\partial t}\right)_{E_d} = -A_d F \exp\left(-E_d \middle/ RT\right) \quad . \tag{2.25}$$

This equation can be integrated, using the initial distribution of active sites, to yield the updated, normalized distribution of activation energies,

$$F(E_d,t) = \frac{(E_d-\delta)^{\alpha-1}}{\Gamma(\alpha)\beta^{\alpha}} \exp\left(-\frac{(E_d-\delta)}{\beta}\right) \exp\left(-A_d t \exp\left(-E_d \middle/ RT\right)\right). \tag{2.26}$$

The fraction of active sites remaining at any time, $N(t)/N_0$, is obtained by integration over all activation energies:

$$\frac{N(t)}{N_0} = \int_0^{\infty} F(E_d)\,dE_d \,. \tag{2.27}$$

The char's post-heat treatment reactivity towards O_2, CO_2, etc. at any time, k_{HT}, is the original, un-annealed reactivity, k_0, multiplied by the fraction of active sites remaining, $N(t)/N_0$.

$$k_{HT} = k_0 \frac{N(t)}{N_0} \tag{2.28}$$

The same formulation may be used whether the heat treatment is isothermal, or as is the case in practice, the temperature varies significantly with time. Although not stated explicitly in [25], this may be handled by dividing the temperature-time history into discrete time bins of uniform temperature, and applying Eq. (2.25) to each bin. The initial condition for each bin is the distribution function $F(t, E_d)$ where t is now the time at the end of the previous bin. This continues for each temperature-time bin, giving the following equation for the fraction of active sites remaining at a given time:

$$F(E_d,t) = \frac{(E_d-\delta)^{\alpha-1}}{\Gamma(\alpha)\beta^{\alpha}} \exp\left(-\frac{(E_d-\delta)}{\beta}\right) \exp\left(-\sum_{bin} A_d\, t_{bin} \exp\left({}^{-E_d}\!\big/_{RT_{bin}}\right)\right), \tag{2.29}$$

which can again be integrated over all activation energies, E_d, to obtain k_{HT}. Equation (2.29) is the equation governing concurrent annealing incorporated into the modeling framework.

2.6. Kinetics

The determination of reaction rate expressions and their associated kinetic parameters for heterogeneous reactions is quite difficult. Not only is it necessary to perform measurements that are free from transport limitations (preferably at all scales), but complications arising from the heterogeneity of the char structure must be taken into account if the mechanism and parameters are to be used for chars and operating conditions different from those of the kinetic experiments. The intrinsic reaction rate of char with oxygen, carbon dioxide and steam is highly dependent on the parent coal or solid fuel, the conditions to which it is subjected during devolatilization and the spatial and size distribution of catalytic mineral inclusions, such as K, Na, Ca, Mg and their oxides, within the char [58,59]. The latter is thought to increase in importance as rank of the parent coal decreases [58]. These factors all influence the concentration of active surface sites on which the heterogeneous reactions occur. Ideally, universally applicable intrinsic kinetics (normalized per unit of *reactive* surface area [43] for each reaction) could be determined if a full heterogeneous reaction mechanism was formulated and was valid for different chars, if the catalytic effects of mineral inclusions were quantified and if the effect of carbon crystallinity on the reactive surface area could be elucidated. However, since such a task is daunting, it is necessary to determine reaction rate forms valid for a subset of chars and preparation conditions and to absorb differences between individual chars (due to hydrogen content, catalytic effects, etc.) into the reaction rate coefficients. To obtain reliable rate data for a given solid fuel and char formation conditions, this necessitates the performance of measurements for a particular char under the relevant operating conditions.

Heterogeneous reaction mechanisms can be described by a range of kinetic expressions. The simplest are power law expressions, of the form,

$$R = kP_i^n \tag{2.30}$$

with a rate coefficient given by the Arrhenius expression

$$k = A\exp(-E/\overline{R}T)\,. \tag{2.31}$$

This type of expression can be fit to experimental data to determine the order of reaction, n, using measurements of log R vs. log P_i, whereas A and E can be determined using Arrhenius plots of log k vs. $1/T$. These expressions are limited in validity to pressure ranges under which the measurements were taken and for which the order, n, is observed to be constant. Furthermore, despite the fact that k accounts for a dependence on temperature, the range of temperatures over which a power law expression is valid may also be limited, due to the fact that in different temperature ranges, the elementary surface pathways governing the overall reaction may change. For instance, it has been suggested by Hurt and Calo [60], based on their review of work by many researchers (e.g. [61–63]), that as temperature increases, the overall reaction order for char oxidation goes through a minimum, due to the fact that, according to their mechanism, at low temperatures the reaction is oxygen-surface-complex controlled, at intermediate temperatures it is desorption controlled and at high temperatures it is adsorption controlled. However, it is difficult to perform kinetic measurements at higher temperatures due to diffusion limitations, which must be accounted for in a simplified manner. This results in significant uncertainties when trying to extract diffusion-free kinetics at high temperatures.

It should be noted that experimental evidence exists suggesting that power law expressions are valid for char oxidation reactions, spanning several orders of magnitude in oxygen partial pressure [64]. While power law rate forms are sometimes thought to lack a clear theoretical basis, it has been shown that for heterogeneous reactions, the distribution of activation energies for desorption due to the heterogeneity of surface sites can lead to persistent n^{th} order behavior [64]. This behavior has been noted in the literature over a range of total and partial pressures, up to $P_{Total} = 32$ atm [65].

As mentioned above, since char gasification reactions occur on surfaces, some type of adsorption, reaction and desorption mechanism must occur. Furthermore, when a mixture of several gas species is present, more complex rate mechanisms based on these phenomena can, in principle, account for the inhibition of the reaction by reactant or product species. This is especially important during char gasification, which occurs in a background gas of CO_2, CO, H_2 and H_2O, typically at high pressures. Examples of this type of reaction mechanism are the Langmuir, Langmuir-Hinshelwood and semi-global (three step) kinetic mechanisms that have been proposed for char oxidation [60,66] and gasification (e.g. [67-70]). Based on a comprehensive literature review, Liu and Niksa recommend this type of mechanism for combustion and gasification at high pressure [70]. Equation (2.32) shows the proposed expression for oxidation, while Eqs. (2.33) shows the expressions for gasification

$$R_{C+O_2} = \frac{k_1 k_2 P_{O_2}^2 + k_1 k_3 P_{O_2}}{k_1 P_{O_2} + k_3/2} \tag{2.32}$$

$$R_{C+H_2O} = \frac{k_6 P_{H_2O}}{1 + \frac{k_4}{k_5} P_{CO_2} + \frac{k_4'}{k_5} P_{CO} + \frac{k_6}{k_7} P_{H_2O} + \frac{k_6'}{k_7} P_{H_2}} \tag{2.33a}$$

$$R_{C+CO_2} = \frac{k_4 P_{CO_2}}{1 + \frac{k_4}{k_5} P_{CO_2} + \frac{k_4'}{k_5} P_{CO} + \frac{k_6}{k_7} P_{H_2O} + \frac{k_6'}{k_7} P_{H_2}} \tag{2.33b}$$

While different elementary processes have been incorporated into such mechanisms, the commonality is that the surface intermediates are assumed to be in pseudo-steady state, which permits the formulation of rate laws containing only the concentrations of major species. The rate laws resultant from this assumption also contain a single expression for the overall reaction rate (either char consumption or gas production). Even more elaborate approaches relax the assumption that surface intermediate species (e.g. surface oxides) are in quasi-steady state, and the reaction expression must therefore be written as a multi-step mechanism that explicitly includes the concentration(s) of surface intermediates [71,72].

The heterogeneous reaction rate expression employed for a given (set of) reaction(s) necessarily depends upon the application for which it is being employed. When considering the fitting of experimental data taken in the kinetic regime in the presence of a single reactant and at low pressures, it is often sufficient to employ power law kinetics. Conversely, for applications in which high-pressures and multiple inhibiting species are present, the use of independent power law expressions may give erroneous results [36,68–70] and more detailed expressions should be considered. In other words, the choice of kinetic expressions should be done on a case-by-case basis and depends upon the experimental kinetic characterization that is available and the application for which that expression will be employed.

The single particle model in this thesis considers both heterogeneous and homogeneous reactions. The question of whether homogeneous reactions occur within the pore space (or within certain pore sizes) or only in the boundary layer appears to be unresolved, but in any case, it is a simple matter to modify the model one way or the other. In this thesis the homogeneous reactions have been confined to the particle boundary layer. As the model focuses on the interplay between transport, kinetics and pore structure evolution, species equations for surface or gas phase intermediates are not solved. Therefore, adsorption/desorption mechanisms which assume the intermediates to be in pseudo-steady state, like Langmuir-Hinshelwood expressions, can be incorporated, but detailed kinetic mechanisms for gas-phase or solid phase reactions are not included in the modeling framework at this time. Up to six gaseous species may be present (O_2, H_2, H_2O, CO, CO_2 and N_2), with three heterogeneous (R1-R3) and two homogeneous (R4, R5) reactions considered:

$$C + CO_2 \rightarrow 2CO \tag{R1}$$

$$C + \frac{\xi + 2}{2(\xi + 1)} O_2 \rightarrow \frac{\xi}{\xi + 1} CO + \frac{1}{\xi + 1} CO_2 \tag{R2}$$

$$C + H_2O \rightarrow CO + H_2 \tag{R3}$$

$$CO + \tfrac{1}{2} O_2 \rightarrow CO_2 \tag{R4}$$

$$H_2 + \tfrac{1}{2} O_2 \rightarrow H_2O \tag{R5}$$

The expression for homogeneous reaction (R4) is from [73] and that for (R5) is taken from [74]. A final issue needing clarification is the CO/CO_2 product ratio for reaction (R2). We adopt the results of Tognotti et al. [75] for Spherocarb oxidation, which gives,

$$\xi = 70 \exp(-3070/T). \tag{2.34}$$

2.7. Fragmentation

Fragmentation of char particles during combustion and gasification can influence carbon conversion and the production of particulate matter, having a positive effect on the former and a deleterious effect on the latter. Kerstein and Niksa explained the observation of char fragmentation using percolation theory, which studies the connectivity of disordered media and the impact of the local structure on the connectivity of the entire lattice [76]. As the solid char is consumed by reaction, its porosity increases to a level at which the connectivity of the solid is insufficient to maintain its structural integrity.

When the pore network is assumed to be random, Kerstein and Niksa found that the predicted critical porosity, at which the structure undergoes a sudden transition from a connected, infinite lattice to a disconnected lattice, is near 70%, irrespective of the pore shape and size [76]. This model can be applied to particles of uniform porosity, for which the entire particle is viewed as the infinite lattice and disintegrates at once, or to conditions in which the porosity varies throughout the particle (zone II) and fragmentation occurs locally when the critical porosity is attained. The latter scenario requires that local volume averaging holds; in other words, the variation in porosity with location in the particle must occur over scales larger than those of the pore radii or distance between pores. They also found that for five different types of graphite and amorphous carbon, the critical porosity in the kinetic regime was between 50% and 85%, although the particular value was distinct (and repeatable) for a particular carbon sample [76]. For coal combustion and gasification, however, a given feedstock produces a wide range of char particles during devolatilization, in terms of density, porosity, pore size distribution, etc.

Other researchers have investigated char fragmentation using simulations of the consumption of ordered or disordered lattices. Sahimi and Tsotsis [77,78] simulated the consumption of porous solids in the kinetic and diffusion-limited regimes on square and cubic lattices and derived the exponents for scaling laws for the size and number of fragments at any time in the conversion. The fragments that result from char burning in the diffusion-limited regime are much smaller than those obtained when fragmentation occurs uniformly throughout the particle. Salatino and Massimilla performed a Monte Carlo simulation of a 2-D lattice and also concluded that increasingly severe diffusion limitations yields smaller fragments [79].

Using imaging of single char particles derived from four coals of different rank during combustion at 1250 K, Hurt and Davis found that peripheral fragmentation was a relatively rare event and speculated that in more realistic combustion conditions, fragmentation behavior is the result of a competition between adhesive and disruptive forces [80]. For particles with high ash content, the char particle size changed little during this low temperature combustion, likely due to the ash maintaining a solid framework around which the combustion occurred. When the lower ash content particles experienced noticeable fragmentation, spontaneous agglomeration was often observed. It should be noted, however, that the resolution was only sufficient to see fragments of size 2-4 μm or larger.

In a series of papers, Kantorovich, Bar-Ziv and coworkers formulated a combined model of fragmentation and non-fragmenting shrinkage which is quite complex [81–83]. Their main conclusion, with respect to fragmentation, was that only meso- and macro-porosity contributes to fragmentation, whether in zone I or zone II. Shrinkage was determined to originate in the microporous regions.

Using resistivity measurements and optical imaging, Bhatia and Feng observed peripheral fragmentation during char reaction in zone II conditions [84]. During peripheral fragmentation, the char size was observed to shrink and many fragments, as small as the optical resolution of 400 nm, were observed. Their results also were consistent with the model of a local critical porosity being maintained at the moving char surface as peripheral, percolative fragmentation occurs [84], consistent with the model of Gavalas [11] discussed below.

While percolative fragmentation is actually a discrete phenomenon, with a distribution of finite particle sizes [78], it can be modeled using an equation for a continually moving particle radius, since the fragments are quite small for the case of perimeter fragmentation [84]. According to this model by Gavalas, there are two stages to the particle's size evolution. Prior to the outermost volume of the particle achieving the critical porosity, i.e. when $\phi(r_0,t) < \phi_{critical}$, the recession of the particle radius due to reaction on the external surface is minimal [10,11]. Once the critical porosity/conversion is reached at the outermost section, an equation for the particle radius can be obtained by taking the total time derivative of $\phi(r = s(t),\, t) = \phi_{critical}$, which yields [11]:

$$\frac{d\phi}{dt} = \frac{\partial\phi}{\partial r}\frac{ds}{dt} + \frac{\partial\phi}{\partial t} = 0, \tag{2.35}$$

which can be rearranged to give,

$$\frac{ds}{dt} = \begin{cases} 0 & if\ \phi(s = r_0, t) < \phi_{critical} \\ -\left[\dfrac{\partial\phi}{\partial t} \Big/ \dfrac{\partial\phi}{\partial r} \right]_{r=R(t)} & if\ \ \phi(s(t), t) = \phi_{critical} \end{cases} . \tag{2.36}$$

This is the differential equation for the evolution of particle radius, for the case of peripheral fragmentation, that has been incorporated into the modeling framework. Char, as well as any ash contained therein, is liberated and assumed to react quickly, away from the particle.

2.8. Ash Behavior

Not all chars exhibit fragmentation during reaction in regime I or II. While the reasons for this are not known, one possibility for the absence of fragmentation is the presence of ash. For some high ash chars reacting at temperatures below ash melting, it is possible that a solid ash shell remains surrounding a carbon rich core, causing the particle to maintain its original size.

However, in many practical cases, the temperature of the particle is such that the included ash will become soft, sticky or melted. It is possible that the presence of sticky ash inclusions prevents the char from fragmenting. In such a case, the ash particles would not be liberated once local conversion reaches unity, but rather, ash particles would adhere to the receding char particle surface [85,86], possibly contributing to an increased resistance to gas transport late in the particle's conversion [27].

The behavior of the included mineral manner is one of many factors that affects the size and composition distribution of the fly ash and much work attempting to understand and predict those distributions using available physical and chemical characterization of char particles has been performed [85–88]. These researchers model char combustion with shrinking core behavior and follow the evolution of the number, size and composition of ash particles as they adhere to the receding surface. Some inputs regarding the fraction, size, composition and coalescence properties of the ash particles are required. Monroe and coworkers used a Monte Carlo simulation and assumed instantaneous coalescence of ash droplets on the surface of cenospheres [85]. Barta and coworkers successfully predicted the size and SiO_2 distribution of a lignite's fly ash for the combustion of a distribution of coal particles by combining the particle-level random coalescence model [86] with the urn model [87] and using computer controlled scanning electron microscopy to obtain the required inputs. In the model of Barta et al. [86] the char burning proceeds first as a shrinking core (external diffusion control), during which the number of coalesced particles on the receding char surface is calculated following Mack [89], and eventually in kinetic control, which results in the fragmentation of the char and the release of the partially coalesced ash.

Miccio et al. [90] and Kurose at al. [91] used Monte Carlo simulations that considered ash migration *within* a burning char particle. The ash coalescence was assumed to occur over a finite time and the results are highly-dependent on the mobility of the ash inclusions (which, in turn, is dependent on ash softening/melting/fluid properties and the particle temperature). The simulations indicated that a range of behaviors are possible: inhibition of percolation occurred in the presence of large amounts of immobile ash, many fragments formed for intermediate ash mobility, while only a few large fragments remain when ash mobility is high (which is similar to the assumption of instantaneous coalescence) [90].

While the single particle model developed here is not concerned with the properties of the resulting fly ash distributions, ideas from the above-referenced works that pertain to the behavior of ash within single char particles have been incorporated into the modeling framework. Modeling char/ash morphological behavior in the limiting case of a coherent ash structure corresponds to char consumption occurring within a particle of constant size. This may be realistic for chars with a large fraction of ash that does not undergo melting. For chars with little ash, whether or not the ash is mobile and undergoes coalescence, it may not be present in sufficient quantities to inhibit the percolation behavior of the char. In such a case, it can be assumed that if the char undergoes fragmentation, the ash inclusions simply fragment away as well. When ash is present in sufficient quantities and the particle temperature and ash properties are such that the ash possesses sufficient mobility, the adherence and coalescence of sticky may be responsible for char particle size reduction without fragmentation [27].

In modeling such a case in the present framework, there are essentially three stages to the evolution of the particle's radius, rather than the two that exist for the case of peripheral fragmentation outlined above. During the first stage, the particle's radius is constant while its outermost volume hasn't been fully converted. Once the porosity at the particle edge reaches a value approaching 100%, the particle begins to shrink with ash particles adhering to the surface. These two stages are identical, mathematically, to the two stages that exist for peripheral fragmentation, with the only difference being that in the case of ash adherence, the "critical porosity" is closer to unity. During the second stage the ash particles are assumed to be too few in number to affect the transport of gas to and from the porous matrix.

Once the particle's surface has receded enough to liberate a "critical volume" of ash, a continuous ash layer is formed [27]. There are now three separate regions in the computational domain: porous char, porous sticky ash and a gas-phase boundary layer. Due to the process of ash melting/sintering that occurs at a finite rate, the porosity of the ash layer may decrease in time. However, since the outermost portion of the ash layer has been exposed and free to coalesce for longer than portions closer to the char surface, the porosity of the ash layer may also be a function of position. Once the porosity (at any radial location) within the ash layer decreases below a given threshold, such that diffusion of reactants is no longer possible, it is assumed that all reactions cease and any remaining char has been encapsulated inside the ash.

In this thesis, this critical ash volume is calculated as follows. Ash inclusions are assumed to be spheres of radius L_{ash}, which become exposed on the particle surface as it recedes. The probability that any point on the char surface is covered by a particular ash particle is

$$\Pr(particular\, ash) = \frac{L_{ash}}{4\pi s(t)^2}, \tag{2.37}$$

and therefore, the probability that a point on the surface is not covered by any ash particles, is

$$\Pr(no\,ash) = \left(1 - \frac{L_{ash}}{4\pi s(t)^2}\right)^{N_{ash}}, \tag{2.38}$$

and the probability that a given point is covered by any ash particle is

$$\Pr(any\,ash) = 1 - \left(1 - \frac{L_{ash}}{4\pi s(t)^2}\right)^{N_{ash}}, \tag{2.39}$$

where the total number of ash particles on the char surface is given by,

$$N_{ash}(t) = \left[1 - \left(\frac{s(t)}{R_0}\right)^3\right] N_{ash,total} \tag{2.40}$$

and,

$$N_{ash,total} = \frac{V_{ash,total}}{\frac{4}{3}\pi L_{ash}^3} = f_{ash}\left(\frac{R_0}{L_{ash}}\right)^3. \tag{2.41}$$

Substituting into Eq. (2.39) we obtain,

$$\Pr(any\,ash) = 1 - \left(1 - \frac{L_{ash}}{4\pi s(t)^2}\right)^{\left[1 - \left(\frac{s(t)}{R_0}\right)^3\right] f_{ash}\left(\frac{R_0}{L_{ash}}\right)^3}. \tag{2.42}$$

The critical coverage can now be specified and compared to the calculated surface coverage given by Eq. (2.42). Once this threshold is achieved, the ash layer adhering to the surface is assumed to constitute its own layer and the calculation of two separate moving boundaries, *s(t)* and $r_{ash}(t)$, is required. This derivation assumes that the ash particle radii do not change before the critical volume has been reached, which is not strictly accurate, since coalescence of ash particles will occur and change the particle size.

Loewenberg [38] calculated the radius of a char particle with a surrounding ash layer, $r_{ash}(t)$, using a balance on the mineral matter contained in the char and the instantaneous char radius, *s(t)*. A balance on the mineral matter in the char that is modified to allow the ash layer porosity to vary with position, assuming none is lost to vaporization, yields

$$r_0^3 f_{ash} = s^3(t) f_{ash} + 3 \int_{s(t)}^{r_{ash}(t)} r^2 (1 - \phi_{ash}(r,t)) dr . \tag{2.43}$$

We are interested in solving for $r_{ash}(t)$, which only appears in the limit of the integral in Eq. (2.43). Taking the time derivative of both sides and using the Leibnitz rule on the integral gives

$$-f_{ash} s^2 \frac{ds}{dt} = \int_{s(t)}^{r_{ash}(t)} \frac{\partial(1 - \phi_{ash}(r,t))}{\partial t} r^2 dr + r_{ash}^2 (1 - \phi_{ash}(r_{ash},t)) \frac{dr_{ash}}{dt} - s^2 (1 - \phi_{ash}(s(t),t)) \frac{ds}{dt} . \tag{2.44}$$

It will be assumed that the local porosity of the ash layer is a linearly decreasing function (with rate Υ) of the time that the ash is both above the softening temperature and exposed on the surface of the char, which can be represented using a sigmoid function,

$$\phi_{ash}(r,t) = \phi_{ash,0} - \Upsilon \int_{t\_exposed(r)}^{t} \frac{dt}{1+\exp\left[-10(T_{ash} - T_{melt})\right]}. \tag{2.45}$$

If the ash temperature is assumed to be uniform, which is fairly accurate, the integrand in Eq. (2.44) is only a function of $T_{ash}(t)$ and is independent of position. It can therefore be brought outside the integral, which is now easily evaluated. Equation (2.44) can be rearranged to give an equation for the ash layer thickness as a function of the char particle radius, its time derivative and the rate at which the ash is decreasing in porosity:

$$\frac{dr_{ash}}{dt} = \frac{s^2(t)\left[\left(1-\phi_{ash}(s(t))-f_{ash}\right]\frac{ds}{dt} - \frac{\Upsilon}{3}\frac{\left(r_{ash}^3(t)-s^3(t)\right)}{\left(1+\exp[-10(T_{ash}-T_{melt})]\right)}}{r_{ash}^2(t)\left[1-\phi_{ash}(r_{ash}(t))\right]} \tag{2.46}$$

Equations (2.45) and (2.46) are the equations governing ash layer behavior incorporated in the model. Unless there is a discontinuity in the value of the ash porosity at the char/ash interface, then the first term in the numerator of Eq. (2.46) is zero. Note that the linear rate of decrease in ash porosity, Υ, is simplistic, not least due to the fact that the porosity obviously levels off as it approaches zero. However it is necessary for a tractable solution, because other forms would not allow the integral in Eq. (2.44) to be evaluated analytically. Also note that the entire reaction ceases when the porosity anywhere in the ash layer reaches some minimum (percolation) threshold. This is physically plausible as well as necessary to maintaining Eq. (2.44) independent of *r*. This somewhat alleviates the problem of a linear rate being unrealistic near a porosity of zero, since the porosity would never approach zero before reactions have ceased.

Finally, gas diffusion through the ash layer must be described. The dusty gas model approach is adopted (FSM with a single pore size) with an average pore size given by the hydraulic radius, $R_{ash} = 2\phi_{ash} / S_{ash}$. The porosity of the ash is given by Eq. (2.45) and the surface area of the ash has been taken as constant, but could be made a function of ϕ_{ash} and further information on ash particle size.

2.9. Conclusions

There are several chemical, transport and morphological processes that are important to incorporate in a *generally applicable* model of char combustion and gasification, and these processes have been reviewed in this chapter. A spherically symmetric, transient model of a reacting, porous char particle and its surrounding boundary layer has been developed which incorporates the flux relations of Feng and Stewart with a slight variation and the adaptive random pore model (to be described in Ch. 3), both of which are consistent with an evolving, discrete pore size distribution. The modeling framework also allows for different types of kinetic expressions, concurrent annealing, particle size reduction and the possibility of ash adherence to the particle surface, although the latter sub-model requires the specification of several parameters which may be difficult to determine experimentally.

Nomenclature and Units

A = pre-exponential factor (mol /m^2_C s $(\text{atm})^\text{n}$) or (g /m^2_C s $(\text{atm})^\text{n}$)

A_d = pre-exponential factor for annealing (1/s)

B_f = matrix defined by Eq. (2.9) (s/m^2)

B_0 = Permeability (m^2)

C = concentration (mol/m^3)

C_p = specific heat (J/mol K)

$C(E_d)$ = post heat-treatment distribution of annealing activation energies (mol/J)

D = diffusion coefficient (m^2/s)

E = activation energy (J/mol) or (kJ/mol)

E_d = activation energy for annealing (J/mol)

f_{ash} = volume fraction of ash in char ( )

f = fraction of pore volume

F = distribution of active sites with activation energy (mol/J)

J = diffusive flux (mol/m^2 s)

$\vec{J}$ = diffusive flux vector for all species (mol/m^2 s)

k = thermal conductivity (W/m K)

k, k_{HT} = (post-annealing heat treatment) reaction rate constant (mol_C /m^2_C s $(\text{atm})^\text{n}$)

$\vec{l_\Omega}$ = unit vector along pore axis

$l_{0,i}$ = total length of pores i per unit volume (m/m^3)

L_{ash} = radius of included ash particles (m)

MW = molecular weight (g/mol)

n = number of pore bins, number of gas species, or reaction order

$n'_{i,j}$ = expected number of intersections of pores *i* and *j* per unit length of pores *i* (1/m)

$N(t)/N_0$ = fraction of active sites remaining ( )

N_j = Species flux (mol j/m^2 s)

N_{Tot} = Convective flux (mol/m^2 s)

p = pressure or partial pressure (Pa) or (atm)

q, q_i = pore growth variable (uniform or individual) (m)

q_{rad} = radiative heat flux (W/m^2)

r = radial position (m)

r_{ash} = position of moving ash boundary (m)

r_h = hydraulic radius (m)

R = pore radius (m)

$\Re$ = intrinsic heterogeneous reaction rate (mol/m^2_C s)

$\overline{R}$ = universal gas constant (J/mol K)

RHS = vector of driving forces for diffusion (mol/m^4)

s = position of moving char boundary (m)

S = total pore surface area (m^2_C/m^3)

S_i = pores *i* surface area (m^2_C/m^3)

t = time (s)

T = temperature (K)

u = radial velocity (m/s)

x = mole fraction

X = total solid conversion (-)

V = volume (m^3)

Greek Symbols

α = shape parameter in gamma distribution

β = scale parameter in gamma distribution, or sigmoid function defined in Eq. (40)

δ = shift parameter in gamma distribution (J/mol)

ϕ_i = porosity ($m^3_{pore\ i}/m^3$)

ϕ_{Tot} = total porosity (m^3_{pore}/m^3)

$\eta_{i,k}$ = effectiveness factor for pore *i* in reaction *k* (-)

μ = viscosity (kg/m s)

ν = stoichiometric coefficient (mol/mol)

ρ = density (kg/m^3)

ρ_{True} = true solid density (helium density) (kg/m^3)

ς = dimensionless radial coordinate (-)

ξ = coefficient in determining CO/CO_2 ratio from reaction (R2)

Δ = expression for DGM or FSM defined in text (m^2/s)

Δh_r = heat of reaction at a given temperature (J/mol)

Φ = Thiele modulus (-)

Γ = gamma function

Υ = rate of decrease in ash layer porosity (1/s)

Ω = pore orientation (str)

Subscripts

0 = at initial time $t=0$ or initial conversion $X=0$

ash = property of ash

bin = associated with particular annealing temperature bin

bulk = property at the bulk gas conditions

continuum = molecular diffusion coefficient

critical = at the critical conversion or porosity

C = char

eff = effective coefficient accounting for gas and solid phase

Final = at final time, at X=1

gas = property of gas

hold = length of time at a given temperature heat treatment

i = pore size

j = gas species

k = reaction index

Kn = Knudsen diffusion coefficient

melt = Temperature at which ash "melts"

$s^{+/-}$ = at location just below or beyond porous medium/gas interface

s = gas species

solid = property of solid

t = gas species

Tot = total

True = helium density

References

[1] R.E. Mitchell, R.J. Kee, P. Glarborg, M.E. Coltrin, Twenty-Third Symposium (International) on Combustion (1990) 1169-1176.

[2] S.Y. Cho, R.A. Yetter, F.L. Dryer, Journal of Computational Physics 102 (1992) 160-179.

[3] J.C. Lee, R.A. Yetter, F.L. Dryer, Combustion and Flame 101 (1995) 387-398.

[4] S. Goel, C.H. Lee, J.P. Longwell, A.F. Sarofim, Energy and Fuels 10 (1996) 1091-1098.

[5] R. Stauch, U. Maas, International Journal of Heat and Mass Transfer 52 (2009) 4584-4591.

[6] M.Y. Ha, B.R. Choi, Combustion and Flame 97 (1994) 1-16.

[7] V. Raghavan, V. Babu, T. Sundararajan, R. Natarajan, International Journal of Heat and Mass Transfer 48 (2005) 5354-5370.

[8] F.J. Higuera, Combustion and Flame 152 (2008) 230-244.

[9] J. Lee, A.G. Tomboulides, S.A. Orszag, R.A. Yetter, F.L. Dryer, Twenty-Sixth Symposium (International) on Combustion (1996) 3059-3065.

[10] G.R. Gavalas, AIChE Journal 26 (1980) 577-585.

[11] G.R. Gavalas, Combustion Science and Technology 24 (1981) 197-210.

[12] C. Feng, W.E. Stewart, Ind. Eng. Chem. Res. 12 (1973) 143-147.

[13] S.K. Bhatia, D.D. Perlmutter, AIChE Journal 26 (1980) 379-386.

[14] S.K. Bhatia, D.D. Perlmutter, AIChE Journal 27 (1981) 247-254.

[15] S.V. Sotirchos, N.R. Amundson, AIChE Journal 30 (1984) 537-549.

[16] S.V. Sotirchos, N.R. Amundson, AIChE Journal 30 (1984) 549-556.

[17] E.A. Mason, A.P. Malinauskas, Gas Transport in Porous Media: The Dusty-Gas Model, Elsevier, 1983.

[18] G. Ballal, C.-hsien Li, R. Glowinski, N.R. Amundson, Computer Methods in Applied Mechanics and Engineering 75 (1989) 467-479.

[19] J.I. Morell, N.R. Amundson, S.K. Park, Chemical Engineering Science 45 (1990) 387-401.

[20] R. Jackson, Transport in Porous Catalysts, Elsevier, New York, 1977.

[21] S. Reyes, K.F. Jensen, Chemical Engineering Science 41 (1986) 345-354.

[22] S. Srinivasachar, M.A. Toqan, J.M. Beer, H.M. Ettouney, Combustion Science and Technology 57 (1988) 55-70.

[23] M.J. Biggs, P.K. Agarwal, Chemical Engineering 52 (1997) 941-952.

[24] F.Y. Wang, S.K. Bhatia, Chemical Engineering Journal 56 (2001) 3683-3697.

[25] A. Zolin, A. Jensen, Combustion and Flame 125 (2001) 1341-1360.

[26] E.M. Suuberg, M. Wojtowicz, J.M. Calo, Carbon 27 (1989) 431-440.

[27] R. Hurt, J.K. Sun, M. Lunden, Combustion and Flame 113 (1998) 181-197.

[28] Y. Cai, K. Zygourakis, Ind. Eng. Chem. Res. 42 (2003) 2746-2755.

[29] R.E. Mitchell, L. Ma, B. Kim, Combustion and Flame 151 (2007) 426-436.

[30] G. Ballal, K. Zygourakis, Ind. Eng. Chem. Res. 26 (1987) 1787-1796.

[31] R.H. Hurt, A.F. Sarofim, J.P. Longwell, Fuel 70 (1991) 1079-1082.

[32] I. Aarna, E.M. Suuberg, Twenty-Seventh Symposium (International) on Combustion 27 (1998) 2933-2939.

[33] L.R. Radovic, P.L. Walker, R.G. Jenkins, Fuel 62 (1983) 849-856.

[34] P. Salatino, O. Senneca, S. Masi, Carbon 36 (1998) 443-452.

[35] B. Feng, S.K. Bhatia, Carbon 41 (2003) 507-523.

[36] D.G. Roberts, D.J. Harris, T.F. Wall, Energy & Fuels 17 (2003) 887-895.

[37] R. Sahu, R.C. Flagan, G.R. Gavalas, Combustion and Flame 77 (1989) 337-346.

[38] M. Loewenberg, Y.A. Levendis, Combustion and Flame 84 (1991) 47-65.

[39] M. Sahimi, G.R. Gavalas, T.T. Tsotsis, Chemical Engineering Science 45 (1990) 1443-1502.

[40] R.G. Jenkins, S.P. Nandi, P.L. Walker, Fuel 52 (1973) 288-293.

[41] S. Dutta, C.Y. Wen, Ind. Eng. Chem., Process Des. Dev. 16 (1977) 20-30.

[42] S. Dutta, C.Y. Wen, Ind. Eng. Chem., Process Des. Dev., Vol. 16 (1977) 31-37.

[43] A. Lizzio, H. Jiang, L.R. Radovic, Carbon 28 (1990) 7-19.

[44] A. Wheeler, Advances in Catalysis: Reaction Rates and Selectivity in Catalyst Pores, Vol. 3, 1951.

[45] G.A. Simons, M.L. Finson, Combustion Science and Technology 19 (1979) 217-225.

[46] G. Ballal, K. Zygourakis, Ind. Eng. Chem. Res. 26 (1987) 911-921.

[47] S.V. Sotirchos, V.N. Burganos, AIChE Journal 34 (1988) 1106-1118.

[48] S.V. Sotirchos, AIChE Journal 35 (1989) 1953-1961.

[49] R. Krishna, J.A. Wesselingh, Chemical Engineering Science 52 (1997) 861-911.

[50] O. Senneca, P. Russo, P. Salatino, S. Masi, Carbon 35 (1997) 141-151.

[51] A. Zolin, A. Jensen, K. Dam-johansen, Fuel 81 (2002) 1065-1075.

[52] R. Hurt, Symposium (International) on Combustion 27 (1998) 2887-2904.

[53] A. Zolin, A. Jensen, K. Dam-Johansen, Proceedings of the Combustion Institute 28 (2000) 2181-2188.

[54] O. Senneca, P. Salatino, S. Masi, P.V. Tecchio, Fuel 77 (1998) 1483-1493.

[55] A. Zolin, A. Jensen, P.A. Jensen, F. Frandsen, K. Dam-johansen, Energy and Fuels 15 (2001) 1110-1122.

[56] B. Feng, S.K. Bhatia, J.C. Barry, Carbon 40 (2002) 481-496.

[57] O. Senneca, P. Salatino, S. Masi, Experimental Thermal and Fluid Science 28 (2004) 735-741.

[58] K. Miura, K. Hashimote, P.L. Silveston, Fuel 68 (1989) 1461-1475.

[59] R.P.W.J. Struis, C.V. Scala, S. Stucki, R. Prins, Chemical Engineering Science 57 (2002) 3593 - 3602.

[60] R.H. Hurt, J.M. Calo, Combustion and Flame 2180 (2001).

[61] J. Hong, W.C. Hecker, T.H. Fletcher, Proceedings of the Combustion Institute 28 (2000) 2215-2223.

[62] M.A. Field, Combustion and Flame 5 (1970) 237- 248.

[63] I.W. Smith, Combustion and Flame 17 (1971) 303-314.

[64] R.H. Hurt, B.S. Haynes, Proceedings of the Combustion Institute 30 (2005) 2161-2168.

[65] W.C. Hecker, P.M. Madsen, M.R. Sherman, J.W. Allen, R.J. Sawaya, T.H. Fletcher, Energy & Fuels 14 (2003) 427-432.

[66] B.S. Haynes, Combustion and Flame 126 (2001) 1421-1432.

[67] P.L. Walker, F. Rusinko Jr., L.G. Austin, in:, D.. Elwey, P.W. Selwood, P.B. Weisz (Eds.), Advances in Catalysis, Vol XI, 1959, pp. 133-221.

[68] H.-J. Muhlen, K.H. van Heek, H. Juntgen, Fuel 64 (1985) 944-949.

[69] D.G. Roberts, D.J. Harris, Energy & Fuels 26 (2012) 176-184.

[70] G.-su Liu, S. Niksa, Progress in Energy and Combustion Science 30 (2004) 679-717.

[71] P.A. Campbell, R.E. Mitchell, L. Ma, Proceedings of the Combustion Institute 29 (2002) 519-526.

[72] P.A. Campbell, R.E. Mitchell, Combustion and Flame 154 (2008) 47-66.

[73] J.B. Howard, G.C. Williams, D.H. Fine, Symposium (International) on Combustion 14 (1973) 975-986.

[74] A.K. Varma, A.U. Chatwani, F.V. Bracco, Combustion and Flame 64 (1986) 233-236.

[75] L. Tognotti, J.P. Longwell, A.F. Sarofim, Symposium (International) on Combustion 23 (1990) 1207-1213.

[76] A.R. Kerstein, S. Niksa, Proceedings of the Combustion Institute 20 (1984) 941-949.

[77] M. Sahimi, T.T. Tsotsis, Physical Review Letters 59 (1987) 888-891.

[78] M. Sahimi, Physical Review A 43 (1991) 5367-5376.

[79] P. Salatino, L. Massimilla, Symposium (International) on Combustion 22 (1988) 29-37.

[80] R. Hurt, K. Davis, Combustion and Flame 116 (1999) 662- 670.

[81] X. Zhang, A. Dukhan, I.I. Kantorovich, E. Bar-Ziv, Combustion and Flame 106 (1996) 203-206.

[82] I.I. Kantorovich, E. Bar-Ziv, Combustion and Flame 113 (1998) 532-541.

[83] E. Bar-ziv, I.I. Kantorovich, Progress in Energy and Combustion Science 27 (2001) 667-697.

[84] B. Feng, S.K. Bhatia, Energy & Fuels 14 (2000) 297-307.

[85] L.S. Monroe, An Experimental and Modeling Study of Residual Fly Ash Formation in Combustion of a Bituminous Coal, M.I.T., 1989.

[86] L.E. Barta, T.M. A, B.J. M, A.F. Sarofim, Symposium (International) on Combustion 24 (1992) 1135-1144.

[87] L.E. Barta, F. Horvath, J.M.B. Beer, A.F. Sarofim, Symposium (International) on Combustion 23 (1990) 1289-1296.

[88] L. Yan, R.P. Gupta, T.F. Wall, Fuel 81 (2002) 337-344.

[89] C. Mack, Mathematical Proceedings of the Cambridge Philosophical Society 50 (1954) 581-585.

[90] F. Miccio, P. Salatino, W. Tina, Proceedings of the Combustion Institute 28 (2000) 2163-2170.

[91] R. Kurose, H. Makino, N. Hashimoto, A. Suzuki, Powder Technology 172 (2007) 50-56.

Chapter 3. An Adaptive Random Pore Model for Multimodal Pore Structure Evolution

3.1. Introduction

The structural evolution of porous particles undergoing gasification or combustion in the kinetically-limited (zone I) or pore diffusion-limited (zone II) regimes is important for predicting burnout behavior provided intrinsic kinetic expressions are known, and conversely, for determining proper intrinsic kinetic data from zone I experiments [1–4]. Many models of pore structure evolution have been developed [5–8], with the random pore models (RPM) being the most ubiquitous due to their relative simplicity and success at reproducing experimental data obtained under kinetically controlled conditions.

Many porous solids, including coal and biomass char, are known to possess multi-modal pore structures [9,10]. Even in what is ostensibly the kinetically controlled regime, it has been observed that pore sizes below roughly 1-2 nm may not participate in certain char gasification reactions, and therefore, the entire initial surface area may not always be the correct initial structural data to be used as input to the pore structure evolution model [1,6,11–13].

It was observed by Hurt that CO_2 did not react significantly in the micropores of a sub-bituminous coal char, possibly due to the preferential location of catalyst particles in the larger pores, or the fact that very small pores represent less reactive regions between basal planes [1]. Other researchers have observed on several occasions that O_2 does not react significantly in char micropores with radii below 1-2 nm, and this has been attributed to: (i) slow activated diffusion of O_2 in these small pores [10,14], (ii) a reaction mechanism that leads to strong chemisorption of oxygen on micropore surfaces [15], or (iii) micropores comprising less reactive sites between basal planes, which can be revealed by the removal of relatively large, obstructing hydrocarbon molecules, but which do not participate in oxidation reactions [13].

Consequently, depending on whether the reactant is oxygen, carbon dioxide or steam, normalized reaction rate versus conversion curves can exhibit widely differing behavior for the same char. This is manifested in the observation that for chars with significant initial microporosity, the normalized rate versus conversion curve may exhibit a distinct maximum when reacted with oxygen, while it may be monotonically decreasing when reacted with carbon dioxide or steam [10,15]. Other studies on coal chars which apparently contain significant amounts of closed porosity conclude that O_2 is more effective than CO_2 at opening micropores early in the conversion process, by removing disorganized hydrocarbon molecules leftover from pyrolysis, but that neither gas actually reacts substantially on the surface of the micropores [13,16].

To apply a pore structure evolution model when intra-particle species gradients are present, the practice has typically been simply to apply the same structural evolution equations *locally*, while also solving a species conservation equation to account for the fact that the reactant concentration will vary across the porous particle [17–20]. This implicitly assumes that at each position in the particle, the entire pore structure evolves in the same manner with local conversion, although this evolution may happen at varying rates due to the intra-particle species and temperature gradients.

In the pore diffusion regime, zone II, typical of many combustion and entrained flow gasification processes, simulations have indicated that the pore structure evolution has strong effects on the temperature, burnout times, fragmentation, ignition and extinction behavior of reacting porous char particles [18–20]. Specifically, when the available internal surface area increases and displays a maximum with conversion, particles burn at higher temperatures, ignite at lower ambient temperatures, experience extinction at higher conversions and have lower burning times than particles with an available internal surface area that decreases monotonically with conversion. Furthermore, under certain conditions the latter particles exhibited a conversion profile with a maximum inside the particle, while the former always had the maximum local conversion at the particle surface [18–20]. These particle-scale effects are due to both the influence of the pore surface area on the heterogeneous reaction rates as well as the influence of the pore structure on the intra-particle diffusion of gaseous species. It should be mentioned that these authors [18–20] modeled the intra-particle fluxes using the Dusty Gas Model, while other flux models that explicitly account for the distribution of pore sizes could also be implemented [21].

During entrained flow gasification and oxy-combustion in particular, coal or biomass char particles with multimodal porous structures may be subjected to multiple reactions with widely varying rates, which may occur concurrently or sequentially. Since in most cases the reactions occur in the regime of mixed kinetic/intra-particle diffusion control (zone II), the evolving porous structure plays an important role in both the heterogeneous reaction rate as well as the intra-particle transport. Because of species gradients, temperature gradients or time-dependent boundary conditions, at certain times and locations within a char particle the conversion may occur on the surface of the smallest pores, e.g., if $C+H_2O$ is the main reaction at that location and time, while at other times and locations the reaction may proceed mostly on the surface of larger pores, e.g., if $C+O_2$ is the main reaction at that position and time. The resultant pore structure evolution with local conversion will therefore not be the same throughout the particle and cannot be predicted based solely on the initial structure. This will in turn affect the reaction rate and intra-particle gaseous transport and may influence particle temperature, burning times, relative reaction rates, etc.

The above considerations indicate that in contrast with the often-invoked assumption, as conversion proceeds and the intra-particle gradients develop, the solid structure does not necessarily evolve in the same manner with local conversion at different *positions* in the porous solid. Additionally, due to local species and/or temperature variations, a given location may shift *in time* from reactions occurring on one subset of pores to reactions occurring on a different subset. Furthermore, the assumption of a strict *cutoff* of pore sizes, e.g., 2 nm, that participate in a given heterogeneous reaction may not always be realistic, since this implies that the entire range of pore sizes considered by the structural evolution model (i.e. above the cutoff) are exposed to the local smooth field concentration of reactant, while pores below the cutoff size are assumed not to be penetrated by reactants whatsoever (although they may contribute a constant additional surface area considered as surface roughness [6]) .

In other words, most random pore models designate the pores, *a priori*, as either being in kinetic control (with full reactant penetration) or in complete diffusion control (with no reactant penetration), but a particular pore size cannot be in mixed control and cannot switch from one regime to the other with time or with location. In what follows, concepts introduced by several researchers [2,6,22–24] are used to relax these assumptions and extend the RPM to account for various pore sizes growing at different rates depending on the local, instantaneous pore-scale reactant penetration throughout the solid particle. This is accomplished by incorporating pore-scale effectiveness factors, consistent with the random pore geometry, into equations for the growth of individual pore sizes.

This extension has important implications for particles reacting in the kinetic regime and for conditions of industrial relevance in which intra-particle gradients are present (zone II) and/or gaseous reactants change over the course of conversion, making it likely that pores of certain sizes will behave differently according to their location in the particle and with time. Furthermore, under zone II conditions, in addition to affecting the internal surface area (and thus the reaction rate), the pore structure evolution affects the intra-particle fluxes as well. When the structure is not strictly unimodal, implementation of a flux model that can explicitly account for this multi-modal nature [22,25], such as the Feng and Stewart model [26] may be beneficial . In such a case, accounting for various pore sizes growing at different rates can improve the accuracy of the flux model as well.

In Sections 3.2 and 3.3 we review the original RPM in discrete form and implement a slightly altered version using equations that allow the evolution of pores of different sizes to be followed separately, which results in a framework with the flexibility necessary to overcome the shortcomings mentioned above. In Section 3.4 we develop a method for quantifying the participation of various pore sizes in any reaction, using pore-scale effectiveness factors, which is consistent with the framework presented in Section 3.3. In Section 3.5 we apply the method of Section 3.4 to normalize measured kinetic data by the participating surface area in order to determine intrinsic (i.e. per unit surface area) kinetic rates. Like the original RPM, the current modified version is completely predictive in nature if the necessary initial measurements are performed. In Section 3.6, validation of the model using data from the literature is performed and examples that illustrate the flexibility of the model in cases of intra-particle gradients and time-dependent boundary conditions are presented.

3.2. The Random Pore Model

The random pore model, developed by Bhatia and Perlmutter [5] and separately by Gavalas [6] (who called it the random capillary model), is the basis for predicting the structural evolution of the porous solid and we will follow the development presented by Gavalas. The RPM was derived under the assumption that the pores consist of straight cylindrical capillaries with axes randomly located and oriented in three-dimensional space, although it can be extended to pores of other shapes [13]. By simply measuring the initial porosity distribution with pore radius, $\phi(R)$, using porosimetry and gas adsorption experiments, the random pore model can be used to predict the pore radii, surface area and porosity of the reacting porous solid at all subsequent conversions.

Due to the assumption of randomly located pores, the density of pore intersections with any plane is a Poisson process with mean, λ, meaning that the number of pores intersecting a spatial area element ds is given by $\lambda\, ds$. Gavalas also demonstrates that the total length of pore axes per unit volume is given by $l = 2\lambda$, which is constant in time if no new porosity is created or uncovered. Hurt modified the RPM to allow λ to vary in time as a way of simulating the creation of new pores, in addition to considering pore enlargement due to reaction [27]. The method was used to explain the data of Hurt [28] and Murrell [29], but it is not fully predictive because the ratio of conversion from pore creation to pore widening must be given as an input to the model or adjusted to fit the experimental data.

In order to have the flexibility to allow various pore sizes to behave differently, we adopt the discrete formulation of the random pore model as a starting point [22]. When species gradients are present at the particle scale it may be advantageous to use a discrete form of the RPM to provide consistency with an intra-particle flux model that is designed for multi-modal porous structures [22,25,26]. The discrete formulation of the RPM assumes that at time $t = 0$ there are n discrete pore sizes with radii $R_{0,i}$ and associated porosities $\phi_{0,i}$, which are defined such that the largest pores at $t = 0$ are denoted by (R_n, ϕ_n) at all times, and smaller pores by the subscripts $i = n\text{-}1, n\text{-}2$, etc.

Based on the volume of cylindrical pores i, the Poisson distribution dictates that the probability that a point in space is *not* covered by any pore of size i, is:

$$\textit{Probability point not covered by any pore } i = \exp\left(-\pi l_{0,i} R_i^2\right), \tag{3.1}$$

where the length of pore axes i per unit volume, including those axes that are overlapped by larger pores, is $l_{0,i} = 2\lambda_i$ (in Bhatia and Perlmutter's derivation and notation, the sum of all $l_{0,i}$ would correspond to $L_{E,0}$ rather than L_0) .

A volume which is covered by more than one overlapping pore size is assigned to the largest pore size that overlaps it, which makes physical sense and is consistent with experimental determinations of $\phi(R)$. Based on this definition and the fact that the probabilities of coverage by different pore sizes are independent, it is possible to write equations for the individual porosities corresponding to pores i, ϕ_i, and the total porosity, ϕ_{Tot} [22]:

$$\phi_i = \left[1 - \exp\left(-\pi l_{0,i} R_i^2\right)\right] \exp(-\pi \sum_{j=i+1}^{n} l_{0,j} R_j^2) \tag{3.2}$$

$$\phi_{Tot} = 1 - \exp(-\pi \sum_{j=1}^{n} l_{0,j} R_j^2) \tag{3.3}$$

The right-hand side of Eq. (3.2) represents the probability that a volume *is* covered by a pore i (the first term in brackets) *and* that it is *not* covered by any pores of size j larger than i (second term), which, according to the convention mentioned above, would render that volume part of pore j. The two probabilities on the right-hand-side of equation (3.2) are independent, and therefore their product gives the joint probability of a volume belonging to pores i. Equation (3.3) for the total porosity simply results upon summing equation (3.2) over all pore sizes i.

More conveniently from the standpoint of measurements, it is possible to rearrange equation (3.2) in order to determine the total length of pore axes of each size, $l_{0,i}$, using the discrete values of initial porosity, $\phi_{0,i}$, and radius, $R_{0,i}$, which can be obtained experimentally:

$$l_{0,i} = \frac{1}{\pi R_{0,i}^2} \ln\left(\frac{1 - \sum_{j=i+1}^{n} \phi_{0,j}}{1 - \sum_{j=i}^{n} \phi_{0,j}} \right) \tag{3.4}$$

In order to model the changing structure (i.e. the pore radii, total porosity and pore surface area) of the porous solid as it is consumed, most implementations of the random pore model (with some exceptions that will be discussed later [23,30]) have assumed that *all* pores considered by the model (either all the pores, or the entire range of pores above a cutoff radius) at a given location increase their radii by the same amount, $q(r,t)$, which depends on the local conversion, $X(r,t)$:

$$R_i(r,t) = R_{0,i}(r) + q(r,t) \tag{3.5}$$

Based on Eqs. (3.3), (3.5), and by noting that as the pore radius increases by an amount dq, the volume of the pores per unit volume increases by an amount $d\phi = S\,dq$, Gavalas obtains an expression relating the pore surface area per unit volume, *S*, to the pore growth variable, *q*, by differentiating equation (3.3) with respect to *q* (for clarity, from this point we drop reference to *r* and *t* in equations):

$$S = \frac{\partial \phi_{Tot}}{\partial q} = \left(1-\phi_{Tot}\right)\sum_i 2\pi l_{0,i}(R_{0,i}+q) = \left(1-\phi_{Tot}\right)\sum_i 2\pi l_{0,i}R_i \qquad (3.6a)$$

It can be verified, after some manipulations, that this is exactly equivalent to the equation for surface area evolution derived by Bhatia and Perlmutter [5],

$$S = S_0(1-X)\sqrt{1-\psi\ln(1-X)}\,, \qquad (3.6b)$$

where S_0 is the initial surface area and the structural parameter of the random pore model, ψ, given in terms of quantities employed in the random capillary model, is

$$\psi = \frac{\left(\sum_i l_{0,i}\right)}{\pi\left(\sum_i l_{0,i}R_{0,i}\right)^2}\,. \qquad (3.6c)$$

The surface area multiplies the intrinsic heterogeneous reaction rate, $\Re_k$ (mol/m^2 s), in the differential equation describing the evolution of the solid conversion with time:

$$\frac{dX}{dt}=\frac{-MW}{\rho_{True}(1-\phi_{0,tot})}S\sum_k \nu_{C,k}\Re_k\,, \tag{3.7}$$

where MW is the solid's molecular weight, $\nu_{C,k}$ is the stoichiometric coefficient of the solid (char) in reaction k and ρ_{True} is the true solid density. Assuming an initially uniform porosity, solid conversion, which varies from zero to unity, is related to the porosity by,

$$X=\frac{\phi_{Tot}-\phi_{0,Tot}}{\phi_{Final}-\phi_{0,Tot}}\,, \tag{3.8}$$

and upon substituting for $\phi_{Tot,0}$ and ϕ_{Tot} in the definition of conversion and taking $\phi_{Final}=1$ even with ash present, similar to Lu and Do [31], a quadratic equation relating q and X can be derived:

$$\left(\pi\sum_i l_{0,i}\right)q^2+\left(2\pi\sum_i l_{0,i}R_{0,i}\right)q+\ln(1-X)=0. \tag{3.9}$$

This closes the set of equations needed to determine conversion (Eq. (3.7)), pore radii (Eqs. (3.5) and (3.9)), total porosity (Eq. (3.3)) and pore surface area (Eq. (3.6a)).

3.3. Adaptive Random Pore Model (ARPM)

To address the shortcomings mentioned in the introduction, we implement for each pore size, *i*, its *own* pore growth variable, $q_i(r,t)$, which is the amount that the radii of pores *i* have increased at given location *r* in the particle, at time *t*, due to solid consumption:

$$R_i = R_{0,i} + q_i \tag{3.10}$$

This gives one the flexibility to deal with situations in which the degree of participation of pores *i* in different heterogeneous reactions varies with position and time according to reactant concentration, temperature, conversion, etc. The differential equations describing the consumption of the porous solid in time will be written in terms of dq_i/dt, since writing the differential equation as dX/dt will not be useful in this formulation, as will be discussed later in this section.

We can determine the individual surface areas of pores *i*, $S_i(r,t)$, from the increase in total pore volume due to an incremental expansion of pores *i*, dq_i:

$$S_i = \sum_j \frac{\partial \phi_j}{\partial q_i} = \frac{\partial \phi_{Tot}}{\partial q_i} = (1-\phi_{Tot})2\pi l_{0,i}(R_{0,i}+q_i)\,. \tag{3.11}$$

Finally, although it is not necessary for implementation, to gain insight into the solid conversion process, we also define for *each* pore size, *i*, its *own* conversion variable, $X_{True,i}$. However, using the usual linear relationship between conversion and porosity analogous to equation (3.8),

$$X_i = \frac{\phi_i - \phi_{0,i}}{\phi_{Final,Tot} - \phi_{0,Tot}}, \tag{3.12}$$

is not meaningful in this case, because it accounts for changes in porosities other than solid-gas reactions on pores i. In fact, using this definition, X_i could even become negative if ϕ_i decreases below $\phi_{0,i}$ due to encroachment by larger pores. Rather, we define $X_{True,i}$ as the solid conversion associated solely with the increases in ϕ_i due to solid-gas reactions on the surface of pores i. However, it is not convenient to use $X_{True,i}$ in the differential equations, because it will be impossible to *algebraically* relate the various $X_{True,i}$ to the q_i, which are needed in the expressions for S_i.

To elaborate on the last point, we note that although it is possible to use the Poisson distribution to calculate the overlap volume between many different combinations of porosity, correcting for the contributions to $X_{True,i}$ due to overlap cannot be accomplished without knowing the *history* of the pore structure evolution. For example, consider a small volume which initially contains solid (char), but at time t is covered by two different pore sizes. If the larger pore size expanded into the volume after the smaller one, one must correct for the respective porosity gain and loss caused by the overlap, because the overlap caused the porosities to be reclassified. However, if a smaller pore expands into the volume after the larger one, no correction is necessary, since the overlap volume is already included in the larger pore size by definition, consistent with Eq. (3.2). Thus, knowledge of the *order* of the expansion of all pores is required to make the corrections necessary to relate $X_{True,i}$ to q_i algebraically.

Therefore, we simply use q_i as the state variables [22] and write differential equations relating these variables to the solid reaction rates on the walls of pores *i*, as well as to pore scale effectiveness factors, $\eta_{i,k}$, that quantify the participation of each pore size, *i,* in each reaction, *k*,

$$\frac{dq_i}{dt} = f(\sum_k \Re_{i,k}, \eta_{i,k}) . \tag{3.13}$$

The form of the right hand side of Eq. (3.13) and the pore scale effectiveness factors will be discussed in more detail in the Section 3.4.

As mentioned above, both Bhatia [23] and Sotirchos et al. [30] have developed models in which each discrete (or discretized) pore size evolves separately, and have analogues of equations (3.10), (3.11) and (3.13). With the goal of modeling the structural evolution in cases where pores may experience plugging (due to solid products possessing greater volume than the solid reactants), those authors considered situations in which the reaction rate on each pore size depends on the reactant concentration reaching the reaction surface after penetrating from the pore surface through a product layer. Thus, reaction rate and pore growth could vary with pore size and location in the particle.

This development differs from theirs in that we consider the effects of transport limitations caused by the competition between reaction and diffusion throughout the entire random pore structure, whereas Bhatia and Sotirchos [23,30] consider all pores, regardless of size and interconnectedness, to possess the smooth field value of reactant concentration at the pore surface. The different applications are manifested as different forms of the right-hand-side of the pore growth evolution equations, Eq. (3.13).

Although it is not possible to determine $X_{True,i}$ analytically, the instantaneous change in $X_{True,i}$ is related to the instantaneous increase in q_i by:

$$\frac{dX_{True,i}}{dt} = \frac{S_i}{(1-\phi_{0,Tot})}\frac{dq_i}{dt}, \tag{3.14}$$

and $X_{True,i}(r,t)$ is therefore given by numerically integrating

$$X_{True,i}(q_i) = \frac{1}{(1-\phi_{0,Tot})}\int_0^{q_i} S_i \, dq_i^{'} , \tag{3.15}$$

where $q_i^{'}$ is a dummy variable of integration. S_i depends on the history of q_i and all other q_j, which is the reason why numerical integration is necessary. Even though $X_{True,i}$ is not required for implementation of the model, it is useful in analyzing the amount of conversion attributable to reactions on various pore sizes.

To our knowledge, previous random pore models have not utilized separate q_i and S_i for different pore sizes together with pore-scale effectiveness factors to quantify of the participation of different pore sizes in different reactions. This extension of the RPM, embodied by Eqs. (3.2), (3.3), (3.4), (3.10), (3.11), and (3.13), provides a framework with the flexibility necessary to deal with cases when different pore sizes grow at different rates due to the interplay between transport and kinetics, and allows the pore structure evolution to adapt to instantaneous, local conditions within the solid particle. Equation (3.13) is now discussed in more detail.

3.4. Pore-Scale Effectiveness Factors

Now that separate expressions for all of the variables associated with the individual pore sizes have been given, it is possible to deal with the fact that at any location and time, any of the pore sizes may be in a state between complete kinetic and diffusion control for any reaction. We seek to *quantify* the participation of all pore sizes i, at any location, in each reaction k. This information can then be used to describe how the individual pore sizes evolve by writing appropriate ODEs for the individual pore growth variables, dq_i/dt.

In the appendix of the original random capillary model paper [6], Gavalas uses the *pore-scale* Thiele modulus [32], Φ, a non-dimensional number representing the ratio of the reaction rate to diffusion rate, to determine when pore sizes may be assumed to be in kinetic control so that the RPM applies to those pores. Typically $\Phi < 0.3$ is sufficient to assume kinetic control and therefore Gavalas checks to verify whether this condition is satisfied for all pore sizes considered in his example. For a single cylindrical pore of radius R_i, with n^{th} order kinetics (more complex kinetic expressions could also be incorporated [33,34]), reactant concentration at the pore boundary, C_{SF}, intrinsic rate constant, $k_{intrinsic,k}$, stoichiometric coefficient, υ, length, $L_i^{'}$, (to be discussed later in this section), and an appropriate diffusion coefficient, D_{eff} (to be discussed in Section 3.5), the Thiele modulus is given by [35]:

$$\Phi_{i,k} = \frac{L_i^{'}}{2}\sqrt{\frac{(n+1)}{2}\frac{2\nu k_{intrinsic,k} C_{SF}^{n-1}}{R_i D_{eff}}} \tag{3.16}$$

We expand on this idea by calculating at all times (and locations, if smooth field gradients are present) an overall effectiveness factor, $\eta_{Tot,i,k}$, based on $\Phi_{i,k}$ and the random pore structure, which quantifies the degree of participation of pores *i*, in reaction *k*, in a manner that is consistent with the geometry of the adaptive random pore model. The effectiveness factor, $\eta_{Tot,i}$ (we now drop reference to reaction *k*), is then used in conjunction with each individual state equation dq_i/dt to shift smoothly from full to partial to negligible reactant penetration for each pore size *i*, and to allow the pores to evolve accordingly.

For the simple pore-scale, steady-state, reaction-diffusion equation on which the Thiele modulus is based, it is possible to derive the effectiveness factor, η_i, defined as the actual rate of conversion in a pore *i* divided by the theoretical rate if there were no diffusion limitations in the pore. For this situation, the effectiveness factor is given by [35]:

$$\eta_i = \frac{\tanh(\Phi_i)}{\Phi_i} \tag{3.17}$$

Equations (3.16) and (3.17) are exact only for first order reactions, $n=1$. For other rate forms it has been established that the use of the "general modulus" provides a good analytical approximation to the exact solution [33]. For general n^{th} order rates, the inclusion of the factor $(n+1)/2$ in Eq. (3.16) results from the development of the general modulus (the original Thiele modulus omits this factor).

Equation (17) represents the effectiveness factor for a single pore. However, the porous solid has a distribution of pore lengths for each pore size *i* (recall that *i* refers to radius), so the quantity of interest is actually an overall effectiveness factor $\eta_{Tot,i}$ (where the subscript "Tot" indicates it is a function of the distribution of pore lengths) defined as the actual reaction rate for the entire length distribution of pores *i*, for each reaction, at a given location, divided by the theoretical rate if there were no diffusion limitations in any of those pores. However, as we will see, the fully coupled, non-linear nature of the final equations for the effectiveness factors will limit our ability to solve for $\eta_{Tot,i}$ while also accounting for the full distribution of lengths, so we will apply a first order analysis in determining $\eta_{Tot,i}$. In other words, we will simply use the *mean* pore length, $L_i^{'}$, in evaluating Φ_i in Eq. (3.17) and this will yield a first order approximation to the mean effectiveness factor, η_i, which we will take as $\eta_{Tot,i}$. Some of the branching pore models, which assume a fractal porous structure with known pore lengths and radii, have employed the concept of calculating a Thiele modulus and effectiveness factor for each level of the assumed hierarchical pore structure [14,24,36]. Here we apply this concept to the evolving geometry of the random pore model.

To derive the Thiele modulus given by Eq. (3.16), one non-dimensionalizes a simplified version of a pseudo-steady reaction-diffusion equation (neglecting multicomponent diffusion and Stefan flow) for the pertinent geometry, which in our case is a single cylindrical pore. One of the parameters required for the Thiele modulus is the characteristic length for pore-scale diffusion, which in this case is half the mean length of a pore *i*. Gavalas' derivation of the RPM is quite flexible, and he derives the expected number of intersections, per unit length of pores *i*, between pores *i* and *j* [6]:

$$n_{i,j}^{'} = \frac{\pi l_{0,j}(R_i + R_j)}{2} \tag{3.18}$$

The mean length for a pore, *i*, is defined as the distance between intersections with any larger pores [6]. Since the intersections are independent Poisson processes and we seek the distance between intersections with *any* larger pores, we can simply sum the individual $n'_{i,j}$ to get the new rate parameter representing the frequency of intersections with any larger pore size. Then, since the number of intersections with larger pores is still Poisson distributed, the length between intersections follows an exponential distribution. Therefore the mean distance between intersections of pores *i* with larger pores, L'_i, is given by the inverse of the Poisson rate parameter [6]:

$$L'_i = \left(\sum_{j=i+1}^{n} n'_{i,j} \right)^{-1} \tag{3.19}$$

The mean length of pores *i* is a diffusion length scale; it is a distance over which the local smooth field reactant concentration, which serves as the pore-scale boundary condition, may be depleted upon penetrating pore *i*. Equation (3.19) implicitly assumes that all of the larger pores intersecting a given pore size *i* are themselves locally fully penetrated by reactant, such that the concentration in those pores equals the smooth field concentration, C_{SF}, which is used as the boundary condition for pores *i*. When using a continuum description for transport in the porous particle, $C = C_{SF}$ within the largest pores, *i=n*, is typically a good assumption [21], so full local penetration is assumed for the largest pores and $\eta_{i=n} = 1$. For the next smallest pore size, *i=n-1*, we know that all of the intersections with larger pores have the boundary condition $C = C_{SF}$. However, for all subsequently smaller pore sizes, *i=n-2*, *n-3*... we must account for the fact that some of the larger pores intersecting pores i may not be in kinetic control, and therefore the boundary condition $C = C_{SF}$ is not applicable to those intersections. In that case, Eq. (3.19) overestimates the number of relevant intersections and underestimates the mean length for diffusion.

For pores i to have boundary condition $C = C_{SF}$, the larger pores with which they intersect must be fully penetrated by the local smooth field reactant concentration. The effectiveness factor given by Eq. (3.17) accounts for species gradients reducing the reaction rate ($\Re = k_{intrinsic} C_{SF}^{n}$), as well as the fact that the entire pore surface area may not be accessible, due to the reactant concentration essentially going to zero within the pore.

It is possible, however, to idealize the concept by visualizing the effectiveness factor as being due solely to a reduction in accessible surface area within pores i, but with a reactant concentration which remains C_{SF} throughout that exposed area. In accordance with this idealized view of the effectiveness factor, the fraction of the entire length of larger pores, j, with the smooth field boundary condition $C = C_{SF}$, is now given by η_j. Therefore, when calculating the mean pore length between intersections, we utilize the number of intersections between pores i and larger pores j which have the local smooth field concentration, instead of the total number of i-j intersection. Since this fraction can be approximated using the effectiveness factor, η_j, of the larger pores, the following expression should be used in place of Eq. (3.19):

$$L_i' = \left(\sum_{j=i+1}^{n} n_{i,j}' \eta_j \right)^{-1} \tag{3.20}$$

In calculating the Thiele modulus for the interconnected geometry of the ARPM, we must also account for the fact that a given pore has many other smaller pores that intersect it [6,24], and therefore, the surface area for reaction on a pore *i* is larger than simply $2\pi R_i L_i^{'}$, so Eq. (3.16) must be modified to account for this as well. The surface area of smaller pores *j* intersecting a unit length of pore *i* is given by $2n_{i,j}^{'}\pi R_j L_j^{'}$ and the reaction on the surfaces of pores *j* may also be subject to diffusion limitations. Therefore, Φ_i depends on η_j for all smaller pore sizes *j*, and is given by,

$$\Phi_i = \frac{L_i^{'}}{2}\sqrt{\frac{(n+1)}{2}\left(\frac{\nu k_{intrinsic} C_{SF}^{n-1}}{D_{eff,i}}\right)\left(\frac{2}{R_i}+\sum_{j=1}^{i-1}\frac{2R_j L_j^{'} n_{i,j}^{'}\eta_j}{R_i^2}\right)}, \tag{3.21}$$

in which the summation term accounts for the surface area of smaller pores *j* which intersect pore *i*.

The definition of an appropriate mean length, $L_j^{'}$, for the smaller pores *j* branching from the pores *i* requires consideration as well. $L_j^{'}$ should be calculated by considering the intersections of pores *j* with any pores *i* (whether or not pore *i* has $C=C_{SF}$) and the intersections between pores *j* with any other pores *k*, larger than or equal to *i*, that have the local smooth field concentration (this fraction being η_k for each $k \geq i$).

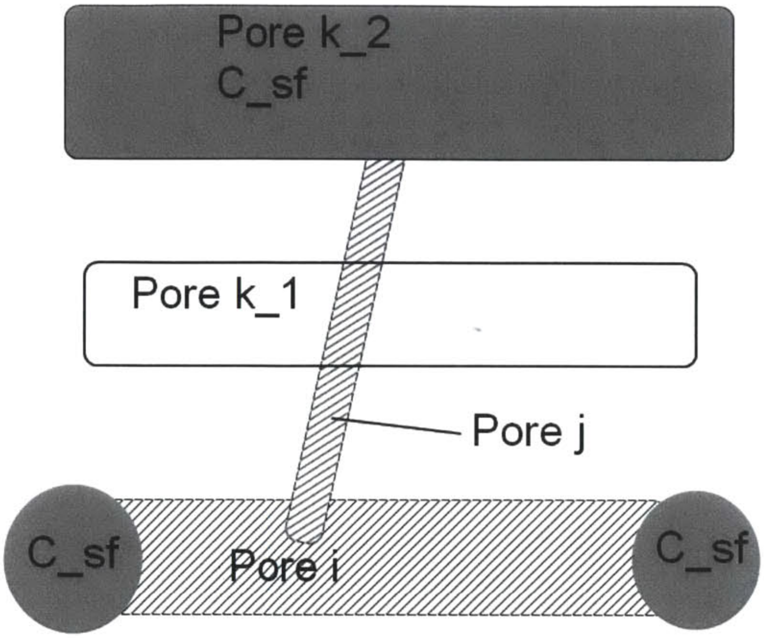

Figure 3.1. Schematic illustration of the need to consider all *j-i* intersections but only a fraction, η_k, of *j-k* intersections when calculating $L_j^{'}$.

We note that for the purpose of calculating $L_j^{'}$ we consider all pores *i* and not just the fraction η_i (as we do with pores *k*) because we are calculating $L_j^{'}$ in order to determine the surface area of smaller pores *j* branching from pores *i*. This situation is illustrated in Figure 3.1. The surface area under consideration is the dashed areas of pore *i* and pore *j*; pore k_1 does not have the smooth field concentration, while the pore k_2 does. The area of pores *i and j*, between the smooth-field boundary conditions shown in gray, is what contributes to the depletion of C_{SF} between the two ends of pore *i*, so whether or not pore *i* has the smooth field reactant concentration, the *j-i* intersection must be considered in determining the length of pore *j*. However, one must only consider intersections of pore *j* with pores *k* that have the smooth field reactant concentration, because accounting for the j - k_1 intersection will underestimate the surface area branching from pore i that contributes to the depletion of C_{SF} along pore i, since this area actually extends to the $j - k_2$ intersection.

To calculate this mean length, $L_j^{'}$, we first consider the rate parameter for the Poisson process representing all j-k intersections (where $k \geq i$), $\lambda_{j-k,j-k}$, which is simply

$$\lambda_{j-k,j-k} = \sum_{k=i}^{n} n_{j,k}^{'} . \tag{3.22}$$

Then we *thin* this rate parameter by the probability that for a given intersection and its closest neighboring intersection, one is a j-i intersection (irrespective of whether pore i has C_{SF}) and the other is any j-k_{SF} intersection where k has C_{SF} (i.e. k can be any size, larger or equal to i, but it must have C_{SF}). For all the j-k intersections, each intersection and its nearest neighbor can be either with pore size i or with $k > i$, and can either be amongst the fraction that has $C = C_{SF}$ or $C \neq C_{SF}$. We therefore determine the thinning probability by simply summing all seven of the 16 joint probabilities (which are the products of the marginal probabilities) that fulfill the above criteria, which are shown in Table 3.1.

Table 3.1. Marginal probabilities for each *j-k* intersection (column entries) and its nearest neighbor (row entries), and the combinations which satisfy the thinning criteria.

	Probability of *j-k* intersection being:	**Pore i with C_{SF}**	**Pore i without C_{SF}**	**Pore k > i with C_{SF}**	**Pore k > i without C_{SF}**
Probability of nearest neighboring *j-k* intersection being:		$\frac{n_{j,i}\eta_i}{\sum_{k\geq i} n_{j,k}}$	$\frac{n_{j,i}(1-\eta_i)}{\sum_{k\geq i} n_{j,k}}$	$\frac{\sum_{k>i} n_{j,k}\eta_k}{\sum_{k\geq i} n_{j,k}}$	$\frac{\sum_{k>i} n_{j,k}(1-\eta_k)}{\sum_{k\geq i} n_{j,k}}$
Pore i with C_{SF}	$\frac{n_{j,i}\eta_i}{\sum_{k\geq i} n_{j,k}}$	Yes	Yes	Yes	
Pore i without C_{SF}	$\frac{n_{j,i}(1-\eta_i)}{\sum_{k\geq i} n_{j,k}}$	Yes		Yes	
Pore k > i with C_{SF}	$\frac{\sum_{k>i} n_{j,k}\eta_k}{\sum_{k\geq i} n_{j,k}}$	Yes	Yes		
Pore k > i without C_{SF}	$\frac{\sum_{k>i} n_{j,k}(1-\eta_k)}{\sum_{k\geq i} n_{j,k}}$				

After combining terms in the numerator, the thinning probability is given by:

$$P_{Thinning} = \frac{2n_{j,i}^2\eta_i - n_{j,i}^2\eta_i^2 + 2n_{j,i}\sum_{k=i+1}^{n} n_{j,k}\eta_k}{\left(\sum_{k=i}^{n} n_{j,k}\right)^2}. \tag{3.23}$$

The new rate parameter for determining the frequency of $j\text{-}i/j\text{-}k_{SF}$ intersections pairs is therefore,

$$\lambda_{j-i,j-k_{SF}} = \lambda_{j-k,j-k} P_{Thinning} = \frac{2n_{j,i}^2\eta_i - n_{j,i}^2\eta_i^2 + 2n_{j,i}\sum_{k=i+1}^{n} n_{j,k}\eta_k}{\sum_{k=i}^{n} n_{j,k}} \tag{3.24}$$

and the length between such $j\text{-}i$ and $j\text{-}k_{SF}$ intersections is still exponentially distributed with mean length, L_j', given by the inverse of Eq. (3.24):

$$L_j' = \frac{\sum_{k=i}^{n} n_{j,k}}{2n_{j,i}^2\eta_i - n_{j,i}^2\eta_i^2 + 2n_{j,i}\sum_{k=i+1}^{n} n_{j,k}\eta_k} \tag{3.25}$$

Inserting Eqs. (3.20) and (3.25) into (3.21), the final equation for the Thiele modulus for each pore size is given by:

$$\Phi_i = \left[\frac{(n+1)}{2}\frac{\nu k_{intrinsic}C_{SF}^{n-1}}{4D_{eff,i}\left(\sum_{j=i+1}^{n} n_{i,j}'\eta_j\right)^2}\left(\frac{2}{R_i}+\frac{2}{R_i^2}\sum_{j=1}^{i-1}\left(\frac{R_j n_{i,j}'\eta_j\sum_{k=i}^{n} n_{j,k}}{\left(2n_{j,i}^2\eta_i - n_{j,i}^2\eta_i^2 + 2n_{j,i}\sum_{k=i+1}^{n} n_{j,k}\eta_k\right)}\right)\right)\right]^{1/2} \tag{3.26}$$

Equations (3.17) and (3.26) are applied to determine the effectiveness factor for each pore size, at each location and for each reaction. Although it appears somewhat complex, Eq.

(3.26) can be implemented without too much trouble using matrix operations. Furthermore, these non-linear equations converge quickly given that the solutions are bounded between zero and unity and that the effectiveness factors do not change too much between time steps. (For this reason, during the integration of the q_i, it is possible to lag the η_i on the right hand side of Eq. (3.26).) Since each Φ_i and η_i are now coupled to the effectiveness factors for all pore sizes, both smaller and larger, we have a system of non-linear, fully coupled equations. It is for this reason that we have used the mean length between intersections rather than accounting for the entire exponential distribution of lengths.

Other phenomena that occur during char gasification could also be incorporated into this modeling framework. It is possible to modify the model to take into account that there may be a minimum utilization of any pore due to reaction near the pore mouth, even if negligible penetration into the pore occurs [14,37], which is similar to the constant roughness provided by the non-reacting micropores discussed by Gavalas [6]. Other modifications, such as more complex reaction mechanisms which account for inhibition and adsorption/desorption phenomena [38], could be accounted for by modifying the pore scale, Thiele modulus equation and will be discussed in Ch. 6 with respect to high pressure gasification reactions. The ARPM framework could also potentially be helpful in capturing the presence of initially inaccessible porosity, since it seems to be a phenomenon associated with certain pore sizes [13,16,39].

It should be mentioned that since the ARPM allows situations of partial reactant penetration into the pores, some pores do not react uniformly along their length, distorting their cylindrical shape, which is an assumption that is built into the equations of the random pore model. The model essentially redistributes the uneven conversion on a given pore size into a uniform conversion along those pores, shown schematically in Figure 3.2, thus maintaining cylindrical pores in the ARPM equations. We believe that it is better to take this effect into account using the method outlined above, even though it means that we will be overtly acknowledging the limits of the geometric assumptions of the RPM, which exist in any case. Furthermore, in many cases, the pore-scale effectiveness factors spend much of the conversion near zero or unity, or transition quickly between the two, as will be seen later, minimizing the effects of this assumption.

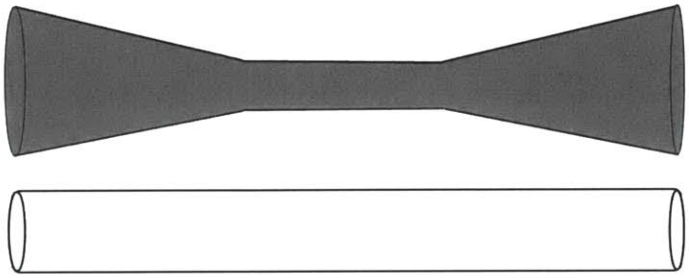

Figure 3.2. Schematic of the redistribution of the actual uneven conversion (gray pore) to a conversion which is uniform along the pore axis (white pore).

The overall effectiveness factor quantifying the participation of pores *i* in heterogeneous reaction *k* at any location is now given by $\eta_{i,k}$. To complete the structural evolution model, at each location, state equations (ODEs) for the pore growth variables due to reactions on each pore size *i*, by all reactants *k*, are written:

$$\frac{dq_i}{dt} = \frac{-MW_C}{\rho_{True}} \sum_k \eta_{i,k} \nu_{C,k} \Re_k , \tag{3.27}$$

where $\Re_k = k_{intrinsic,k} C_{SF,k}^n$ is the heterogeneous reaction rate, and all other variables are as before. It should be noted that pores which are originally not penetrated significantly by reactants ($\eta_i \approx 0$) can eventually begin to react (even though q_i and R_i have not increased) due to the decrease in $L_i^{'}$ as larger pores expand and decrease the distance between intersections.

Compared to previous implementations of the random pore model, which required a class of pores to be either fully reacting or fully non-reacting, this fraction better represents the actual situation, and instead of dq_i/dt being either zero or its full value, it may assume intermediate values and may change with conversion, which can capture the reality of the interplay between reaction and diffusion at the pore scale as well as at the particle scale. Essentially, through the value of η_i, these ODEs become complicated, non-linear functions of q_i. These n equations (3.27) for pore growth replace the single equation (3.7) used in most previous models. When particle-scale gradients are present, these n solid-phase "species equations" can be used in conjunction with any appropriate form of the conservation equations for gaseous species, energy and momentum in the porous medium. These equations are described in Ch. 4. The source terms due to heterogeneous reactions in the equations for gaseous species and energy conservation are proportional to $\Re_k \sum_i \eta_{i,k} S_i$ for each reaction, k, so equation (3.11) for the surface areas is utilized explicitly when the ARPM is coupled with other conservation equations. This formulation allows the quantification of the participation of various pores i in different reactions to vary with position, time and degree, without any prior assumptions in this regard.

3.5. Method for Determination of Intrinsic Kinetic Rates

Given the initial porosity distribution, $\phi(R)$, the true solid density, ρ_{True}, and the inorganic fraction of the reacting solid, the model is fully deterministic *if* the intrinsic reaction rate is known. However, as mentioned above, in many cases there is uncertainty associated with intrinsic rate constants, often due to incomplete penetration of reactants into very small pores, even in what is ostensibly the "purely kinetic" regime. In other words, to determine the intrinsic kinetic rate from conversion measurements, the measured overall reaction rate for the particle must be normalized by the surface area that is participating in the reactions, which is unknown, and is in fact an output of the current model.

Sometimes experimental evidence exists which can be used to determine whether pores of a certain size participate in a particular reaction. As discussed in Section 3.1, it has been observed for certain chars reacting with O_2 that the reaction occurs largely within the mesopores (diameter 2-50 nm) and macropores (diameter > 50 nm), while the micropores (diameter < 2 nm) are mostly inaccessible to oxygen, and the measured rate is therefore best normalized by the meso- and macro-pore surface areas [11,13,15]. However, this type of information is often only qualitative in nature and may be lacking for the purposes of predicting intrinsic reaction rates if the pores straddle the range between micro- and meso-pores.

Using the equations presented in Section 3.4 together with the measured overall conversion rate, dX/dt, and pore structure parameters (S_i, $n'_{i,j}$, etc.) derived from measurements of $\phi(R)$, a quantitative estimate of the surface area that participates in a reaction, and thus, the intrinsic reaction rate, can be obtained. This assumes the intrinsic rate is constant with conversion, but if it is not, the following procedure can be performed more than once, at any point in the conversion that the overall rate and the pore structure data are *both* measured (or known through interpolation). Whenever the overall conversion rate and the pore structure, determined from $\phi_i(R_i)$, are both known, all terms in Eqs. (3.17) and (3.26) are known with the exception of $k_{intrinsic}$, which appears in Eq. (3.26), and can be written for each reaction, *k*, as:

$$k_{intrinsic,k} = \frac{k_{Overall,measured,k}}{\sum_i \eta_{i,k} S_i} \qquad (3.28)$$

Now for each pore size *i*, Eq. (3.28) is substituted into Eq. (3.26), which in turn is substituted into Eq. (3.17), yielding *n* nonlinear algebraic equations for *n* unknowns, $\eta_{i,k}$, which can be solved simultaneously. Again, these non-linear equations should converge quickly given the fact that the solutions are bounded between zero and unity. Once the individual $\eta_{i,k}$ have been obtained by solving the coupled non-linear equations above, they can be substituted into Eq. (3.28) to determine the intrinsic reaction rate(s).

3.6 Results and Discussion

In order to validate and explore the flexibility of the ARPM, we apply it to the simulation of char gasification. To test the model without using any fitting parameters, data on the complete initial porosity distribution, $\phi(R)$, as well as the true density, ash content, and kinetic parameters (overall pre-exponential factor, activation energy and reaction order) are required as inputs to the model. Although many studies provide initial surface area and/or porosity values, sometimes even divided into micropore and macropore fractions, ideally the entire $\phi(R)$ distribution should be used to determine representative discrete radii, $R_{0,i}$, and porosity values, $\phi_{0,i}$, to be used in Eq. (3.4).

The data reported by Su and Perlmutter [9] is one of a few studies [9,40–42] that reports the necessary measurements for testing the model. The pore volume distributions reported by Su and Perlmutter are the most complete. However, the char consumption experiments of Su and Perlmutter were performed in the kinetic regime (i.e. without any smooth field species gradients). So while the data can be used to validate the ARPM, it does not allow the model to exhibit its flexibility in adapting to evolving smooth-field species and temperature gradients or time-dependent boundary conditions.

For chars generated at varying pyrolysis rates and temperatures, Su and Perlmutter performed CO_2 and N_2 adsorption experiments along with mercury porosimetry to determine the entire initial pore volume distribution as a function of pore radius. In order to test the predictive power of the original random pore model, the conversion rate versus conversion curves were measured and the RPM structural parameter ψ determined from the original pore structure was compared to the value of ψ determined by fitting the data. The structural-based ψ was determined using the equation given by Bhatia and Perlmutter [5]:

$$\psi = \frac{4\pi L_{0,Tot}(1-\phi_{0,Tot})}{S_{0,Tot}^{2}}, \tag{3.29}$$

It can be shown that this expression for ψ is identical to equation (3.6c), although it should be noted that $L_{0,Tot} = (1-\phi_{0,Tot})\sum_{i} l_{i,0}$. When certain pore sizes are assumed to be non-reacting, it can also be shown that equation (3.6c) should only be summed over the reacting pore sizes (see Appendix A.2).

As mentioned by Bhatia and Vartak [43], the structure-based ψ should be determined from the initial porosity distribution by assuming that pore overlap exists at $X = 0$, using summations of equations (4) and (11), or their continuous counterparts integrated over all pore sizes:

$$L_{0,Tot} = (1-\phi_{0,Tot})\int_0^\infty \frac{\phi(R)}{\pi R^2\left[1-\int_R^\infty \phi(R')dR'\right]}dR \tag{3.30}$$

$$S_{0,Tot} = (1-\phi_{0,Tot})\int_0^\infty \frac{2\phi(R)}{R\left[1-\int_R^\infty \phi(R')dR'\right]}dR \tag{3.31}$$

This is in accordance with Gavalas [6] and in contrast to the procedure originally adopted by Su and Perlmutter and several others, which neglected overlapping porosity at $X = 0$. This has been taken into account in determining ψ in the comparisons presented below.

Oxidation measurements on coal chars were performed by Su and Perlmutter in air at several temperatures, all in the kinetically controlled regime, as determined by the lack of change in reaction rate with varying particle size, as well as the constancy of the activation energy. For application of the ARPM and determination of $k_{intrinsic}$, the overall reaction rate at zero conversion is required, since this was the point at which the pore structure was measured. Since the first data point for reaction rate was taken at a conversion of ~10%, extrapolation back to X = *0* was required. Assuming that the effectiveness factor for each pore size is roughly constant throughout conversion, plotting $\left(1/(1-X)\times dX/dt\right)^2$ vs. $-\ln(1-X)$ should yield a straight line. The overall reaction rate constant $k_{Overall,measured} = A\,\mathrm{e}^{\left(-E/\bar{R}T\right)}$ can then be determined by measuring the intercept at $-\ln(1-X)=0$, which yields $\left(k_{Overall,measured}C_{O_2}^n/(1-\phi_{0,Tot})\right)^2$. The reaction order, *n*, was determined experimentally to be unity and the activation energy was also determined experimentally using Arrhenius plots for each sample [9].

Su and Perlmutter assumed that the entire measured surface area was accessible for reaction at $X = 0$, i.e., $k_{Overall,measured} = k_{intrinsic}S_{0,Tot}$, and used this value in determining $k_{intrinsic}$. Rather than assuming the entire pore surface area is available for reaction, we use the method outlined in Section 3.5 to determine the participating surface area and to calculate the intrinsic reaction rate constant, $k_{intrinsic}$. As mentioned by Su and Perlmutter, there is some uncertainty in $k_{Overall,measured}$ since the plots are not perfectly linear, especially at higher conversions. Following the procedure described above, and assuming that all η_i remain roughly constant through the conversion (which turns out to be true), we recalculated extrapolated values for the initial reactivity based on just the first five data points.

All of the chars from Su and Perlmutter were produced by pyrolizing coal at very slow heating rates (10 K/min or less) and three of the six chars have initial porosities of less than 20% (it appears that the porosity given for sample D in their Table 4 is in error) [9]. To ensure that the pore structure was well connected [44] and a uniform smooth field reactant concentration prevailed throughout the particle, we chose the two highest porosity samples, B and E, for validation of the adaptive random pore model. Furthermore, we used the highest temperature runs available for each char, since those conditions would correspond to the maximum *pore-scale* diffusion limitations, if such limitations were to exist.

Using the initial continuous $dV/d\ln(r)$ distribution given by Su and Perlmutter which naturally divided the pore sizes into three ranges (although the delineation is not very sharp for sample E) we determined the discrete values of radii and porosity for equation (4). When increasing the number of pore sizes beyond three, whether for the micro-, meso- or macropores, we divided that porosity bin into equal parts and determined the mean radii for the new, smaller, pore size bins. After determining $k_{Overall,measured}$ and using Eqs. (3.4) and (3.11) to determine $S_{0,i}$, we applied Eqs. (3.17), (3.26) and (3.28) to solve simultaneously for the initial effectiveness factors and $k_{intrinsic}$. Table 3.2 displays some of the relevant parameters used in the validation. In some cases, the discrete porosity values have been further divided, as described above.

Table 3.2. Parameters employed in testing the ARPM with chars B and E from the experiments of Su and Perlmutter [9].

Sample (Temp)	ϕ_{micro} [-] (R_{micro} [Å])	ϕ_{meso} [-] (R_{meso} [Å])	ϕ_{macro} [-] (R_{macro} [Å])	E_{O_2} [kJ/mol]	$k_{intrinsic}C_{O_2}^n\rho_{true}$ [μg/m^2 s]	ρ_{true} [g/cm^3]
B (728 K)	0.109 (7.1)	0.031 (58.9)	0.148 (1877)	89.96	3.48	1.42
E (703 K)	0.089 (6.7)	0.034 (105.5)	0.137 (1918)	110.87	3.20	1.54

In calculating the Thiele modulus and effectiveness factors, both at time zero and throughout the conversion, we accounted for the fact that several studies, including Su and

Perlmutter [9], have uncovered evidence that oxygen is subject to severe configurational diffusion limitations in char micropores, since transport becomes an activated process when the diffusing molecule is always under the influence of the pore walls. Experiments quantifying this effect for oxygen on coal char are limited, aside from Salatino [14], who incorporates the effects of configurational diffusion into the Knudsen diffusion term following the ideas of Satterfield [35] and Floess [45] and uses the following combined expression:

$$D_{Knudsen/Configuration,\,i} = \frac{2R_i}{3}\sqrt{\frac{8\bar{R}T}{\pi MW}}\exp\left(-\frac{\sigma}{R_i}\right) \tag{3.32}$$

The pore scale effective diffusivity, for each species, location and pore size, is then approximated as:

$$\frac{1}{D_{eff}} = \frac{1}{D_{continuum}} + \frac{1}{D_{Kn/Config}} \tag{3.33}$$

By incorporating this definition of diffusivity into the pore-scale Thiele modulus and effectiveness factor, we have accounted for the phenomenon of reduced diffusion of O_2 in micropores from any type of diffusion [10,14], as well as the possibility that the reaction mechanism leads to strong chemisorption of oxygen in micropores, since Salatino suggests that the strong chemisorption can be described by the incorporation of a configurational diffusion resistance [15].

The parameter σ in Eq. (3.32), which is related to the activation energy for configurational diffusion, has a significant impact on the diffusion in micropores. Salatino estimates a value of $\sigma = 2\times10^{-8}\ [m]$ for oxygen diffusion in a bituminous coal char at 693 K (which is quite similar to the temperatures used by Su and Perlmutter), which is relatively high due to the propensity of oxygen to chemisorb on the surface of the carbon [14]. Instead of using σ as a fitting parameter, we also employ the value given by Salatino, due to the similarity of the experimental conditions. Since experiments determining σ for H_2O and CO_2 on coal char were not found, we have assumed σ for H_2O and CO_2 to be $(5-10)\times10^{-9}\ [m]$ in the results shown later, corresponding to the known smaller configurational limitations of these molecules [9,10]. In any case, the validation data requires only the configurational diffusion parameter for oxygen.

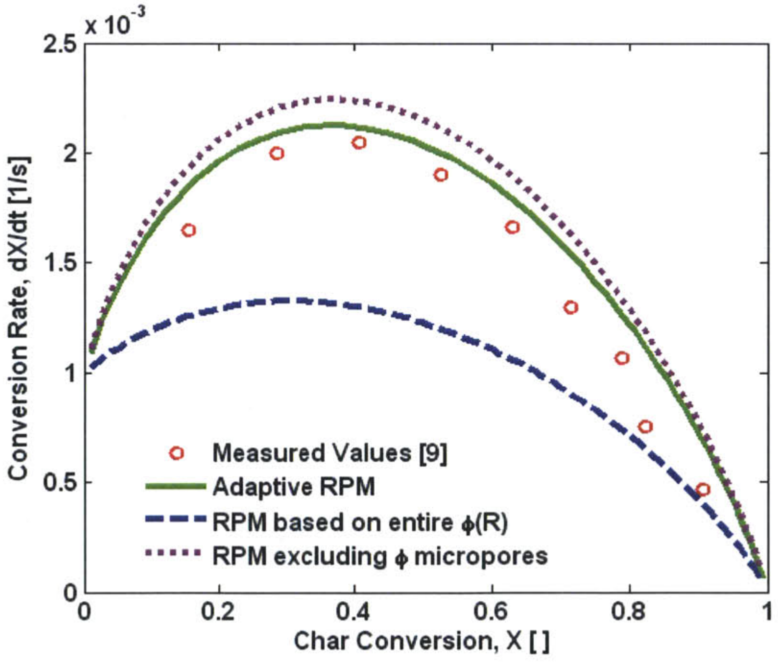

(a)

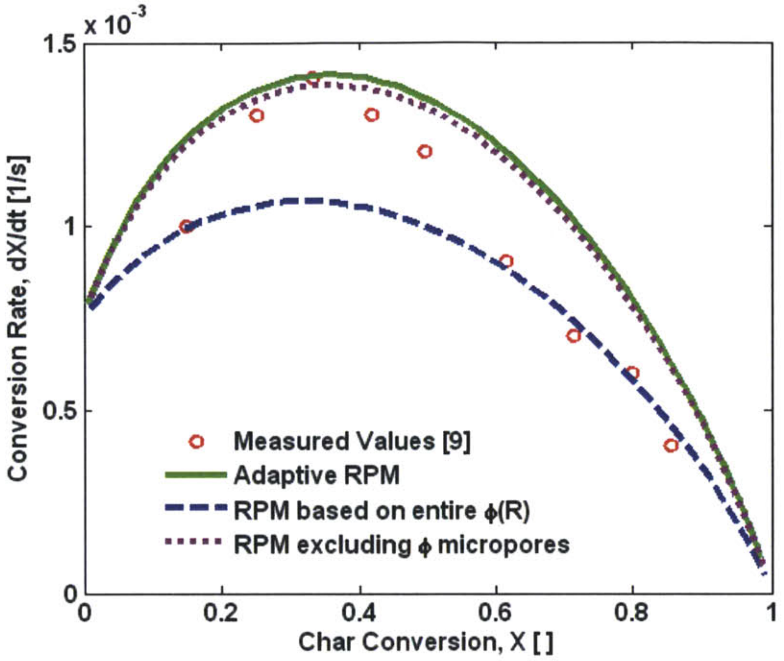

(b)

Figure 3.3. Rate versus conversion using the ARPM with five pore size bins, the RPM based on the entire pore size distribution, the RPM using the pore size distribution excluding micropores and experimental values [9], for (a) char sample B in air at 728 K and (b) char sample E in air at 703 K.

Figure 3.3 (a) shows the results for sample B at 728 K. The adaptive random pore model is compared to the measured data [9], and to the original random pore model using structural parameters calculated from Eq. (3.29), with L_0 and S_0 calculated from Eqs. (3.30) and (3.31). Without doing any parameter fitting, including for the determination of the intrinsic reactivity, the ARPM matches the experimental data well. Using the original RPM with ψ determined using the entire spectrum of pore sizes clearly does not fit the data as well, since diffusion limitations prevent oxygen from penetrating the smallest pores in these samples. In fact, according to the results of the ARPM, the smallest pores' surface area contribute negligibly to the reaction at $X = 0$. The original RPM with ψ calculated using L_0 and S_0 based only on the mesopores and macropores produces a curve that nearly coincides with the results of the adaptive model (the discrepancy is due to the discretized pore sizes used in the ARPM), because in this case, the pore scale effectiveness factors are essentially zero for the micropores and unity for all other pores and are basically constant with conversion. Figure 3.3(b) illustrates the same comparison for sample E at 703 K. Without using any fitting parameters, the ARPM provides a better match to the shape of the data than the original RPM using ψ based on all pore sizes, although in this case, neither match the data very well. The same observations regarding the two determinations of ψ apply to this sample as well.

Based on these comparisons we can conclude that the pore-scale effectiveness factors in the ARPM correctly account for the observation that oxygen does not penetrate the small pores to a significant extent. Furthermore, the method of Section 3.5 provides an internally consistent manner of determining the intrinsic reactivity that when used in conjunction with the adaptive random pore model, provides a fully predictive model for solid consumption that matches the data of Su reasonably well, without any fitting parameters.

Figure 3.4 illustrates the effect of increasing the number of pore size bins considered by the model. For sample B, once five discrete pore sizes are used, there is only a small change in the results upon increasing the number of pore sizes further. It should be noted, however, that the best method for determining the discrete pore sizes and radii used in Eq. (3.4) may vary with the particular sample and conditions. For example, for this char reacting with oxygen, the sub-division of the micropores into smaller bins has a minimal effect, since the micropores are not penetrated by oxygen to a significant extent, whereas sub-dividing the mesopores into two or three bins has a larger effect since they provide the main surface for reaction with oxygen in this case.

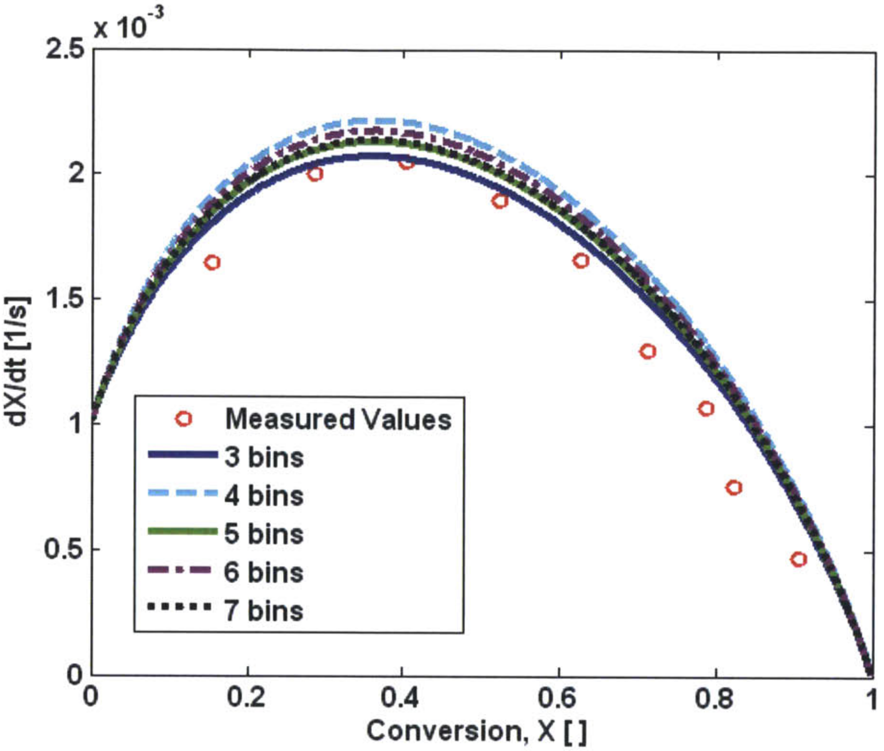

Figure 3.4. Rate versus conversion using the ARPM with different numbers of pore size bins compared to the experimentally measured values [9] for char sample B in air at 728 K.

As mentioned above, the experiments of Su were done in the kinetically controlled regime, which in this case implies only *smooth field* kinetic control, since there are significant diffusion limitations in the micropores. The ARPM predicts values of η_i near unity for all pores above micropore size, and near zero for the micropores, although it changes slightly as conversion proceeds. Nonetheless, the ARPM is capable of handling more complex situations and can predict $\eta_{i,k}(r,t)$ for conditions when variations in pore utilization exist with pore size, *i*, reactant, *k*, and location, *r,* and vary substantially as conversion proceeds due to the evolution of smooth field species and temperature gradients. To demonstrate this, the ARPM has been integrated into a simulation of a reacting, spherical, porous particle and its surroundings, consisting of partial differential equations for each gas species, overall mass conservation, energy conservation and radial momentum conservation, which are described in Ch. 4.

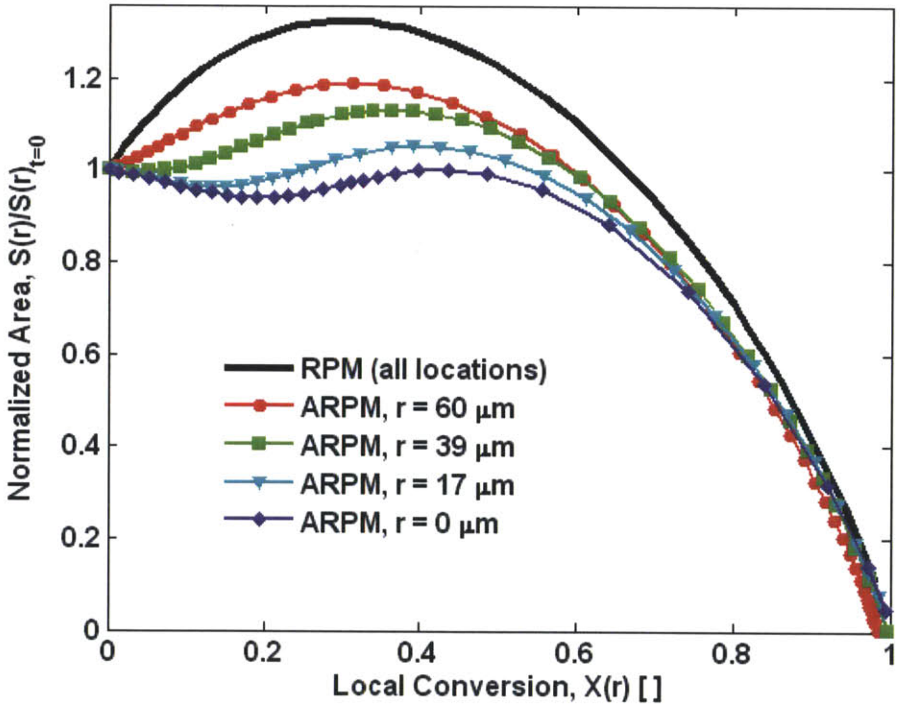

Figure 3.5. Normalized, local surface area evolution with local conversion for different radial locations in a 128 μm diameter spherical particle with the properties of char sample B [9], in an environment of 10% H_2O, 40% CO_2 and 50% N_2 at 2000 K and 1 atm.

Figure 3.5 illustrates the ability of the model to allow the porous structure at different locations in the particle to evolve in different manners. This figure was obtained by simulating the gasification of a 128 μm diameter particle with the properties of char B from Su and

Perlmutter, using four pore size bins, in a reducing atmosphere of 10% H_2O, 40% CO_2 and 50% N_2 at a temperature of 2000 K. The intrinsic kinetic parameters employed for these two reactions are shown in Table 3.3. In order to illustrate the ARPM's flexibility in handling variations in pore utilization with pore size, location and reaction, we have chosen simple n^{th} order expressions for the gasification reactions. Although char gasification reactions may be better represented by Langmuir-Hinshelwood kinetics in many cases, due to the adsorption-desorption nature of surface reactions and the ability of reaction products to inhibit heterogeneous reactions [38,46], our goal here is simply to illustrate the flexibility of the ARPM, and n^{th} order rate forms have been employed. Computing analytical expressions for the effectiveness factors for Langmuir-Hinshelwood kinetics (with product inhibition) will be discussed in Ch. 6.

Table 3.3. Kinetic parameters used for gasification reactions [47].

Reaction	A [g/m^2 s atm^n]	E [kJ/mol]	n
$C+CO_2$	202,000	243.2	0.4
$C+H_2O$	226,000	238.2	0.4

Despite the fact that the initial pore structure is identical throughout the particle, Figure 3.5 shows that the surface area evolves differently with local conversion at different locations. Near the outer edge of the particle (r = 60 μm), the surface area first increases and exhibits a peak at roughly 34% local conversion. Further towards the particle center, the surface area is either flat or actually decreases with local conversion before beginning to rise and peaking, with the maximum occurring at larger values of local conversion at locations closer to the particle center. Plotting the normalized surface area (rather than the normalized reaction rate, which is affected by the particle-scale species and temperature gradients) shows that the often-used assumption that the structure evolves in the same manner with local conversion may not always be correct. Furthermore, the restriction on the conversion at which the surface area is maximized that is imposed by the RPM ($X_{max} < 0.393$) [5,6] is not applicable when the assumptions inherent in the RPM are relaxed, as they are here.

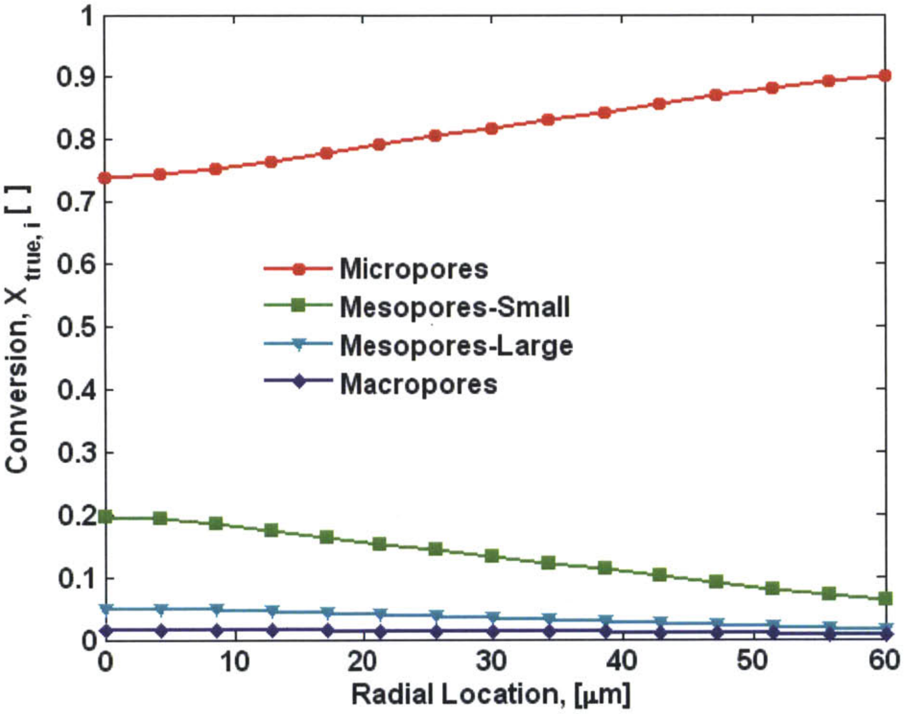

Figure 3.6. Final true conversion profiles for char B [9] in 10% H_2O, 40% CO_2 and 50% N_2 at 2000 K and 1 atm.

For the same case, examining the final true conversion profiles in Figure 3.6, which are calculated using Eq. (3.15), provides insight into the phenomenon exhibited in Figure 3.5. Toward the char surface, the particle experiences more conversion on the micropores and less conversion on the larger pores compared to locations further toward the particle center. Since

Figure 3.5 normalizes the surface area by the *total* initial surface area, inner locations where the smallest pores participate less in the reaction have smaller normalized areas as conversion proceeds, because the smallest pores experience mostly overlap with larger pores and less growth, until later conversions. At locations closer to the particle surface, the smallest pores experience a greater degree of growth before overlap begins to dominate. The ability of the ARPM to capture an initially uniform pore structure evolving differently depending on its location stems from the fact that the model separates the local conversion variable q into separate entities, q_i, and then calculates a separate $\eta_{i,k}(r,t)$ for each one.

There are two possible reasons why the micropores participate in the conversion near the particle edge more so than at the center. For these conditions, intra-particle species gradients exist for both reactants (regime II), but of the two gasification reactions, at these conditions and with the kinetic expressions employed, the char-steam reaction is roughly 50% faster than the reaction of char with CO_2 and there is less H_2O in the system, leading to steeper gradients of H_2O. Therefore, the $C+H_2O$ reaction dominates near the edge of the particle (at least initially) and the $C+CO_2$ reaction dominates towards the center of the particle. Furthermore, for the sake of elucidation, we have taken the value of $\sigma_{CO_2} = 2\sigma_{H_2O}$, which is plausible given the reported ability of H_2O to penetrate very small micropores [48] and the faster configurational diffusion of H_2O in carbon micropores as compared to CO_2 [49,50]. This means that CO_2 is more diffusion-limited in the smallest pores than H_2O. Therefore, due to depletion of H_2O across the particle, near the edge the smallest pores participate in the reaction more than towards the center of the particle, leading to the conversion profiles observed in Figure 3.6. Secondly, since for both reactions we have employed a fractional reaction order, as reactant concentrations are depleted toward the particle center, the Thiele modulus increases and the effectiveness factor decreases.

The micropores effectiveness factors are more sensitive to this than those of the larger pores and thus there is less conversion on the micropores near the particle center.

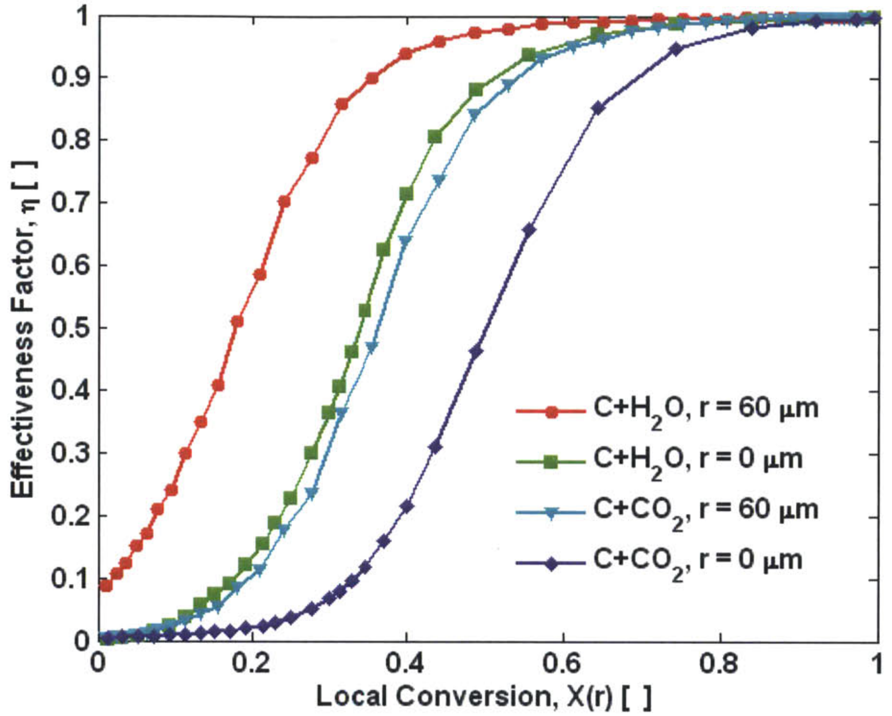

Figure 3.7. Evolution of micropore effectiveness factors with local conversion for both reactions, for char sample B [9] in an environment of 10% H_2O, 40% CO_2 and 50% N_2 at 2000 K and 1 atm.

For this same case, Figure 3.7 depicts the evolution of the micropore effectiveness factors, $\eta_{i=1,k}(r,t)$, with local conversion, for the C+H_2O and C+CO_2 reactions at two different locations (center, $r = 0$ μm and edge, $r = 60$ μm). Over the course of conversion, all effectiveness factors increase as pore lengths, $L_i^{'}$, decrease and pore radii increase. It is observed that throughout conversion, the micropore effectiveness factor is larger for the C+H_2O reaction than for the C+CO_2, at both locations.

More interestingly, even for the C+CO_2 reaction, throughout the conversion the micropore effectiveness factor is larger for the edge location (r = 60 μm) than for the center location (r = 0 μm). This could be explained by the presence of intra-particle species gradients reducing the effectiveness factor towards the particle center for the C+CO_2 reaction, as mentioned above. However, this could also be due to the fact that near the edge, steam penetrates the smallest pores and reacts, which increases the size of these pores and thus increases the effectiveness factor for the C+CO_2 reaction as well. In other words, steam activates the micropores near the surface to a greater degree. This explanation is substantiated later by Figure 3.10.

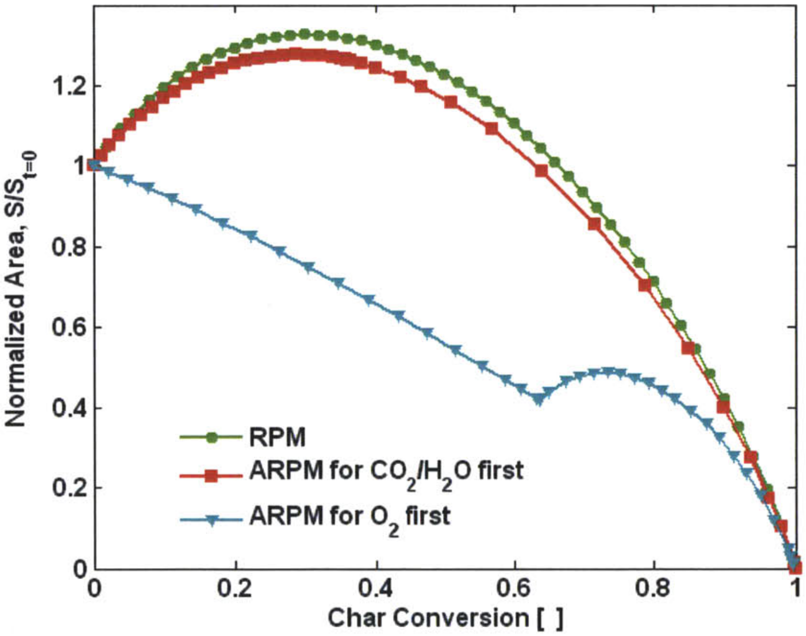

Figure 3.8. Evolution of normalized surface area with conversion for char sample B [9] reacting in kinetic control, when exposed first to a gasifying atmosphere followed by an oxidizing one and vice versa, according to the RPM (for which there is no difference) and the ARPM.

Another situation of practical interest is when the reactant gas to which the particle is exposed changes over the course of conversion. Figure 3.8 depicts the evolution of the ratio of char surface area to the original surface area with overall conversion for a particle subjected to boundary conditions that change with time. Specifically, the same particle considered above (char B, five pore size bins) is either exposed to an oxidizing atmosphere followed by a reducing atmosphere or a reducing atmosphere followed by an oxidizing one. Unlike Figures 3.5-3.7, both conditions correspond to reactions occurring under smooth field kinetic control, although pore level limitations exist for the oxygen atmosphere, as has been mentioned above. In both cases, the char-O_2 reaction accounts for 64% of conversion and the char-CO_2 and char-H_2O reaction for 36%. Figure 3.8 compares the surface area ratio predicted by the ARPM for both situations, as well as predictions of the original RPM with ψ based on the entire pore size distribution.

When the particle reacts first with oxygen, Figure 3.8 shows that $S(t)_{Total}/S_{0,Total}$ decreases monotonically, since oxygen cannot penetrate the smallest pores to a significant degree; therefore these pores do not experience growth, rather, they only coalesce with larger pores. This monotonic decrease in normalized total surface area should not be confused as being contradictory with the observed maximum in the normalized *reaction rate* when using O_2 as a reactant, as reported by others [10,15], since we have already seen in Figures 3.3 and 3.4 that the reaction rate of sample B exhibits a distinct peak when reacting under these same oxidizing conditions. In fact, when plotting the normalized reaction rate, the oxidizing conditions show a larger peak than the reducing conditions, consistent with the experiments [10,15].

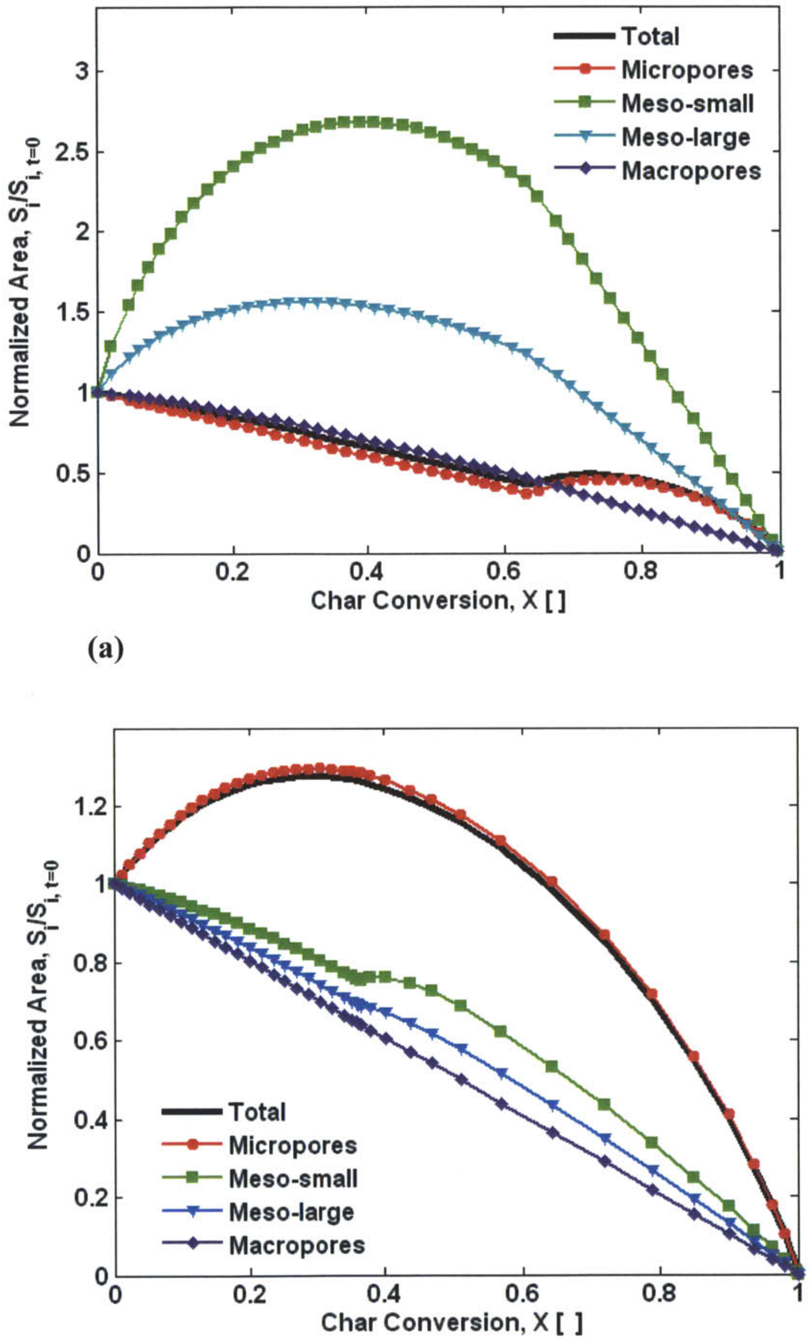

(a)

(b)

Figure 3.9. Evolution of normalized total and individual surface areas, *S_i*, with conversion for char sample B [9] reacting under kinetic control, predicted by the ARPM, (a) when exposed first to the oxidizing atmosphere and (b) when exposed first to the gasifying atmosphere.

Rather, as shown in Figure 3.9(a), since the micropores contribute the majority of the surface area, the normalized total surface area, $S(t)_{Total}/S_{0,Total}$, closely follows the micropore surface area evolution, which is monotonically decreasing due to the effect of overlap when exposed first to oxygen. When the particle reacts first with CO_2 and H_2O, the normalized surface area increases with conversion and shows a peak before decreasing, as shown in Figure 3.9(b). This is due to the participation of the micropores in the reactions to a greater extent. It can be verified that the evolution of $S(t)_{Total}/S_{0,Total}$ and $(dX/dt)/(dX/dt)_0$ coincide only when there are negligible diffusion limitations in all pore sizes (i.e. all $\eta_{i,k}(t)=1$).

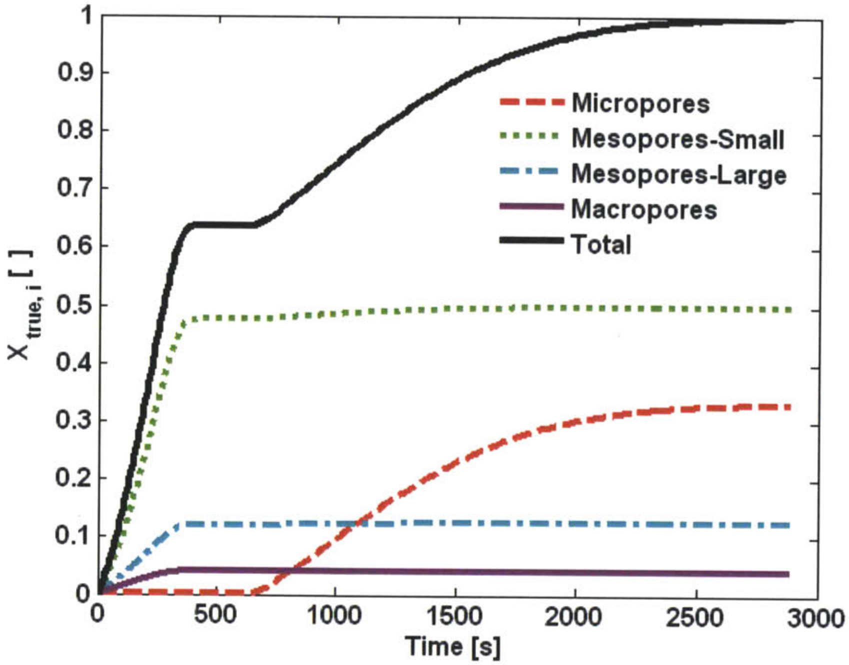

(a)

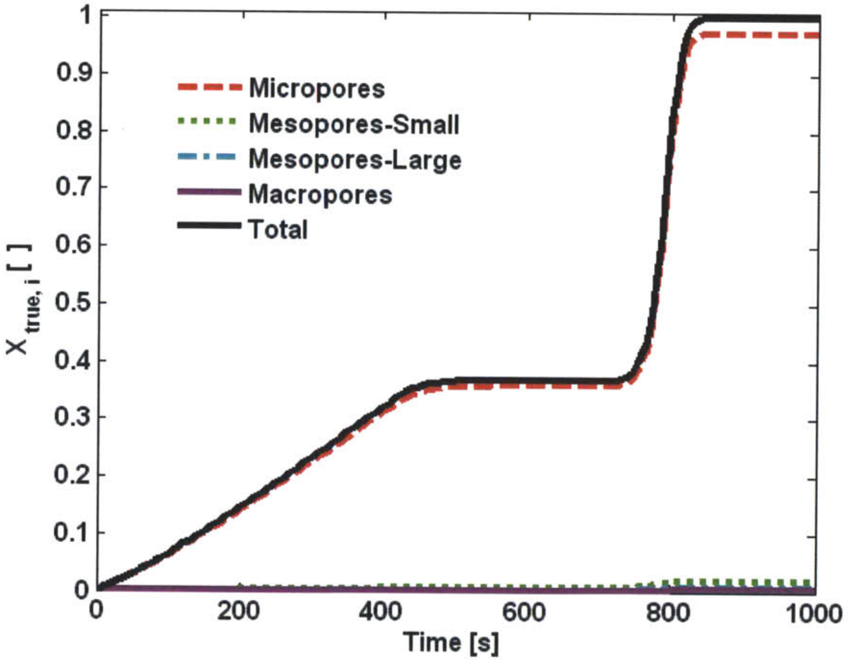

(b)

Figure 3.10. Evolution of X and $X_{True,i}$ on each pore size (a) when exposed first to an oxidizing atmosphere and (b) when exposed first to an atmosphere of CO_2 and H_2O.

It is interesting to note that when the char particle reacts first with CO_2 and H_2O, the subsequent reaction with O_2 *does* occur on the micropores as well. This can be seen in Figures 3.10(a) and 3.10(b), which show conversion-time behavior for each pore size corresponding to the cases of Figures 3.8(a) and (b), respectively. In Figure 3.10(b), oxygen is slowly added to the system as a boundary condition beginning at t = 730s, and even after the switchover to oxygen is completed, the majority of the char conversion is still due to oxidation reactions occurring on the micropores. The reason is that during the initial reaction of the char with CO_2 and H_2O the micropores expand and subsequently allow for increased penetration of O_2. In contrast, during the first 600 s of Figure 3.10(a) (when oxidation is occurring) a negligible fraction of the conversion occurs on the micropores, since they have not been "activated" first with CO_2 and H_2O.

3.7. Conclusions

An extension of the random pore model has been developed which allows any pore size, at any location and time, to be in any state between complete kinetic and diffusion control for any reaction. This has been accomplished by considering, for each pore size, separate equations for pore growth, conversion and surface area, (q_i, $X_{True,i}$ and S_i) using the random capillary model formulation and by employing pore-scale effectiveness factors, η_i, to quantify the participation of all pore sizes in all reactions, at all locations and times. At any time when measured reaction rate and structural data are both available, the method can be applied to determine intrinsic (per unit surface area) kinetic parameters. This framework allows the evolution of the char structure with local conversion to adapt to changes in boundary conditions or the development of intra-particle species or temperature gradients, rather than being pre-determined by the value of the structural parameter, ψ. Without any fitting parameters, the ARPM has been validated with the coal char oxidation data of Su and Perlmutter [9] with satisfactory agreement, and examples of the flexibility of the model have been provided. Furthermore, the inherent ability of the model to separately quantify the participation of pores of different sizes in different reactions makes it amenable to extensions that account for more complex phenomena. For example, the opening of initially closed porosity by a particular reactant [13,16] or the existence of a different initial reactivity [51] may be phenomena that are associated with certain pore sizes and reactants.

Nomenclature and Units

A = pre-exponential factor ($\mathrm{mol_C} / \mathrm{m^2_C}\ \mathrm{s}\ (\mathrm{mol_{gas}}/\mathrm{m^3})^n$)

C = concentration ($\mathrm{mol/m^3}$)

D = diffusion coefficient ($\mathrm{m^2/s}$)

E = activation energy (J/mol)

$k_{intrinsic}$ = intrinsic reaction rate constant ($\mathrm{mol_C} / \mathrm{m^2_C}\ \mathrm{s}\ (\mathrm{mol_{gas}}/\mathrm{m^3})^n$)

$k_{Overall\ measured}$ = apparent reaction rate constant ($\mathrm{mol_C} / \mathrm{m^3}\ (\mathrm{mol_{gas}}/\mathrm{m^3})^n$)

l = total length of pores per unit volume ($\mathrm{m/m^3}$)

$l_{0,i}$ = total length of pores i per unit volume ($\mathrm{m/m^3}$)

L'_i = mean distance between intersections of pores i and larger pores (m)

L'_j = mean length between intersections of pores j with any pores i and with pores k, larger than or equal to i, with the smooth field concentration (m)

MW = molecular weight (g/mol)

n = number of pore bins, or reaction order

$n'_{i,j}$ = expected number of intersections between pores i and j per unit length of pores i (1/m)

$P_{Thinning}$ = probability that for a given intersection and its closest neighbor, one is a j-i intersection and the other is any j-k_{SF} intersection (-)

q, q_i = pore growth variable (uniform or individual) (m)

r = radial position within particle (m)

R = pore radius (m)

$\mathfrak{R}$ = heterogeneous reaction rate ($\mathrm{mol_C}/\mathrm{m^2_C}\ \mathrm{s}$)

$\overline{R}$ = gas constant (J/mol K)

S = total pore surface area ($\mathrm{m^2_C}/\mathrm{m^3}$)

S_i = pore i surface area ($\mathrm{m}^2{}_C/\mathrm{m}^3$)

t = time (s)

T = temperature (K)

V = pore volume (units of ref. 9) (cm^3/g)

X = total solid conversion (-)

$X_{True,i}$ = solid conversion due to reaction on pores i (-)

Greek Symbols

ϕ_i = porosity ($\mathrm{m}^3{}_{\mathrm{pore\ i}}/\mathrm{m}^3$)

ϕ_{Tot} = total porosity ($\mathrm{m}^3{}_{\mathrm{pore}}/\mathrm{m}^3$)

$\phi(R)$ = porosity distribution with pore radius (units of ref. 9) ($\mathrm{m}^3{}_{\mathrm{pore\ i}}/\mathrm{m}^3$ Å)

$\eta_{i,k}$ = effectiveness factor for pore i of mean length $L_i^{'}$ in reaction k (-)

$\eta_{Tot,i,k}$ = effectiveness factor for entire length distribution of pores i in reaction k (-)

λ = Poisson density ($1/\mathrm{m}^2$)

ν = stoichiometric coefficient (mol/mol)

ρ_{True} = true solid density (helium density) ($\mathrm{kg/m}^3$)

σ = pore radius at which configurational diffusion becomes significant (m)

ψ = Random Pore model structural parameter (-)

Φ = Thiele modulus (-)

Subscripts

0 = at initial time $t=0$ or initial conversion $X=0$

C = char

continuum = molecular diffusion coefficient

E = hypothetical property of porous structure without pore overlap

eff = effective (diffusion coefficient)

Final = at final time, at X=1

i = pore size

j = pore size

k = pore size, or reaction index

Kn/Config = combined Knudsen and configurational

SF = smooth field

Tot = for the entire distribution of pore lengths

True,i = due to reaction on pores i

References

[1] R.H. Hurt, A.F. Sarofim, J.P. Longwell, Fuel 70 (1991) 1079-1082.

[2] R.H. Hurt, A.F. Sarofim, J.P. Longwell, Energy & Fuels 5 (1991) 290-299.

[3] D.G. Roberts, D.J. Harris, Energy & Fuels (2000) 483-489.

[4] P.A. Campbell, R.E. Mitchell, L. Ma, Proceedings of the Combustion Institute 29 (2002) 519-526.

[5] S.K. Bhatia, D.D. Perlmutter, AIChE Journal 26 (1980) 379-386.

[6] G.R. Gavalas, AIChE Journal 26 (1980) 577-585.

[7] G. Ballal, K. Zygourakis, Ind. Eng. Chem. Res. 26 (1987) 911-921.

[8] H.-chung Yu, S.V. Sotirchos, AIChE Journal 33 (1987) 382-393.

[9] J.L. Su, D.D. Perlmutter, AIChE Journal 31 (1985) 973-981.

[10] G. Ballal, K. Zygourakis, Ind. Eng. Chem. Res. 26 (1987) 1787-1796.

[11] I. Aarna, E.M. Suuberg, Twenty-Seventh Symposium (International) on Combustion 27 (1998) 2933-2939.

[12] L.R. Radovic, P.L. Walker, R.G. Jenkins, Fuel 62 (1983) 849-856.

[13] B. Feng, S.K. Bhatia, Carbon 41 (2003) 507-523.

[14] P. Salatino, F. Zimbardi, Carbon 32 (1994) 51-59.

[15] P. Salatino, O. Senneca, S. Masi, Carbon 36 (1998) 443-452.

[16] I. Kulaots, A. Hsu, E.M. Suuberg, Proceedings of the Combustion Institute 31 (2007) 1897-1903.

[17] S.K. Bhatia, D.D. Perlmutter, AIChE Journal 27 (1981) 247-254.

[18] S.V. Sotirchos, N.R. Amundson, AIChE Journal 30 (1984) 537-549.

[19] S.V. Sotirchos, N.R. Amundson, AIChE Journal 30 (1984) 549-556.

[20] J.I. Morell, N.R. Amundson, S.K. Park, Chemical Engineering Science 45 (1990) 387-401.

[21] R. Jackson, Transport in Porous Catalysts, Elsevier, New York, 1977.

[22] G.R. Gavalas, Combustion Science and Technology 24 (1981) 197-210.

[23] K. Bhatia, AIChE Journal 31 (1985) 642-648.

[24] M. Sheintuch, S. Brandon, Chemical Engineering Science 44 (1989) 69-79.

[25] S.V. Sotirchos, V.N. Burganos, Chemical Engineering Science 41 (1986) 1599-1609.

[26] C. Feng, W.E. Stewart, Ind. Eng. Chem. Res. 12 (1973) 143-147.

[27] R.H. Hurt, A.F. Sarofim, J.P. Longwell, Energy and Fuels 5 (1991) 463-468.

[28] R.H. Hurt, D.R. Dudek, J.P. Longwell, A.F. Sarofim, Carbon 26 (1988) 433-449.

[29] L.L. Murrell, C.T. Ratcliffe, W.J.M. Pieters, L.G. Sherman, N.C. Dispenziere, A.F. Venero, Carbon 26 (1988) 33-39.

[30] S.V. Sotirchos, S. Zarkanitis, Chemical Engineering Science 48 (1993) 1487-1502.

[31] G.Q. Lu, D.D. DO, Carbon 32 (1994) 247-263.

[32] E.W. Thiele, Industrial and Engineering Chemistry 31 (1939) 916-920.

[33] K.B. Bischoff, AIChE Journal 11 (1965) 351-355.

[34] G.W. Roberts, C.N. Satterfield, Industrial and Engineering Chemistry Fundamentals 4 (1965) 288-293.

[35] C.N. Satterfield, Mass Transfer in Heterogeneous Catalysis, 1st ed., M.I.T. Press, 1970.

[36] S. Borrelli, M. Giordano, P. Salatino, The Chemical Engineering Journal 64 (1996) 77-84.

[37] F.H. Verhoff, W. Strieder, Chemical Engineering Science 26 (1971) 245-253.

[38] D.G. Roberts, D.J. Harris, Fuel 86 (2007) 2672-2678.

[39] T. Morimoto, T. Ochiai, S. Wasaka, H. Oda, Energy and Fuels 20 (2006) 353-358.

[40] P. Salatino, F. Zimbardi, S. Masi, Carbon 31 (1993) 501-508.

[41] R. Sahu, Y.A. Levendis, R.C. Flagan, G.R. Gavalas, Fuel 67 (1988) 275-283.

[42] M. Loewenberg, Y.A. Levendis, Combustion and Flame 84 (1991) 47-65.

[43] S.K. Bhatia, B.J. Vartak, Carbon 34 (1996) 1383-1391.

[44] M. Sahimi, G.R. Gavalas, T.T. Tsotsis, Chemical Engineering Science 45 (1990) 1443-1502.

[45] J.K. Floess, Y. VanLishout, Carbon 30 (1992) 967-973.

[46] D.G. Roberts, D.J. Harris, Energy & Fuels 20 (2006) 2314-2320.

[47] S.S. Hla, D. Harris, D. Roberts, Gasification Conversion Model-PEFR: Research Report 80, 2007.

[48] W.K. Chi, D.D. Perlmutter, AIChE Journal 35 (1989) 1791-1802.

[49] J. Koresh, A. Soffer, Journal of the Chemical Society, Faraday Transactions 1 76 (1980) 2457-2471.

[50] P.L. Walker, Carbon 34 (1996) 1297-1299.

[51] J.S. Gupta, S.K. Bhatia, Carbon 38 (2000) 47-58.

Chapter 4. Numerical Approach

4.1 Numerical Implementation

Because of the highly non-linear and stiff nature of the system of governing equations, a method of lines approach has been adopted in order to utilize the sophisticated computational tools that have been developed for solving large systems of ordinary differential equations (ODEs). The partial differential equations (Eqs. (2.1)-(2.3)) are transformed into a set of ordinary differential equation using the well-known control volume discretization along the spatial coordinate [1]. The resulting system of ODEs is then integrated in time using a fully implicit scheme, with a Jacobian-Free Newton-Krylov method employed for the solution of the resulting system of nonlinear algebraic equations at each time step [2]. Banded preconditioning matrices are applied from the left. The code is written in MATLAB and the temporal integration is performed using the CVODE solver [2]. A typical relative tolerance of 10^{-5} and absolute tolerances of 10^{-6} are used for variables that are of order unity.

The physical domain was discretizated using the control volume formulation employed by Patankar [1], with an non-uniform grid generated using general interior stretching functions [3]. The non-uniform grid allows for increased resolution in areas of steep gradients, such as near the particle/gas-phase interface. The grid-points are centered between the control volume faces (as opposed to locating the interfaces halfway between adjacent grid-points). All state variables are calculated at the control volume centers, with the exception of the velocity in the gas phase, which is calculated at the control volume faces. Similarly, all diffusion and convective fluxes are evaluated at the control volume faces. The grid used is shown schematically in Fig. 4.1. Control volume centers are denoted by rr_j, and control volume faces by r_j, where j is the index for position. The particle center ($r = 0$) is located at $r_{j=1}$, and the bulk gas boundary conditions at $r_{j=s+1}$. A control volume face is also located at the particle-gas interface ($r_{j=s\_half+1}$), following the strategy of Patankar [1] for interfaces.

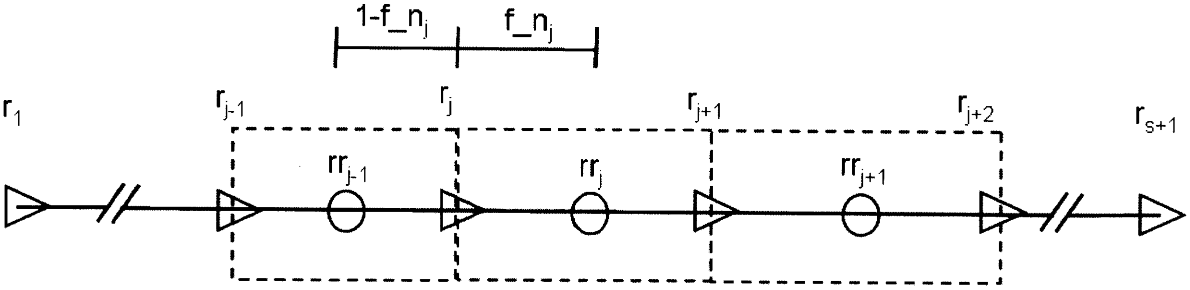

Figure 4.1. Schematic of discretization of the spatial coordinate.

All advective terms in equations (2.1)-(2.2) were evaluated using upwinding, via the sigmoid function given by [4], to ensure a rapid but smooth transition between zero and one as the velocity changes from negative to positive. Although in most cases the velocity is directed away from the char particle (positive velocity, u), the velocity could become negative in some regions of the boundary layer in cases where the gas temperature is rapidly decreasing. The domain typically extended to roughly 10 particle radii.

The multi-component fluxes are evaluated at the control volume faces using the Feng and Stewart model or the Dusty Gas model within the particle and using the Maxwell-Stefan multi-component diffusion relations in the gas phase. The state variables required by these flux models are calculated using linear interpolation between the adjacent grid-point values. For example,

$$T(r_j) = f_{n,j} T(rr_{j-1}) + (1 - f_{n,j}) T(rr_j), \tag{4.1}$$

where, $f_n(j) = \dfrac{rr_j - r_j}{rr_j - rr_{j-1}}$, (4.2)

as shown in Fig. 4.1. The transport coefficients required by these flux models corresponding to "conductivities" (e.g. D_j, $D_{j,s}$) are functions of temperature, mole fraction, pore size, etc., and are evaluated using harmonic averaging of the surrounding grid points, for instance:

$$D_K(r_j) = \left[\frac{(1-f_{n,j})}{D_K(rr_{j-1})} + \frac{f_{n,j}}{D_K(rr_j)} \right]^{-1}. \tag{4.3}$$

The harmonic mean provides a convenient and physically realistic method of accounting for instances of sharp transition of properties [1], which are especially pronounced at the interface between the porous solid and the homogeneous gas-phase, in which pore size and Knudsen diffusivities become infinite. For the case of a Knudsen diffusion coefficient, this yields

$$D_K(r_{s\_half}) \rightarrow \left[\frac{D_K(rr_{s\_half-1})}{(1-f_{n,s\_half})} \right]. \tag{4.4}$$

It should be noted that taking the harmonic mean of the entire matrix of coefficients $[\overline{\overline{B_f}}]^{-1}$ can result in discontinuities in the species profiles; therefore, the harmonic mean of the individual components of the matrices should be calculated.

At the particle/gas-phase interface there is an additional heat flux due to radiative exchange, q_{rad}, between the surface of the char particle and its surroundings. Using two infinitesimal control volumes at the interface, one can derive, from Eq. (2.5c), a non-linear algebraic expression for the interface temperature in terms of the surrounding temperatures on either side of the interface and the temperature with which the particle interacts radiantly. This non-linear equation cannot be solved explicitly for the interface temperature, T_{s_half}. Solving a non-linear algebraic equation would necessitate either solving the model as a differential algebraic system or employing a non-linear equation solving routine at every time step of the ODE solver; both of which are undesirable. Therefore, the non-linear term on the right-hand side is lagged by one time-step to give an explicit equation for the current interface temperature. A similar procedure is adopted in solving for the pore-scale effectiveness factors that appear in Eq. (3.17) via Eq. (3.26), in that the effectiveness factor terms that appear on the right-hand side of Eq. (3.26) are lagged by one time-step. Time steps are typically of the order 10^{-5}-10^{-4} s.

At the interface between particle and gas-phase, the convective flux was calculated using the Feng and Stewart relation. For locations beyond the interface, the velocity, u, was calculated using the continuity equation, since the pressure is nearly constant outside the particle. For the gas-phase, by using the ideal gas law, $p = \rho R_{mix} T$, the continuity equation (Eq. (2.3)), can be converted to an equation in which time derivatives of temperature and species mole fraction appear, but in which the velocity appears only in the spatial derivatives,

$$\frac{1}{r^2}\frac{\partial}{\partial r}\left(r^2 \rho u\right) = \frac{\rho}{T}\frac{\partial T}{\partial t} + \frac{\rho}{R_{mix}}\frac{\partial R_{mix}}{\partial t} \tag{4.5}$$

where the last term can be expressed as,

$$\frac{\rho}{R_{mix}}\frac{\partial R_{mix}}{\partial t}=\frac{-\rho}{MW_{mix}}\sum_{i=1}^{n-1}\left[\left(MW_i-MW_n\right)\frac{\partial x_i}{\partial t}\right] \tag{4.6}$$

In the method of lines approach, this would result in a system of differential algebraic equations upon discretization, which is not desirable, due to the notorious difficulty of initializing DAE solvers with consistent initial conditions. However, for our one-dimensional, constant pressure situation, it is possible to substitute for the temperature and species derivative terms using the discretized right-hand-sides of the species and energy equations (2.1, 2.2) and to take advantage of the fact that all velocity terms in the equation appear linearly, whether in the first-order spatial derivative or in the advective terms in the energy and species equations. The velocities can then be obtained sequentially by solution of the linear system shown below,

$$\begin{bmatrix} B & & & 0 & \\ A & B & & & \\ & A & B & & \\ 0 & & A & B & \\ & & & & \ddots \end{bmatrix}\begin{bmatrix} u(r_2) \\ u(r_3) \\ u(r_4) \\ u(r_5) \\ \vdots \end{bmatrix}=\begin{bmatrix} RHS(rr_1) \\ RHS(rr_2) \\ RHS(rr_3) \\ RHS(rr_4) \\ \vdots \end{bmatrix}, \tag{4.7}$$

where the *r*-locations are the control volume faces, at which the velocity is calculated and the *rr*-locations are the control volume centers, at which the temperature and mole fractions are calculated. *A* and *B* contain all coefficients of the velocities from Eq. (4.5), both from the left-hand side and from the advective terms on the right hand side, and *RHS* contains all the *non-velocity* terms from the right-hand side of Eq. (4.5). The boundary condition for this first order equation is the porous medium/gas-phase interface velocity calculated from the FSM, so an outflow boundary condition is not needed for the velocity.

Essentially, the velocities have been eliminated (converted to non-state variables), much like the convective velocity in the porous phase and the diffusive fluxes in both phases. This allows the numerical solution to treat the system as one of ODEs rather than DAEs, with the penalty being that there is no longer explicit error control on the velocities themselves. However, this can be mitigated by tightening the tolerances on the energy and species equations. Another, simpler option, is to calculate the time-derivatives on the right-hand side of eq. (4.5) using a manual first order discretization using current and lagged values for T and R_{mix} (or x_i). In many cases, the contribution of the unsteady terms to the convective velocity is quite small compared to that induced by Stefan flow. The latter option is followed for the results presented in later chapters.

Computation of the fraction of active sites remaining in the annealing model requires numerical integration over all activation energies for annealing at every time. The temperature of a bin is calculated as a weighted average over the time bin, either once a minimum time interval has passed, or once the temperature difference between the current temperature and the last bin's temperature exceeds a minimum value (20 K was used in this study).

For the calculations involving a single moving boundary, the front-fixing coordinate transformation given by Landau [5], and utilized by many previous investigators (e.g., [6–8]), is used,

$$\varsigma = \frac{r}{s(t)} . \tag{4.8}$$

This immobilizes the porous solid/gas interface at $\varsigma = 1$. This transformation induces pseudo-convective terms in all time derivative terms (the empty parentheses represent any variable) taken at constant ς, which are given by,

$$\left.\frac{\partial(\ )}{\partial t}\right|_{\varsigma} = \left.\frac{\partial(\ )}{\partial t}\right|_{r} + \left(\frac{\varsigma}{s(t)}\frac{ds}{dt}\right)\frac{\partial(\ )}{\partial \varsigma}. \tag{4.9a}$$

Of course, the transformation also modifies spatial derivatives:

$$\frac{\partial(\ )}{\partial r} = \frac{1}{s(t)}\frac{\partial(\ )}{\partial \varsigma}. \tag{4.9b}$$

The spatial derivatives in the pseudo-convective terms are generally evaluated using centered finite difference expressions appropriate for unevenly spaced grid points, but the spatial derivative of conversion (or equivalently, porosity, or q_i) in the equation for the position of the char/gas-phase interface is calculated using a second order, one-sided expression.

For cases in which the build-up of an ash layer is modeled on top of a shrinking char particle, there are two moving boundaries toward the end of conversion, once the adhering ash forms its own layer. It is possible to employ two front-fixing transformations, but this presents a problem in using local volume averaging, since one must, *a priori*, assign a certain number of grid-points to the ash layer, which initially is very thin. Therefore, in this study, the interface between the porous solid (whether it be char or ash) and the gas phase is always fixed via the Landau transformation. This is convenient because the porous medium, with its particular equations and sub-models, is always on one side of $\varsigma = 1$, while the gas-phase is on the other.

When there is an ash layer accumulating on top of the char, this means that $r_{ash}(t)$ replaces $s(t)$ as the variable used in Eqs. (4.8) and (4.9) for non-dimensionalization, and the equation for the char/ash interface position, Eq. (2.36), is modified as

$$\frac{ds}{dt}=\frac{-r_{ash}(t)\left.\dfrac{\partial\phi}{\partial t}\right|_{\varsigma=\frac{s(t)}{r_{ash}(t)}}}{\left.\dfrac{\partial\phi}{\partial\varsigma}\right|_{\varsigma=\frac{s(t)}{r_{ash}(t)}}}. \tag{4.10}$$

However, the location of the char/ash interface is no longer immobilized on a grid-point, since it migrates inwards with respect to the ash layer, crossing grid-points as it goes. Therefore, the location of the char/ash interface is calculated using a front-tracking method [9] with the spatial derivative in Eq. (4.10) calculated using Lagrange polynomials and the value of porosity, ϕ, at the point $s(t)$, where it is constant at its critical value, and the values at the nearest two grid-points inward. The time derivative in Eq. (4.10) is calculated using temperature, mole fractions, etc. at the interface that are determined by linear interpolation. When $s(t)$ crosses a grid point, there is a sudden change in the values used in the calculation of the spatial derivative. To smooth out this behavior, a one-sided derivative evaluated using ϕ_{crit} and the porosity at the two nearest gridpoints, $\phi_{\varsigma-1}$, $\phi_{\varsigma-2}$ was averaged with a one-sided derivative evaluated using ϕ_{crit}, and $\phi_{\varsigma-2}$, $\phi_{\varsigma-3}$, using the expression,

$$\left.\frac{\partial\phi}{\partial\varsigma}\right|_{\varsigma=\varsigma_0=\frac{s(t)}{r_{ash}(t)}}=\beta\left.\left(\frac{\partial\phi}{\partial\varsigma}\right)\right|_{\varsigma_0,\,\varsigma_{-1},\,\varsigma_{-2}}+(1-\beta)\left.\left(\frac{\partial\phi}{\partial\varsigma}\right)\right|_{\varsigma_0,\,\varsigma_{-2},\,\varsigma_{-3}}, \tag{4.11}$$

where

$$\beta = \frac{1}{\left(1+\exp\left(-2\left(\frac{\varsigma_0-\varsigma_{-1}}{\varsigma_{+1}-\varsigma_{-1}}-0.5\right)\right)\right)}. \tag{4.12}$$

4.2 Calculation of properties

Gas-phase properties are calculated dynamically as functions of the local state variables. The heat capacity of the gas mixture is evaluated as a function of temperature using the values from the NIST property database [10]. Binary diffusion coefficients are calculated following Reid [11] and Knudsen diffusion coefficients are given by $D_{Knudsen} = \frac{2R_i}{3}\sqrt{\frac{8\bar{R}T}{\pi MW}}$. Thermal conductivities are calculated using the relations given by Donskoi [12,13] which were fitted to detailed expressions based on molecular theory. The viscosity of the gas mixture only enters into the Darcy term in the FSM and is simply evaluated using the expression of Morell [8], $\mu = 1.13\times10^{-5}T^{1/2}$. In the porous phase, the thermal conductivity and heat capacity is that of the effective medium, comprised of solid and gas. The expressions are also taken from Morell [8], and are given by,

$$C_{p,eff} = (1-\phi)C_{p,solid} + \phi C_{p,gas} \tag{4.13}$$

$$k_{eff} = (1-\phi)^2 k_{solid} + \phi^2 k_{gas} \tag{4.14}$$

The gas properties were evaluated as described above and those of the solid were taken as weighted averages of the local ash fraction and char fraction in the solid phase. The values for the char were taken from Sotrichos [14] and those of the ash were based on various authors [15–17]. Finally, the temperature, T, and pore growth variables, q_i, were non-dimensionalized, in some cases, in order to bring their values closer to unity to facilitate error control during the integration.

Nomenclature and Units

A = term defined by Eq. (4.7) (kg/m^4)

B = term defined by Eq. (4.7) (kg/m^4)

B_f = matrix defined by Eq. (2.9) (s/m^2)

C_p = specific heat (J/mol K)

D = diffusion coefficient (m^2/s)

f_n = length ratio defined by Eq. (4.2) ( )

k = thermal conductivity (W/m K)

MW = molecular weight (g/mol)

p = pressure (N/m^2) or (atm)

q_{rad} = radiative heat flux (W/m^2)

r = radial position of control volume face (m)

rr = radial position of control volume center (m)

r_{ash} = position of moving ash boundary (m)

R = pore radius (m)

$\overline{R}$ = universal gas constant (J/mol K)

R_{mix} = specific gas constant (J/kg K)

RHS = vector of driving forces for diffusion (mol/m^4)

s = position of moving char boundary (m)

t = time (s)

T = temperature (K)

u = radial velocity (m/s)

x = mole fraction

X = total solid conversion (-)

Greek Symbols

β = weighting sigmoid function defined in Eq. (4.12)

ϕ = total porosity (m$^3_{\text{pore}}$/m^3)

$\eta_{i,k}$ = effectiveness factor for pore i in reaction k (-)

ν = stoichiometric coefficient (mol/mol)

ρ = density (kg/m^3)

ς = dimensionless radial coordinate (-)

Subscripts

0 = at initial time $t=0$ or initial conversion $X=0$

ash = property of ash

critical = at the critical conversion or porosity

C = char

eff = effective coefficient accounting for gas and solid phase

gas = property of gas

i = species

j = grid point

Kn = Knudsen diffusion coefficient

$s_{\_half^-}$ = at porous medium/gas interface

solid = property of solid

Tot = total

References

[1] S. Patankar, Numerical Heat Transfer and Fluid Flow, Hemisphere Publishing, Washington D C, 1980.

[2] A.C. Hindmarsh, P.N. Brown, K.E. Grant, S.L. Lee, R. Serban, D.A.N.E. Shumaker, C.S. Woodward, ACM Transactions on Mathematical Software 31 (2005) 363-396.

[3] M. Vinokur, Journal of Computational Physics 50 (1983) 215-234.

[4] R.J. Kee, M.E. Coltrin, P. Glarborg, Chemically Reacting Flow, Wiley-Interscience, Hoboken, 2003.

[5] H.G. Landau, Q. Appl. Math 8 (1950) 81-94.

[6] G.R. Gavalas, Combustion Science and Technology 24 (1981) 197-210.

[7] S.V. Sotirchos, N.R. Amundson, AIChE Journal 30 (1984) 549-556.

[8] J.I. Morell, N.R. Amundson, S.K. Park, Chemical Engineering Science 45 (1990) 387-401.

[9] J. Crank, Free and Moving Boundary Problems, Oxford University Press, 1984.

[10] NIST Standard Reference Database Number 69, Webbook.nist.gov/chemistry, Accessed (2011).

[11] R.C. Reid, J.M. Prausnitz, T.K. Sherwood, The Properties of Gases and Liquids, 3rd ed., McGraw-Hill, New York, 1977.

[12] E. Donskoi, D.L.S. McElwain, Metallurgical and Materials Transactions B 34 (2003) 93-102.

[13] S.S. Hla, D. Harris, D. Roberts, Gasification Conversion Model-PEFR: Research Report 80, 2007.

[14] S.V. Sotirchos, N.R. Amundson, AIChE Journal 30 (1984) 537-549.

[15] M. Loewenberg, Y.A. Levendis, Combustion and Flame 84 (1991) 47-65.

[16] M. Seggiani, Fuel 77 (1998) 1611-1621.

[17] K.C. Mills, J.M. Rhine, Fuel 68 (1989) 904-910.

Chapter 5. Model Validation and Demonstration

5.1. Introduction

In this chapter, the comprehensive model developed in previous chapters is validated using a well-characterized char from the literature and combustion experiments performed in zone II that are suited to testing the model without requiring parameter tuning. The impact of reaction on different pore sizes is investigated and the differences between the RPM and ARPM are examined. The capabilities of the ash adherence sub-model are also demonstrated for a hypothetical case of combustion near the ash melting temperature.

5.2. Inputs and Experiments for Model Validation

To test the single particle char consumption model without using fitting parameters, it is necessary to have, as input, measurements of the char's pore size distribution, particle size, density and ash content, as well as zone I reaction rate data at a conversion level at which the pore size distribution has also been measured (see Ch. 3.5). For purposes of validation, zone II measurements of interest such as conversion, temperature or surface area vs. time or conversion, for the same char, must be available, together with the boundary conditions to which the particle has been exposed throughout its conversion.

We have attempted to validate the model with zone II Spherocarb oxidation data from the literature [1,2]. Spherocarb, a synthetic char, has been employed by several research groups for fundamental studies of char gasification and oxidation. Its pore structure has been well characterized, it contains minimal amounts of ash, a small amount of remaining volatiles and moisture (~4% wt) and is highly spherical and uniform (mean diameter of 140 μm), which makes it very suitable for validation of the model.

The initial pore structure of Spherocarb and its reaction rate with oxygen in the kinetically controlled regime has been characterized extensively and is summarized by D'Amore, et al. [3–5], and the results presented therein were employed to divide the pore size distribution into discrete bins of porosity and pore radius [6,7]. The surface area in the (A)RPM is completely determined by the measured pore size distribution, $\phi(R)$, therefore in order to match the surface area to the measured values, the average radius of the smallest micropore bin was adjusted downward. This should not have a large effect on the results because, as will be discussed, the micropores seem to negligibly participate in the oxidation of Spherocarb, although gasification can occur on the micropores to some extent depending on the conditions. Table 5.1 shows the discretized pore structure determined from the data of D'Amore, et al. [3]. The initial surface area associated with each pore size can be calculated from $\phi_i(R_i)$ using Eq. (3.11), and is also shown in Table 5.1.

Table 5.1. Parameters employed in pore size distribution of Spherocarb char.

	Micropores		Mesopores		Macropores	
R_i (Å)	4.0	10.8	65.1	665.2	5721.8	26078.0
ϕ_i (m^3/m^3)	0.1289	0.0204	0.0364	0.0707	0.1001	0.3241
S_i (m^2/m^3)	5.41x10^8	2.6x10^7	7.3x10^6	1.2x10^6	1.8x10^5	1.0x10^5

D'Amore has measured the reaction rates for Spherocarb particles in oxygen at several different temperatures and oxygen concentrations as a function of conversion [4] using an electrodynamic balance and a TGA and also summarized measurements taken by Floess [8] and Hurt using a TGA apparatus [9]. Since the pore structure characterization is done at zero conversion, the reaction rate must be extrapolated back to zero conversion as well in order to apply the method of the ARPM to determine the intrinsic (per unit area) rate of oxidation. For this purpose, we used the method of Su and Perlmutter [10] described in Chapter 3.6 and applied it to the Spherocarb data measured via TGA at temperatures of 673, 703 and 768 K and using only the data points up to 50% conversion for accuracy [10]. Figure 5.1 illustrates the procedure of Su and Perlmutter [10] applied to determine the initial apparent oxidation rate of Spherocarb char for the three low temperature experiments summarized by D'Amore et al. [4]. Once the apparent rate is calculated, the intrinsic pre-exponential factor is estimated using the method of the ARPM described in Chapter 3.5, since the activation energy and the order of reaction have also been experimentally determined [4].

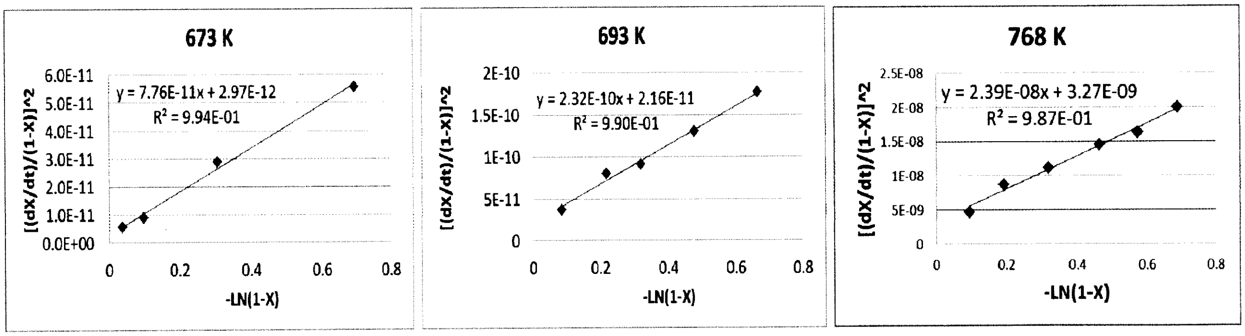

Figure 5.1. Procedure of Su and Perlmutter [10] **to extrapolate the reaction rate to the conversion at which the pore size distribution has also been measured, using the assumption that the pore structure evolution parameter of the ARPM is constant.**

Using the method of the ARPM to estimate the surface area participating in the oxidation reaction [7], it has been calculated that the micropores contribute negligibly to the oxidation of Spherocarb, even in what is ostensibly the kinetically controlled regime. This is in agreement with the evidence of D'Amore et al. [4] who found that the normalized micropore size distribution of Spherocarb was remarkably constant with conversion during oxidation experiments and with the results of D'Amore et al. [5] based on the reaction rate variation with conversion, but is opposite the conclusion of Hurt et al. [11], which was based on the absence of a particle-size effect, SEM observation that macropores did not exhibit growth with conversion and a pore-scale Thiele analysis. The intrinsic rate of oxidation determined by the ARPM is shown in Table 5.2. The reaction order and activation energy were also taken from [4].

Indirect evidence for the non-participation of micropores in the oxidation of Spherocarb has also been obtained. Similar to the analysis performed by D'Amore et al. [5], the normalized reaction rate with conversion has been calculated for the discretized pore structure of Spherocarb char, based on the assumption that all pore sizes participate fully in the oxidation reactions and also based on the assumption that micropores are completely excluded, while other pore sizes participate fully. The two profiles are also compared to the kinetic measurements at the three temperatures shown above, appropriately normalized. The two assumptions yield qualitatively different profiles: when micropores are excluded, the rate vs. conversion curve exhibits a peak, ($\Psi_{RPM} = 9.31$), while it is almost monotonically decreasing ($\Psi_{RPM} = 2.65$) in the case of micropore participation. It is also evident from Fig. 5.2 that exclusion of micropores yields a curve that more closely fits the experimentally measured kinetic data. For the measurements performed at 693 and 768 K, the random pore (capillary) model based solely on the initial pore structure with $\eta_{micro} = 0$ and $\eta_{meso/macro} = 1$ produces quite satisfactory results throughout conversion without the use of any fitting parameters.

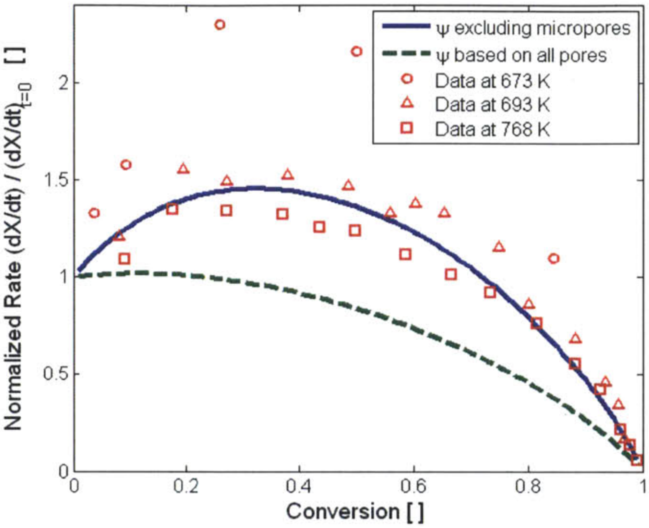

Figure 5.2. Normalized rate versus conversion for the low temperature oxidation data summarized in D'amore et al. [4] **and comparison with the random pore model, with full participation of all pores and with the assumption that micropores do not participate whatsoever.**

It was argued by Floess et al. that the reaction rate of Spherocarb char versus conversion exhibited a maximum due to the adsorption of oxygen early in conversion, distorting (decreasing) the TGA measurement of mass loss and under-estimating the reaction rate early in conversion [12]. Although no figures were presented, it was mentioned that after partial conversion, upon out-gassing the sample and then restarting oxidation, a peak (it was not mentioned if it was to the same extent) could be observed.

It is quite possible that both effects occur and can be reconciled, largely based on the interpretation of Salatino [13]. Early in conversion, chemisorption of oxygen in char micropores occurs. However, its desorption as CO or CO_2 is limited, and instead, oxygen slowly migrates along micropore surfaces until reaching an active site for oxidation, whereupon it can complete the reaction. This can be modeled as configurational diffusion, as described in Chapter 3. Overall, this process is quite slow and results in minimal oxidation occurring on char micropores [13]. The main question, then, is whether the oxidation rate extrapolated back to zero conversion is too low. Taking this into consideration, and also examining Fig. 5.2, in which the data of Floess et al. (673 K) shows a much larger peak and a much worse fit to either the RPM or ARPM (no micropore participation) and a moderately lower reactivity than the other two temperatures, it was decided to base the oxidation pre-exponential factor, A, shown in Table 5.2 on the data at 693 K and 738 K collected by Hurt, exclusively.

Although it hasn't been considered in previous attempts at modeling the experiments of Waters et al. [1,2], char gasification reactions may be significant, since the gas mixture is 16-20% H_2O and 2-3% CO_2 by volume and particle temperatures typically peak between 1700 and 2100 K; conditions under which gasification might be expected to play a non-negligible role. Furthermore, although the intrinsic reaction rate of carbon with steam is much slower than the reaction with oxygen [14], steam is known to be able to penetrate and react in small pores that are often inaccessible to oxygen [15] and Spherocarb particles have a *very* high level of microporosity compared to typical char particles.

For this validation study, which simulates combustion at atmospheric pressure, n^{th} order heterogeneous reactions are considered. For carbon oxidation, n^{th} order behavior has been explained as being a consequence of the distribution of activation energies for combustion among the carbon sites [16]. Although gasification reactions (R1) and (R3) are most realistically modeled using a Langmuir-Hinshelwood rate form [17], especially at high pressures [18], for the low and limited partial pressure ranges encountered throughout the char conversion in these experiments, a power law rate form was deemed acceptable and employed for its simplifying effects and due to the limited knowledge of all of the rate constants contained in a Langmuir-Hinshelwood expression [19]. Shaddix and coworkers have discussed the advantages of employing simply n^{th} order rate forms for representing char gasification reactions [19,20].

Steam gasification data for uncatalyzed Spherocarb does not exist in the literature. However, Floess et al. performed kinetic measurements on the reaction rate parameters of Spherocarb char with carbon dioxide [8] and this can be used to estimate the steam gasification rate as well. Walker et al. [21] has suggested that the apparent reaction rate of char with steam is roughly three times its rate with carbon dioxide, while Harris and Smith have also found a similar ratio to hold for different chars in their measurements [14]. Shaddix et al. have summarized data from several researchers and concluded that for a given char, the reaction rate with steam is indeed roughly three times its rate with CO_2 [19]. Furthermore, the experimental data in the literature as well as theoretical considerations indicate the activation energy for the $C+H_2O$ reaction is very close to that of the $C+CO_2$ reaction, meaning that the pre-exponential factor of the former is simply three times that of the latter [19].

The same procedure used to determine the intrinsic kinetics of Spherocarb oxidation was followed for the $C+CO_2$ kinetics. The procedure of Su and Perlmutter [10] was applied to determine the initial apparent gasification rate of Spherocarb char based in the data of Floess et al. [8], at each temperature. Floess' data was taken at four temperatures ranging from 1240-1350 K. The apparent pre-exponential factor was determined from the Arrhenius equation, using the activation energy determined by Floess et al. [12]. Although the order of reaction was not measured, based on the order determined for several chars in the literature [22], a value of n=0.4 was assigned. The method of the ARPM was employed to estimate the fraction of the surface area participating the in the gasification reaction, and the intrinsic pre-exponential factor was again calculated using Eq. (3.28). The intrinsic reaction rate parameters for steam and carbon dioxide are shown in Table 5.2. The homogeneous reaction of carbon monoxide with oxygen in the boundary layer surrounding Spherocarb particles is deemed to be important by Waters et al. [1] and Tognotti et al. [23], especially in the presence of water vapor. Therefore reactions (R4) and (R5) for the oxidation of carbon monoxide and hydrogen were also included in the simulation.

Table 5.2. Kinetic parameters for Spherocarb combustion and gasification.

Reaction	A [mol /m^2 s atm^n]	E [kJ/mol]	n
$C+O_2$	29,180	150.6	1.0
$C+H_2O$	55,248	281.2	0.4
$C+CO_2$	18,416	281.2	0.4

It was not necessary to include a sub-model for the ash behavior in this case, since Spherocarb has minimal ash content [5]. However, it was necessary to decide whether to allow for peripheral fragmentation in the simulation. Spherocarb, like some other highly microporous chars, has been known to undergo shrinkage in the kinetic regime, which is thought to be caused by atomic rearrangements (densification) rather than peripheral fragmentation [24]. Although it is not negligible, the shrinkage is less significant earlier in the char's conversion (see Figure 1 in [24]), where Waters' data was mostly collected. Since Waters' data is taken in regime II, in which the mechanism of shrinkage is unknown, and because the extent of shrinkage is smaller at the lower conversion levels measured and there is not a predictive model consistent with the (A)RPM that can account for shrinkage, in what follows we simply use the measured (r/r_0) vs. X data to form a differential equation for particle radius, without allowing for any conversion to be caused by the shrinkage, so that the mass balance is satisfied. In other words, the only effect shrinkage has in the simulation is to reduce the particle's diameter; no structural rearrangements (e.g. densification, pore elimination) are incorporated and no conversion due to diameter reduction is counted toward the overall conversion. If, as hypothesized [3], micropore elimination is the mechanism by which shrinkage occurs for this char, this approach seems an appropriate way to calculate conversion, since micropores do not participate in the char oxidation. This implies, however, that the gasification rates may be over-estimated in what follows, since char gasification does occur on the micropores to a large extent, and the microporosity (and surface area) would be smaller than calculated due to shrinkage.

Aside from the required inputs mentioned above, it is necessary to know the temperature-time history of the solid fuel particle to apply the annealing sub-model, described in Chapter 2. Since Spherocarb was manufactured commercially, its preparation conditions have not been publicized. However, annealing measurements on as-received Spherocarb (which has already been annealed, to some extent, during its production) have been summarized [25] and can be used to set up an inverse problem for determining the distribution of annealing activation energies for as-received, Spherocarb. For reaction times of 1800 s, at three different temperatures, $N(t)/N_{received}$ was measured, where $N_{received}$ represents the as-received, post-production-heat-treatment value. Thus, $C(E_d)$ is to be determined from the following equation, using the three pairs of $(T, N(t)/N_{received})$ shown in Table 5.3:

$$\frac{N(t)}{N_{received}} = \int_0^{\infty} C(E_d)\exp[-At\exp(-E_d / \bar{R}T)]dE_d \tag{5.1}$$

Table 5.3. Annealing measurements (summarized in [25]**) and calculations for Spherocarb subject to different heat treatment temperatures for 1800 s.**

T_{HT} [K]	1173	1473	1673
$(N(t)/N_{received})$ measured	1.0	0.66-0.72	0.37-0.38
$(N(t)/N_{received})$ calculated	1.0	0.709	0.392

Consistent with these measurements, it has also been shown by Raman Spectroscopy [26] that annealing of Spherocarb is negligible at temperatures of 1173 K, but does occur at 1473 K. In practice, however, solving this integral equation using only three data points would be very difficult. For this reason, simple trial and error was employed. The annealing model of Zolin et al. [27] was adopted, with all the recommended values of the shifted gamma distribution, with the exception of β, which was increased slightly to 45000, which is still within the recommended range. Assuming that during its production, Spherocarb is heated with a simple temperature ramp followed by a temperature hold, the ramp rate, hold temperature (the most important parameter) and hold time were varied until the ratio of the reactivity after experiment to the reactivity of as-received Spherocarb approached the three experimentally determined data points. The values determined by this trial-and-error procedure for Spherocarb's heat treatment are shown in Table 5.4. While this is certainly not the actual heat treatment undergone by Spherocarb, it yields results reasonably consistent with annealing measurements, as shown by Figure 5.3 and Table 5.3.

Table 5.4. Parameters determined for heat treatment of Spherocarb.

Ramp [K/s]	T_{Hold} [K]	t_{Hold} [s]
100	1373	900

Once the production (devolatilization) heat treatment is known, it is possible to apply the annealing model as outlined above by simply appending the temperature-time history during combustion to that of the heat treatment during production. The intrinsic rates determined above (Table 5.2) can account for the fact that the char has already undergone an initial heat treatment during production by dividing the pre-exponential factors by $N_{received}/N_0$ and appending the production heat treatment to the concurrent annealing model. In this way, at the beginning of combustion, the reactivities are the same as those given in Table 5.2 based on measurements.

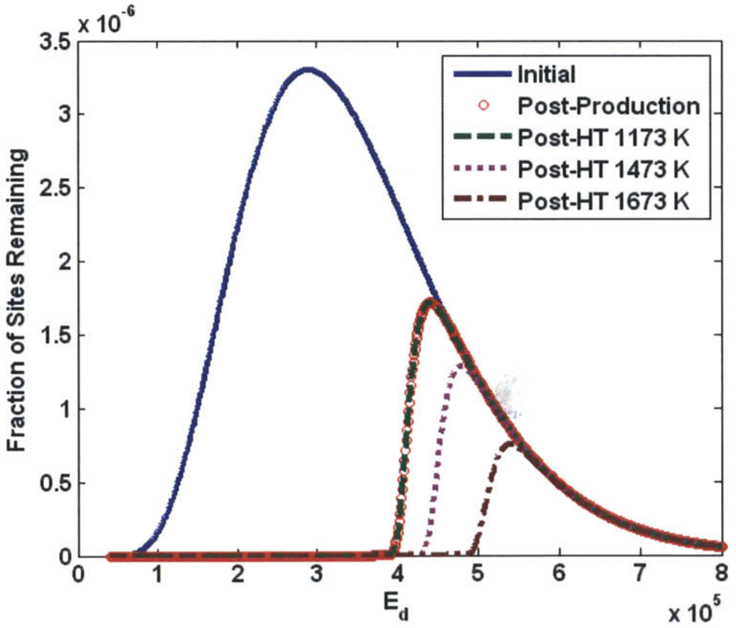

Figure 5.3. Distribution of remaining active sites for annealing after heat treatment to different temperatures for 1800 s, using the results shown in Table 5.4 to calculate the "post-production" distribution of Spherocarb.

Finally, the time-dependent boundary conditions to which the particles have been exposed must be described. The experiments described by Waters et al. were performed in the Sandia entrained flow reactor that has been described in a number of papers [28–30]. Gas-phase flames are used to generate a variety of conditions in the downstream region of the reactor. The post-flame region has a uniform gas composition around its centerline and a gas temperature profile that decreases linearly with distance along the axis at a rate of roughly -1 K/mm [28]. Based on Fig. 2 in the study by Murphy and Shaddix [30], the location of the peak temperature was estimated. The gas temperature in the region before the peak temperature is given by comparison with Fig. 2 in Molina and Shaddix [31] and with Fig. 1 in the study of Shaddix and Molina [32]. The particle velocity is roughly 2.5 m/s [1], enabling conversion of position in the reactor to residence time of the particles. The gas flow relative to the particle has typically been neglected in modeling this reactor since the Reynolds number based on the slip velocity is $\sim 10^{-6}$ [30], permitting the use of a spherically symmetric domain with only a radial velocity component, consistent with the model developed in this thesis. The wall temperature, used in calculating radiation heat loss from the particle, is given as 500 K for this reactor [1,29,30] and the particle emissivity is given as 0.85 [1]. Measurements of char conversion and particle temperature were performed at three heights in the reactor (12.7, 19.1 and 25.4 cm) and have been described in more detail by Waters et al. [1].

5.3. Model Validation and Discussion

To validate the model, cases 2, 4 and 5 in Waters' experiments have been simulated. The gas temperature profiles are shown in Fig. 5.4, and the species mole fraction boundary conditions are shown in Table 5.5, with the balance of the gas being nitrogen [1].

Table 5.5. Boundary conditions for Cases 2, 4 and 5.

	X_{O2}	X_{H2O}	X_{CO2}
Case 2	0.12	0.18	0.02
Case 4	0.12	0.20	0.03
Case 5	0.24	0.16	0.02

The simulation results for the particle temperature (at the edge of the particle) are also included in Fig. 5.4 for comparison. Case 5, which has the highest bulk gas oxygen concentration, has the lowest bulk gas temperature. For the cases with 12% O_2, the particle temperature rise is roughly 100 K toward the end of the reactor, while for case 5, which has 24% O_2 in the bulk gas, the particle temperature rise exceeds 400 K, despite the occurrence of endothermic char-steam gasification reactions.

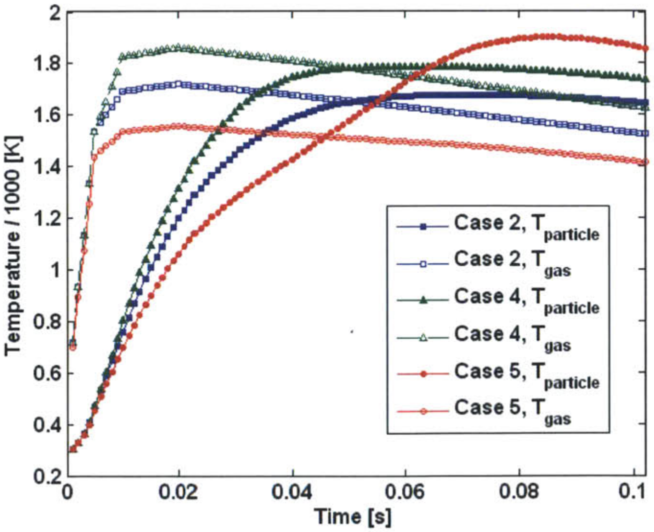

Figure 5.4. Bulk gas (and calculated particle) temperatures along the reactor for cases 2, 4 and 5.

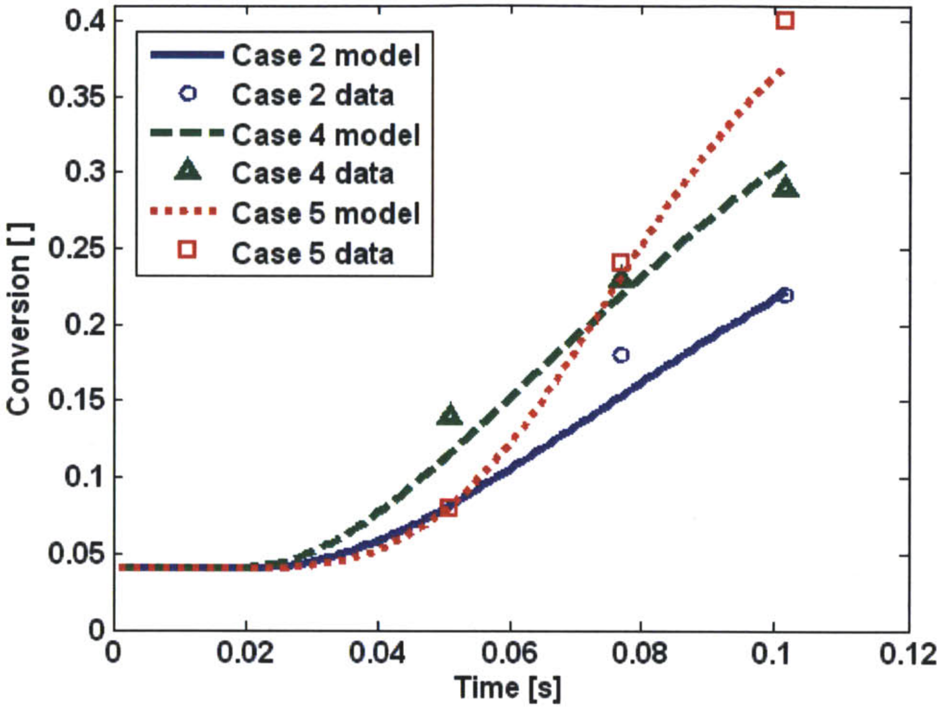

Figure 5.5. Experimental [1] **and simulation results for conversion versus time for cases 2, 4 and 5.**

Measured data points [1] and simulation results, using the inputs described above, for particle conversion vs. time for the three cases, are shown in Fig. 5.5. A mass loss of 4% due to moisture and volatile evolution was incorporated [1]. The qualitative trends are good and the quantitative agreement is quite reasonable. However, the first conversion data points of case 2 are under-predicted by the model. Given that cases 2 and 4 have the same oxygen concentration, but case 2 has a significantly lower gas temperature, it is unclear why case 2 and case 4 have the same measured conversion at t=0.051 s. The last data point for conversion of case 5 is also slightly under-predicted. The qualitative trends predicted for cases 4 and 5 both match the experimental trends well; that predicted for case 2, less so.

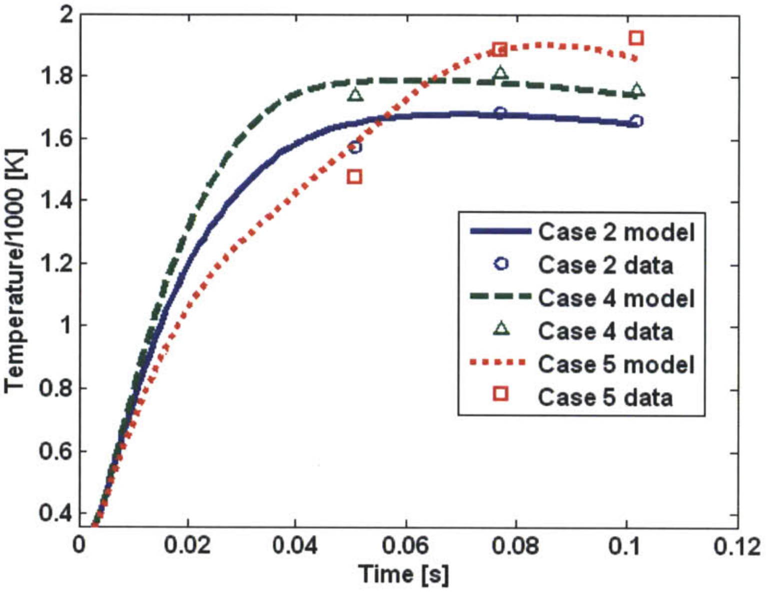

(a)

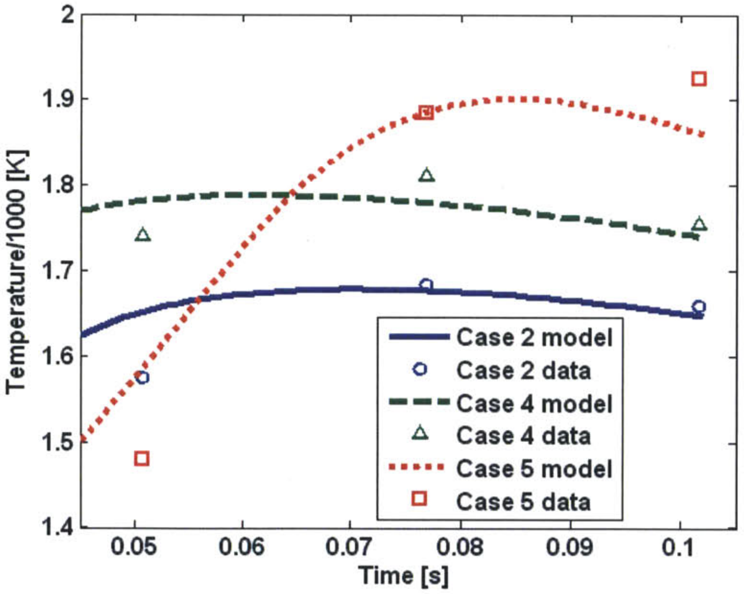

(b)

Figure 5.6. Experimental [1] **and simulation results for particle temperature versus time for cases 2, 4 and 5, for (a) the entire reactor and (b) a magnification of the region of high particle temperatures.**

Measured data points [1] and calculated particle temperatures vs. time for the three cases are shown in Fig. 5.6. The simulations indicate that the particles are almost of uniform temperature (the surface temperature is shown in Fig. 5.6). Again, both the qualitative trends and the quantitative agreement are reasonable, with the largest discrepancies occurring for the measurements at the earliest times. In accordance with the measurements, the simulation results for cases 2 and 4 both predict that the particle temperature decreases slightly between the data points at t=0.077 s and t=0.102 s. However, the particle temperature predicted for case 5 decreases quickly after peaking near 0.08 s, while the experimental data shows a continued rise in the char particle temperature.

The simulated particle temperature decreases due to the decrease in surface area and particle size. The source of this qualitative discrepancy with Waters' data for case 5 is unclear. One possibility, suggested by the under-prediction of both conversion *and* particle temperature at the last data point, is that late in conversion, after H_2O and CO_2 have reacted on the surface of the micropores, increasing their width, and after oxidation on mesopores has decreased the length of micropores, oxygen begins to react to a greater extent on the micropores than predicted by the model, in a manner similar to Fig. 3.10(b). Another possible contribution to the under-prediction of particle temperature could be shrinkage (densification), which is thought to be caused by the elimination of microporosity, as discussed above, and which decreases the micro-porous surface area available for the endothermic gasification reactions.

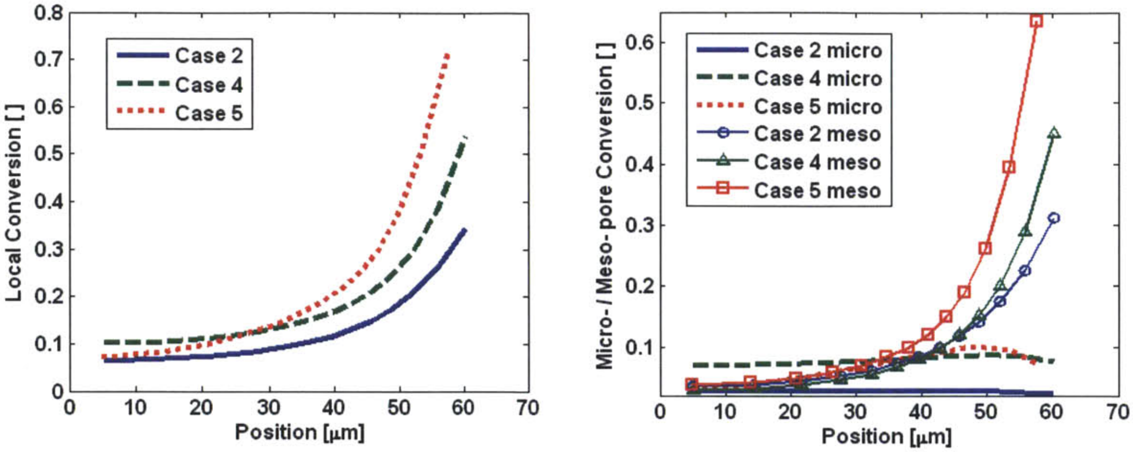

Figure 5.7. Final conversion profiles for (a) conversion on all pores and (b) conversion attributable to reaction on micro- and meso-pores.

The final conversion profiles (at *t*=0.102 s) are shown in Figs. 5.7(a) and (b). The total conversion profiles (Fig. 5.7(a)) suggest that overall, char consumption occurs in zone II, with reaction occurring throughout the particle, although to a much lesser extent in the interior. Cases 2 and 4, with 12% bulk oxygen, exhibit similar profiles, while case 5 has relatively less conversion near the particle interior. The attribution of conversion to reaction on the various pore sizes can be accomplished using Eq. (3.15). Figure 5.7(b) shows that the mesoporous surface area dominates the char consumption, due to the limitations on char oxidation in the micropores due to configurational diffusion. Char gasification occurs predominantly on the surface of the micropores, due to the assumed small configurational diffusion limitations and the large micropore surface area of Spherocarb.

Cases 2 and 4 exhibit micropore conversion profiles that are nearly constant with position (slightly higher toward the particle interior for case 2 and slightly lower toward the interior for case 4). The micropore conversion profile for case 5, on the other hand, decreases toward the particle center. The reason for this discrepancy can be inferred from Figure 5.8, which shows species mole fraction profiles for all species except nitrogen (so that the species with small mole fractions can be clearly seen), throughout the particle ($r < \approx 70$ μm) and the surrounding boundary layer. Due to the higher particle temperature achieved during case 5, even H_2O becomes mass-transport limited in the particle's interior, as its concentration approaches zero during the high-temperature period of case 5, which can be seen in Fig. 5.8(f). This is to be contrasted with cases 2 and 4, for which the steam mole fraction profiles do not approach zero toward the interior of the particle.

Figure 5.8 indicates that for all cases, the char-oxygen reaction is significantly transport-limited, while the gasification reactions are transport-limited to a much lesser extent. CO is the main by-product of char oxidation at these temperatures, which can be inferred from the comparison of the CO and CO_2 profiles throughout the particles. Figure 5.8(e) is the lowest temperature snapshot of the six case/time combinations shown in Fig. 5.8 and it is evident that the CO/CO_2 ratio decreases with temperature. Outside of the particles, homogeneous CO oxidation occurs which contributes to the small peak in CO_2 in the gas boundary layer. All species profiles indicate that concentration gradients in the boundary are much less severe than within the particle, although near the particle, O_2, H_2 and CO_2 are consumed via homogeneous reaction. In accordance with the simulation results of other researchers, all species mole fractions are continuous across the gas/porous medium interface, although the slopes exhibits a discontinuity due to the change in the governing flux sub-models [19,20,33].

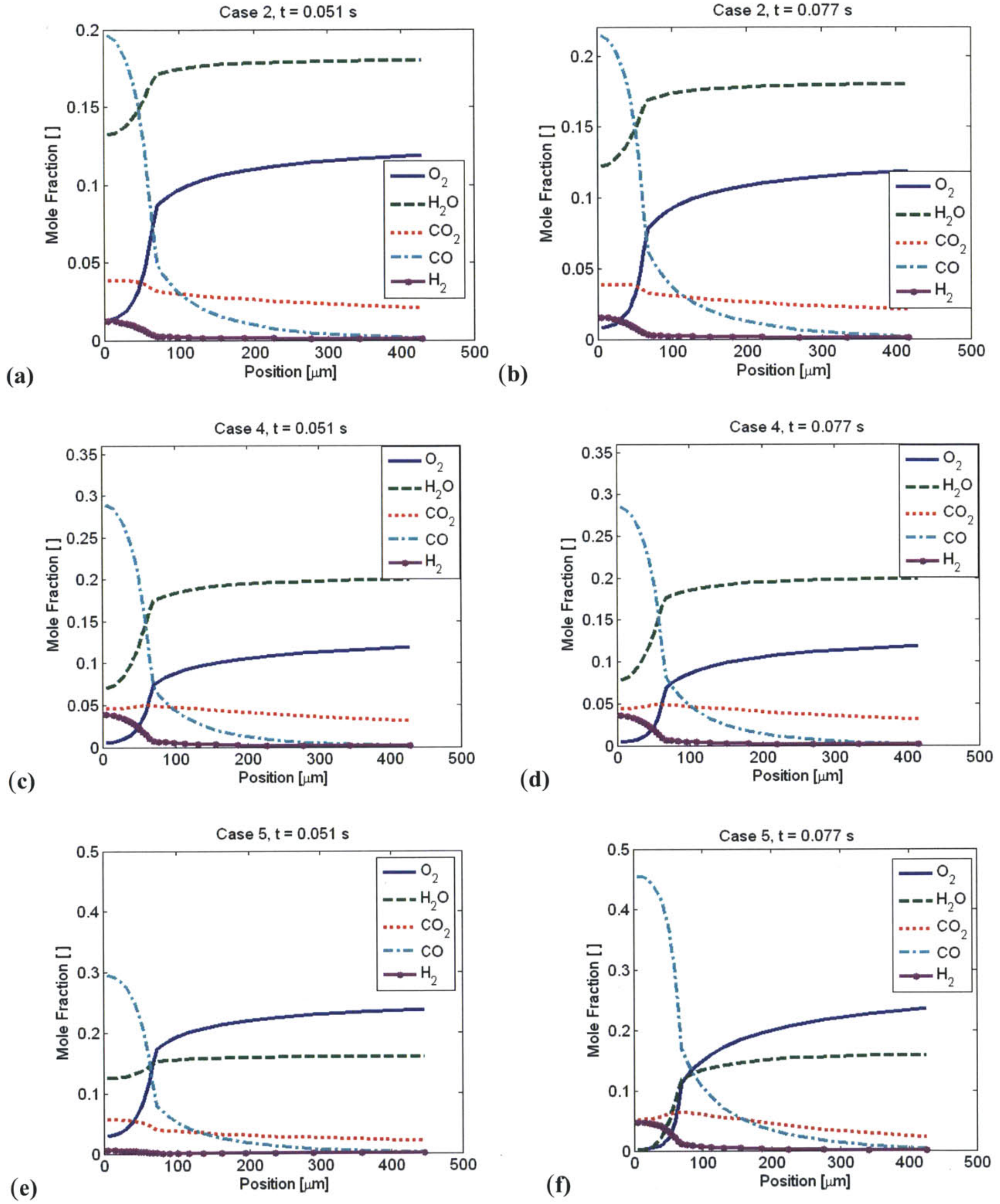

Figure 5.8. Species mole fraction profiles in and around burning Spherocarb particles, at two different times for (a)-(b): Case 2, (c)-(d): Case 4 and (e)-(f): Case 5.

Taken together, Figs. 5.5 and 5.6 provide a reasonable level of confidence in the overall model and in its ability to predict the behavior of well-characterized char particles subject to conditions in which multiple reactions occur in the regime of intra-particle diffusion limitations. This has been done without using fitting parameters to adjust the results to the measured data, although the σ parameters, representing the pore size at which configurational diffusion becomes significant, are not well-known and can have a significant influence on the simulations. This is particularly true in this case, because Spherocarb particles have such a large microporous surface area.

As mentioned in Ch. 3.6, the configurational diffusion parameter for the reaction of char with oxygen has been taken directly from the literature, although this was extracted in an indirect manner for a bituminous coal char reacting at 693 K. Since configurational diffusion is thought to be a temperature-dependent phenomenon, this adds another layer of uncertainty to the σ parameters. However, it has been shown experimentally that micropores are largely excluded from participation in both zone I and zone II char oxidation [34,35]. A numerical model of high temperature Spherocarb oxidation (100% oxygen) also reached the same conclusion [36]. For this reason, the constant value of $\sigma_{O_2} = 20\ nm$ is taken as a best-available estimate that qualitatively captures observed char oxidation behavior.

Also important to the simulation results, is the value of σ_{H_2O}, which is not available from the literature. Microporous diffusion limitations have been observed for char reacting with O_2 [13,35,37,38] and CO_2 [35,39] but we are not aware of reported configurational diffusion limitations for the reaction of char with H_2O. Researchers have reported enhanced surface area development during the reaction of the same char with CO_2 compared to O_2 [38,40], substantiating the hypothesis that configurational diffusion limitations for CO_2 are less severe than for O_2, although conflicting results also exist [35]. Upon reacting the same lignite char with O_2, CO_2 and H_2O, Harris and Smith found that the surface area developed at 30% conversion was 500, 600 and 976 m^2/g, for the three reactants, respectively, suggesting that H_2O reacts to a greater extent on smaller pores than does O_2 or even CO_2 [14]. The same qualitative order for configurational diffusion limitations is also supported by Walker [41] and the studies of Koresh [42], although there is disagreement in the literature regarding the facility with which CO_2 and H_2O may enter small pores [43].

Based on the lack of any qualitative information suggesting incomplete reaction of steam in char micropores and given the lack of quantitative information about σ_{H_2O} to use as input, this parameter was chosen such that in zone I, complete micropore penetration occurred and the intrinsic char-steam reaction rate was thus normalized by the entire surface area. The base-case simulations were performed with a value of $\sigma_{H_2O} = 1$ nm, which implied that even at the higher temperatures of Waters' data, *configurational* diffusion limitations were minimal. In summary, in the base-case, steam was assumed to have minimal configurational diffusion limitations at all temperatures, whereas oxygen was assumed to have negligible micropore participation at all temperatures due to slow configurational diffusion. CO_2 was assigned an intermediate value of $\sigma_{H_2O} = 5$ nm, qualitatively consistent with the experiments described in the preceding discussion.

At the higher temperatures of Waters' experiments, the variation of σ_{H_2O} can affect the results of the simulation. Due to the lack of quantitative information about this parameter, simulations were performed as σ_{H_2O} was varied from 1-5 nm (a range for which low temperature gasification still occurred throughout the micropore structure) in order to assess the impact it had on the conversion and temperature profiles. Figure 5.9 shows the effect of σ_{H_2O} on temperature and conversion for cases 2 and 5. For both cases, $\sigma_{H_2O} = 3\,\text{nm}$ yields results similar to $\sigma_{H_2O} = 1\,\text{nm}$. For the lower temperature experiment, case 2, the difference in particle conversion and temperature is small when using a value of $\sigma_{H_2O} = 5$ nm, but for case 5, such a change lowers the conversion at *t*=0.102 s from ~37% to ~32% and increases the particle temperature by roughly 100 K. This is due to the fact that the very large micropore surface area now participates to a smaller extent in the endothermic steam gasification reaction.

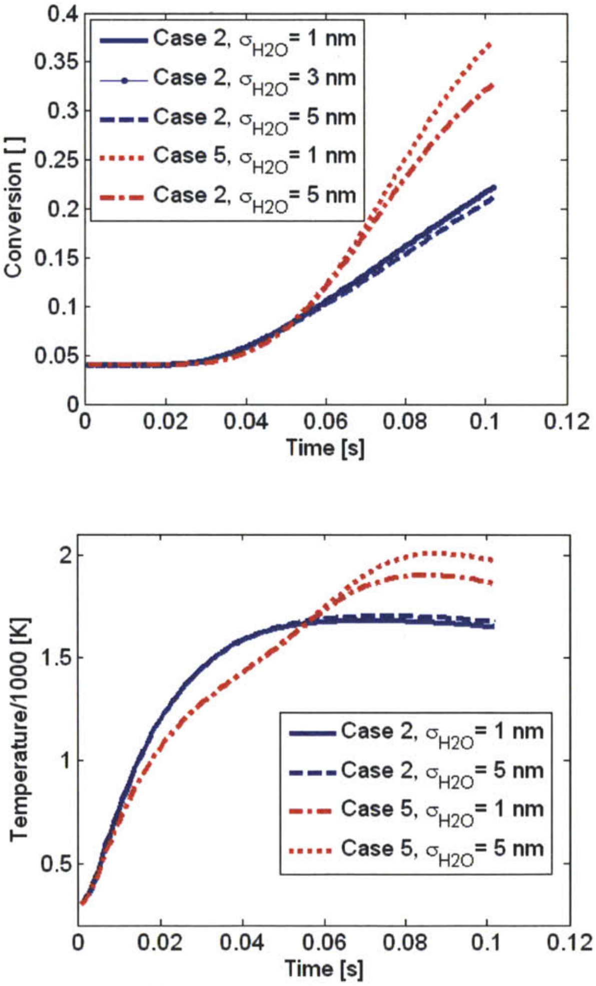

Figure 5.9. Effect of variation of σ_{H_2O} on conversion (top) and particle temperature (bottom) for cases 2 and 5.

Figure 5.10 shows final conversion profiles for these cases and indicates that the loss in overall conversion is mostly caused by decreased micropore conversion, since gasification reactions mostly occurs on micropores (at least when $\sigma_{H_2O} = 1\,\text{nm}$). This is to be expected since mesopores diffusion limitations are hardly affected by the value of σ_{H_2O}. Micropore conversion profiles are calculated from numerical integration of Eq. (3.15).

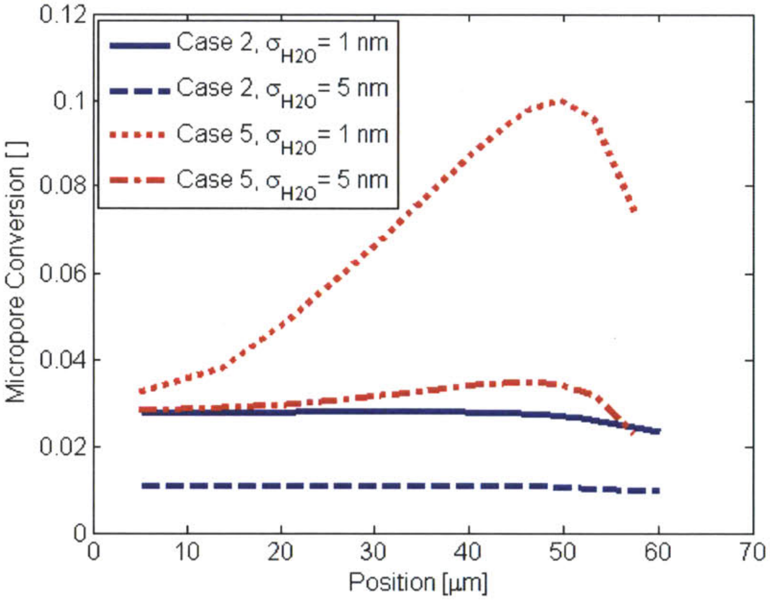

Figure 5.10. Effect of variation of σ_{H_2O} on micropore conversion profiles for cases 2 and 5.

Figure 5.11 shows the evolution of the normalized, total surface area with time for these cases. Upon increasing the configurational diffusion limitations, the surface areas decrease relative to the base cases, even though conversion is lower at a given time. This is because micropores now expand less, while still experiencing the same degree of overlap by larger pores.

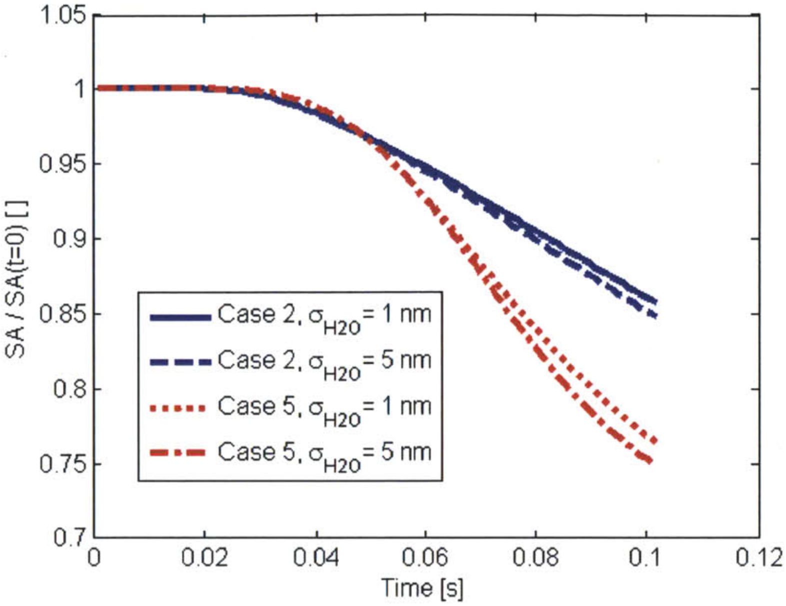

Figure 5.11. Effect of variation of σ_{H_2O} on surface area evolution for cases 2 and 5.

The impact of the pore structure evolution and the gasification reaction during these combustion simulations are illustrated in Figs. 5.12 and 5.13, which show conversion and particle temperature profiles, respectively, for case 2, using both the ARPM and the RPM, with and without accounting for the gasification reactions, for the base-case. In applying the RPM, all pore-scale effectiveness factors are set to unity and the reaction rate parameters are re-normalized accordingly. In other words, the *intrinsic* char oxidation reaction is much lower for the RPM, since the surface area on which it occurs is taken to be much larger. In this way, the initial apparent reactivity is identical for the RPM and ARPM, although the pore structure will evolve differently in the two cases.

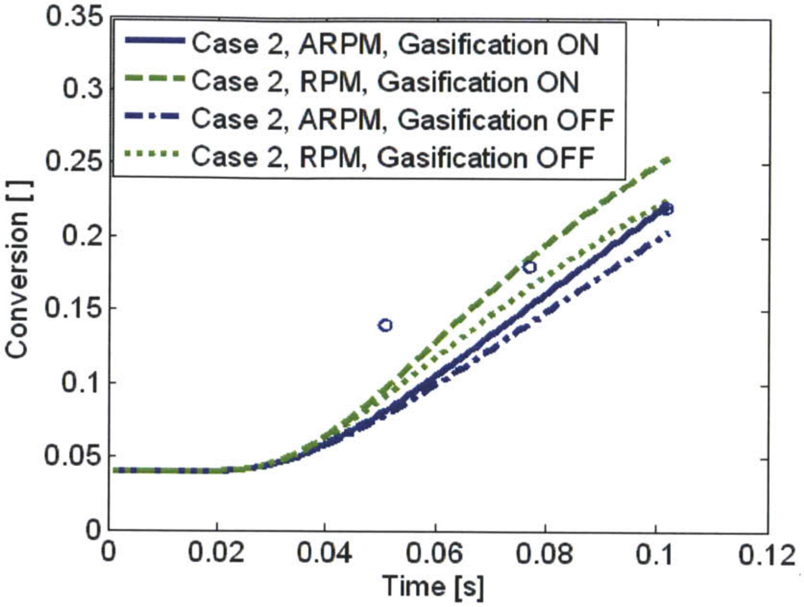

Figure 5.12. Conversion versus time for case 2, using the RPM and the ARPM, both of which with and without gasification reactions turned on.

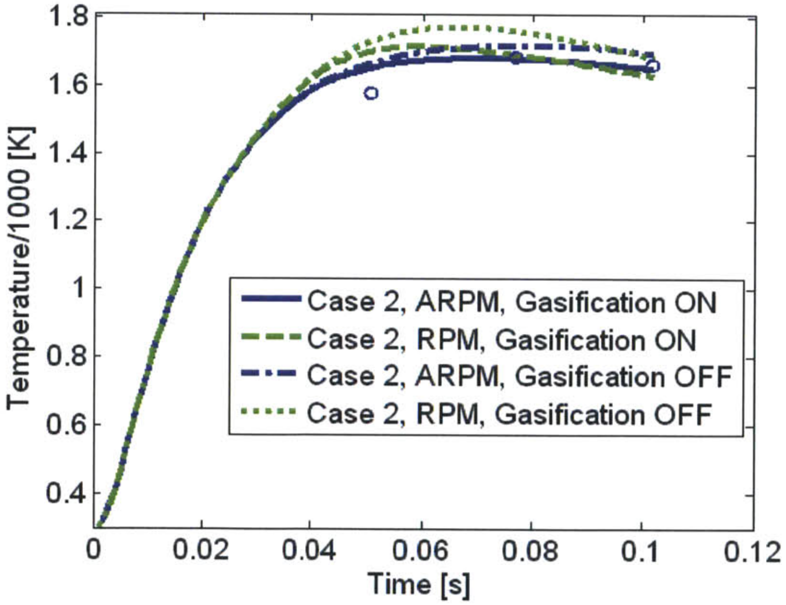

Figure 5.13. Particle temperature versus time, for case 2, using the RPM and the ARPM, both of which with and without gasification reactions turned on.

Figures 5.12 and 5.13 show that, in the case of the ARPM, neglecting the gasification reactions decreases conversion at t=0.102 s from 0.22 to 0.205 and increases particle temperature by a maximum of 40 K. For the RPM, these disparities are somewhat greater (0.255 to 0.225 and ~65 K). When using the original RPM, the conversion is higher for both cases (gasification on and off), respectively, than when using the ARPM. This is because the RPM allows all pore sizes to participate in all reactions fully and therefore the micropore growth (q_{micro}) is the same as the growth of all other pores (instead of experiencing mostly overlap), thus slowing the decrease in surface area with conversion experienced by the particle. This is evident from examination of Figure 5.14.

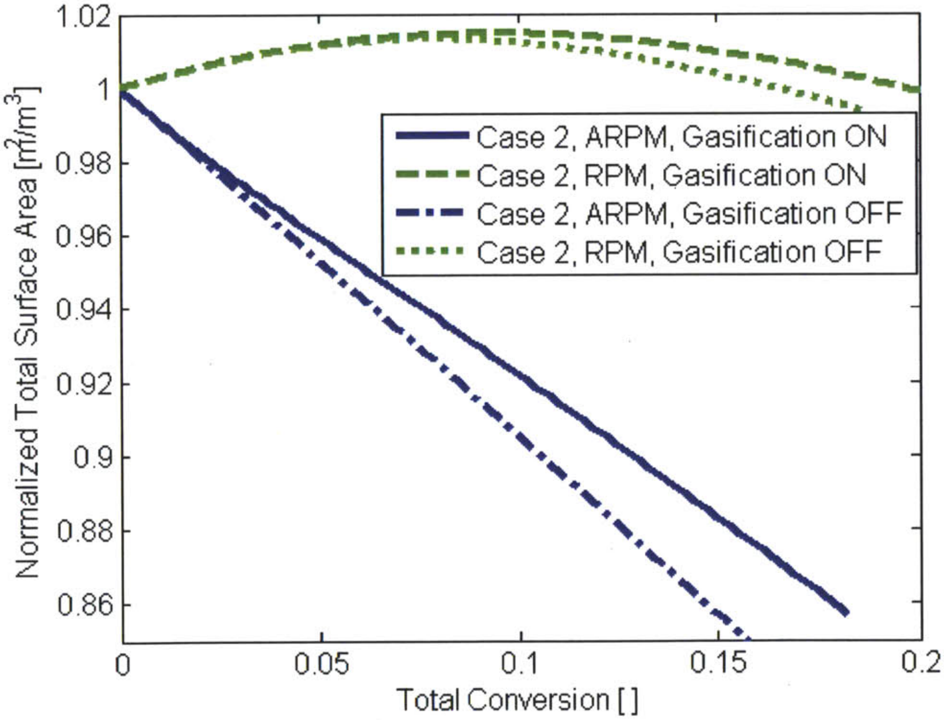

Figure 5.14. Normalized total surface area versus total conversion, for case 2, using the RPM and the ARPM, both of which with and without gasification reactions turned on.

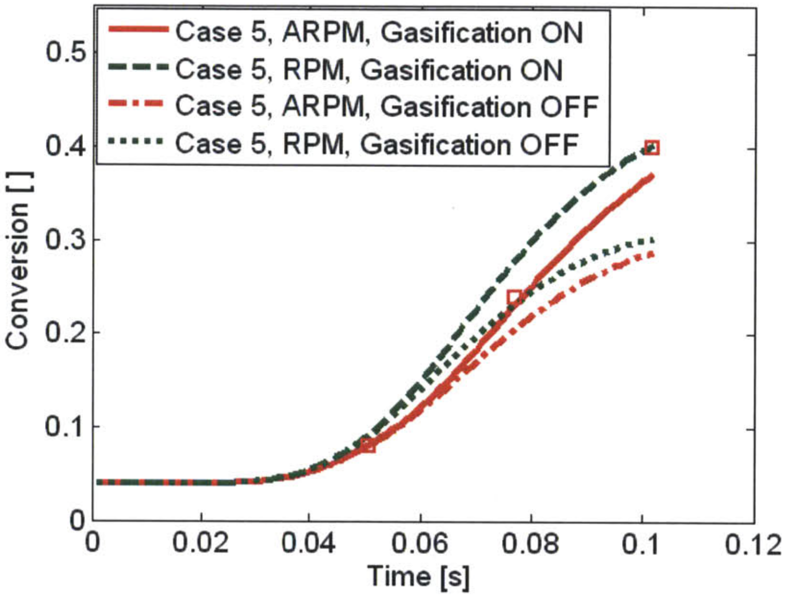

Figure 5.15. Conversion versus time for case 5, using the RPM and the ARPM, both of which with and without gasification reactions turned on.

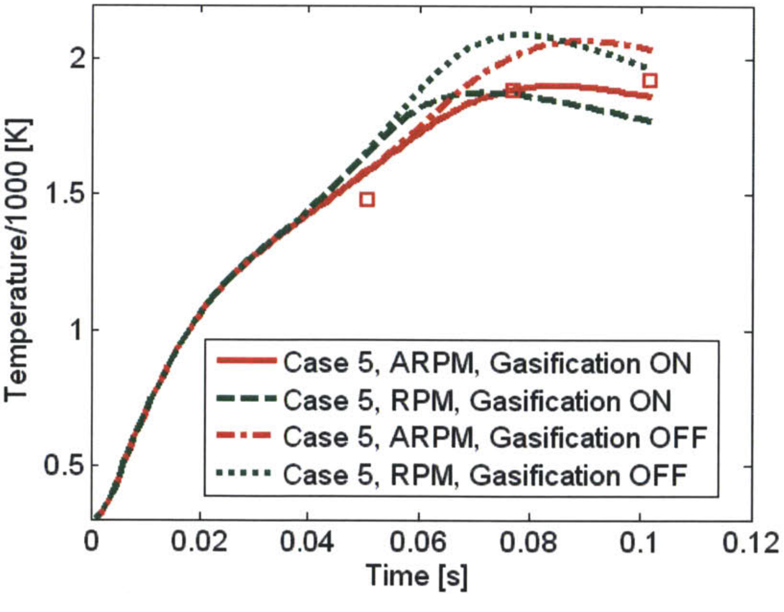

Figure 5.16. Particle temperature versus time, for case 5, using the RPM and the ARPM, both of which with and without gasification reactions turned on.

Figures 5.15 and 5.16 show the same plots for case 5. The trends regarding gasification described for case 2 also hold for case 5, but there is a larger difference in conversion and particle temperature between cases in which gasification is turned on and off. For the ARPM, neglecting gasification in case 5 decreases the conversion from 0.37 to 0.29 at *t*=0.102 s, while increasing char particle temperature by roughly 200 K, which is over 100 K above the measured temperatures. For the RPM, the differences are even greater. The steady-state char combustion simulations performed by Shaddix et al. report a similar qualitative trend [19]: at 1690 K, the total char consumption rate, which also accounts for concurrent steam gasification, increases as O_2 mole fraction increases from 0.12 to 0.24 to 0.36. This is in contrast to their results for concurrent CO_2 gasification, which they find increases the rate of char consumption for 12% O_2, while having a negligible and a negative influence on char consumption rates for 24% and 36% O_2, respectively [20]. The difference between the gasifying agents is attributed to the greater endothermicity of the $C+CO_2$ reaction.

Similar to Fig. 5.13, the particle temperature simulated with the RPM is initially higher than that calculated using the ARPM, but eventually becomes lower at a given time. (This trend is beginning to become apparent for case 2 but is clear for case 5.) Furthermore, the difference in conversion between the RPM and ARPM reaches a maximum and then begins to decrease as time progresses.

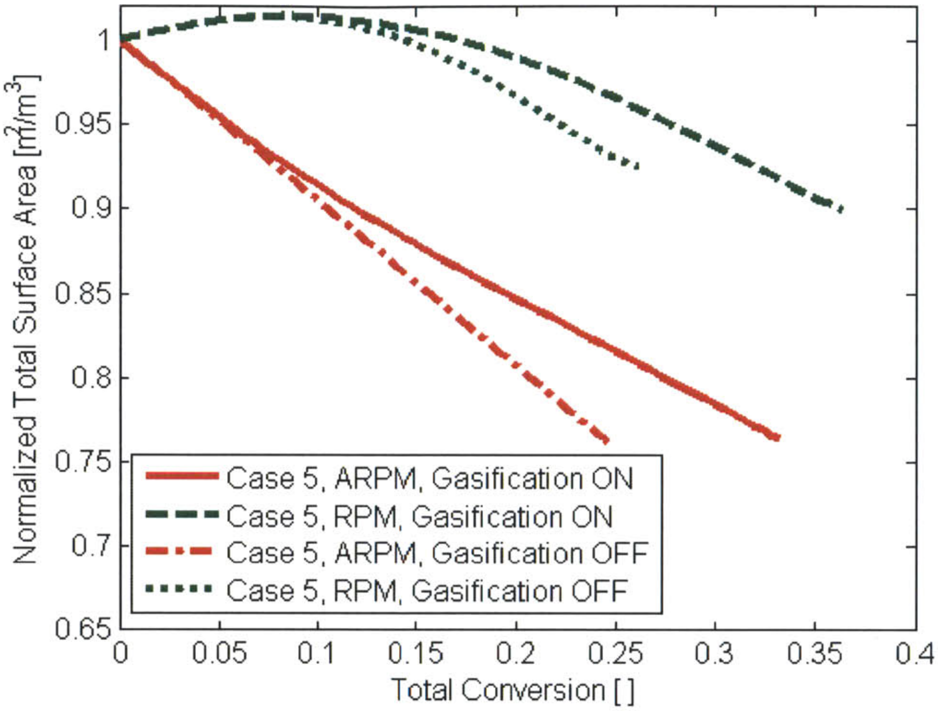

Figure 5.17. Normalized total surface area versus total conversion, for case 5, using the RPM and the ARPM, both of which with and without gasification reactions turned on.

The same qualitative observation as was made for case 2 in Figure 5.14 can be made regarding case 5, as shown in Figure 5.17. It is also worth mentioning that when gasification reactions are turned on, the surface area is larger in both cases. In the case of the RPM (in which all pore-scale effectiveness factors are unity anyway), the reason is that gasification reactions change the conversion profile within the particle, which affects dS_{Tot}/dX_{Tot}, even though the local dS/dX is identical everywhere. For the ARPM, this is due to the additional fact that, in contrast to oxidation, gasification occurs on the micropores to a degree, increasing the surface area compared to the case of pure oxidation.

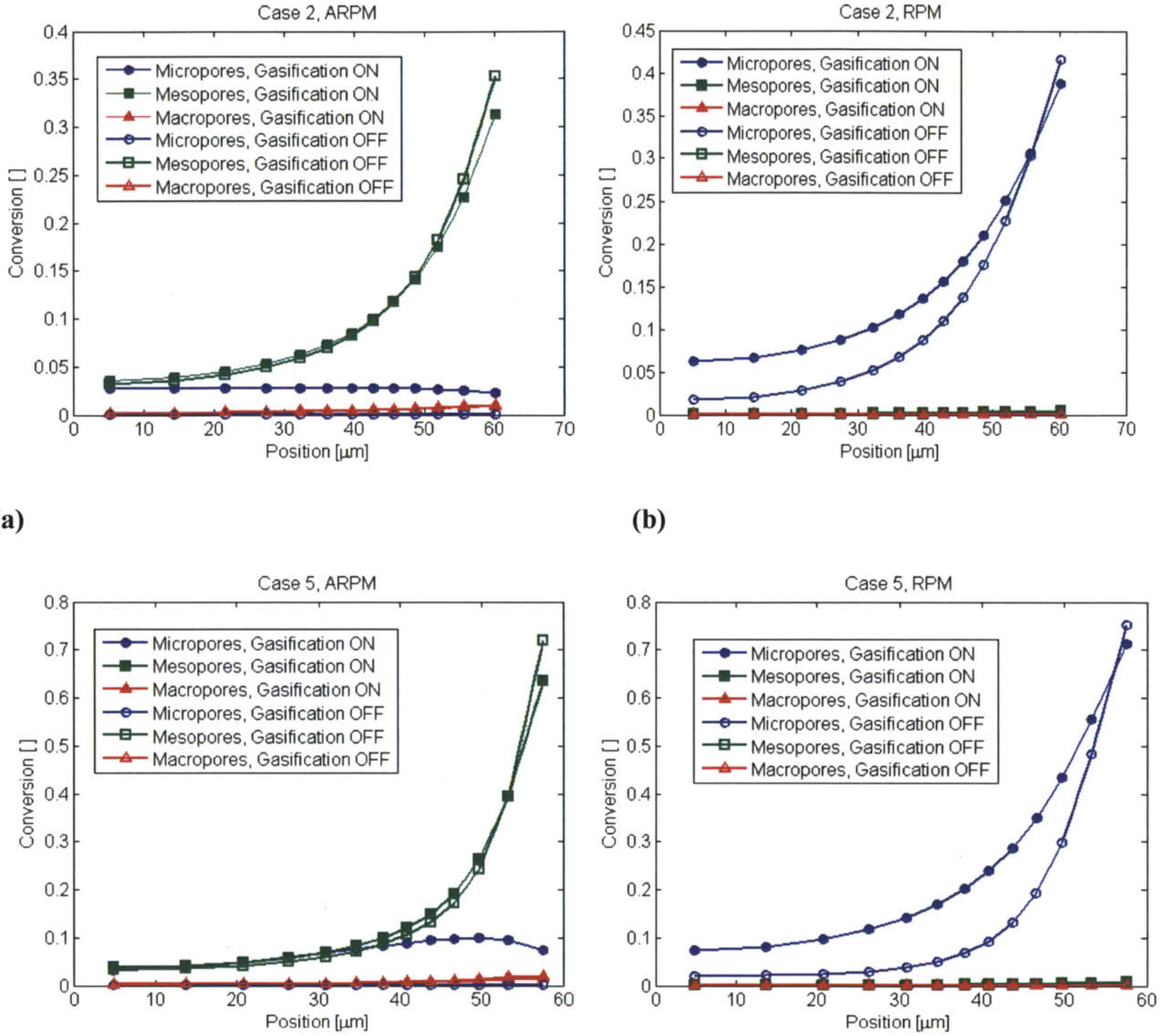

(a)

(b)

(c)

(d)

Figure 5.18. Conversion profiles, on micro-, meso- and macro- pores, with gasification reactions on and off, for (a) Case 2, using the ARPM, (b) Case 2, using the RPM, (c) Case 5, using the ARPM and (d) Case 5, using the RPM.

Figure 5.18 shows conversion profiles on each pore class for the ARPM and RPM, with gasification reactions both considered and neglected, at *t*=0.102 s, for cases 2 and 5. For the ARPM, when gasification reactions are considered, it is indeed seen that micropores are able to participate in char conversion, due to the ability of H_2O, in contrast to O_2, to react on small pores. Furthermore, the total conversion profile within the particle is more uniform when gasification reactions are considered because H_2O and CO_2 experience fewer diffusion limitations than O_2. When gasification reactions are neglected, micropore conversion is negligible. Conversion is confined to the outer regions of the particle to a greater extent for case 5 than it is for case 2. When using the RPM, it is safe to assume that all conversion occurs on the micropores for Spherocarb char.

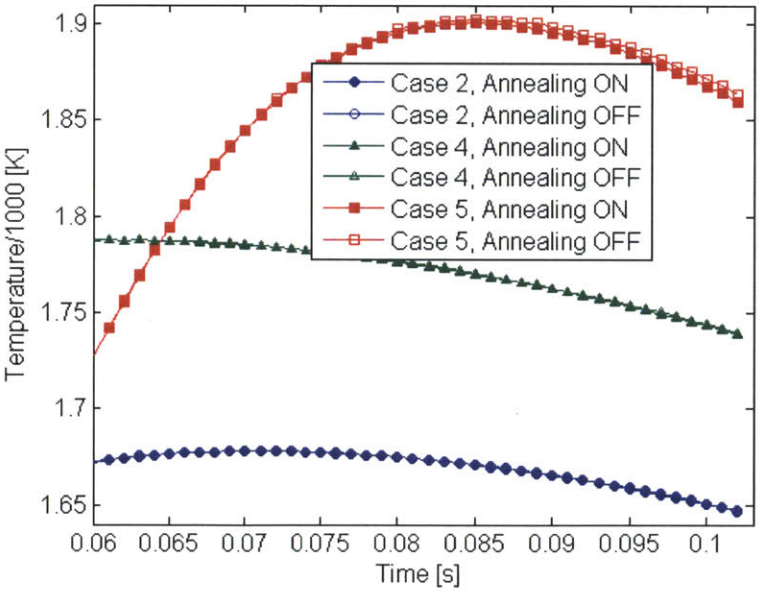

Figure 5.19. Calculated particle temperature for cases 2, 4 and 5, each with the concurrent annealing sub-model turned on and off.

Finally, the impact of the *concurrent* annealing sub-model was evaluated in Figs. 5.19 and 5.20. Figure 5.19 shows the particle temperatures for the three cases with and without the annealing sub-model. When the model was turned off, the reaction rates are simply decreased by a fraction equal to the amount of annealing experienced during the production of Spherocarb, whereas when the annealing model is turned on, the entire heat treatment (production and concurrent combustion) is considered. Figure 5.19, which shows the particle temperatures late in the simulations, indicates that there is practically no need to consider concurrent annealing in the present experiments/simulations. This is due to the fact that the production heat treatment that has been included (Table 5.4) occurs over a much longer period of time than do the experiments of Waters et al. [1,2].

Despite the high temperatures achieved, the fraction of active sites that are deactivated during combustion is at most (case 5 in Figure 5.20(c)) a few percentage points below the post-production/pre-combustion value. Nonetheless, this would not necessarily have been known *a priori*, because the annealing model and fraction of active sites remaining is dependent on the temperature-time history achieved during combustion.

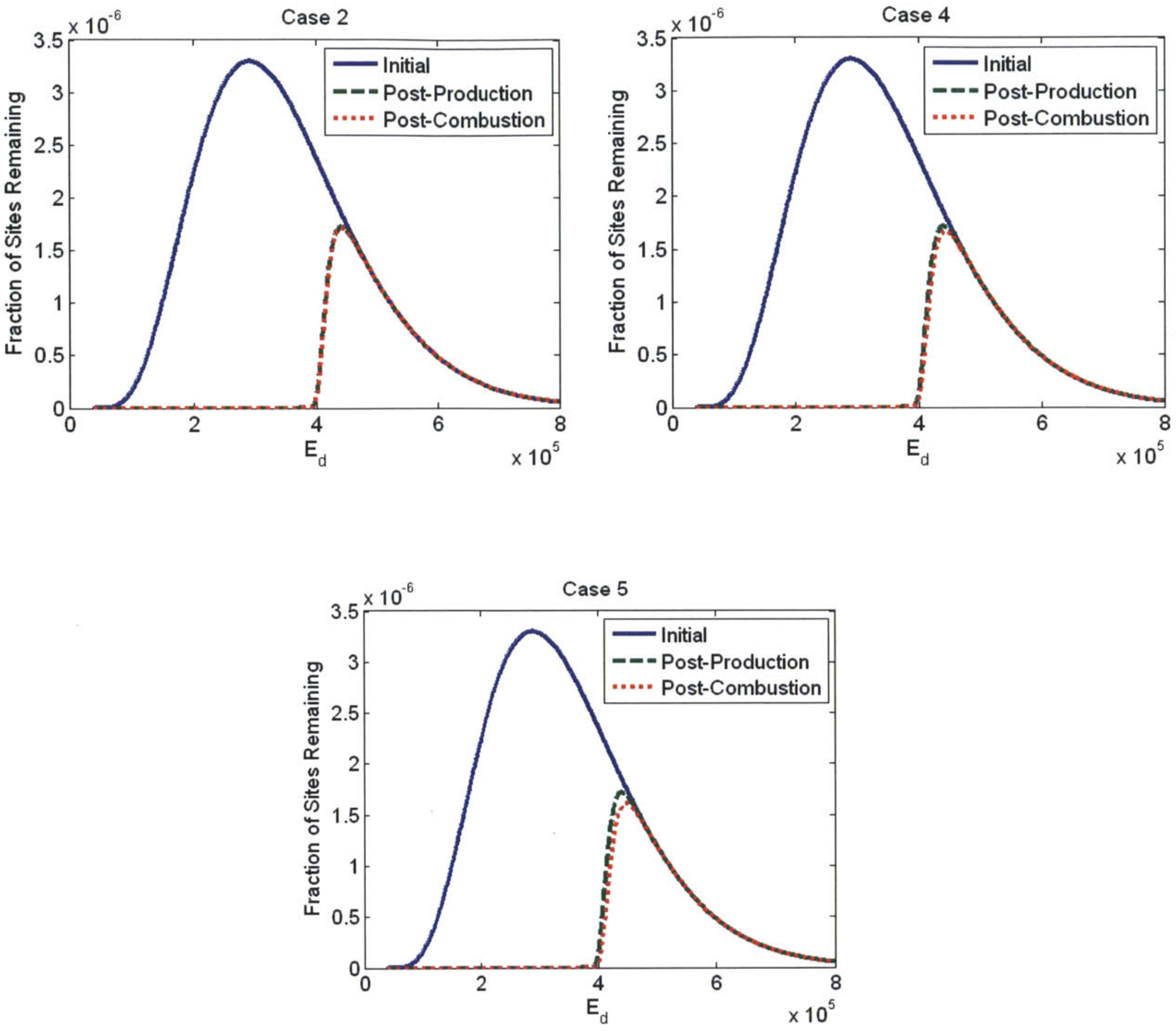

Figure 5.20. Distribution of fraction of active sites remaining after Spherocarb production and after the simulated particle temperature time history, for (a) Case 2, (b) Case 4 and (c) Case 5.

5.4. Effect of Flux Model

When using the Feng and Stewart model, the flux in the micropores may not satisfy the smooth field hypothesis in the presence of fast reactions (e.g. oxidation), as mentioned in Ch. 2, and the correction of Jackson is not applicable in this case [44]. As also mentioned by Jackson, the contribution of the micropore flux is typically small compared to transport in other pore sizes. A comparison of simulations of case 2 employing the FSM with and without accounting for the micropore contribution to the fluxes was performed. The difference in the overall conversion results is negligible; they are identical to the third decimal place.

The Feng and Stewart model explicitly accounts for multi-modal pore structures, while the Dusty Gas model uses an average pore size and porosity in its calculation of the parameters characterizing continuum diffusion, viscous flow and Knudsen diffusion contributions. Without the ability to perform experiments to determine the values of the adjustable parameters in the DGM, determining a representative average pore size for an *evolving*, multi-modal pore structure may be problematic. Some investigators have assumed that reaction occurs solely on the micropores, due to their large surface area, while the gas transport occurs solely via the macropores [45,46].

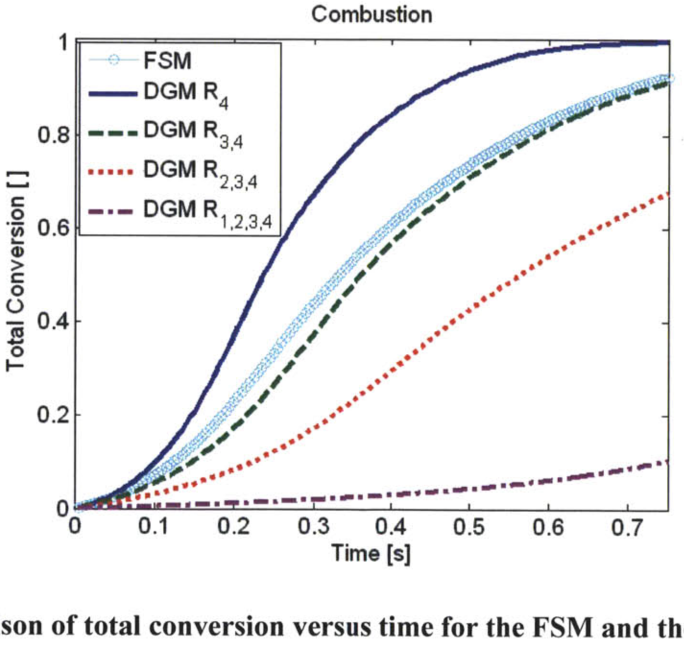

Figure 5.21. Comparison of total conversion versus time for the FSM and the DGM using several calculations of the average pore size, for combustion conditions.

Figure 5.21 compares the integrated char conversion profiles for a 60 μm radius particle with the properties of "Char B" from Su and Perlmutter [10], with its pore size discretized into four bins (micropores (R_1), small mesopores (R_2), large mesopores (R_3) and macropores (R_4)) as in [7] and as shown in Table 5.6, undergoing combustion in an environment of 21% O_2 and 78% N_2 at 1400 K and atmospheric pressure, using the FSM and the DGM. The tortuosity required by the DGM is set to three, in accordance with the FSM of $\kappa = 1/3$.

Table 5.6. Discretized pore size distribution for "char B".

R_i (Å)	7.1	40	90	1877
ϕ_i	0.1089	0.016	0.015	0.1483

The average pore radius in the DGM has been obtained by taking the hydraulic radius, $r_h = 2\phi/S$, where the porosity and surface area include contributions from different pore sizes, as indicated in the legend of Fig. 5.21. All other model parameters are identical, and the ARPM has been applied in both cases.

It is observed that inclusion of the micropores in the calculation of r_h produces results that differ significantly from the predictions of the FSM, while calculation of r_h by including all macropores and large mesopores produces a result most similar to the FSM predictions. Figure 5.21 was obtained for a situation in which intra-particle diffusion limitations were deemed significant throughout the course of conversion, based on the profiles of the reactants and products throughout the porous structure.

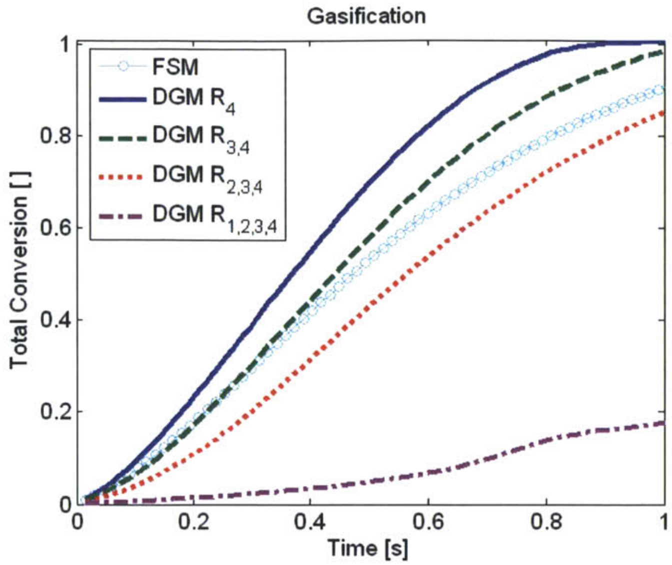

Figure 5.22. Comparison of total conversion versus time for the FSM and the DGM using several calculations of the average pore size, for gasification conditions.

Figure 5.22 shows an identical plot for gasification conditions. The char structure is the same as that of Figure 5.21, but the environment consists of 10% H_2O, 40% CO_2 and 50% N_2 at 1900 K and atmospheric pressure. The results are somewhat different than Fig 5.21 in that the FSM is closest to the DGM with r_{avg} based on the two largest pore sizes, but later in conversion, the results from the FSM begin to approach that of the DGM with r_{avg} based on the three largest pore sizes. In fact, both figures indicate that the FSM yields a conversion that increases less rapidly than the DGM later in conversion.

These figures indicate that the practice of using the DGM for calculation of the fluxes by excluding the micropores and small mesopores yields results similar to the slightly more complex Feng and Stewart model, which explicitly considers each pore size separately. The reason for the distortion of the results of the DGM by including the micropores is due to their large contribution to the surface area, which drastically reduces the average pore radius parameter, whereas neglecting all the mesopores in the calculation results in fluxes that are too large. This is not to say, of course, that either model is "correct."

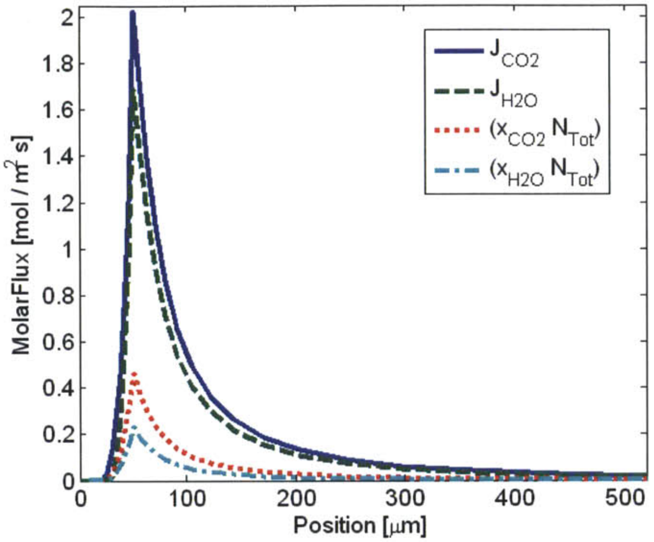

Figure 5.23. Diffusive and convective fluxes of CO_2 and H_2O in and around a char particle in a gasifying environment.

Figure 5.23 examines the molar fluxes in and around a 50 μm radius char particle, also using char B with the same discretized pore size distribution, reacting in a gasification environment of 10% H_2, 20% H_2O, 20% CO, 40% CO_2 (and 10% N_2) at 1800 K, at an overall conversion of 5%, using the FSM. To assess the magnitude of the convective term, the molar fluxes, for both gasifying agents, are divided into their diffusive (J_j) and convective (x_jN_{Tot}) contributions. For these conditions, the convective contribution to species transport in the boundary layer is about 13% and 21% of the contribution of diffusive transport for H_2O and CO_2, respectively, while within the particle, the convective contribution to species transport varies with position but tends to be somewhat larger. The convective term should not be omitted from simulations of char consumption, especially for fast heterogeneous reactions.

5.5. Demonstration of Ash Adherence Sub-model

As mentioned in Ch. 2, previous investigators have examined the effects of concurrent annealing and of fragmentation on the overall burnout behavior and dynamic temperature response of char particles. Here we show results of the comprehensive model with the ARPM, FSM, concurrent annealing, *particle shrinkage* and *ash layer sub-models* included, to illustrate the capabilities of the present model with regard to prediction of char and ash layer evolution. Of course, the true behavior of the ash layer and char particle size require experimental determination; the results presented here are simply to exhibit the capability of the model in this regard.

The simulated char particle is again sample B from Su and Perlmutter [10], the porosity of the macropores is increased to 0.54, a high-ash coal char is examined (10% by volume) and a base-case ash melting temperature is taken as 1450 K. The rate at which the porosity of the ash layer decreases when its temperature is above T_{melt}, in Eq. (2.45), is taken to be $\Upsilon=0.4$ (1/s). The particles react in a uniform environment of 14% O_2 and 5% H_2O with a bulk gas temperature of 1500 K and a wall temperature of 1000 K with which the particles interact radiantly. The particle emissivity is again taken as 0.85. The conditions were such that the particles reacted in the regime of mixed reaction/pore-diffusion control. The critical char porosity is 95%, which means that some char is left in the ash layer and is assumed to be encapsulated.

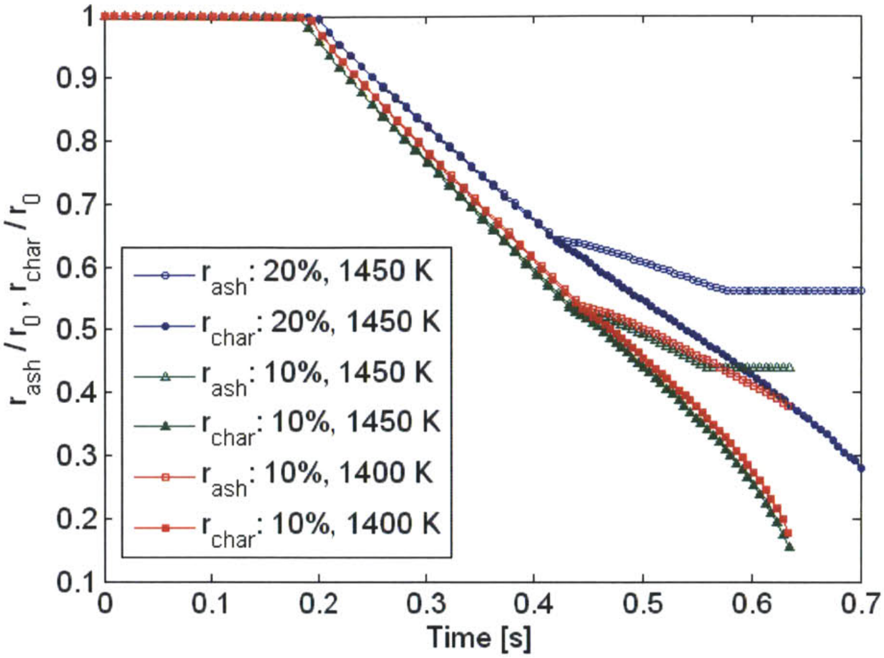

Figure 5.24. Evolution of normalized ash (open symbols) and char (closed symbols) radii with time for three combinations of ash "melting temperature" and ash volume fraction.

Figure 5.24 shows the evolution of the outer particle dimension, $r_{ash}(t)$, and the char radius, $s(t)$, with time for three cases: the base-case of 10% ash, T_{melt}=1450 K, a case with a higher ash content (20%) and the same melting temperature and a case with a lower melting temperature (1400 K) but the same ash content (10%). These chars contain a high, but not unrealistic [47], fraction of ash, to highlight the differences between the cases.

When the chars reach their critical porosities, diameter reduction begins and when the critical ash coverage on the surface reaches 50%, the ash layer is assumed to constitute its own layer, with the open and closed symbols diverging for each case. This occurs earlier for the case with higher ash content (20%), but the same case exhibits lower temperatures, as shown in Fig. 5.25, and also slower conversion, due to the increased diffusion resistance from the increased ash content.

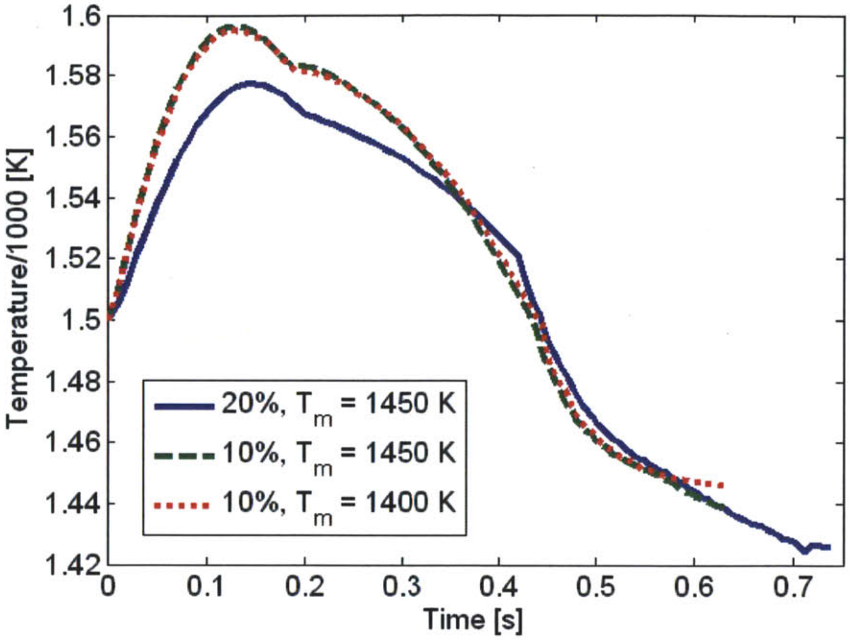

Figure 5.25. Particle temperature versus time for the same three combinations of ash "melting temperature" and ash volume fraction.

Compared to the base-case, the case with the lower ash melting temperature (1400 K) exhibits a continual decrease in both $r_{ash}(t)$ and $s(t)$, since the particle temperature remains above the melting temperature throughout conversion. For both cases with a melting temperature of 1450 K, the particle's temperature eventually falls below the melting temperature and the ash layer ceases its densification, causing $r_{ash}(t)$ to flatten out while $s(t)$ continues to decrease.

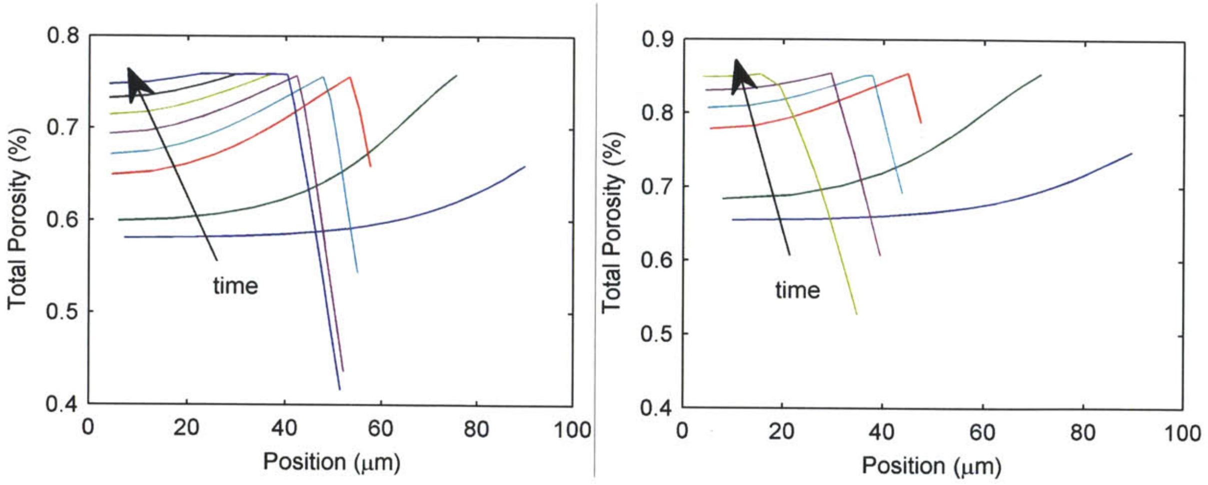

Figure 5.26. Total Porosity profiles throughout conversion for (a) 20% ash, T_m=1450 K particle, and (b) 10% ash, T_m=1400 K particle.

Figure 5.26 shows the total porosity profiles, which account for the presence of both ash and char, for the cases with 20% ash, T_{melt}=1450 K and 10% ash, T_{melt}=1400 K. It is observed in Fig. 5.26(a) that the porosity profile in the ash layer eventually ceases to change with time as the particle's ash layer temperature decreases below the melting temperature and ash densification stops, while this is not the case in Fig 5.26(b), since the melting temperature is lower and the particle temperature higher (above T_{melt}) in this case. It is also observed that the porosity of the ash layer, in Fig 5.26(a), decreases below the values observed in Fig 5.26(b), because the ash layer has had a longer time to undergo densification, since the higher ash content leads to a faster buildup of ash on the surface.

5.6. Conclusions

The comprehensive single particle char consumption model developed in previous chapters has been validated using zone II combustion data for Spherocarb char without the use of fitting parameters (although the configurational diffusion parameters employed were based on best-estimates) and reasonable agreement with experimental measurements of particle temperature and conversion have been obtained. For this char, the participation of various pore sizes in reaction and the occurrence of gasification reactions in certain combustion conditions are shown to have non-negligible effects on the overall conversion and temperature evolution. An examination of the impact of the flux sub-model was performed and it has been shown that inclusion of the micropores in the average pore radius of the DGM produces results very dissimilar to those of the FSM. Examples of high-ash char particles reacting in an environment of 14% O_2 and 5% H_2O near the ash melting temperature have been used to illustrate the full capabilities of the model in calculating the size and porosity of both char and ash layers.

References

[1] B.J. Waters, R.G. Squires, N.M. Laurendeau, R.E. Mitchell, Combustion and Flame 74 (1988) 91-106.

[2] B.J. Waters, R.G. Squires, N.M. Laurendeau, Combustion Science and Technology 62 (1988) 187-209.

[3] M. D'Amore, L. Tognotti, A. Sarofim, in:, ACS Fuels Division, 1991, pp. 939-949.

[4] M. D'Amore, L. Tognotti, A.F. Sarofim, Combustion and Flame 95 (1993) 374-382.

[5] M. D'Amore, F.P. Di Maio, P.G. Lignola, S. Masi, Combustion Science and Technology 89 (1993) 71-82.

[6] G.R. Gavalas, Combustion Science and Technology 24 (1981) 197-210.

[7] S.L. Singer, A.F. Ghoniem, Energy and Fuels 25 (2011) 1423-1437.

[8] J.K. Floess, The Effect of Calcium on the Gasification Reactions of Carbon, M.I.T., 1985.

[9] R.H. Hurt, Chemical and Physical Phenomena Determining Carbon Gasification Reactivity, M.I.T., 1987.

[10] J.L. Su, D.D. Perlmutter, AIChE Journal 31 (1985) 973-981.

[11] R.H. Hurt, A.F. Sarofim, J.P. Longwell, Energy & Fuels 5 (1991) 290-299.

[12] J.K. Floess, J.P. Longwell, A.F. Sarofim, Energy and Fuels 2 (1988) 18-26.

[13] P. Salatino, O. Senneca, S. Masi, Carbon 36 (1998) 443-452.

[14] D.J. Harris, I.W. Smith, Symposium (International) on Combustion 23 (1990) 1185-1190.

[15] W.K. Chi, D.D. Perlmutter, AIChE Journal 35 (1989) 1791-1802.

[16] R.H. Hurt, B.S. Haynes, Proceedings of the Combustion Institute 30 (2005) 2161-2168.

[17] D.G. Roberts, D.J. Harris, Fuel 86 (2007) 2672-2678.

[18] D.G. Roberts, D.J. Harris, Energy & Fuels 26 (2012) 176-184.

[19] C.R. Shaddix, E.S. Hecht, M. Geier, A. Molina, B.S. Haynes, The 35th International Technical Conference on Clean Coal & Fuel Systems (2010).

[20] E.S. Hecht, C.R. Shaddix, A. Molina, B.S. Haynes, Proceedings of the Combustion Institute 33 (2011) 1699-1706.

[21] P.L. Walker, F. Rusinko Jr., L.G. Austin, in:, D.. Elwey, P.W. Selwood, P.B. Weisz (Eds.), Advances in Catalysis, Vol XI, 1959, pp. 133-221.

[22] S.S. Hla, D. Harris, D. Roberts, Gasification Conversion Model-PEFR: Research Report 80, 2007.

[23] L. Tognotti, J.P. Longwell, A.F. Sarofim, Symposium (International) on Combustion 23 (1990) 1207-1213.

[24] R.H. Hurt, D.R. Dudek, J.P. Longwell, A.F. Sarofim, Carbon 26 (1988) 433-449.

[25] P. Salatino, O. Senecca, Third European Combustion Meeting (2007) 1-15.

[26] T. Livneh, E. Bar-ziv, O. Senneca, P. Salatino, Combustion Science and Technology 153 (2000) 37-41.

[27] A. Zolin, A. Jensen, K. Dam-Johansen, Proceedings of the Combustion Institute 28 (2000) 2181-2188.

[28] W. McLean, D.R. Hardesty, J.H. Pohl, Symposium (International) on Combustion 18 (1981) 1239-1248.

[29] R.E. Mitchell, Combustion Science and Technology 53 (1987) 165-186.

[30] J.J. Murphy, C.R. Shaddix, Combustion and Flame 144 (2006) 710-729.

[31] A. Molina, C.R. Shaddix, Proceedings of the Combustion Institute 31 (2007) 1905-1912.

[32] C.R. Shaddix, A. Molina, Proceedings of the Combustion Institute 32 (2009) 2091-2098.

[33] G. Ballal, C.-hsien Li, R. Glowinski, N.R. Amundson, Computer Methods in Applied Mechanics and Engineering 75 (1989) 467-479.

[34] I. Kulaots, I Aarna, M. Callejo, R.H. Hurt, E. Suuberg, Proceedings of the Combustion Institute 29 (2002) 495-501.

[35] I. Kulaots, A. Hsu, E.M. Suuberg, Proceedings of the Combustion Institute 31 (2007) 1897-1903.

[36] V. Cozzani, L. Petarca, S. Pintus, L. Tognotti, Combustion and Flame 103 (1995) 181-193.

[37] G. Ballal, K. Zygourakis, Ind. Eng. Chem. Res. 26 (1987) 1787-1796.

[38] B. Feng, S.K. Bhatia, Carbon 41 (2003) 507-523.

[39] R.H. Hurt, A.F. Sarofim, J.P. Longwell, Fuel 70 (1991) 1079-1082.

[40] O. Senneca, P. Salatino, S. Masi, P.V. Tecchio, Fuel 77 (1998) 1483-1493.

[41] P.L. Walker, Carbon 34 (1996) 1297-1299.

[42] J. Koresh, A. Soffer, Journal of the Chemical Society, Faraday Transactions 1 76 (1980) 2457-2471.

[43] J. Alcanizmonge, Carbon 35 (1997) 1665-1668.

[44] R. Jackson, Transport in Porous Catalysts, Elsevier, New York, 1977.

[45] S.V. Sotirchos, N.R. Amundson, AIChE Journal 30 (1984) 537-549.

[46] J.I. Morell, N.R. Amundson, S.K. Park, Chemical Engineering Science 45 (1990) 387-401.

[47] R.C. Everson, H.W.J.P. Neomagus, H. Kasaini, D. Njapha, Fuel 85 (2006) 1076-1082.

Chapter 6. Applications of the Single Particle Char Consumption Model

In this chapter, the single particle model is applied to study char consumption in oxy-combustion and entrained flow gasification environments. The majority of the chapter is devoted to oxy-combustion, specifically, to an examination of the importance of accounting for gasification reactions under oxy-combustion conditions. The importance of accounting for annealing during entrained flow gasification modeling is also highlighted.

6.1. The Influence of Gasification Reactions during Oxy-Combustion

6.1.1. Introduction

Oxyfuel combustion of pulverized coal is one of three major carbon capture technologies that can be used with coal-fired power plants and has been the subject of significant research over the past three decades [1–4]. During oxyfuel combustion, pulverized coal is burned using nearly pure oxygen from an air separation unit, while recycled flue gas is used to moderate the combustion temperature in order to maintain heat transfer and combustion characteristics similar to those encountered in conventional air-fired combustion environments.

Recent experimental and modeling studies have investigated the effects of CO_2 (and H_2O) on char combustion/gasification under oxy-fired combustion conditions, in which the CO_2 partial pressure is significantly higher than that in conventional air-fired combustion [5–11]. The elevated levels of CO_2 may influence char combustion via the reduced diffusivity of oxygen in CO_2 [7,10]; its higher specific heat; the endothermicity of the gasification reactions and their contribution to the char consumption rate [5,8,11,12]. Because reactions may occur in different limiting regimes depending on the temperature, bulk oxygen concentration, coal rank and particle size, the char conversion rate in O_2/CO_2 may be higher or lower than in O_2/N_2. Chen et al. [3] reviewed oxyfuel coal combustion experiments and classified the operating conditions into three regimes. At low temperatures, the presence of CO_2 does not change the char consumption rate because of the slow gasification kinetics; at high temperatures and sufficiently high O_2 mole fractions, where oxidation is diffusion-limited, the char consumption rate is lower because of the lower diffusivity of O_2 in CO_2; at high temperatures and lower O_2 mole fractions, the char-CO_2 gasification reaction can increase the char consumption rate.

Hecht et al. [13] reviewed the experimental literature and performed single char particle simulations of oxyfuel combustion and emphasized the uncertainty and variability of the CO_2 gasification rate. Using a detailed mechanism for char and CO oxidation and a single-step expression for char gasification, they performed single particle simulations at 1724 K and at oxygen mole fractions of 12, 24 and 36% to obtain steady-state species and temperature profiles and char consumption rates. For their simulation conditions, and for the entire range of pre-exponential factors evaluated, the gasification reaction increased the rate of char consumption at O_2 mole fractions below 24%, beyond which it slightly decreased the rate, because the lower particle temperatures that result from the endothermic gasification reactions reduced the rate of char oxidation.

The detailed char modeling studies referenced above [7,8,13] were performed using time-independent boundary conditions and assuming steady-state. However, in a furnace or utility boiler, all particles experience time-dependent boundary conditions along their trajectories as they undergo conversion. Depending on the coal rank and burner setup, the oxygen mole fraction and surrounding gas temperatures can vary significantly during a particle's lifetime as it penetrates the volatile flame zone and traverses the post-flame region. It is important to study the transient char consumption behavior under realistic, time-dependent boundary conditions in order to ascertain the effect of gasification reactions in practical oxyfuel combustion systems.

In what follows, the effects of char gasification reactions are investigated throughout conversion using realistic boundary conditions present during oxyfuel combustion. Coal particle time-dependent boundary conditions are tracked in a CFD simulation [14] of a 100 kWth pilot scale test facility, and representative regions and trajectories are identified. The comprehensive, time-dependent, single-particle char consumption model is then used to investigate the effect of the gasification reactions on char particle consumption for three representative regions, as well as for two typical particle trajectories identified within the furnace.

6.1.2. CFD Modeling of a Pilot-Scale Oxyfuel Coal Combustion Test Facility

Andersson and coworkers [15,16] conducted a series of experiments using the Chalmers 100 kW_{th} test facility under air-fired and oxyfuel combustion conditions. In a previous study [14], a 3D CFD approach was used to simulate the flow-field, heat transfer and gas and solid phase combustion under air-fired and oxyfuel conditions. The simulation successfully predicted the volatile flame shape near the burner, and the results agreed reasonably well with experimental measurements in terms of temperature and major species distributions.

The geometry and operating conditions of the pilot-scale oxyfuel combustion test facility were given in [16]. The facility consists of a gravimetric coal feeder, a swirl burner, a cylindrical refractory-lined furnace with an inner height of 2.4 m and an inner diameter of 0.8 m, a fabric filter and a flue gas recycle system. The coal burner consists of a fuel lance (i.d.=34 mm), surrounded by cylindrical primary and secondary feed-gas registers. The primary register is swirled with a fin angle of 45° and has an outer diameter of 52 mm, whereas the secondary register has a more moderate swirl number with a fin angle of 15° and outer diameter of 92 mm. A German lignite coal (Lausitz) was used in the experiments. Four different cases were investigated [15,16]: an air-fired case and three oxyfuel combustion cases with decreasing flue gas recycle rates. The oxygen mole fractions were 25%, 27% and 29% in both the primary and secondary streams. The current study focuses on the case with 29% oxygen, which has the highest oxygen concentration and most stable combustion characteristics.

6.1.3. Application of Single Particle Char Consumption Model

The comprehensive, time-dependent, single particle char consumption model developed in the previous chapters is applied to study oxy-combustion. The incorporation of the ARPM, which can account for the fact that, for many chars, oxidation on the surface of micropores is limited to a much greater extent than gasification [17–20], is particularly relevant to oxy-combustion environments in which both O_2 and CO_2 (and H_2O) react simultaneously, possibly in different regions of the char particle.

The characterization of the char that is formed during this oxy-combustion experiment is not available, but the coal's proximate analysis indicates that it loses ~60% of its mass as volatiles. Therefore, the char particles were assumed to be highly porous, and consistent with the high-volatile yield and the non-swelling nature of lignites, were assigned the same pore size distribution as Spherocarb char particles, which have been well-characterized [21]. The pore size distribution ranges over several orders of magnitude, and was divided as shown in Table 5.1. The true density of the particles was assumed to be 1700 kg/m^3 to bring the mass and diameter of the particles in line with those used in the CFD simulation, as particle mass and diameter were considered to be the most important variables affecting the calculated particle trajectories.

Based on their literature review, Hecht et al. [13] found that the relative apparent rate of the C+CO_2 reaction to the C+O_2 reaction is roughly 0.1-3.0x10^{-4} at 1073 K. They also determined that a best guess value of the activation energy for the C+CO_2 reaction is ~251 kJ/mol, compared to the typically much-lower activation energy for oxidation of ~160 kJ/mol. Using these values yields a ratio of the gasification to oxidation reaction of 0.1-3.0x10^{-2} at 2000 K. The reactivity of Spherocarb char, with both oxygen [21] and carbon dioxide [22], has been measured in the kinetic regime over a range of temperatures, and the activation energies and pre-exponential factors have been determined. The oxidation rate law fit a first order kinetic expression, while the gasification reaction was only measured at 1 atm and thus, not fit to a particular rate law. A power law expression of order n=0.4 for the gasification reaction will be assumed, similar to the six chars gasified by Hla et al. [23] and also similar to the value n=0.45 determined by Gonzalo-Tirado et al. [12]. Using these kinetic expressions, the relative rates at both 1073 K and 2000 K fall into the ranges given by Hecht et al. [13]. At 1073 K the ratio of rates is 1.779e-05, while at 2000 K, the ratio increases to 0.0157. The char-steam reaction rate has not been measured for this char, so its activation energy was taken to be the same as the C+CO_2 reaction [8], and as a conservative estimate, its pre-exponential factor is assumed to be double that of the C+CO_2 reaction [8].

When applied to the actual particle trajectories, however, these expressions yielded final char conversions in the furnace of only 40-60%; clearly too low for these lignite char particles. This is not surprising, given the high activation energies and the annealing results reviewed in Ch.5 that indicate that Spherocarb undergoes a significant heat treatment during its production.

Therefore, to bring the intrinsic reactivity with oxygen in line with that of a typical lignite at 1073 K [24], all of the pre-exponential factors from [21,22] were multiplied by a factor of roughly four, thus increasing the reactivities while maintaining the same ratios that fall within the range summarized by Hecht et al. [13]. The values of the intrinsic kinetic parameters employed in the simulation are given in Table 6.1.

Table 6.1. Kinetic parameters used for combustion and gasification reactions.

Reaction	A [mol/m_C^2 s atm^n]	E [kJ/mol]	n
$C+O_2 \rightarrow CO/CO_2$	1.2387 x10^5	150.6	1.0
$C+CO_2 \rightarrow 2CO$	7.8048 x10^4	281.2	0.4
$C+H_2O \rightarrow CO+H_2$	1.56096 x10^5	281.2	0.4

Note that the pore surface area (m_C^2) that participates in the gasification reactions is much larger than the area participating in char oxidation, since the intrinsic rates (per unit internal area) of the respective reactions are estimated using the method of the ARPM [25]. The values of both σ_{H_2O} and σ_{CO_2} are taken, conservatively, as 5 nm. The thermal annealing sub-model has been turned off in this section. Finally, following Hecht et al. [13], who, based on a detailed gas-phase CO oxidation mechanism, found the single film model to be adequate at 1724 K and bulk oxygen mole fractions below 12%, gas-phase reactions were turned off, since the oxygen mole fraction rarely exceeded 15% anywhere (and 6% in high temperature regions).

The pore structure of Spherocarb, combined with the intrinsic reactivity enhanced to match the lignite char from the literature, is thought to be a good representation of the relatively high volatile lignite used in the oxy-combustion experiments [15,16].

Simulations have been performed for particles of constant radius, R_0=50 μm, and for particles of initially the same size which shrink ($s(t)<R_0$) due to peripheral fragmentation at a critical porosity, $\phi_{critical}$, of 81%. The expression for reduction in particle radius has been derived by Gavalas [26] and is given in Eq. (2.36).

Of course, the true evolution of the char particles' external dimensions requires experimental determination. However, the aim of the simulations, in this regard, is simply to capture qualitative differences between the two behaviors (shrinking and constant particle size) and any possible effects of gasification reactions.

6.1.4. Results and Discussion

6.1.4.1. CFD Simulation and Particle Trajectories

Figure 6.1 shows CFD simulation results for the distributions of the gas temperature, O_2, CO_2 and H_2O mole fractions in the first meter of the furnace with 29% oxygen mole fraction in the burner streams [14]. The temperature distribution indicates that a volatile diffusion flame is stabilized in the vicinity of the burner supported by the internal recirculation zone formed by the swirling burner flow. The oxygen mole fraction is high near the burner outlet (up to 29%) and declines along the axis due to volatile and char combustion. CO_2 is the major species in most of the furnace, with a mole fraction above 70%, except in the region near the burner, where higher volatile and steam concentrations are produced by de-moisturization and devolatilization following the coal particles' injection into the furnace.

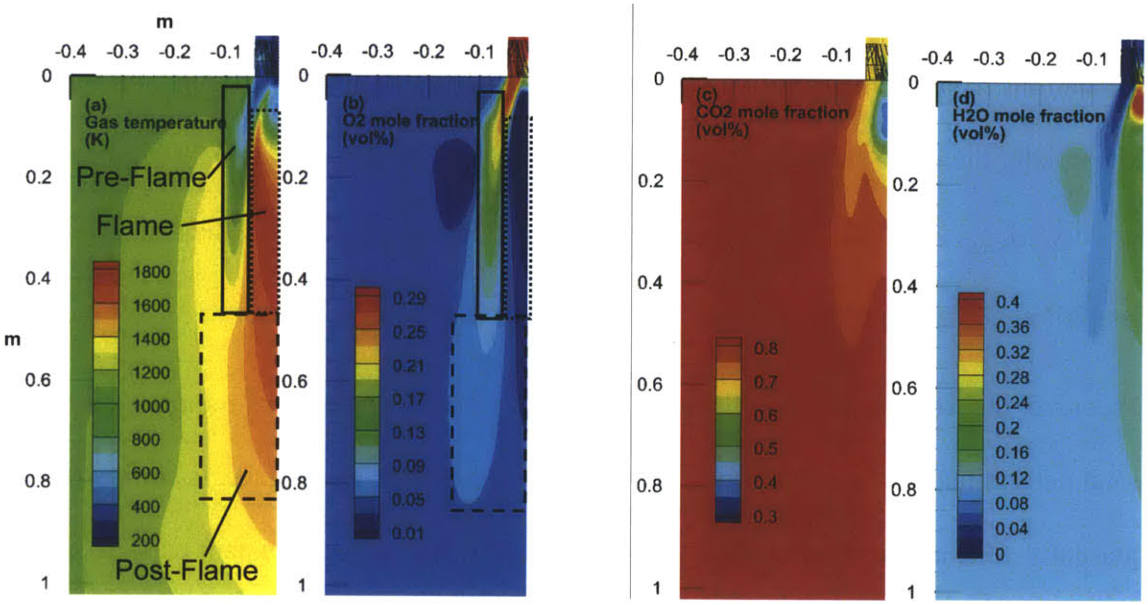

(a) **(b)** **(c)** **(d)**

Figure 6.1. CFD simulation results for (a) temperature, (b) O_2, (c) CO_2 and (d) steam distributions in the first meter of a 100 kW_{th} pilot scale test facility under oxyfuel combustion with 29% oxygen.

It can be seen in Fig. 6.1 that, while not entirely distinct, several regions can be identified for char consumption. Downstream of the primary and secondary gas-registers, the gas temperature is relatively low and the oxygen mole fraction is relatively high due to penetration of the cold oxidizer stream; this is termed the "pre-flame" region. Closer to the furnace centerline, in the volatile flame zone, the gas temperature is at its peak and the oxygen concentration is low due to volatile combustion; this is termed the "flame" region. Further downstream of the pre-flame and flame regions is the post-flame region, in which the oxygen concentration is supplemented by the secondary stream and the temperature varies depending on the radial location. Far downstream from the burners (beyond 1 m), the environment becomes more uniformly low temperature and rich in CO_2. Char consumption is slow in this region and thus is not considered important. Table 6.2 lists typical boundary conditions for the aforementioned variables in the three regions.

Table 6.2. Bulk gas conditions in the three regions identified for char consumption.

	Pre-Flame Region	Flame Region	Post-Flame Region
T (K)	1373	1773	1573
x_{O2}	0.12	0.03	0.06
x_{CO2}	0.74	0.77	0.80
x_{H2O}	0.10	0.16	0.10

Particle trajectories from the CFD simulation were analyzed. Several trajectories, in terms of their bulk gas temperature and oxygen fraction, are shown in Fig. 6.2, which indicates that particle trajectories can be grouped into two modes (shown as blue and red lines). Some coal particles travel through the pre-flame region, where the gas temperature is relatively low (1000-1400 K) and the oxygen mole fraction is relatively high (10-15%), while other particles are injected closer to the centerline and traverse the flame region, where the volatile matter is burned at higher gas temperatures (~1800 K) and the oxygen mole fraction is low (≤3%). These trajectories have been termed Particle Modes 1 and 2, respectively. All the particles then travel to the post-flame region, where the gas temperature varies, but in which Mode 2 particles generally experience temperatures that are higher by 100-200 K.

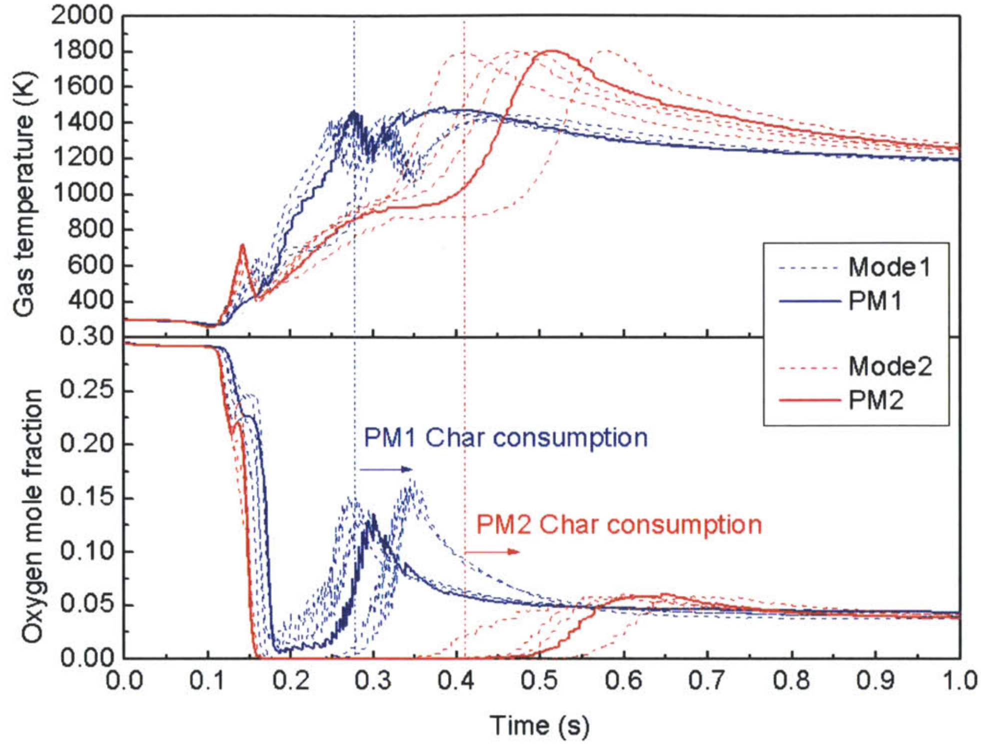

Figure 6.2. Histories of gas temperature and oxygen mole fraction along several coal particle trajectories in the CFD simulation. Trajectories with solid lines (PM1 and PM2) were chosen to be investigated using the comprehensive char combustion model.

It should be noted that the fuel burned in the experiment and modeled in the CFD simulation has a high volatile content, and hence the oxygen present during char combustion is relatively low due to the relatively high percentage of oxygen consumed in burning the volatiles. In practice, the oxygen mole fraction present during char combustion depends on the stoichiometry, flue gas recycle ratio, the coal's volatile content and the path of the particle.

The representative boundary conditions employed in the single particle simulations for Modes 1 and 2 are delineated in Fig. 6.2 as PM1 (solid blue line) and PM2 (solid red line). The single particle simulation of char consumption begins at the point when the volatile content of the coal particle has been depleted, which is also indicated in Fig. 6.2. The conversion characteristics of the char particles in the various regions present within the furnace, as well as along the trajectories, will be examined using the comprehensive single particle char consumption model. The effect of the gasification reactions will be studied as a function of the boundary conditions and extent of conversion.

6.1.4.2. Single Particle Model at Constant Particle Size

Figure 6.3 shows the radial profiles of the mole fractions of O_2 and CO_2, temperature and char conversion at two levels of total char particle conversion (integrated for the entire particle) with and without consideration of the gasification reactions, for a porous char particle ($r < 50$ μm) and its surrounding boundary layer (calculated to > 10 particle radii), reacting at the constant boundary conditions of the pre-flame, flame and post-flame regions (Table 6.2). In the pre-flame region, gasification reactions had a relatively small effect on most of the particle-scale profiles because of the low gas temperature and the dominance of char oxidation. A small difference between simulations with gasification reactions on and off is evident in the CO_2 profiles and temperature profiles at 25% overall conversion and in the conversion profiles at 75% overall conversion. These differences are small. However, gasification reactions become more significant in the other two regions.

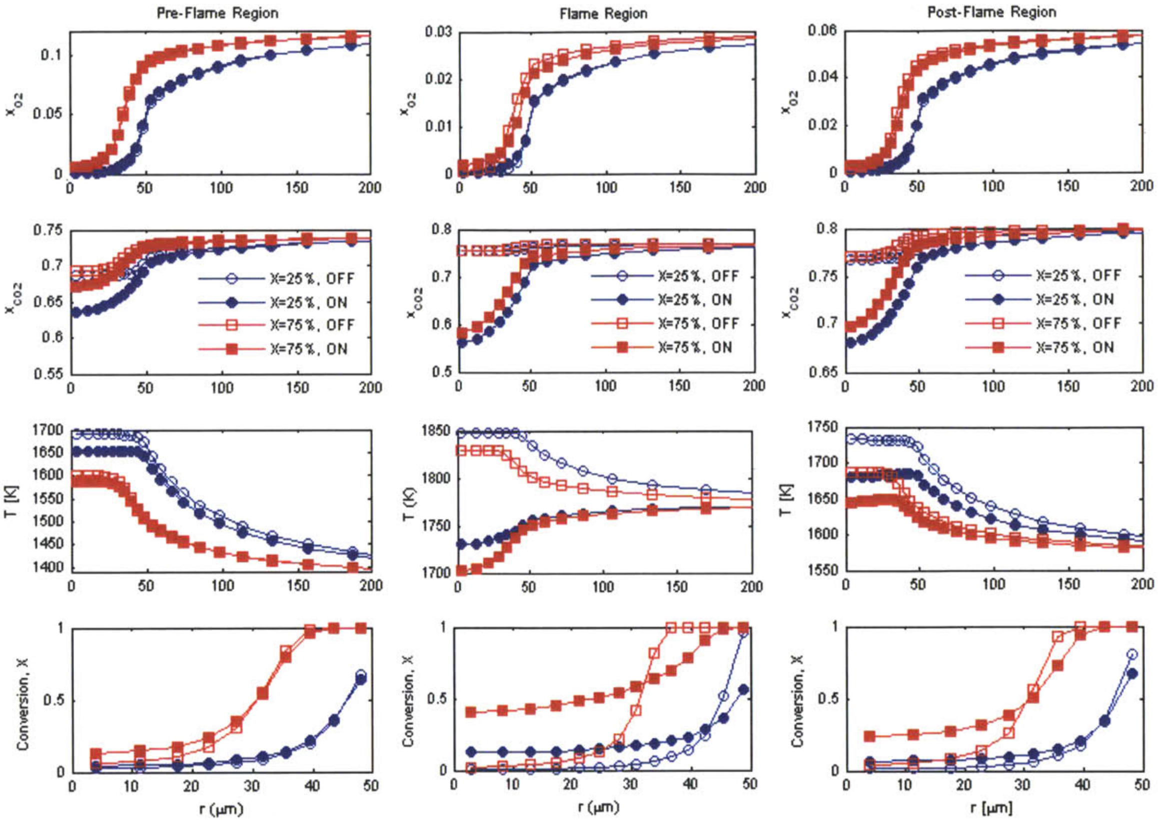

(a) (b) (c)

Figure 6.3. O_2 and CO_2 mole fractions, temperature and char conversion profiles in and around char particles at overall conversions of 25% and 75%, with gasification reactions turned off and on. (a) Pre-Flame region, (b) Flame region, and (c) Post-Flame region.

In both the flame and post-flame regions, and at both conversions, the effect of the gasification reaction on the oxygen profiles is small, while there are, of course, steeper gradients of CO_2 and lower particle temperatures (lower than the bulk gas, for the flame region) when gasification is considered. The conversion profiles illustrate that the gasification reactions can significantly alter the location within the particle where char consumption occurs. When the gasification reactions are turned on, more char consumption occurs toward the center of the particle, because of the ability of CO_2 and H_2O to penetrate the particle before they become depleted, as compared to O_2. The conversion profiles may affect char consumption rates and fragmentation behavior, given that when present, peripheral fragmentation may be inversely proportional to porosity gradients (Eq. 2.36).

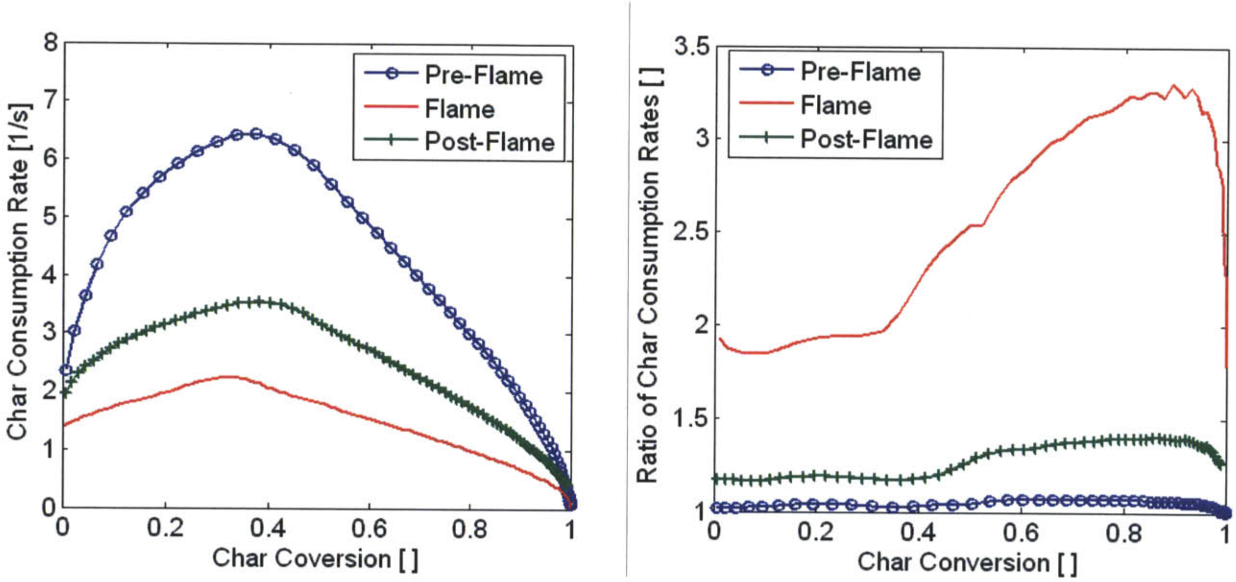

(a) (b)

Figure 6.4. (a) Char consumption rates vs. conversion for the three regions, without gasification reactions, and (b) the ratio of the rates calculated with and without gasification.

Figure 6.4(a) shows the char consumption rate for particles in the three regions without considering the gasification reactions, throughout their conversion, while Fig. 6.4(b) shows the ratio of the conversion rates with and without allowing for gasification, in each region. In the pre-flame region, the consumption rate and the particle temperature rise (up to 320 K according to Fig. 6.3(a)) are the highest of the three regions, and the rates are almost identical with and without gasification, due to the high oxygen concentration and the relatively low temperature of the bulk gas. In the post-flame region, there is a discernible difference between the two char consumption rates, which varies with conversion, from a minimum 16% increase at low conversions to a maximum increase of 40% at higher conversions. Finally, in the volatile flame region, gasification is important and can increase the char consumption rate by up to 200%, varying significantly with conversion. This is, of course, due to the high temperatures and low oxygen concentration in the flame region, due to the consumption of volatiles.

Using the equations presented in Ch. 3, it is possible to examine the contributions of reaction on the various pore sizes to the overall char consumption rate. Figure 6.5(a) and (b) shows the individual conversion rates for each pore class, integrated for the whole particle, with gasification reactions on and off, for the flame and the post-flame regions, respectively. In both regions, the macropores contribute a small fraction of the total char consumption, irrespective of the occurrence of gasification reactions, since the pore-scale effectiveness factors are essentially unity for the macropores and the intrinsic char oxidation rate is much higher than the intrinsic gasification rates. In both regions, when gasification reactions are turned off, the micropores participate negligibly in the char consumption, since configurational diffusion limitations for oxygen in the micropores are assumed to be sufficiently severe such that the micropore aren't penetrated by reactive O_2 to a significant degree, as in Ch. 5. When gasification reactions are turned on, reaction on the micropore surfaces contributes significantly to the overall conversion. In the flame region, the micropores provide the highest amount of reactive char surface area.

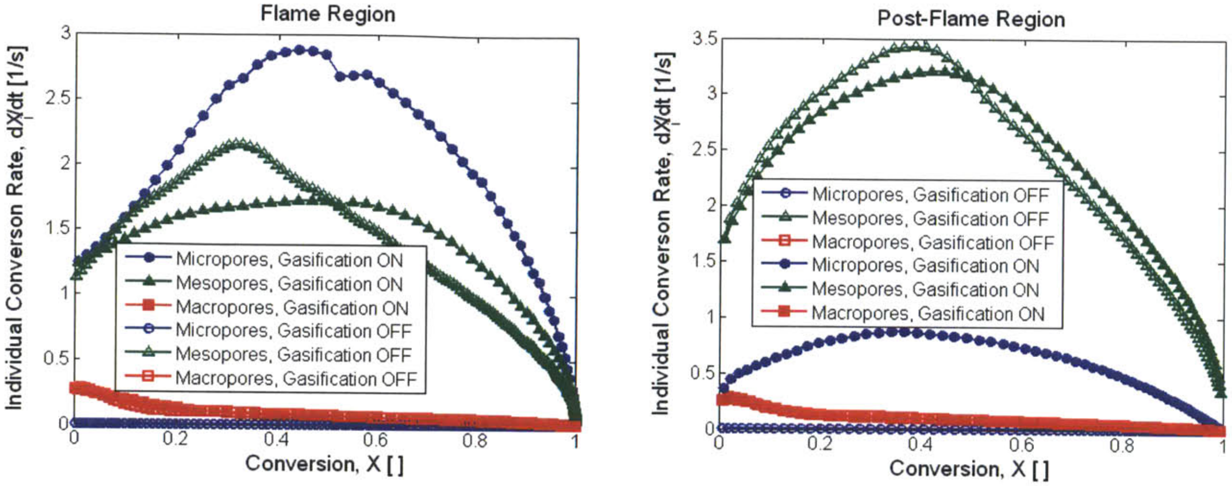

(a) **(b)**

Figure 6.5. Contribution to total char consumption rate for reaction on different pore sizes, with gasification reactions turned both on and off, for (a) the flame region and (b) the post-flame region.

The char conversion rate due to reaction on the mesoporous surface area is more interesting. For both regions it is observed that up to a total conversion of between 45-50%, $(dX/dt)_{meso}$ is higher with gasification reactions turned off, after which, it is higher for the case when gasification reactions are turned on. The increase in the ratio with conversion in Fig. 6.4(b) is due to the more quickly decreasing contribution of the mesopores to the conversion rate later in conversion for the case when gasification reactions are turned off. Although there are many interacting effects that may contribute to this behavior, it is thought to be caused by the steeper conversion profiles present at any given overall conversion, when the gasification reactions are turned off. This results in total mesopore surface areas (i.e. integrated for the entire particle) that peak and decrease earlier in the conversion compared to the case with gasification reactions turned on. This can be seen in Fig. 6.6, which plots the evolution of the normalized total and mesoporous surface areas with gasification reactions on and off, for the post-flame region.

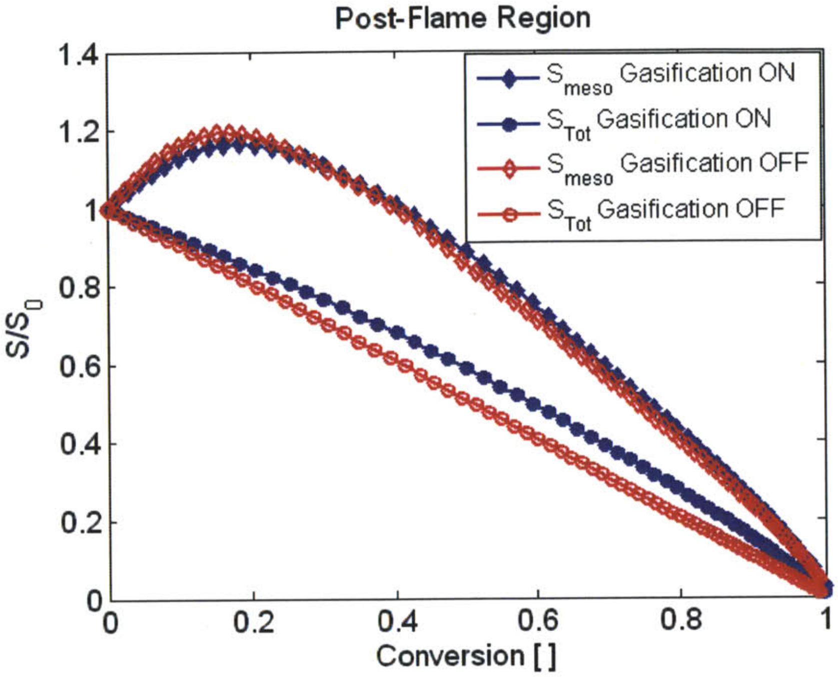

Figure 6.6. Evolution of the normalized total and mesoporous surface areas with gasification reactions on and off, for the post-flame region.

When gasification reactions are turned on and when they are non-negligible (in the flame and post-flame regions) the *local* change in surface area with conversion shows a less rapid decrease than the case with gasification reactions turned off, due to the participation of micropores in the expansion, as opposed to being only subject to overlap by larger pores. This is evident from comparing the blue and red lines in Fig. 6.7. It is also noticed that, similar to Fig. 3.5, the local surface area evolves differently with local conversion depending on the location within the particle. This is especially pronounced for the intermediate case, i.e. post-flame region, for which it seems that oxygen dominates the reaction near the exterior while gasification is more important in the interior.

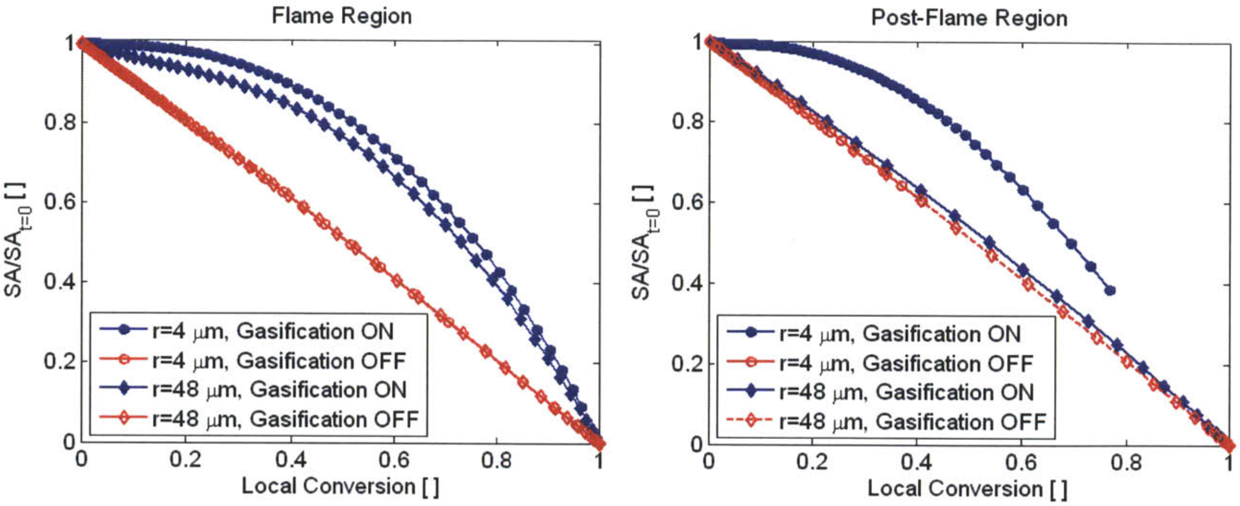

(a) **(b)**

Figure 6.7. Variation of the normalized, local surface area with local conversion for the particle interior (*r* = 4 μm) and exterior (*r* = 48 μm), with gasification reactions both on and off, for (a) the flame region and (b) the post-flame region.

Figure 6.8 shows the char conversion rates for particles subject to time-dependent boundary conditions corresponding to the two representative trajectories extracted from the CFD simulation, PM1 and PM2, each with the gasification reactions turned on and off. It is observed that the PM1 trajectory particle behaves similar to particles in the pre-flame region, in that char oxidation is dominant and gasification plays only a small role throughout conversion. Even in the post-flame region, PM1 particles experience lower temperatures than PM2 particles, due to their trajectory being further from the high-temperature, low-oxygen region near the furnace's axis, and therefore gasification is minimal.

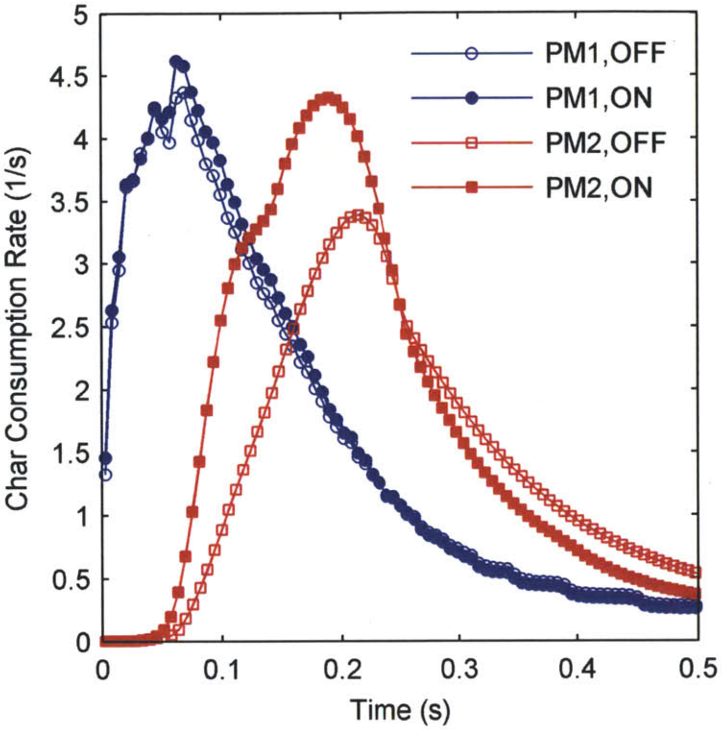

Figure 6.8. Char consumption rates versus time along the two typical trajectories (PM1 and PM2), each with gasification reactions turned off (open symbols) and on (closed symbols), as indicated in the legend.

The PM2 trajectory particle, however, exhibits significant differences in consumption rate when accounting for gasification. At char consumption times below 0.25 s, which, as can be seen in Fig. 6.2, correspond to the time-frame during which the PM2 particle experiences high temperatures (1800 K decreasing to 1550 K) and during which the oxygen mole fraction increases from 1% to 6% in the flame and post-flame regions, the rate is significantly enhanced by the gasification reactions. Beyond this time, however, the rate for the case with gasification reactions is *lower* than in the case of pure oxidation. At char consumption times of 0.25 s, the particle conversion is roughly 20% higher with gasification occurring, therefore when the PM2 particles enter the post-flame zone where gasification reactions are slow, the participating pore surface area is also smaller, causing the consumption rate to fall below the calculated rate in the case for which gasification reactions are turned off.

Examining the final conversion profiles throughout the particles resultant from reaction on each pore size, Fig. 6.9 shows that for PM2 particles, consideration of the gasification reaction substantially alters the internal evolution of the char particles. The majority of the conversion occurs on mesopores in both cases, although micropore participation is very significant when gasification reactions are considered, which can be seen in Fig. 6.9(b). This is especially the case toward the particle interior, where micropore reaction contributes almost 50% of the total conversion. Similar to the observations made regarding Figs. 6.3(b) and 6.3(c), this is due to the fact that gasification agents can penetrate the particle and react, due to both their higher concentrations and slower kinetics, whereas oxygen tends to be consumed closer to the particle surface. For this reason, the mesopores, to which oxidation is confined, dominate the final conversion near the particle's exterior.

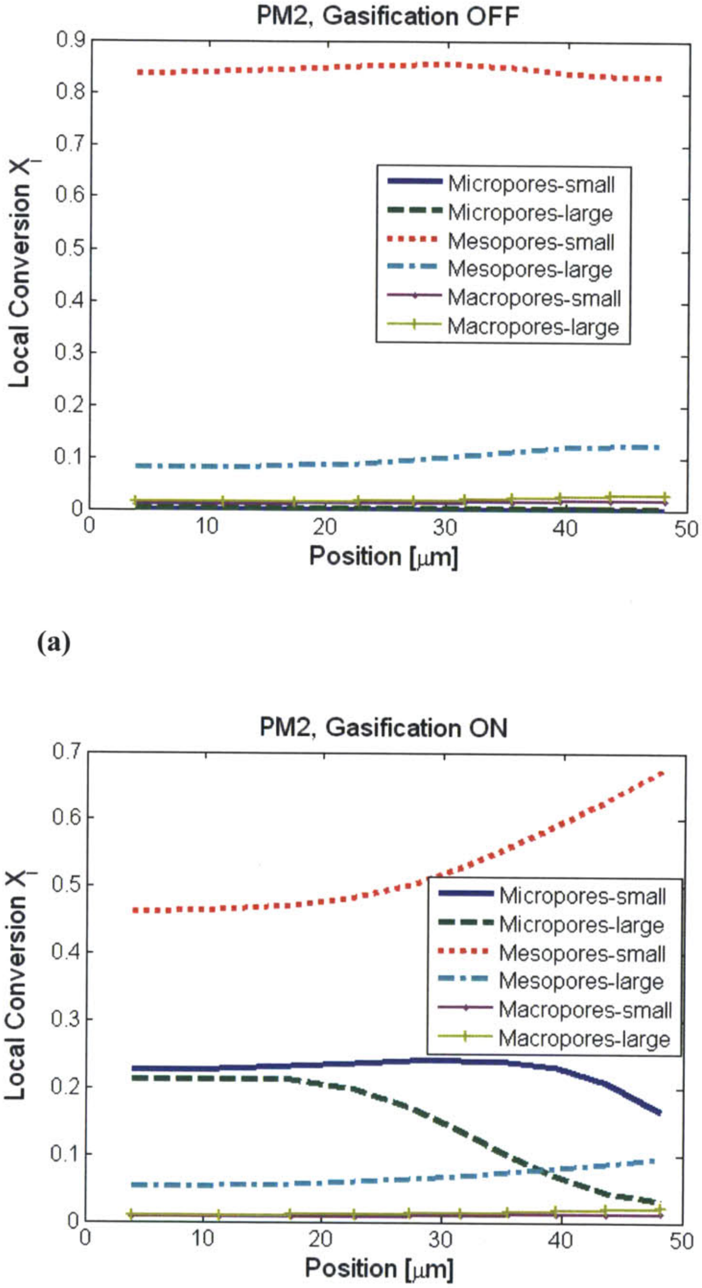

(a)

(b)

Figure 6.9. Final conversion profiles for each pore size throughout the PM2 trajectory particle, for (a) gasification reactions neglected and (b) gasification reactions turned on.

6.1.4.3. Single Particle Model with Fragmentation

The preceding analysis was performed for particles of constant size. As mentioned in Section 6.1.3, it is not known how the size of the particular lignite char particles in the experiment evolves with conversion. Nonetheless, the char particles could conceivably undergo peripheral fragmentation, and this possibility is explored using the model of Gavalas [26] described in Ch. 2. According to Eq. (2.36), shown again below, internal conversion, which decreases gradients in porosity, accelerates the reduction in particle radius due to fragmentation, where in the limit of pure kinetic control, fragmentation occurs instantaneously throughout the particle.

$$\frac{ds}{dt} = \begin{cases} 0 & \text{if } \phi(s = r_0, t) < \phi_{critical} \\ -\left[\dfrac{\partial \phi}{\partial t} \bigg/ \dfrac{\partial \phi}{\partial r} \right]_{r=R(t)} & \text{if } \phi(s(t), t) = \phi_{critical} \end{cases} \tag{6.1}$$

The evolution of total particle conversion, which is calculated for the fragmenting case by assuming the fragments are counted toward conversion (i.e. they are small and react quickly), is shown in Fig. 6.10 for the constant boundary conditions of the intermediate, post-flame region, with a critical porosity of 81%. When the particles are assumed to fragment, conversion is accelerated, with the conversion occurring fastest when gasification reactions are also turned on.

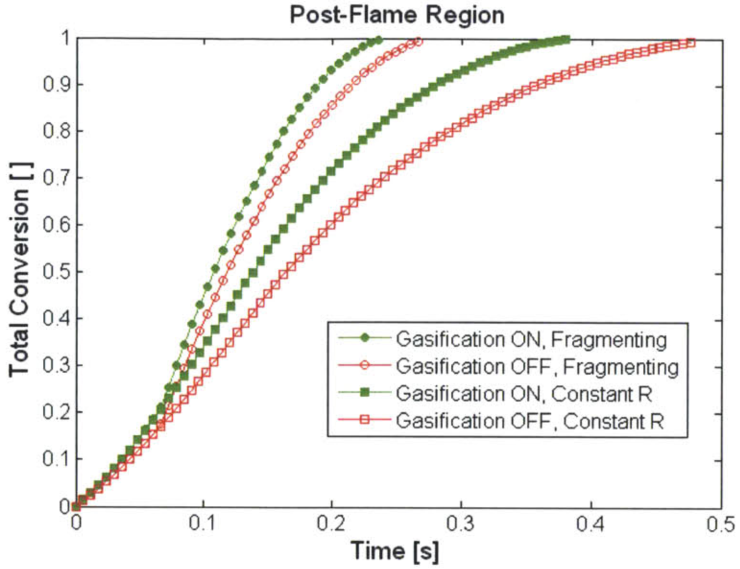

Figure 6.10. Evolution of total conversion with time, for fragmenting and constant radius particles, for gasification reactions both on and off, for the post-flame region.

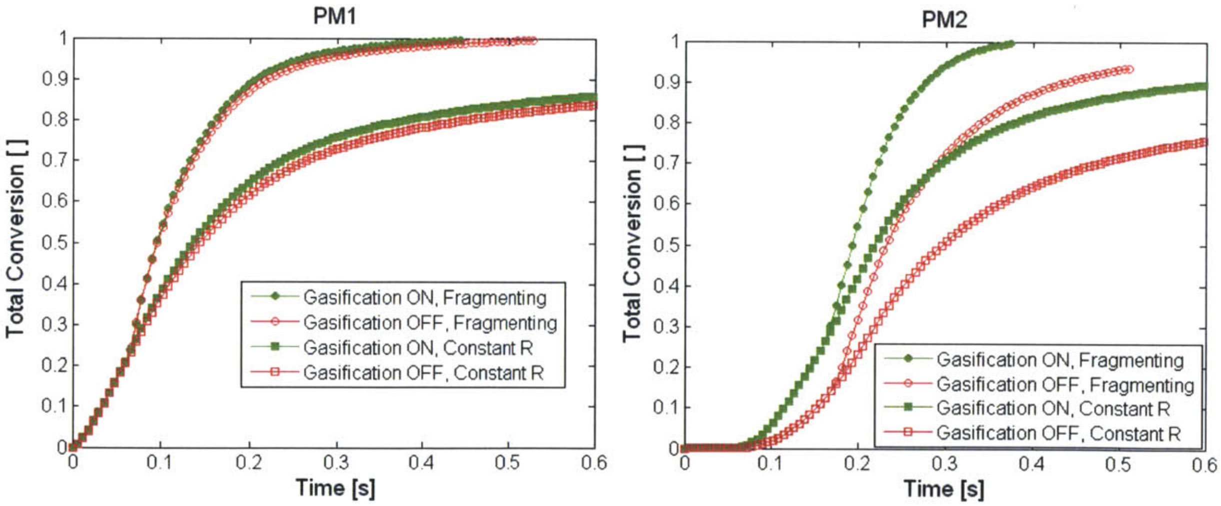

(a) **(b)**

Figure 6.11. Evolution of total conversion with time, for fragmenting and constant radius particles, for gasification reactions both on and off, for (a) the PM1 trajectory particle and (b) the PM2 trajectory particle.

Figure 6.11 plots the same variables as Fig. 6.10, for char particles subject to the time-dependent boundary conditions of the PM1 and PM2 trajectories. The difference in overall conversion between the fragmenting and non-fragmenting cases (for a given assumption about gasification reactions) is larger for the PM1 particles than for PM2 particles. This is due to the fact that conversion of PM1 particles is confined to the exterior, to a greater degree, so that the acceleration of exterior conversion is more important to the overall particle conversion. This difference would decrease as the critical porosity is increased.

In terms of the effect of gasification reactions, the PM1 trajectory shows little change when gasification reactions are turned on, as expected. The PM2 trajectory particle shows marked increases in total conversion at a given time when gasification reactions are considered, also as expected. Furthermore, it appears that the difference shown in Figure 6.11(b) is larger for the fragmenting case than for the constant radius particle.

To verify this, Fig. 6.12 examines the *difference* in conversion with gasification reactions turned on and off, for PM2 particles that shrink due to peripheral fragmentation at a critical porosity of 81%. As mentioned above, the total conversion, X_{TOT}, includes the fragmented char volume in the conversion calculation, while apparent conversion, X_{APP}, simply accounts for the conversion of the remaining char.

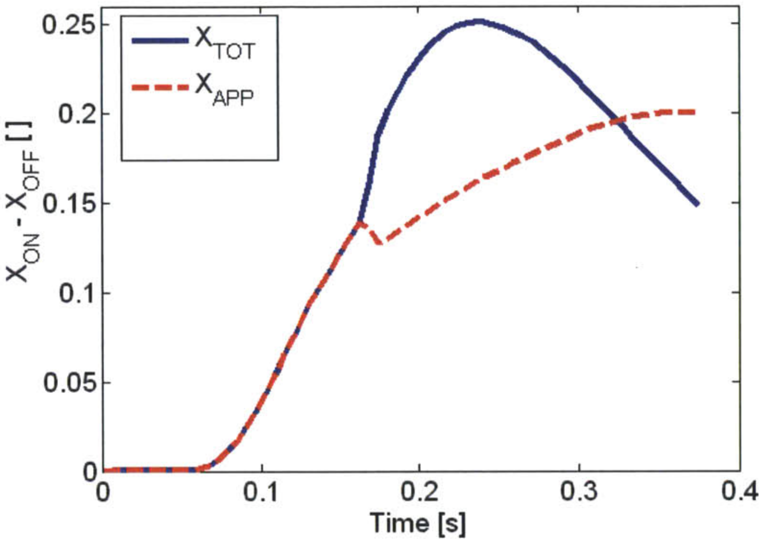

Figure 6.12. Difference in total and apparent conversion vs. time between cases with gasification reactions turned on and off, for PM2.

While both measures of char conversion are higher when gasification reactions are turned on, Fig. 6.12 shows that the *difference* in X_{TOT} between the two cases is almost double the difference in X_{APP} at some points along the PM2 trajectory. Peripheral fragmentation begins within 6 ms of each other for the two cases, but with gasification reactions turned on, the reduction in particle size is much faster. This is due to the fact that CO_2 and H_2O penetrate further into the particle than O_2, because of their higher mole fractions and slower gasification rates, decreasing the porosity gradients in the char as conversion proceeds and enhancing the rate of peripheral fragmentation, according to Eq. (6.1). At later times, when X_{TOT} levels off as it approaches unity (full conversion) for the case with gasification reactions turned on (which can be seen in Fig. 6.11(b)), this trend reverses.

6.1.4.4. Sensitivity to Kinetic Parameters

The base-case char particle employed in this study has a relatively high microporous surface area and has higher activation energies, for both oxidation and gasification, than the best-estimate values, as reviewed by Hecht et al. [13]. The ratio of apparent gasification to oxidation reactivity, neglecting contributions of reactant concentration and reaction order, is given by

$$\frac{\Re_{CO_2}}{\Re_{O_2}} = \frac{\left(\sum_i \eta_{i,CO_2} S_i\right)}{\left(\sum_i \eta_{i,O_2} S_i\right)} \frac{A_{CO_2}}{A_{O_2}} \exp\left(\frac{E_{O_2} - E_{CO_2}}{RT}\right). \tag{6.2}$$

The value of $E_{O_2} - E_{CO_2}$ in the base case is roughly -130 kJ/mol. The lignite studied by Harris and Smith [24] has an activation energy for oxidation, E_{O_2}, of 127 kJ/mol, and an activation energy for gasification, E_{CO_2}, of 230 kJ/mol, which gives a value of $E_{O_2} - E_{CO_2}$ = -103 kJ/mol. The absolute, and difference in, activation energies are lower than the base-case.

To ensure a fair comparison, the pre-exponential factors are adjusted to achieve the same ratio of initial apparent rates, $\Re_{CO_2}/\Re_{O_2}$, as the base-case at 1073 K. When scaled to higher temperatures characteristic of oxy-combustion furnaces, this lower absolute difference in activation energies implies that the ratio would increase *less* than the base-case. While the base case kinetics result in a ratio, $\Re_{CO_2}/\Re_{O_2}$, that may be towards the upper end of the spectrum at high temperatures, this new ratio, based on $E_{O_2} - E_{CO_2}$ = -103 kJ/mol, is likely near the lower end of the spectrum at high temperatures. The activation energies and pre-exponential factors for this situation are shown in the second row of Table 6.3. These kinetic parameters were applied to the same char particles as used above, with constant radii and were applied to the PM2 trajectory particle to assess the importance of gasification reactions.

6.1.4.5. Sensitivity to Pore Structure

The char employed in the base-case above also has a very high microporous surface area. While the kinetics employed in this study are chosen to give *apparent* rates (units of [mol/m^3 s]) in line with literature estimates, thus removing the effect of the pore structure on the *initial* rates, nonetheless, the evolution of the pore structure and its influence on the importance of gasification reactions should be examined. To this end, the pore structure of the char employed in the study was also varied by maintaining the same initial porosity, but using a pore structure without any micropores (the smallest pore radius was 3 nm). This was performed for both the high ΔE_a and low ΔE_a kinetics described in the preceding section. The kinetics and the RPM parameters, ψ_{all} and $\psi_{meso+macro}$, which characterize the evolution of the pore structure, are also shown in Table 6.3. Note that for the low surface area case, ψ_{all} and $\psi_{meso+macro}$ are identical. The initial, apparent rates, without accounting for any pore-level transport limitations, are identical for the two pore structure, which is indicated in Table 6.3 by the values of $A_{CO2}\,S_{all}$ and $A_{O2}S_{meso+macro}$. Note that $S_{all} = S_{meso+macro}$ for the non-microporous char.

Table 6.3. Kinetic and pore structure parameters for sensitivity study. Top row corresponds to the base case.

SA	ΔE_a	ψ_{all}	$\psi_{meso+macro}$	$A_{O2}S_{meso+macro}$ [mol/m^3 s atm^n]	E_{O2} kJ/mol	$A_{CO2}\ S_{all}$ [mol/m^3 s atm^n]	E_{CO2} kJ/mol	$\Re_{CO_2}/\Re_{O_2}$ @ 1073 K	$\Re_{CO_2}/\Re_{O_2}$ @ 1800 K
High	High	**2.65**	**9.31**	1.118e12	150	4.502e13	281	**1.779e-05**	**0.0066**
High	Low	**2.65**	**9.31**	7.913e10	127	1.454e11	230	**1.779e-05**	**0.0019**
Low	High	**3.17**	**3.17**	1.118e12	150	4.502e13	281	**1.779e-05**	**0.0066**
Low	Low	**3.17**	**3.17**	7.913e10	127	1.454e11	230	**1.779e-05**	**0.0019**

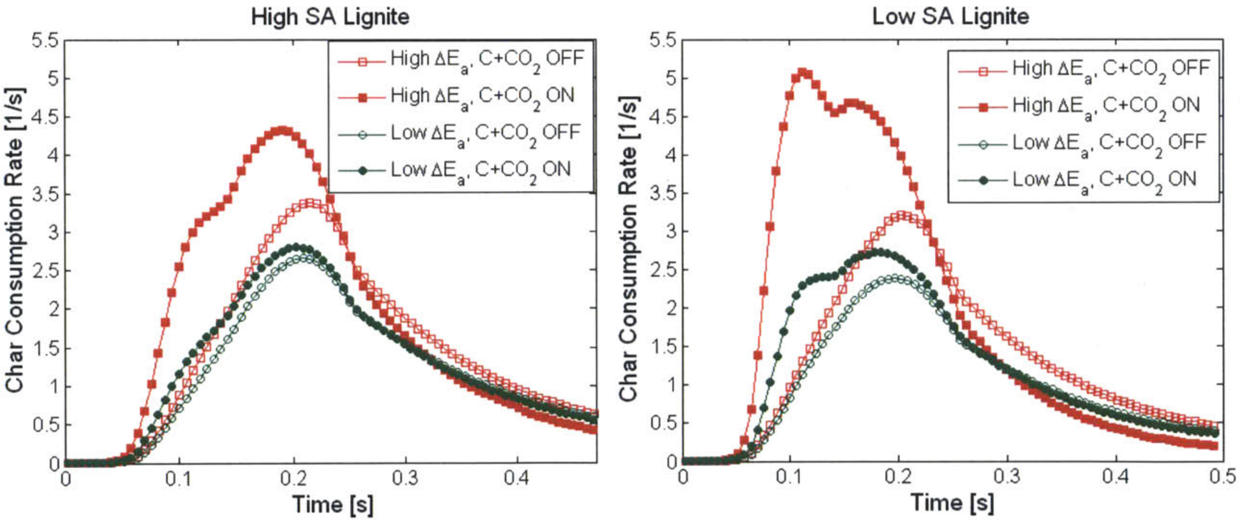

(a) **(b)**

Figure 6.13. Char consumption rates for with and without considering gasification reactions, for high and low ΔE_a kinetics, for (a) the base case, highly microporous particle and (b) a non-microporous particle with a lower surface area.

Figures 6.13 and 6.14 summarize the importance of gasification reactions for the four char/kinetic combinations, each performed with gasification reactions both on and off, as shown in Table 6.3. Figure 6.13(a) is for the highly microporous char and Fig. 6.13(b) is for the non-microporous char. Focusing first on Fig 6.13(a), it is observed that indeed, when the lower activation energies measured by Harris and Smith [24] for a lignite coal char are employed, the difference between the cases with and without gasification is reduced significantly. Nonetheless, gasification reactions are still important for the PM2 particle, especially at times before 0.2 s. The red lines in Fig. 6.13(a) are the same as those in Fig. 6.8 (the base-case).

For the non-microporous char shown in Fig. 6.13(b), both kinetic expressions (high and low ΔE_a) actually exhibit a higher difference between cases with gasification on and off than does the highly microporous char. This is shown more concisely in Fig. 6.14, in which the ratios of the rates with and without accounting for gasification are shown for all cases. The reason that the non-microporous char shows a greater difference than the highly microporous char can, to a large extent, be attributed to the surface area participating in the gasification reactions. Figure 6.15 shows the total surface area, on all pore sizes, *participating* in the C+CO_2 reaction normalized by the initial total surface area, as a function of time and position, for each particle. In the high temperature region, around t=0.1 s, the highly microporous char experiences significant transport limitations in the small pores (Fig. 6.15(a)), a phenomenon that is not a present for the non-microporous char which has larger pore sizes and whose area increases early in conversion. It can be concluded that, for this particular oxy-combustion furnace, for certain trajectories, the gasification reactions are important over a range of particle structures and kinetic parameters and should not be excluded from modeling or CFD studies, although the magnitude of their importance depends on the particular char's physical and chemical characterization.

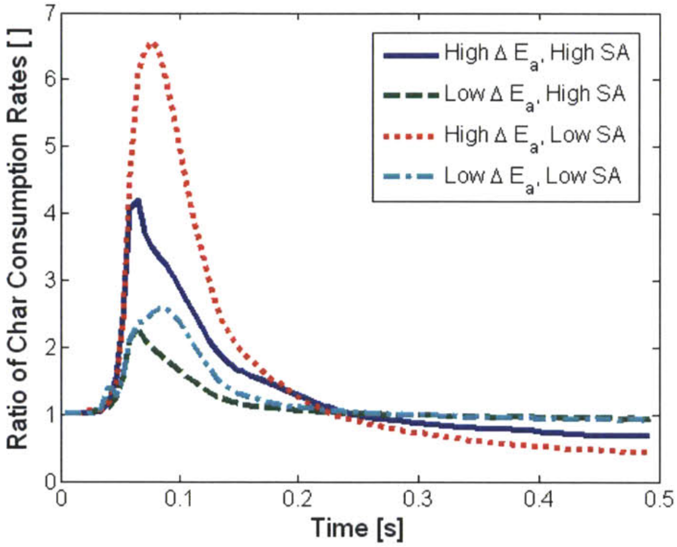

Figure 6.14. Ratio of char consumption rates with and without consideration of gasification reactions, for the four rows of Table 6.3, for PM2 trajectory particles.

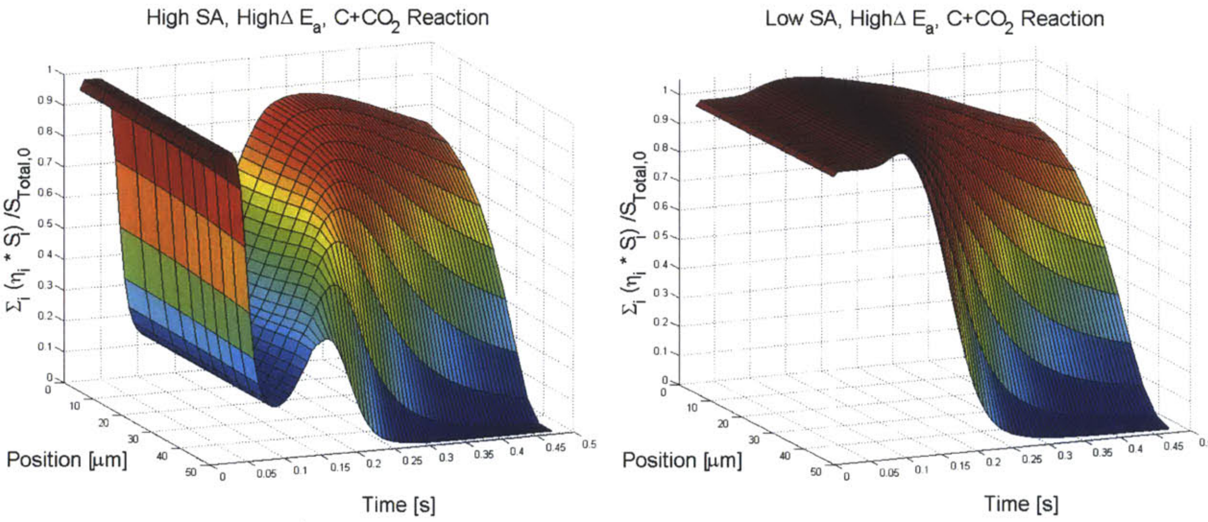

(a) (b)

Figure 6.15. Ratio of surface area participating in the C+CO_2 reaction to the total, initial surface area, as a function of position and time, for the high ΔE_a kinetics and the PM2 trajectory, for (a) the highly microporous (high SA) particle and (b) the non-microporous (low SA) particle.

6.1.5 Conclusions

A CFD simulation of a pilot-scale furnace has been employed to determine the boundary conditions to which char particles are subjected during oxyfuel combustion of a high-volatile coal. Particles typically follow one of two trajectories, taking them through different regions in the furnace. The first trajectory (Mode 1) causes char particles to react under relatively high oxygen concentrations and lower temperatures, while the second (Mode 2) results in char particles that react in more varied conditions, with higher temperatures and lower oxygen concentrations.

Employing these representative regions and trajectories as boundary conditions, single-particle char consumption simulations have been performed to evaluate the importance of char gasification reactions on char consumption rates and the effects of conversion and particle history. Most of the Mode 1 char conversion occurs in the pre-flame region and the effect of gasification reactions is minimal. Mode 2 particles react in the flame and post-flame regions and the effect of gasification reactions can be significant. For a lignite char in this particular furnace, this conclusion holds true for reaction ratios ($C+CO_2$ to $C+O_2$) on both ends of the spectrum for typical chars, as well as for high and low initial surface areas. Furthermore, CO_2 and H_2O react more uniformly throughout the particle compared to O_2, which is more diffusion-limited. This affects the relative importance of the gasification reactions with conversion and can also induce structural changes in the char that result in accelerated conversion via peripheral fragmentation. For modeling char consumption in moderate- to high-volatile oxyfuel conditions, the char gasification reaction should not be neglected without careful consideration of the reaction rates of the particular char and typical trajectories through the furnace.

6.2. Entrained Flow Gasification

6.2.1. Introduction

Entrained flow gasifiers typically operate at pressures in excess of 25 atm and use pure oxygen, instead of air, as the oxidizing gas. Fuel particles are subject to very high heating rates, quickly releasing their volatiles which burn with oxygen and subsequently undergo much slower char gasification. Entrained flow gasification within a 1000 tons per day, slurry-fed, GE Cool Water entrained flow gasifier operating at 41.45 atm with an exit gas temperature of ~1600 K has recently been studied using a 2-D CFD simulation, with Lagrangian particle tracking employed for the solid coal/char particles [27].

Typically, only the smallest particles undergo any significant char oxidation in this particular system. Since the oxygen is completely consumed within 1 meter of the injectors, mostly via reaction with volatiles (the gasifier length is ~7 meters) and is confined to a region near the reactor's centerline, only small particles that finish devolatilization relatively quickly are still located in regions with oxygen present when char consumption begins (it is assumed that the outflow of volatiles prevents oxygen from reaching the char surface and reacting) [28]. Therefore, most char particles react predominately with CO_2 and H_2O for this particular gasifier. Even for the smaller particles, any char oxidation that does occur is likely to take place very near zone III, due to the very high temperatures present in this region [28]. According to the analysis by Kumar, it is only for the particles of diameter < 85 μm that decreasing the particle size by grinding has any effect on the time required to achieve 75% conversion, since larger char particles react almost exclusively in the kinetically controlled regime [28]. Therefore, in what follows, attention is focused solely on the gasification reactions, since any oxidation that would occur would likely simply reduce the char particle diameter without affecting its density (~zone III).

6.2.2. Langmuir-Hinshelwood Kinetic Expressions and Char Characterization

If gasification in this entrained flow system is, in fact, near the kinetically controlled limit for the vast majority of the mass of solid char, then it is extremely important to incorporate accurate kinetic expressions into any models. Kinetic measurements for conditions relevant to entrained flow gasification have not been reported widely in the literature, although Liu and Niksa provide a good review of the data that is available [29]. Entrained flow conditions are conspicuous for the presence of multiple reactants (CO_2, H_2O) and products (CO, H_2) at high total pressures. For this reason, most investigators have concluded that a Langmuir-Hinshelwood type reaction mechanism must be employed, since simple power law expressions cannot account for reactant competition for active sites or product inhibition, particularly at elevated pressures [29–31]. Liu and Niksa recommend a kinetic expression of the form of Eq. (2.33) shown below, with pressures in units of atm and give apparent kinetic parameters, assuming as Arrhenius form for the rate constants, for each of the k_i based on averaged data from several coal chars. These are shown in Table 6.4. The pre-exponential factors for kinetic parameters k_5 and k_7 were extracted from Figs. 13 and 14(a) in Liu and Niksa, respectively [29].

$$R_{C+H_2O} = \frac{k_6 P_{H_2O}}{1 + \frac{k_4}{k_5} P_{CO_2} + \frac{k_4'}{k_5} P_{CO} + \frac{k_6}{k_7} P_{H_2O} + \frac{k_6'}{k_7} P_{H_2}} \qquad (6.3a)$$

$$R_{C+CO_2} = \frac{k_4 P_{CO_2}}{1 + \frac{k_4}{k_5} P_{CO_2} + \frac{k_4'}{k_5} P_{CO} + \frac{k_6}{k_7} P_{H_2O} + \frac{k_6'}{k_7} P_{H_2}} \qquad (6.3b)$$

Table 6.4. Apparent kinetic parameters used in entrained flow gasification simulations [29].

	A [1/s] or [1/ atm s]	E [kJ/mol]
k_4	293	145
k_4'	192	122
k_5	46212	177.4
k_6	4000	160
k_6'	3	70
k_7	36022	152.1

These kinetic expressions have been incorporated into the single particle char consumption model as intrinsic kinetic rates simply by normalizing them with the entire surface area of the char particles considered. Botero et al. also reviewed high pressure kinetics for entrained flow gasification [32]. They employ the rate form given by Muhlen et al. [30], with the main difference being whether CO_2 or H_2O gasification is faster at high temperatures. They determined that for this particular reactor and feedstock, the reactivity is ~10 times higher than the average parameters reported by Liu and Niksa [29] and to deal with the wide disparity in gasification rates that are reported in the literature, they employ a constant factor, the "reactivity parameter", that multiplies Eqs. (6.3) and can be tuned to match overall reactor data (conversion, temperature). This concept was employed here as well and the pre-exponential factors shown in Table 6.4 are all multiplied by ten, since the objective is simply to employ reasonable kinetics and char properties in applying the single particle model to examine any notable features of char gasification under entrained flow conditions. Along these lines, since we aren't validating any particular experiments under entrained flow conditions, a hypothetical pore structure was also assumed, with a total porosity of just over 50%, and with a pore size distribution shown in Table 6.5, with pores spanning the range of micropores to macropores. The particle diameter was chosen as 140 μm, which is toward the higher end of the range for such a gasifier.

Table 6.5. Discrete pore size distribution used in entrained flow gasification simulations.

	Micropores	Small Mesopores	Large Mesopores	Macropores
R_i [Å]	7	40	90	1877
ϕ_i [m^3/m^3]	0.129	0.067	0.064	0.248

6.2.3. Particle Trajectories and Thermal Annealing

Examination of the particle trajectories in the CFD simulation by Kumar shows that typical particles experience a short exposure to a very high temperature during devolatilization, after which the temperature (and bulk gas concentration) during char gasification is relatively constant. Some char particles, however, circulate back to the zone just-downstream of the volatile flame and experience another short exposure to a very high temperature (approaching 2500 K), although still in a region without oxygen present. Based on examination of the boundary conditions of the particles and on Fig. 4.30 in Kumar [28], the boundary conditions shown in Table 6.6 (Low T and High T) were assigned for these two regions. In order to simulate this recirculation in the single particle model, the temperature and species boundary conditions were changed as step functions at various times, with the duration of the high temperature boundary conditions being 0.02 s.

Table 6.6. Boundary conditions used in simulating the gasification of char particles subject to recirculation to the post-flame zone.

	Low T Region: (H_2O slurry)	High T Region (H_2O slurry)
T (K)	1800	2500
x_{H2}	0.30	0.13
x_{H2O}	0.22	0.48
x_{CO}	0.35	0.26
x_{CO2}	0.13	0.13

In their review, Liu and Niksa emphasize the importance of thermal annealing for entrained flow gasification conditions [29]. Due to the very high temperatures present, the concurrent annealing model was employed in conjunction with the char consumption model (they employed an effectiveness factor approach). For the current simulations, it was assumed that during devolatilization char particles were subject to a linear temperature ramp of 10^4 K/s after which they was held at 2000 K for 0.02 s. The kinetic parameters and the annealing model accounted for this pre-char-consumption heat treatment in the same manner as in Ch. 5.

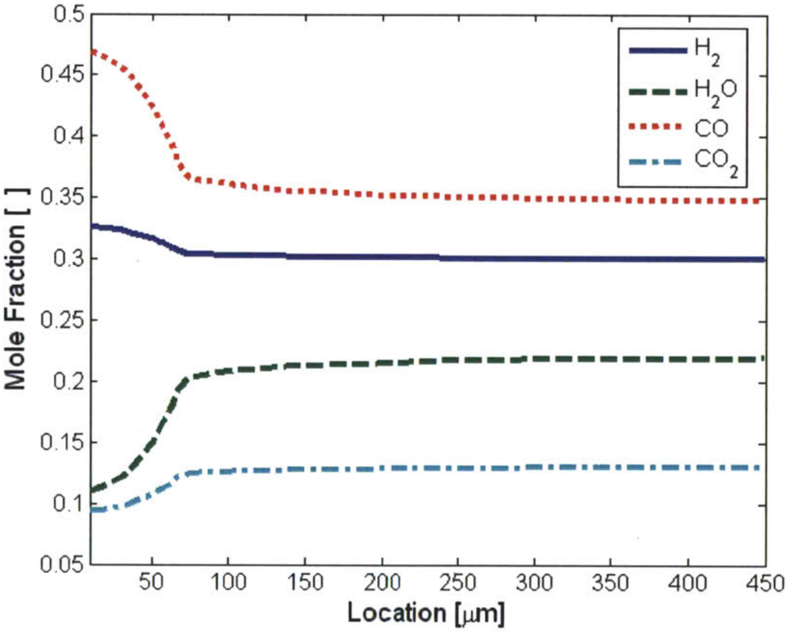

Figure 6.16. Mole fraction profiles in and around a 70 μm radius particle, at *t* = 0.1 s, in the low temperature region.

The species profiles in and around the particle for the base-case (Low T region only) are shown in Fig. 6.16 at a time of 0.10 s. It is observed that (with the tenfold increase in reactivity employed) the char gasification reactions are mildly affected by transport limitations, but not to a great extent. The gradients in char conversion/porosity are even smaller, as shown in Fig. 6.17, although not negligible.

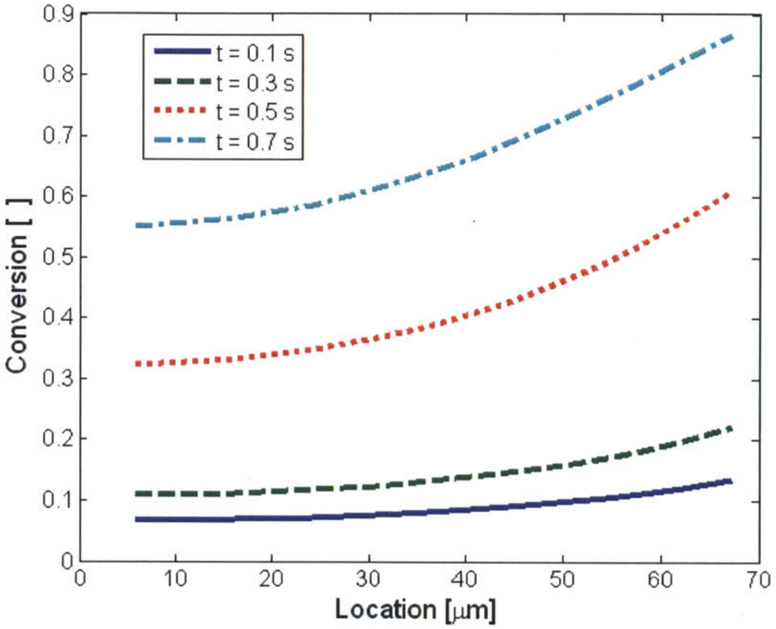

Figure 6.17. Conversion profiles throughout a 70 μm radius particle in the low temperature region at several times.

The overall char conversion vs. time is plotted in Fig. 6.18 for a particle reacting only in the low temperature region and for three hypothetical trajectories that take the particle to the high temperature region for 0.02 s at different times in their history: 0.1-0.12 s, 0.36-0.38 s and 0.6-0.62 s. It can be seen that a sharp increase in conversion occurs while the particles are subjected to the high temperature boundary conditions, with slightly larger increases for earlier jumps. It is also seen that after the particles again reach the low temperature region, the slope of the conversion vs. time plot has decreased markedly. This is due to the influence of annealing while the char is in the high temperature region. Compared to the post-devolatilization reactivity, annealing is minimal for the base-case low temperature region, while for the other cases, annealing has further reduced the char reactivity by roughly 33%. The most notable feature of

Fig. 6.18 is that it appears that the later a particle traverses the high temperature region, the better (at least up until 0.6 s, for this hypothetical situation). This is because the benefits of the high temperature on conversion are obtained without the deleterious effects of annealing taking hold early in the particle's conversion. Although particle trajectories are no doubt difficult to predict and control, this qualitative understanding might be beneficial in planning the design of particle injectors in entrained flow systems.

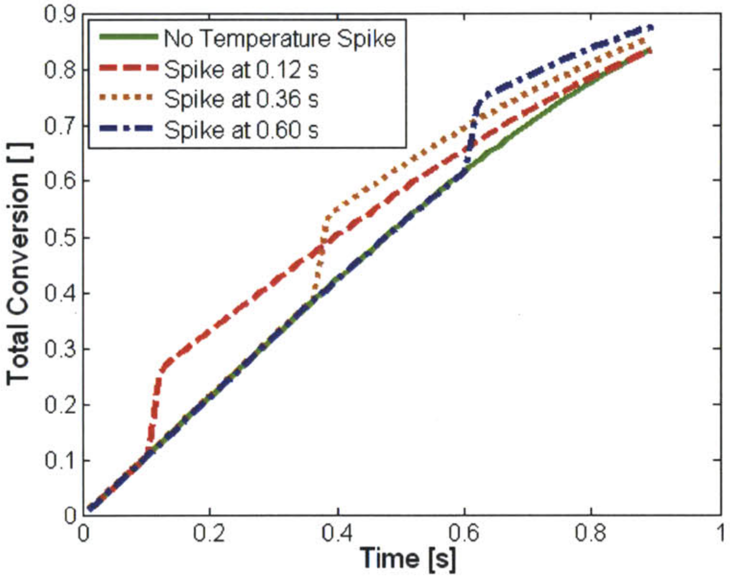

Figure 6.18. Total conversion versus time for the base case and cases where the particle is exposed to the high temperature boundary conditions.

To get an indication of the transport limitations along these trajectories, Figure 6.19 shows ex-post-facto effectiveness factor calculations for these cases using the definition of the effectiveness factor as shown in Eq. (6.4) which accounts solely for species gradients that exist through the particle.

$$\eta_{numerical} = \frac{3\int_r (\Re_{CO_2} + \Re_{H_2O}) r^2 dr}{R_0^3 (\Re_{CO_2,s} + \Re_{H_2O,s})} \tag{6.4}$$

It is seen that for the base case, for these assumed constant sized particles, the effectiveness factor increases from ~78% to ~85% as conversion proceeds, due to a decrease in diffusion limitations. During excursions in the high temperature region, the effectiveness factor falls significantly, but only to ~40%, despite the fact that the gas temperature reaches 2500 K. This is partly due to the slow kinetics of char gasification, even with the "reactivity factor" of ten employed here and partly due to the fact that in just 0.02 s, the char does not reach the gas temperature of 2500 K.

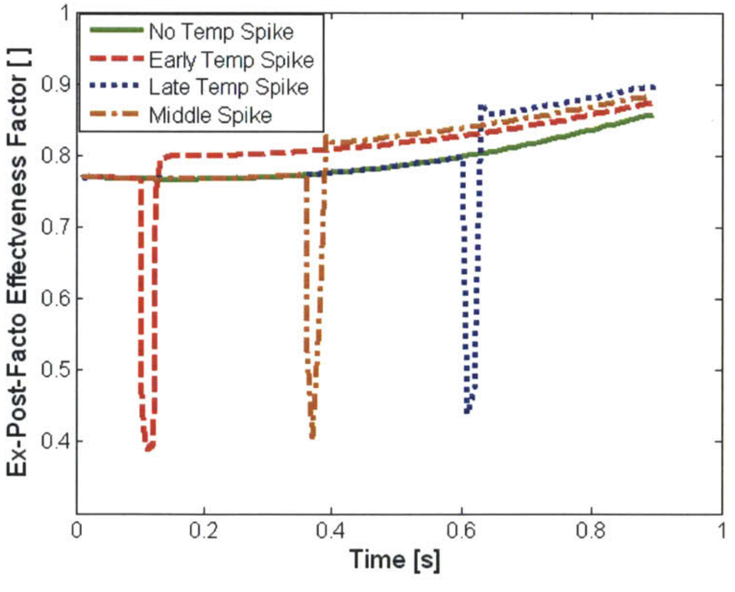

Figure 6.19. Calculated effectiveness factors versus time for the base case and temperature spikes at 0.1, 0.38 and 0.6 s.

6.2.4. Conclusions

The single particle char consumption model has been applied to entrained flow gasification conditions using what is thought to be a realistic combination of kinetics, pore structure and particle size, although the kinetics may be somewhat fast. Even so, it seems that in general, char gasification for most particle sizes and boundary conditions occurs near the kinetically-controlled regime, which implies that it is of utmost importance to incorporate accurate kinetic expressions and parameters for the particular char being studied.

The outstanding feature of the char particle trajectories from a CFD simulation of an entrained flow gasifier [28] was the recirculation of certain particles back to the zone just-downstream of the volatile flame, where they were exposed to a very high temperature (approaching 2500 K) gasifying environment. Such trajectories were examined with the model and the tradeoff between increasing conversion rates and thermal annealing due to the high temperature was discussed. Despite the uncertainty in the kinetics employed, it seems possible to draw the conclusion that, in general, later recirculation to the hot zone is advantageous.

References

[1] B. Buhre, L. Elliott, C. Sheng, R. Gupta, T. Wall, Progress in Energy and Combustion Science 31 (2005) 283-307.

[2] M. Toftegaard, J. Brix, P. Jensen, P. Glarborg, A. Jensen, Progress in Energy and Combustion Science 36 (2010) 581-625.

[3] L. Chen, S. Yong, A. Ghoniem, Progress in Energy and Combustion Science 38 (2012) 156-214.

[4] L. Zheng, Oxy-fuel Combustion for Power Generation and Carbon Dioxide (CO2) Capture, Woodhead Publishing Limited, Philadelphia, 2011.

[5] R.K. Rathnam, L.K. Elliott, T.F. Wall, Y. Liu, B. Moghtaderi, Fuel Processing Technology 90 (2009) 797-802.

[6] P.A. Bejarano, Y.A. Levendis, Combustion and Flame 153 (2008) 270-287.

[7] C.R. Shaddix, A. Molina, in:, The 33rd International Technical Conference on Coal Utilization and Fuel Systems, Clearwater, FL, 2008.

[8] C.R. Shaddix, E.S. Hecht, M. Geier, A. Molina, B.S. Haynes, in:, The 35th International Technical Conference on Clean Coal & Fuel Systems, 2010.

[9] J. Brix, P.A. Jensen, A.D. Jensen, Fuel 90 (2011) 2224-2239.

[10] J. Brix, P.A. Jensen, A.D. Jensen, Fuel 89 (2010) 3373-3380.

[11] P. Naredi, S. Pisupati, Energy and Fuels 25 (2011) 2452-2459.

[12] C. Gonzalo-Tirado, S. Jiménez, J. Ballester, Combustion and Flame (2011) 1-11.

[13] E.S. Hecht, C.R. Shaddix, A. Molina, B.S. Haynes, Proceedings of the Combustion Institute 33 (2011) 1699-1706.

[14] L. Chen, A. Ghoniem, In Preparation (2012).

[15] K. Andersson, R. Johansson, S. Hjartstam, F. Johnsson, B. Leckner, Experimental Thermal and Fluid Science 33 (2008) 67-76.

[16] S. Hjärtstam, K. Andersson, F. Johnsson, B. Leckner, Fuel 88 (2009) 2216-2224.

[17] G. Ballal, K. Zygourakis, Ind. Eng. Chem. Res. 26 (1987) 1787-1796.

[18] P. Salatino, O. Senneca, S. Masi, Carbon 36 (1998) 443-452.

[19] B. Feng, S.K. Bhatia, Carbon 41 (2003) 507-523.

[20] D.G. Roberts, D.J. Harris, T.F. Wall, Energy & Fuels 17 (2003) 887-895.

[21] M. D'Amore, L. Tognotti, A.F. Sarofim, Combustion and Flame 95 (1993) 374-382.

[22] J.K. Floess, J.P. Longwell, A.F. Sarofim, Energy and Fuels 2 (1988) 18-26.

[23] S.S. Hla, D. Harris, D. Roberts, Gasification Conversion Model-PEFR: Research Report 80, 2007.

[24] D.J. Harris, I.W. Smith, Symposium (International) on Combustion 23 (1990) 1185-1190.

[25] S.L. Singer, A.F. Ghoniem, Energy and Fuels 25 (2011) 1423-1437.

[26] G.R. Gavalas, Combustion Science and Technology 24 (1981) 197-210.

[27] M. Kumar, A.F. Ghoniem, Energy & Fuels 26 (2012) 464-479.

[28] M. Kumar, Multiscale CFD Simulations of Entrained Flow Gasification, M.I.T., 2011.

[29] G.-su Liu, S. Niksa, Progress in Energy and Combustion Science 30 (2004) 679-717.

[30] H.-J. Muhlen, K.H. van Heek, H. Juntgen, Fuel 64 (1985) 944-949.

[31] D.G. Roberts, D.J. Harris, Energy & Fuels 26 (2012) 176-184.

[32] C. Botero, R.P. Field, H.J. Herzog, A.F. Ghoniem, Submitted to the Clearwater Coal Conference (2012) 1-13.

Chapter 7. Conclusions and Future Work

7.1. Conclusions

A comprehensive, predictive model for the gasification and combustion of multi-modal, porous char particles has been developed. The model is a transient, one–dimensional, spherically symmetric simulation of a reacting, porous char particle and its surrounding boundary layer. The model incorporates the adaptive random pore model (ARPM), which is consistent with an evolving, multi-modal porous structure and which extends the original random pore model to allow different pore sizes to grow at different rates depending on the instantaneous interplay between transport and kinetics at the pore-scale, at different locations within the particle.

For each pore size, the ARPM employs separate equations for pore growth, conversion and surface area, using the random capillary model formulation and by employing pore-scale effectiveness factors to estimate the participation of all pore sizes in different reactions, at all locations and times. At any time when measured reaction rate and structural data are both available, the method can be applied to estimate intrinsic (per unit surface area) kinetic parameters. This framework allows the evolution of the char structure with local conversion to adapt to time-dependent boundary conditions or the development of intra-particle species or temperature gradients, rather than being pre-determined. Without fitting parameters, the ARPM has been validated using coal char oxidation data in the kinetic regime with reasonable agreement [1].

For the comprehensive model, gas transport within the porous structure is modeled using the flux relations of Feng and Stewart, which are also consistent with a multi-modal pore structure. The model can account for concurrent annealing, which is very important for high temperature conditions, and for particle size reduction due to peripheral fragmentation. A model for the adherence and softening of included ash on the particle surface was also developed and incorporated into the overall modeling framework.

The model has been validated against zone II combustion data for Spherocarb char [2] without the use of fitting parameters and reasonable agreement with experimental measurements of particle temperature and conversion have been obtained. The participation of various pore sizes in reaction and the occurrence of gasification reactions in certain combustion conditions are shown to have non-negligible effects on the overall conversion and temperature evolution in these conditions.

Results from a CFD simulation of a pilot-scale furnace have been used to determine the boundary conditions to which char particles are subjected during oxyfuel combustion of a lignite coal. Employing representative regions and trajectories as boundary conditions, single-particle char consumption simulations have been performed to evaluate the importance of char gasification reactions on char consumption rates and the effects of conversion and particle history. For the pre-flame region of that particular furnace and coal type, the effect of gasification reactions is minimal. For the flame and post-flame regions the effect of gasification reactions can be significant. Furthermore, CO_2 and H_2O react more uniformly throughout the particle compared to O_2, which is more diffusion-limited. This affects the relative importance of the gasification reactions with conversion and can also induce structural changes in the char that result in accelerated conversion via peripheral fragmentation. For modeling char consumption in moderate- to high-volatile oxyfuel conditions, it can be concluded that the char gasification reaction(s) should not be neglected without careful consideration of the reaction rates of the particular char and typical trajectories through the furnace.

The single particle char consumption model has also been applied to entrained flow gasification conditions, represented by time-dependent boundary conditions that exhibit sudden steps in gas temperature and species concentration to conditions typical of the zone just-downstream of the volatile flame. The model was used to examine the tradeoff between increasing conversion rates and thermal annealing due to the high gas temperature. It appears that recirculation to the hot zone later in conversion is advantageous.

7.2. Potential Applications of the Single Particle Model

Interest exists in using CO_2 as a slurrying medium for entrained flow gasification due to the oxygen savings that would result from not having to generate the heat needed to vaporize large amounts of H_2O [3]. However, there is concern that altering the gas concentration within the reactor will result in lower char conversion levels due to the difference in rates between steam and CO_2 gasification and the fact that when using a CO_2 slurry, the mole fraction of CO is greatly increased while that of H_2O is significantly decreased [3]. Interest also exists in the gasification of very high ash coals, which can produce chars with greater than 50% ash by weight [4]. The present model could potentially be useful in studying both such situations. However, to make even useful qualitative predictions about either of these cases, it is important that the kinetic parameters and the parameters required by the ash-adherence sub-model be known with a higher degree of confidence.

References

[1] J.L. Su, D.D. Perlmutter, AIChE Journal 31 (1985) 973-981.

[2] B.J. Waters, R.G. Squires, N.M. Laurendeau, R.E. Mitchell, Combustion and Flame 74 (1988) 91-106.

[3] C. Botero, R.P. Field, H.J. Herzog, A.F. Ghoniem, Submitted to the Clearwater Coal Conference (2012) 1-13.

[4] R.C. Everson, H.W.J.P. Neomagus, H. Kasaini, D. Njapha, Fuel 85 (2006) 1076-1082.

A. Appendix

A.1. Flux Sub-model

We shall now verify that the tortuosity tensor, as defined in the Feng and Stewart model and applied to the geometry assumed by the adaptive random pore model, in which there are no dead-end pores, does in fact reduce to an isotropic tensor. The tortuosity tensor, $\overline{\overline{\kappa(R)}}$, is defined by the equation [1]:

$$dR\int_{\Omega}\overrightarrow{\delta_{\Omega}}\,\overrightarrow{\delta_{\Omega}}\,f(R,\Omega)d\Omega = \overline{\overline{\kappa(R)}}\,d\phi(R), \tag{A.1}$$

where $f(R,\Omega)$ is the fraction of pore-space associated with interconnected pores of radius in the interval $R+dR$, with orientation within the incremental solid angle $d\Omega$ about Ω and $\overrightarrow{\delta_{\Omega}}$ is a unit vector along a pore of orientation Ω. Since the pore size and orientation are uncorrelated,

$$f(R,\Omega) = f(R)f(\Omega), \tag{A.2}$$

and since all orientations are equally probable, $f(\Omega) = {}^{1}\!/_{2\pi}$. When there are no dead-end pores present, the fraction of interconnected pores, *f*, is the same as the porosity, ϕ. In spherical coordinates, the unit vector $\overrightarrow{\delta_{\Omega}} = \cos\theta\,\widehat{e_{\theta}} + \sin\theta\sin\psi\,\widehat{e_{\psi}}$ and the integral over all orientations, Eq. (A.1), can be written as

$$\frac{\phi(R)}{2\pi}dR\int_0^{2\pi}\int_0^{\pi/2}\begin{bmatrix}\cos^2\theta & \cos\theta\sin\theta\sin\psi \\ \cos\theta\sin\theta\sin\psi & \cos^2\theta\end{bmatrix}\sin\theta d\theta d\psi = \overline{\overline{\kappa(R)}}d\phi(R). \tag{A.3}$$

Evaluating the integrals and substituting, $d\phi(R) = \phi(R)dR$, one obtains

$$\overline{\overline{\kappa(R)}} = \begin{bmatrix}\frac{1}{3} & 0 \\ 0 & \frac{1}{3}\end{bmatrix}, \tag{A.4}$$

which implies that the tortuosity is isotropic and equal to 1/3 for the random geometry of the RPM in the presence of a distribution of pore sizes.

It was also verified that the choice of the n^{th} species in the mass transport model did not affect the numerical results. For the gasification case with bulk mole fractions shown below and a bulk temperature of 2500 K and using the kinetic data shown in Table 6.4 with a 57 μm char particle of 41% porosity, it is seen that the results for species mole fraction profiles are identical whether the n^{th} species was taken as N_2 or CO.

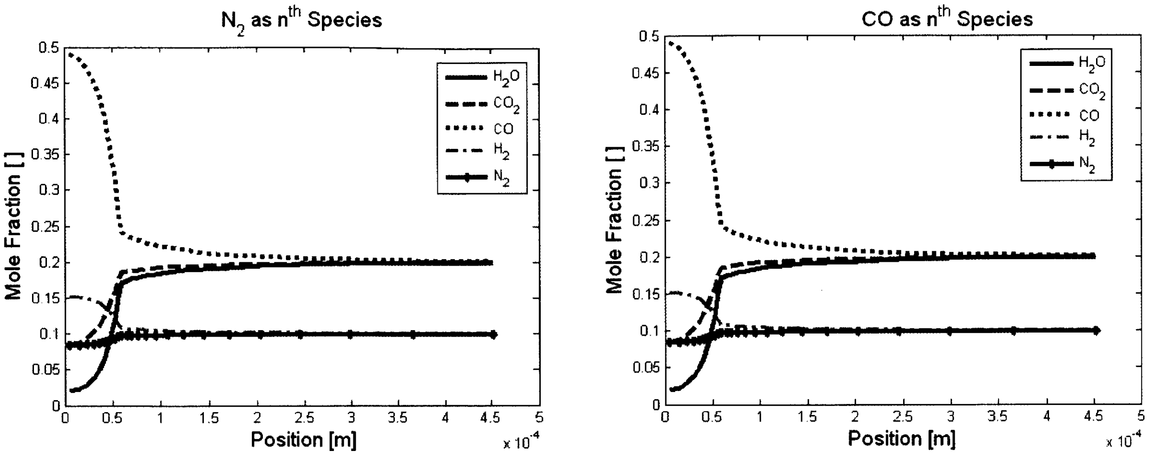

Figure A.1. Mole fraction profiles in and around a 57 μm radius particle, under gasification conditions, using (a) N_2 as the n^{th} species and (b) CO as the n^{th} species in the calculation.

Appendix A.2. Relation between the RPM Structural Parameter, ψ_{RPM}, and the ARPM

We now show that the pore structure evolution predicted by the random pore model [2] and the random capillary model (RCM) are identical [3]. This is not surprising given that they are based on the same assumptions about the pore structure geometry and pore growth mechanism (uniform radial expansion). Nonetheless, the two authors approach the derivation in different ways and there has been some confusion in the literature with respect to the parameters of Gavalas' model. It will also be shown that when certain pore sizes do not participate in the reaction(s), that the structural parameter of the RPM, ψ, when used to predict normalized conversion rates and when calculated using the measurements of the initial pore structure, should employ the entire pore volume, but only the participating surface area and pore length. This is useful in comparing modeling results for the ARPM, which is based on Gavalas' RCM derivation, with literature results for chars based on the RPM derivation.

The expression derived by Gavalas for the dimensionless reaction rate (total char conversion rate) or dimensionless surface area will be manipulated into the form employed by Bhatia and Perlmutter in the RPM. The dimensionless ratio representing the RPM parameter, ψ, will be compared with the expression given by the RPM. This will be performed for the general, discrete case, in which n pore sizes are present but only pore sizes $j > i$ participate in reaction (i.e. pore-scale effectiveness factors, η_i, are either zero or unity). For simplicity, it will be assumed $i=1$ in what follows; in other words $q_{i=1} = 0$ and $q_{j>1} = 1$ at all times (no reaction on the smallest pore size, full penetration on larger pores).

In such a case, using the relationships given for total porosity Eq. (3.3) in the definition of total conversion Eq. (3.8), and separating the exponential term for $i = 1$ from all other pore sizes, j, the total conversion can be written,

$$X = \frac{\exp\left[-\pi\sum_{j\neq i} l_{0,j}R_{0,j}^2\right]\exp\left[-\pi(l_{0,i}R_{0,i}^2)\right] - \exp\left[-\pi\sum_{j\neq i} l_{0,j}(R_{0,j}+q_j)^2\right]\exp\left[-\pi(l_{0,i}R_{0,i}^2)\right]\exp\left[-\pi(l_{0,i}R_{0,i}^2)\right]}{\exp\left[-\pi\sum_{j\neq i} l_{0,j}R_{0,j}^2\right]\exp\left[-\pi(l_{0,i}R_{0,i}^2)\right]}, \quad \text{(A.5)}$$

which after cancellation becomes,

$$X = 1 - \frac{\exp\left[-\pi\sum_{j\neq i} l_{0,j}(R_{0,j}+q_j)^2\right]}{\exp\left[-\pi\sum_{j\neq i} l_{0,j}R_{0,j}^2\right]}. \quad \text{(A.6)}$$

After expanding the term in parentheses and substituting for $q_j = q$, because all pore sizes aside from i grow the same amount, q, we obtain

$$X = 1 - \exp\left[-\pi \sum_{j \neq i} l_{0,j} \left(2R_{0,j} q + q^2 \right) \right] \tag{A.7}$$

and upon differentiation,

$$\frac{dX}{dt} = 2\pi v (1-X) \sum_{j \neq i} l_{0,j} \left(R_{0,j} + q \right), \tag{A.8}$$

where $v = \dfrac{dq}{dt}$ is the rate of pore wall recession for all pores $j > i$, which depends on the reaction rate and char density. Equation (A.7) can be solved for $q(X)$ using the quadratic formula,

$$q = \frac{ -\sum_i l_{0,i} R_{0,i} + \left[\left(\sum_i l_{0,i} R_{0,i} \right)^2 - \dfrac{\ln(1-X)}{\pi} \sum_i l_{0,i} \right]^{1/2} }{ \sum_i l_{0,i} } \tag{A.9}$$

and inserted into Eq. (A.8) to yield, upon cancellation and rearrangement,

$$\frac{dX}{dt} = 2\pi v (1-X) \left(\sum_{j \neq i} l_{0,j} R_{0,j} \right) \sqrt{ 1 - \frac{ \sum_{j \neq i} l_{0,j} }{ \pi \left(\sum_{j \neq i} l_{0,j} R_{0,j} \right)^2 } \ln(1-X) } \,. \tag{A.10}$$

Comparing Eq. (A.10) with Bhatia and Perlmutter's derivation (e.g. Equation (1) in [4]),

$$\frac{dX}{dt} = \frac{kC^n(1-X)S_0\sqrt{1-\psi\ln(1-X)}}{1-\phi_{0,Tot}} \tag{A.11}$$

and substituting for the reaction rate (units of m/s) $v = kC^n$ and for the initial surface area $S_0/(1-\phi_{0,Tot}) = 2\pi\sum_{j\neq i} l_{0,j}R_{0,j}$ (note that it is the surface area of pores *participating* in the *reaction* that goes into the *reaction* rate expression), it is seen that:

(a) the RPM parameter, ψ, is expressed in terms of RCM variables as

$$\psi = \frac{\left(\sum_{j\neq i} l_{0,j}\right)}{\pi\left(\sum_{j\neq i} l_{0,j}R_{0,j}\right)^2}, \tag{3.6c}$$

in which the summation is over only the reacting pore sizes, as was mentioned in Ch. 3, and that (b) the two models are identical, although the formulation of Gavalas offers more flexibility. Substituting in Equation (3.6c) using Eq. (3.11) and noting that $L_{0,Tot} = (1-\phi_{0,Tot})\sum_{j\neq i} l_{j,0}$, because $l_{j,0}$ is constant since it includes overlapped volume, it is seen that Eq. (3.6c) is identical to the RPM definition of ψ given by (3.29). Note that both models require the *entire* pore size distribution to be measured to determine the pore length per unit volume.

References

[1] R. Jackson, Transport in Porous Catalysts, Elsevier, New York, 1977.

[2] S.K. Bhatia, D.D. Perlmutter, AIChE Journal 26 (1980) 379-386.

[3] G.R. Gavalas, AIChE Journal 26 (1980) 577-585.

[4] S.K. Bhatia, D.D. Perlmutter, AIChE Journal 27 (1981) 247-254.